Plasma Physics Reports, Vol. 30, No. 11, 2004, pp. 895–906. Translated from Fizika Plazmy, Vol. 30, No. 11, 2004, pp. 963–975.

TOKAMAKS

Modeling of the Feedback Stabilization of the Resistive Wall Modes in a Tokamak

S. Yu. Medvedev and V. D. Pustovitov

Keldysh Institute of Applied Mathematics, Russian Academy of Sciences, Miusskaya pl. 4, Moscow, 125047 Russia
Russian Research Centre Kurchatov Institute, pl. Kurchatova 1, Moscow, 123182 Russia

Received March 7, 2003; in final form, March 24, 2004

Abstract—The problem of feedback stabilization of the resistive wall modes (RWMs) in a tokamak is discussed. An equilibrium configuration with the parameters accepted for the stationary ITER scenario 4A is considered as the main scenario. The effect of the vacuum chamber's shape on the plasma stability is studied. Ideal MHD stability is analyzed numerically by using the KINX code. It is shown that, in a tokamak with the parameters of the designed T-15M tokamak, RWMs can be stabilized by a conventional stabilizing system made of framelike coils. However, the maximum possible gain in β in such a tokamak is found to be smaller than that in ITER. It is shown that, in this case, a reduction in the plasma–wall gap width by 10 cm allows one to substantially increase the β limit, provided that RWMs are stabilized by active feedback. © *2004 MAIK "Nauka/Interperiodica".*

1. INTRODUCTION

A reactor tokamak will be economically justified only if it will operate stably as a stationary system at sufficiently high β (the ratio of the plasma pressure to the magnetic pressure); according to some estimates, at $3 < \beta_N < 4$ [1], although somewhat higher β_N (up to $\beta_N = 6$ and even to $\beta_N = 8$) are usually mentioned [2]. For comparison, the ITER tokamak is planned to operate at β_N of about 2–2.5 [3]. Here, β_N is the so-called Troyon factor,

$$\beta_N = \beta[\%]\frac{a[\mathrm{m}]B[\mathrm{T}]}{I[\mathrm{MA}]}, \qquad (1)$$

where a is the plasma minor radius, B is the vacuum magnetic field at the plasma center, and I is the net plasma current.

One of the factors limiting β in stationary tokamak discharges can be external kink modes that cannot be completely stabilized by the vacuum vessel wall because of the finite wall conductivity—the so-called resistive wall modes (RWMs) [1]. These modes arise in tokamak discharges at quite moderate values of β when the discharge duration is longer than the skin time of the wall. RWMs have been observed and thoroughly investigated in the DIII-D tokamak over the last few years (see [4–12] and the references therein). At first, these experiments showed [4] that RWMs could be excited in the DIII-D tokamak when β_N was larger than $4l_i$, where l_i is the internal inductance of the plasma column. It was then found that strong RWM instability can also develop in DIII-D at much smaller β_N of about $2.5l_i$ [11] or even $2.4l_i$ [12]. These limits are rather low for discharges with broad current density profiles and are obviously lower than those required for reactor-tokamaks [1, 2]. Therefore, serious consideration is now being given to the RWM problem in tokamak research. ITER will probably enter the parameter range corresponding to RWM instability in some regimes; hence, the problem of RWM stabilization remains one of the main ITER physics issues [1, 3, 13–15].

The RWM stability limits are determined by the properties of the plasma configuration itself. However, the growth rates and the possible gain in β due to the active stabilization of RWMs depend substantially on the shape and electrical properties of the vacuum vessel. In this paper, the feedback stabilization of RWMs is modeled for an ITER-like tokamak, but with another wall shape—specifically, with that proposed in the technical project of the T-15M tokamak [16] (for brevity, this system will be referred below to as T-15M). A version with the ITER's wall shape is also considered for comparison. The problem is treated in a standard formulation as one of suppressing instability by means of external fields created by the feedback-controlled correction coils. In many respects, we rely here on the results of our previous paper [17], where the ideal MHD limits in the ITER and T-15M tokamaks were studied, and use the same numerical methods.

The paper is organized as follows: In Section 2, we discuss the possible gain in β due to RWM feedback stabilization in a tokamak. In Section 3, the formulation of the problem (mainly in regard to the choice of the stabilizing system) is discussed. In Section 4, the results of our calculations are presented. A brief summary of our analysis is given in the Conclusion.

1063-780X/04/3011-0895$26.00 © 2004 MAIK "Nauka/Interperiodica"

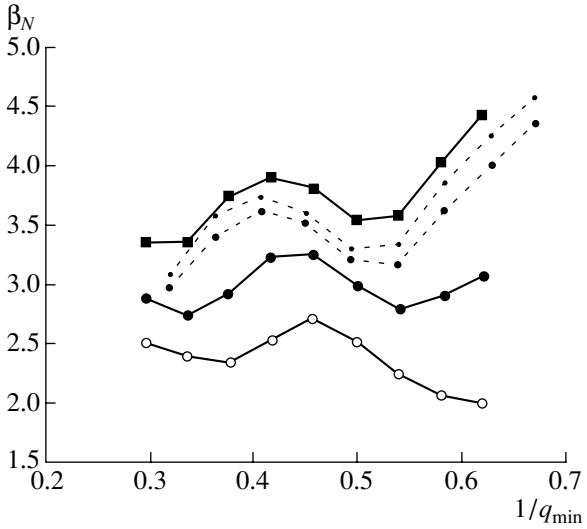

Fig. 1. Dependence of the $n = 1$ mode stability limit β_N on $q_{\min}$ in the T-15M tokamak [17]. Two lower curves show the results for the standard T-15M configuration [16]. The dashed curves show the results for T-15M with the plasma column shifted outward by 10 cm (circles) and shifted simultaneously outward and upward by 10 cm (dots). The upper curve (squares) is for the T-15M configuration, but with a wall similar to the ITER wall. The lowest curve gives the β limit without stabilization by the wall, $\beta_N^{\text{no wall}}$; all other curves give the limits with an ideally conducting wall, β_N^{wall}. The modeling is performed for a scenario with a reversed shear for $p_0/\bar{p} = 2.55$.

2. POSSIBLE GAIN IN β DUE TO RWM STABILIZATION

Before considering specific schemes of RWM stabilization, it is useful to discuss whether or not such stabilization is expedient in principle. For this purpose, we must answer two key questions: (i) at what β the RWMs become unstable and (ii) what could be gained from RWM stabilization if an ideal system for RWM suppression could be used?

For the scenarios under consideration, these questions can be answered using the results from [17], where the ideal β limits in ITER and T-15M were numerically calculated by the KINX code [18]. The results of these calculations are summarized in Fig. 1. The T-15M geometry, the vacuum chamber shape, and the other parameters (the wall thickness and conductivity) used in calculations [17] are taken from the T-15M technical project [16]. The results shown in Fig. 1 are obtained for an equilibrium configuration with the pressure and current profiles corresponding to stationary ITER scenario 4A with noninductive (steady-state) current drive and the pressure peaking factor $p_0/\bar{p} = 2.55$, where p_0 is the plasma pressure at the magnetic axis and $\bar{p}$ is the volume-averaged pressure. This scenario is described in detail in [3, 14] for ITER and in [17] for T-15M. In addition to this "basic" scenario, we will also consider a similar scenario, but with $p_0/\bar{p} = 3.1$.

The lowest curve in Fig. 1, which passes through the open circles, gives the stability limit for ideal MHD modes in T-15M in the absence of a conducting wall (in other words, when the influence of the wall on the plasma stability is negligible). We will call this value $\beta_N^{\text{no wall}}$. It is this value that is the RWM stability limit when the plasma does not rotate or its rotation is not too fast.

The next curve, running through the closed circles, shows β_N^{wall}—the stability limit for ideal MHD modes in T-15M, assuming that its wall is ideally conducting. This is the stability limit for the fast ideal modes with growth rates (in the absence of a wall) of $\gamma \gg 1/\tau_w$, where τ_w is the resistive wall time. In the cylindrical approximation, this time is given by the formula $\tau_w = \mu_0 \sigma_w d_w r_w$, where σ_w, r_w, and d_w are the conductivity, minor radius, and wall thickness, respectively.

RWM instability arises at β_N above $\beta_N^{\text{no wall}}$; therefore, a system for suppressing RWMs is needed for operating in the range $\beta_N > \beta_N^{\text{no wall}}$. In the best case, such a system would allow one to increase the stability limit to β_N^{wall}. For T-15M, the difference $\beta_N^{\text{wall}} - \beta_N^{\text{no wall}}$, which is the largest possible gain in β due to the active RWM feedback stabilization, is not large. This follows from a comparison of β_N^{wall} calculated for T-15M (Fig. 1, closed circles) and β_N^{wall} (squares) for a similar configuration, but with an ITER-like wall (with the same shape as in ITER, but with dimensions reduced by a factor of 4). We will refer to the latter value as the ITER limit.

For a given plasma configuration, β_N^{wall} is only determined by the wall position with respect to the plasma. The narrower the plasma–wall gap, the larger β_N^{wall}. The lower value of β_N^{wall} in T-15M, compared to that in ITER, means that the first wall in T-15M is too far from the plasma. The dashed lines in Fig. 1 show the possible increase in β_N^{wall} in T-15M when the plasma column is shifted outward by 10 cm and when it is simultaneously displaced outward and upward by 10 cm. The upward (or downward) displacement has a little effect; this is evidence of the strong localization of the perturbation at the outer side of the torus and is clearly seen in the subsequent figures. It is very difficult to incorporate such a localization into analytical models; this is confirmed by the fact that there has been only one (to the best of our knowledge) successful attempt at describing toroidal effects in the analytical theory of RWMs [19]. The MHD limits in this case can be pre-

cisely calculated only with the help of reliable numerical codes.

It can be seen from Fig. 1 that, for the scenario in question, the width of the zone $\beta_N^{\text{wall}} - \beta_N^{\text{no wall}}$ depends strongly on $q_{\min}$ (the minimal value of the safety factor in the plasma), which, at given profiles of the plasma current and pressure, is determined by the normalized current

$$I_N \equiv \frac{I[\text{MA}]}{a[\text{m}]B[\text{T}]}, \quad (2)$$

where I, a, and B are the same quantities as in Eq. (1). The numerical results show that, for the same plasma boundary and a fixed net current, $q_{\min}$ is nearly inversely proportional to the normalized current I_N. In particular, for the main scenario with a plasma aspect ratio of $A = 3.1$, an elongation of $\kappa_{95} = 1.76$, and a triangularity of $\delta_{95} = 0.39$, we have $q_{\min} I_N \sim 2.5$ at $\beta_N = 3.53$. The outward displacement of the plasma column by 10 cm increases the aspect ratio to $A = 3.3$; in this case, we have $q_{\min} I_N \sim 2.3$. The quantity $1/q_{\min}$ (for definiteness, it was calculated for the pressure profiles corresponding to $\alpha = 1$ [17]) was chosen as an abscissa on the stability diagram shown in Fig. 1 in order to simplify the comparison of the results for a series of equilibria with various aspect ratios because the local minima in Fig. 1 are related to $q_{\min}$ approaching the resonant values. Another important characteristic is

$$\alpha_b \equiv \frac{\beta - \beta^{\text{no wall}}}{\beta^{\text{wall}} - \beta^{\text{no wall}}}, \quad (3)$$

which determines the extent to which the lower ideal stability limit is exceeded. This parameter is given in the figure captions along with the α value [17], which shows the deviation of the pressure from that prescribed by the initial scenario.

Figure 1 shows that, at $q_{\min} > 2$, the gain in β due to RWM feedback stabilization in the given configuration is relatively small. It can be increased by placing the conducting wall closer to the plasma and/or by choosing a regime with a larger current corresponding to the right part of Fig. 1 ($q_{\min} < 2$). Both of these possibilities are considered below. We note that the increase in the plasma pressure peakedness to $p_0/\bar{p} = 3.1$ results in a substantial decrease in the difference $\beta_N^{\text{wall}} - \beta_N^{\text{no wall}}$ in T-15M [17].

3. FORMULATION OF THE PROBLEM

Plasma perturbations induce wall currents that hamper perturbation growth but then decay because of the finite wall resistivity. To stabilize RWMs and increase the stability limit to β_N^{wall}, it is necessary to completely compensate for the resistive losses in the wall and to sustain the induced currents at a level corresponding to the zero wall resistivity. This can partially be achieved with the help of a special stabilizing system.

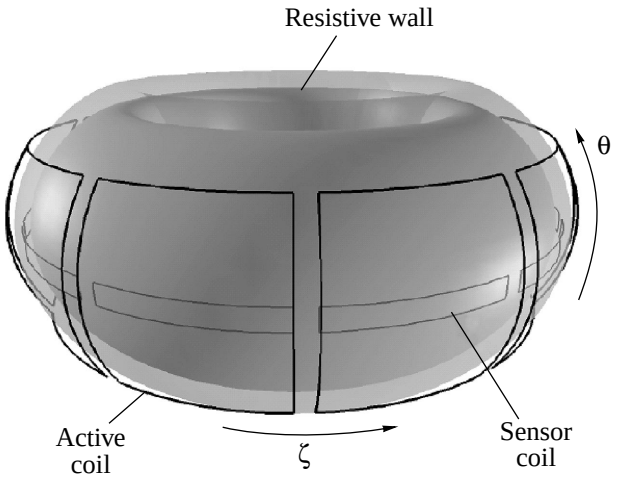

Fig. 2. Typical geometry of the correction coils and magnetic probes in the "conventional" system of RWM stabilization in a tokamak [22].

The stabilizing system must create a helical field; the best system for this purpose would be helical windings with the same helicity as that of the main unstable mode. A stabilizing system that generates a control signal reproducing exactly the structure of the unstable mode (without an admixture of extraneous harmonics) can be called ideal. Such a system would require complicated windings, e.g., such as the modular coils in the Wendelstein 7-X stellarator [20, 21]. However, in modern tokamaks, simpler solutions are preferred. This is explained by the fact that, as was already shown in the DIII-D tokamak, RWMs can be reliably stabilized with the help of a stabilizing system consisting of six saddle coils [7–12], provided that the error fields (on the order of a few gauss on the resonant surface) are suppressed. Such a system, which will be called conventional, is shown schematically in Fig. 2, taken from [22]. A similar system for RWM stabilization is planned for the KSTAR tokamak (Korea) [23] and is being investigated as a possible candidate for use in ITER [24–27]. In all these cases, the correction coils look like simple frames. The question of the advantages of more complex and (potentially) more efficient coil systems still remains open. Here, by analogy to DIII-D, KSTAR, or ITER, we consider a standard simple scheme: a conventional stabilizing system with the number of frame coils that is large enough to create the necessary field with $n = 1$. As was shown in [17], it is the $n = 1$ mode instability that imposes the strongest limitation on β in T-15M.

In our calculations, the active coil system was simulated, as was done in [22, 24, 28], by a single toroidal

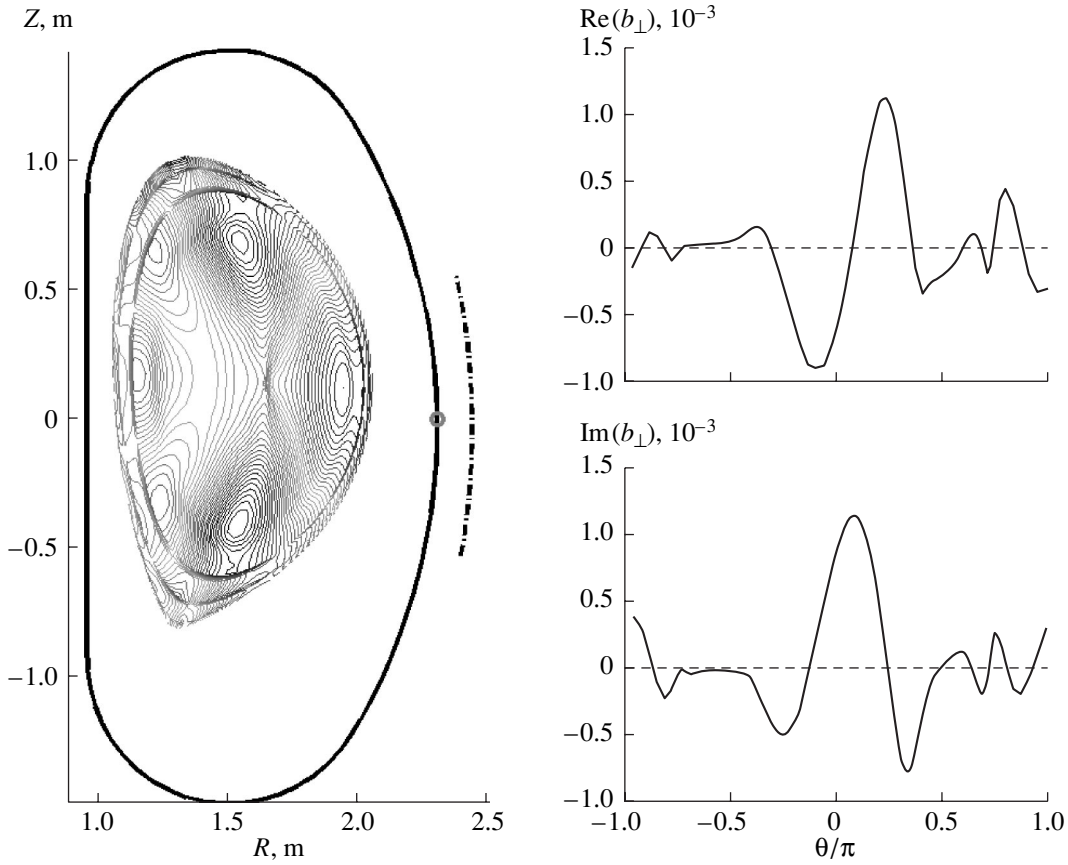

Fig. 3. Structure of an RWM with $n = 1$ (contour lines of the normal component of the plasma displacement) and the normal component of the perturbed magnetic field $b_\perp e^{in\varphi}$ at the T-15M wall (the wall is shown by the heavy solid line). Without active stabilization, $\gamma\tau_w = 2.7$ (where γ is the RWM growth rate). Two elements of the RWM stabilization system are shown schematically at the outer side of the torus: the circle shows the position of the probe measuring the poloidal component of the perturbed magnetic field inside the chamber, and the dashed-and-dotted line shows the active coils. The plasma parameters are $p_0/\bar{p} = 2.55$, $\beta_N = 2.95$ ($\alpha = 0.85$), $I_N = 1.13$, $q_{\min} = 2.2$, $\beta_N^{\text{wall}} - \beta_N^{\text{no wall}} = 3.2 - 2.7 = 0.5$, and $\alpha_b = 0.5$.

harmonic of the surface current on the $\rho = \rho_f$ surface geometrically similar to the wall:

$$\mathbf{j}^f = J_f \delta(\rho - \rho_f) \nabla\rho \times \nabla f \exp(in\zeta). \quad (4)$$

Here, J_f is the effective amplitude of the current in the correction coils; ρ is the radial coordinate; and θ and ζ are the poloidal and toroidal angles, respectively. In [22, 24, 28], the function f was specified as a finite-width smooth distribution approximately representing a finite-width toroidal conductor. In our calculations, we assumed that

$$f(\theta) = \begin{cases} 1, & -\theta_c \le \theta \le \theta_c \\ 0, & \theta_c < \theta < 2\pi - \theta_c, \end{cases} \quad (5)$$

which corresponds to an approximation of infinitely thin stabilizing conductors. For a circular plasma and a concentric wall in the cylindrical approximation, expression (4) under condition (5) is reduced to

$$j_z^f = J_f \delta(\rho - \rho_f) \frac{\delta(\theta - \theta_c) - \delta(\theta + \theta_c)}{\rho_f} \exp(in\zeta), \quad (6)$$

where ρ is the minor radius, which, together with θ and $z = R\zeta$, forms a usual cylindrical coordinate system ($2\pi R$ is the torus length). Such a representation of the current in the stabilizing windings was used in [26, 29].

The existing theory of RWM stabilization by a feedback system shows that the efficiency of such a system substantially depends on the orientation and position of the magnetic probes [8–12, 24–27, 29–31]. On the other hand, a large degree of freedom is allowed for the position of the correction coils. For many years, experiments in the DIII-D tokamak have been performed with the correction coils located outside the vacuum chamber. The design of KSTAR shows that it is technically possible to insert the correction coils inside the

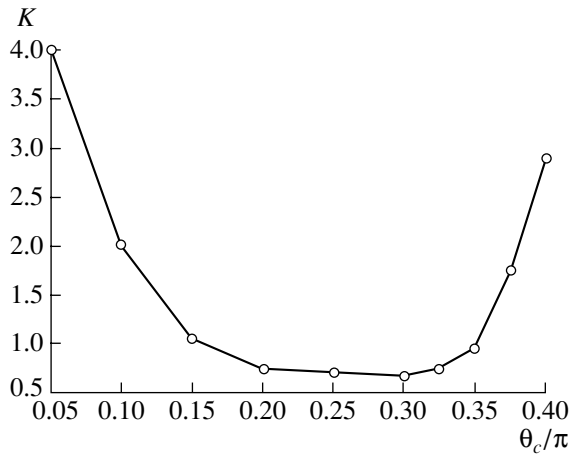

Fig. 4. Minimal gain factor allowing RWM stabilization as a function of the width of the active coils. The plasma parameters are $p_0/\bar{p} = 2.55$, $\beta_N = 2.95$ ($\alpha = 0.85$), $I_N = 1.13$, $q_{\min} = 2.2$, $\beta_N^{\text{wall}} - \beta_N^{\text{no wall}} = 3.2 - 2.7 = 0.5$, and $\alpha_b = 0.5$.

vacuum vessel. From the viewpoint of RWM stabilization, this is obviously the best solution, because it excludes the problem of the penetration of the control field through the wall. This definitely gives rise to certain technical difficulties related to the interaction of the plasma with these conductors, including mechanical problems associated with the large forces acting on the conductors during disruptions. Here, we consider a "standard" version: correction coils outside the chamber. As a control signal, we use the amplitude of the poloidal component of the total perturbed magnetic field inside the vacuum vessel at the outer side of the torus.

4. RESULTS OF CALCULATIONS

To calculate the RWM stability, we used a version of the KINX code [18] in which the tokamak vacuum chamber was represented by a thin shell (henceforth referred to as the wall). The geometry and characteristics of the T-15M vacuum vessel were taken from [16,

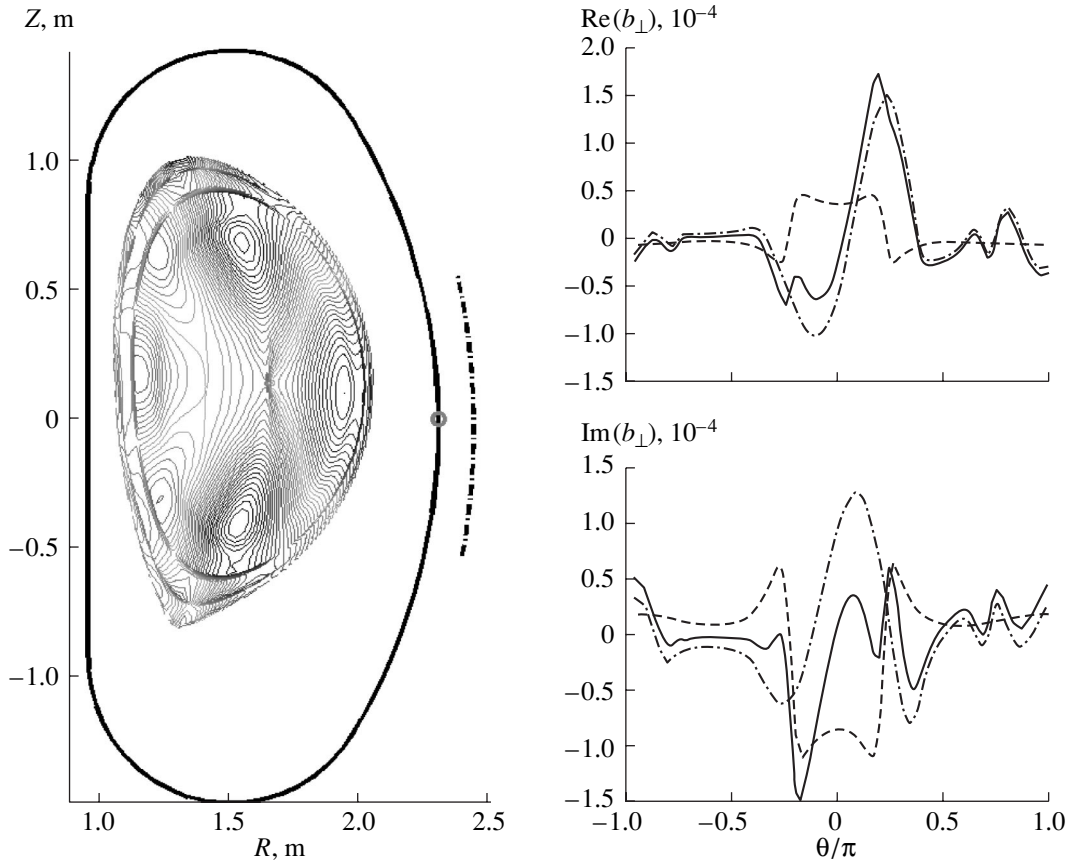

Fig. 5. Structure of an RWM with $n = 1$ near the stability limit ($\text{Re}\gamma = 0$) and the normal component of the perturbed magnetic field $b_\perp e^{in\varphi}$ at the T-15M wall. The solid line shows the total field, the dashed line shows the field produced by the active coils, and the dashed-and-dotted line shows their difference (the sum of the fields produced by the plasma and the wall). The width of the active coils is $\theta_c = 0.2\pi$. The gain factor necessary for RWM stabilization is $K = 0.75$. The plasma parameters are $p_0/\bar{p} = 2.55$, $\beta_N = 2.95$ ($\alpha = 0.85$), $I_N = 1.13$, $q_{\min} = 2.2$, $\beta_N^{\text{wall}} - \beta_N^{\text{no wall}} = 3.2 - 2.7 = 0.5$, and $\alpha_b = 0.5$.

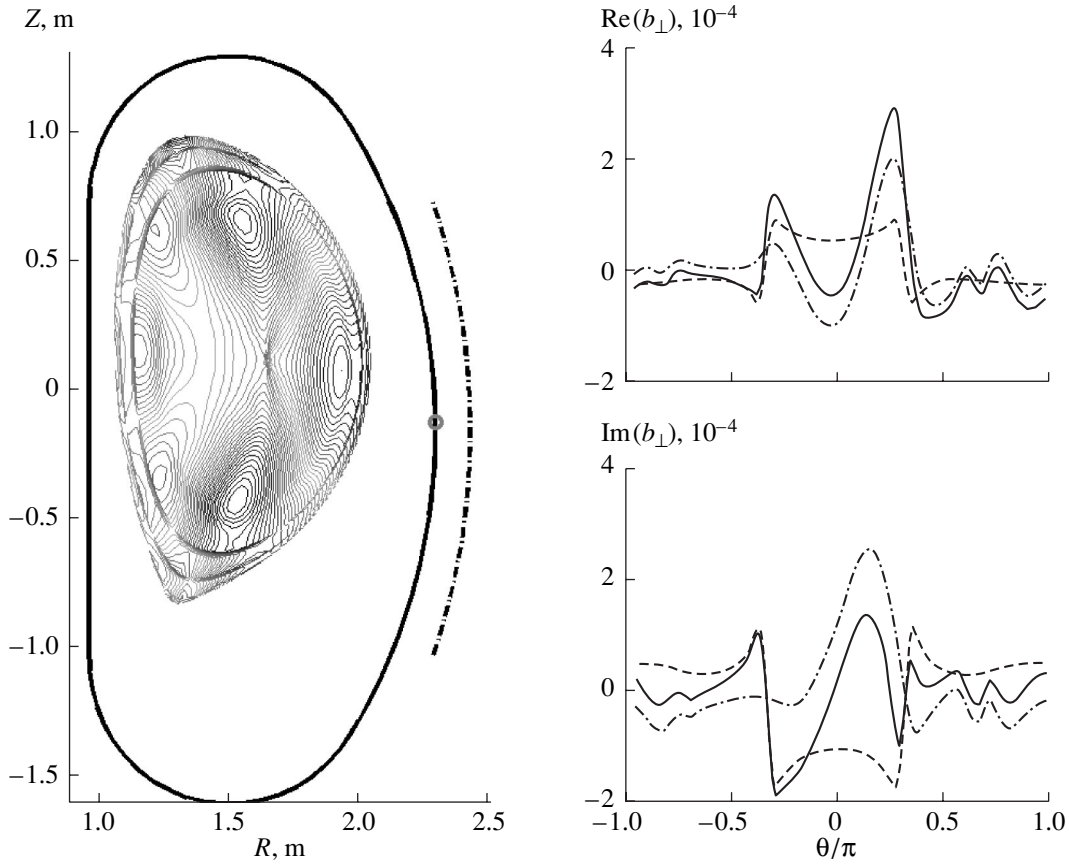

Fig. 6. Structure of an RWM with $n = 1$ near the stability limit ($\mathrm{Re}\,\gamma = 0$) and the normal component of the perturbed magnetic field $b_\perp e^{in\varphi}$ at the T-15M wall under the same conditions as in Fig. 5, but with wider stabilizing coils: $\theta_c = 0.3\pi$. The gain factor is $K = 0.7$.

32]. The simulations were similar to those in [17], but were performed with allowance for the finite conductivity of the first wall and the feedback stabilizing system. In this case, the eigenvalue problem for perturbations depending on time as $\exp\gamma t$ is more complicated than in the case of ideal MHD stability without dissipation because the eigenvalues can be complex and the equations depend nonlinearly on them. The code was tested using the analytical results for a large-aspect-ratio tokamak [33].

The possibility of active RWM stabilization in a tokamak with T-15M parameters was analyzed for an equilibrium state with $\beta_N = 2.95$ and $1/q_{\min} = 0.45$ ($\alpha = 0.85$ and $I_N = 1.13$ in the terms of [17]), which is unstable without a wall but, as can be seen in Fig. 1, could be stabilized by an ideal wall. Figure 3 shows the structure of an unstable RWM without feedback stabilization. Calculations of the growth rate γ of this mode yield $\gamma\tau_w = 2.7$, where $\tau_w = 6.35 \times 10^{-3}$ s is the effective resistive wall time obtained by averaging the thickness of the T-15M wall over the poloidal angle. Since this τ_w value is small, the RWM growth rate γ in the T-15M tokamak will be fairly large. We can say that this wall is too thin to efficiently stabilize kink modes. We note that τ_w in T-15M is approximately 50 times smaller than the effective value of τ_w in ITER.

In all the figures, starting with Fig. 3, θ is the poloidal angle counted counterclockwise from the plane of the wall symmetry ($\theta = 0$ on the outer side of the torus). We analyzed the plasma stability in the framework of a linear MHD; therefore, the amplitude of the perturbed magnetic field in Fig. 3 and the subsequent similar figures are given in arbitrary units.

The structure of the numerically calculated perturbations is shown in Fig. 3 and the subsequent figures by the contour lines of the quantity ξ_n, which is the component of the plasma displacement normal to the magnetic surfaces. Knowing the number of the ξ_n extrema, which look like "islands" surrounded by closed contours, allows one to determine the poloidal number m of the main harmonic. In toroidal geometry, m is a local characteristic that can be different at different distances from the magnetic axis. In Fig. 3, one can see six large "islands." These are the alternate maxima (in our figures, one of them is always located at the outer side of the torus) and minima of ξ_n of the $m = 3$ mode. The condensation of the contour lines in the radial direction, which is clearly seen in Fig. 3 and the subsequent fig-

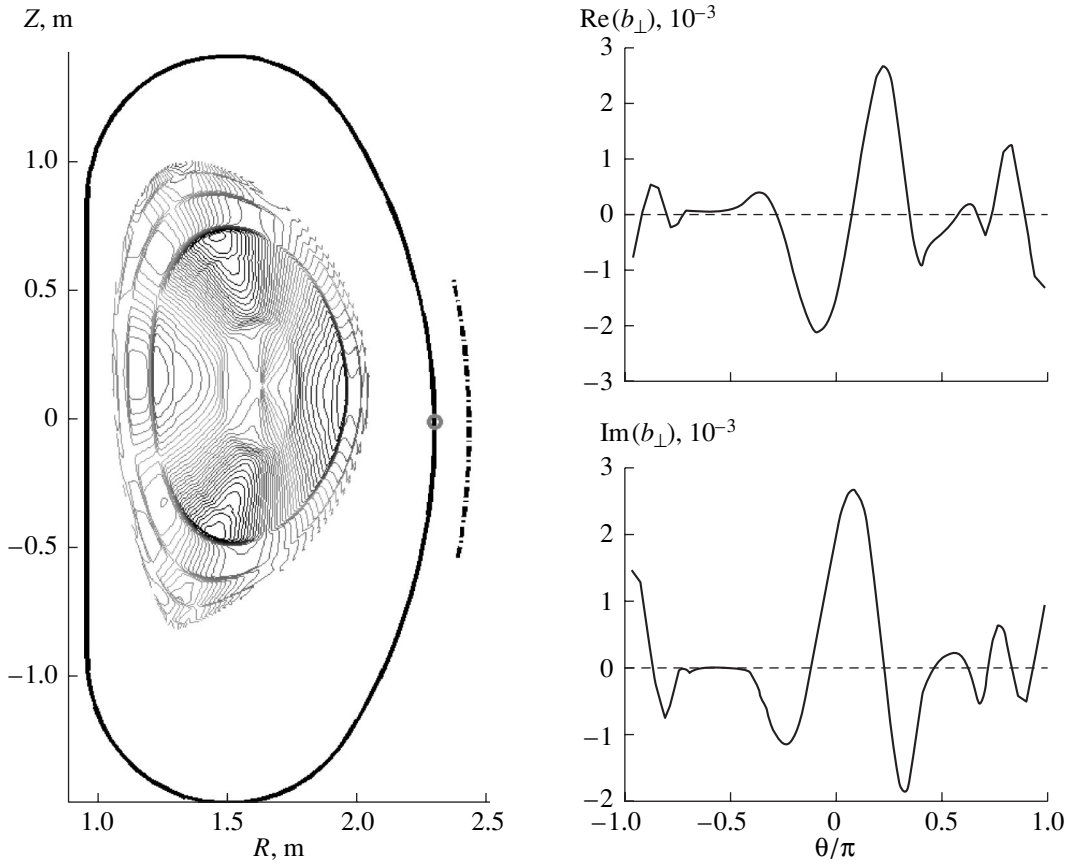

Fig. 7. Structure of an RWM with $n = 1$ and the normal component of the perturbed magnetic field $b_\perp e^{in\varphi}$ at the T-15M wall for a larger pressure peaking factor. Without active stabilization, $\gamma\tau_w = 5.3$. The plasma parameters are $p_0/\bar{p} = 3.1$, $\beta_N = 2.2$ ($\alpha = 0.6$), $I_N = 1.13$, $q_{\min} = 1.9$, $\beta_N^{\text{wall}} - \beta_N^{\text{no wall}} = 2.32 - 1.99 = 0.33$, and $\alpha_b = 0.62$.

ures as closed contours located near the plasma boundary and closely repeating its shape, corresponds to the sharp change of the ξ_n structure in the vicinity of the resonant surfaces.

To model RWM feedback stabilization, we use a simple control algorithm:

$$\delta B_{\text{sens}}^{\text{feedb}} = -K\delta B_{\text{sens}}^{\text{tot}}. \quad (7)$$

Here, K is the gain factor, $\delta B_{\text{sens}}^{\text{feedb}}$ is the radial component (the projection onto ∇r) of the magnetic field created by the stabilizing system, and $\delta B_{\text{sens}}^{\text{tot}}$ is the poloidal component of the total perturbed field. The index "sens" shows that the values of $\delta B_{\text{sens}}^{\text{feedb}}$ and $\delta B_{\text{sens}}^{\text{tot}}$ are taken at the position of the sensor (probe) measuring the poloidal component of the perturbed magnetic field. In Fig. 3 and the subsequent similar figures, this position is shown by a small open circle. As in [22, 24–27], we assume that the probes are placed inside the vacuum chamber in the equatorial plane on the outer side of the torus.

Prescribing the current in the stabilizing coils by Eqs. (4) and (5), we varied θ_c (the half-width of the correction coils in the poloidal direction) and calculated the minimal gain $K_{\min}$ in Eq. (7) that was necessary for RWM stabilization at different θ_c (Fig. 4). The quantity $K_{\min}$ is usually called the "critical gain" [22, 24, 25, 27]. In those papers, curves similar to that shown in Fig. 4 were calculated for different "advanced" equilibria. The absolute values of $K_{\min}$ depend on the parameters of a given equilibrium configuration; however, the dependence of $K_{\min}$ on the poloidal width of the correction coils in [22, 24, 25, 27] was always similar to that shown in Fig. 4. We note that, in [22, 24], the minimal value of $K_{\min}$ was achieved at $2\theta_c/\pi = 0.55$. Our calculations give approximately the same value.

Our calculations show that, for the equilibrium configuration under study, the minimal value of the necessary gain factor, $K \approx 0.7$, is achieved at $\theta_c = 0.2\pi$–0.3π. We note that the distance between the two main maxima of $|b_\perp|$ in the right top panel of Fig. 3 is approximately equal to $\Delta\theta = 0.35\pi$. It follows from Fig. 4 that it is $\Delta\theta$ that determines the necessary width of the cor-

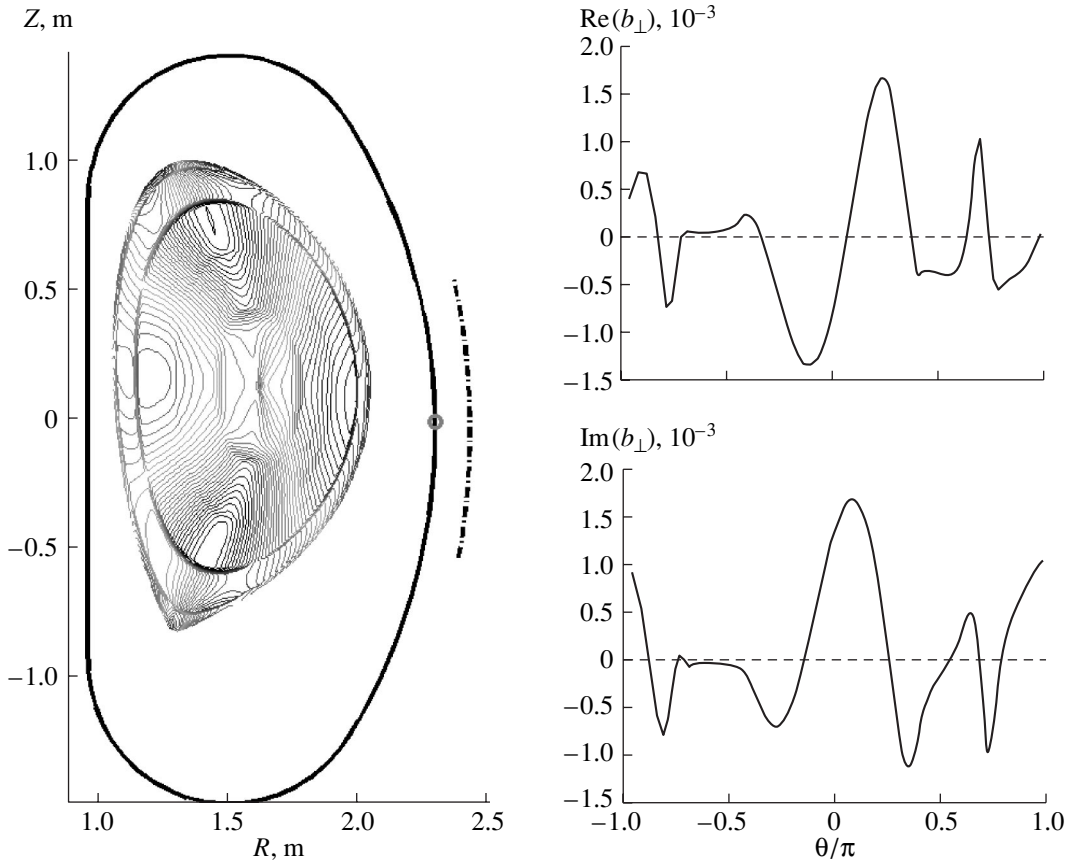

Fig. 8. Structure of an RWM with $n = 1$ and the normal component of the perturbed magnetic field $b_\perp e^{in\varphi}$ at the T-15M wall for a configuration with a larger I_N. Without active stabilization, $\gamma\tau_w = 4.9$. The plasma parameters are $p_0/\bar{p} = 2.55$, $\beta_N = 2.56$ ($\alpha = 0.575$), $I_N = 1.53$, $q_{\min} = 1.7$, $\beta_N^{\text{wall}} - \beta_N^{\text{no wall}} = 3.06 - 1.98 = 1.08$, and $\alpha_b = 0.54$.

rection coils: $K \le 1$ at $0.5\Delta\theta \le \theta \le \Delta\theta$. If θ_c lies outside this range, the efficiency of RWM stabilization with the help of frame coils is sharply reduced and larger gains are required. Therefore, the question of the dimensions of the correction coils should be discussed on the basis of the forecasts of MHD theory for the possible operating scenarios of a tokamak. However, the presence of a wide zone in θ_c where $K_{\min} \le 1$ (see Fig. 4) means that the restrictions imposed on the choice of the correction coils are not too severe.

The presence of a pronounced minimum in Fig. 4 is also explained by the fact that the correction coils with the current prescribed by Eq. (4) and the perturbations produced by the plasma have different symmetry: the perturbation is helical, while the coils are axially symmetric.

The equilibrium state with $\beta_N = 3$, the results for which are shown in Figs. 3 and 4, would be stable if the wall were ideal (in other words, if the condition $b_\perp = 0$ would be satisfied on the wall). With the help of an ideal stabilizing system, this condition could also be satisfied on a real wall with a finite conductivity. The difference between the conventional system, which is considered here, and the ideal one manifests itself in the fact that $b_\perp \ne 0$ at the wall even when the unstable mode is successfully suppressed by the stabilizing system (Fig. 5). In Fig. 6, the same is shown for the case of wider correction coils; here, $\theta_c = 0.3\pi$, while in Fig. 5, $\theta_c = 0.2\pi$.

Figures 3, 5, and 6 show that the mode structure in the plasma changes only slightly under the action of the stabilizing field. This was noted earlier in many numerical calculations [8, 11, 22, 24, 25, 28]. We explain this effect (sometimes called "mode rigidity") by the fact that the weak stabilizing field cannot strongly affect the profiles of the plasma current and pressure, which determine the behavior of perturbations in the plasma.

Thus, in a configuration with $p_0/\bar{p} = 2.55$ and $I_N = 1.13$, RWMs become unstable at $\beta_N > 2.7$. At $\beta_N = 3$, when $\gamma\tau_w = 2.7$, the gain factor $K = 0.70$–0.75 is sufficient for RWM stabilization. If we increase $p_0/\bar{p}$ to 3.1, keeping I_N unchanged, the RWM stability threshold decreases to $\beta_N^{\text{no wall}} = 2.0$ [17] and the open-loop-mode growth rate (without active stabilization) increases to

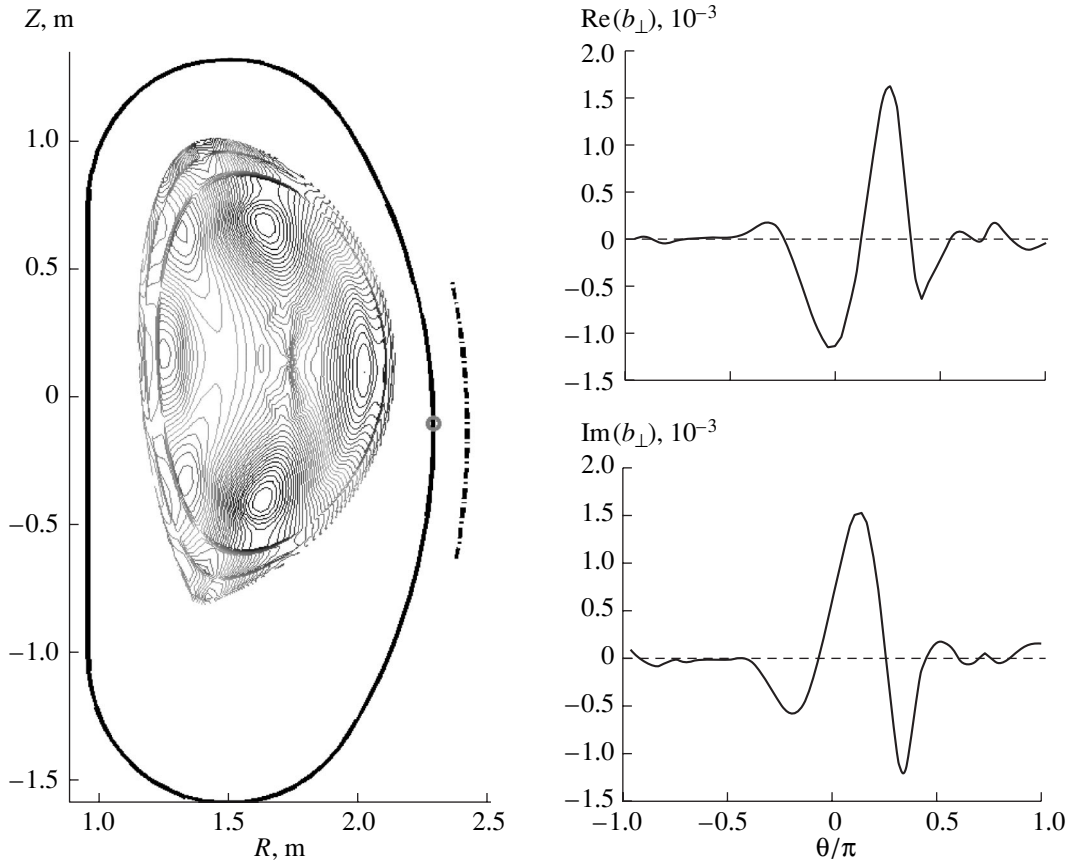

Fig. 9. Structure of an RWM with $n = 1$ and the normal component of the perturbed magnetic field $b_\perp e^{in\varphi}$ at the T-15M wall for a configuration with a narrower plasma–wall gap. Without active stabilization, $\gamma\tau_w = 2.3$. The plasma column is shifted outward and upward by 10 cm. The Z axis is displaced upward by 10 cm, following the plasma shift. The plasma parameters are $p_0/\bar{p} = 2.55$, $\beta_N = 3$ ($\alpha = 1.0$), $I_N = 1.03$, $q_{\min} = 2.2$, $\beta_N^{\text{wall}} - \beta_N^{\text{no wall}} = 3.6 - 2.6 = 1.0$, and $\alpha_b = 0.4$.

$\gamma\tau_w = 5.3$ at $\beta_N = 2.2$. These adverse changes are related to the appreciable reduction in the ideal limit β_N^{wall} from 3.2 in the first case ($p_0/\bar{p} = 2.55$) to 2.3 in the second case ($p_0/\bar{p} = 3.1$). It is worth noting that it is practically impossible to observe the change in the mode structure outside the plasma: the perturbation in Fig. 7 almost repeats that shown in Fig. 3. Nevertheless, a larger gain factor is required for RWM feedback stabilization in the latter case: $K = 1.1$ at $\beta_N = 2.2$.

The results presented in Figs. 3–7 apply to the case $I_N = 1.13$, which corresponds to the middle of the parameter range on the horizontal axis in Fig. 1. We also performed calculations for a configuration with $I_N = 1.53$ ($q_{\min} = 1.7$); in Fig. 1, this configuration is represented by the rightmost points with a larger value of $\beta_N^{\text{wall}} - \beta_N^{\text{no wall}} = 3.06 - 1.98 = 1.08$ (due to an appreciable decrease in $\beta_N^{\text{no wall}}$) as compared to the first version with $I_N = 1.13$ ($q_{\min} = 2.2$). The mode structure in the plasma and the dependence of $b_\perp$ at the wall on the poloidal angle for this case are shown in Fig. 8. The calculations were performed for $\beta_N = 2.56$, when $K = 1.1$ is required for RWM stabilization. In this case, the growth rate γ was again larger than that in the previous case: $\gamma\tau_w = 4.9$.

In Fig. 1, the dashed lines show that the narrowing of the plasma–wall gap at the outer side of the torus increases the stabilizing effect of the wall on the $n = 1$ mode. This is also true for other modes. Let us recall that the β_N^{wall} limits given in Fig. 1 were calculated assuming the wall to be ideal. The results presented in Fig. 9 are obtained with allowance for the finite conductivity of the vacuum chamber. This figure may be compared with Fig. 3 because the profiles of the plasma pressure and current and the values of β_N and $q_{\min}$ are the same in these two cases. Placing the conducting wall closer to the plasma allows one to suppress the RWMs and achieve a higher β_N than those in the standard case at the same requirements to the stabilizing system. Placing the wall closer to the plasma also reduces the RWM growth rate. For the case illustrated

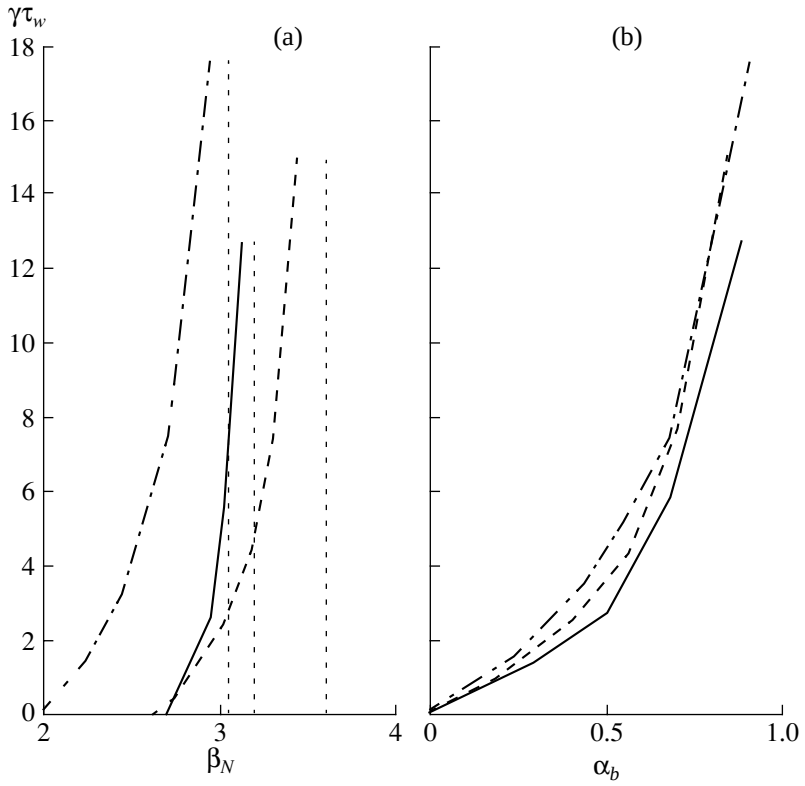

Fig. 10. Growth rate of an RWM with $n = 1$ as a function of (a) β_N and (b) $\alpha_b = (\beta - \beta^{\text{no wall}})/(\beta^{\text{wall}} - \beta^{\text{no wall}})$ for the three equilibrium configurations: $I_N = 1.13$ (solid line) and $I_N = 1.53$ (dashed-and-dotted line) for the standard plasma position relative to the T-15M wall and $I_N = 1.03$ for a plasma column displaced outward and upward by 10 cm (dashed line). The vertical asymptotes shown by the dotted lines in plot (a) correspond to the ideal stability limits $\beta_N = \beta_N^{\text{wall}}$ equal to 3.06, 3.2, and 3.6. In all cases, $p_0/\bar{p} = 2.55$.

by Fig. 9, we obtain $\gamma\tau_w = 2.3$, whereas in the first case, $\gamma\tau_w = 2.7$ at the same $\beta_N = 3$.

Figure 10 demonstrates the stabilizing effect of the conducting wall on an unstable kink mode for the three cases discussed above. Without a wall, the growth rate is on the order of the Alfvén frequency. With a wall, the instability growth rate is determined by the resistive wall time τ_w. In all these cases, the plasma is unstable at $\beta > \beta^{\text{no wall}}$. The instability growth rate is small at a small excess over the $\beta^{\text{no wall}}$ limit and then very rapidly increases with increasing β, reaching a value on the order of $10/\tau_w$ at $\beta - \beta^{\text{no wall}} \approx 0.75(\beta^{\text{wall}} - \beta^{\text{no wall}})$.

The dependences of $\gamma\tau_w$ on β_N in Fig. 10a have different thresholds and different asymptotes for different equilibrium configurations. However, being regarded as functions of α_b, defined by Eq. (3), they turned out to be close to one another, especially at $\alpha_b < 0.5$ (see Fig. 10b).

4. CONCLUSIONS

All the theoretical works on RWM feedback stabilization (see, e.g., [11, 12, 15, 22–31, 33–38]) make optimistic conclusions about the efficiency of the above stabilization methods with a simple geometry of the correction coils and simple operation algorithms. Successful experiments in the DIII-D tokamak [7–12] have proven that these theoretical predictions are quite reliable. One of the greatest achievements in DIII-D was an almost double excess over $\beta_N^{\text{no wall}}$ during approximately 1 s [9]. The possibility of such an excess over $\beta_N^{\text{no wall}}$ in ITER due to active RWM stabilization was earlier predicted in [25]. Our calculations show that the larger the distance between the plasma and the wall, the smaller the gain in β. In particular, in the T-15M tokamak, RWM stabilization would allow operation at $\beta_N = 3$; however, a double excess over $\beta_N^{\text{no wall}}$ in T-15M cannot be obtained because the calculated value of $\beta_N^{\text{wall}} - \beta_N^{\text{no wall}}$ for T-15M is smaller than that for ITER (see Fig. 1). It is explained by the fact that the T-15M vacuum chamber is not so close to the plasma as the first wall in ITER. This difference between T-15M and ITER is illustrated by Fig. 11. The dashed curves in Fig. 1 show that the value of $\beta_N^{\text{wall}} - \beta_N^{\text{no wall}}$ in T-15M could be increased approximately to the ITER level by

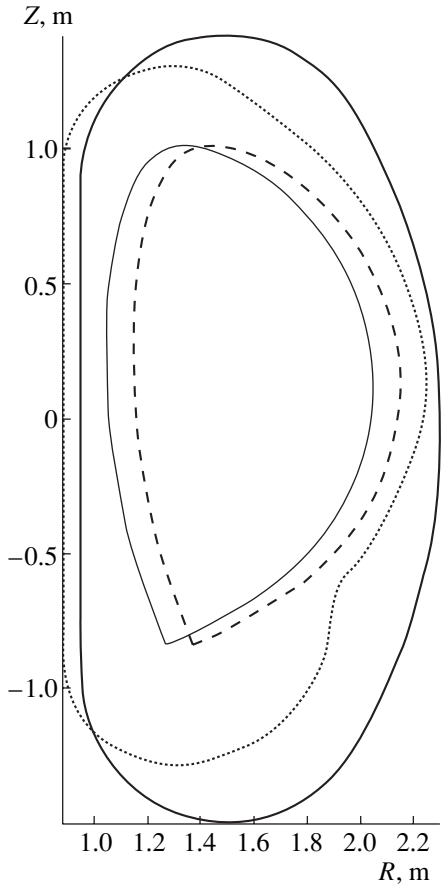

Fig. 11. Plasma boundary (light solid line) and the position of the T-15M wall (heavy line). The dashed and dotted lines show the plasma boundary shifted outward by 10 cm and the rescaled ITER wall, respectively.

placing the wall closer to the plasma by 10 cm at the outer side of the torus.

An important parameter of the problem is τ_w. In our case, this parameter determines the absolute time scale. It can be seen from Fig. 10 that the RWM growth rate is a few units of $1/\tau_w$; this growth rate determines the necessary operation speed of the stabilizing system. The smaller the resistive wall time τ_w, the more difficult it is to stabilize the RWM mode. Let us recall that $\tau_w = 6.35 \times 10^{-3}$ s for the parameters accepted in the T-15M technical project [16], whereas in ITER, we have $\tau_w \approx 0.3$ s for each of its two walls [26, 15]. To increase τ_w in T-15M, it is necessary to increase the thickness of the vessel wall.

The narrowing of the plasma–wall gap at the outer side of the torus and the increase in τ_w can be considered as natural measures for making T-15M more similar to ITER. On the other hand, these measures are absolutely necessary if operation with $\beta_N \geq 3$ is desired in T-15M. For comparison, the JT-60SC project considers the possibility of stationary operation with $\beta_N = 3.5$–5.5 [39].

The problem of RWM stabilization in a tokamak with T-15M parameters has been analyzed here as a purely theoretical task without linking it to any specific engineering solutions. The choice of the scheme of the stabilizing system is a separate important problem. Experiments carried out in the DIII-D tokamak [7, 9–12, 40] showed that RWMs can be successfully stabilized only when the static resonant fields (the so-called error fields) are suppressed. Such fields with an amplitude of a few gauss at the resonant surface can lead to instability even with the "proper" operation of the dynamic stabilizing system [4, 6–9, 12, 40, 41]. Hence, the stabilizing system must suppress not only RWMs but also small static helical harmonics, thus providing a high "purity" of the magnetic field. The necessity of such a suppression, proved by DIII-D experiments, confirms the validity of the "Precision Tokamak" concept proposed many years ago [42].

The results of calculations presented in Fig. 10 show that the dependence of the RWM growth rate on β for different profiles of the safety factor follows approximately the same scaling,

$$\gamma\tau_w \approx \frac{4\alpha_b}{1-\alpha_b}, \tag{8}$$

where α_b is the parameter defined by Eq. (3). The verification of the validity of this scaling over a wider parameter range is a subject for further study. We note that Eq. (8) corresponds to the functional dependence given in [43] for the so-called stability constants.

ACKNOWLEDGMENTS

We are grateful to N.V. Ivanov and P.P. Khvostenko, who inspired and supported this study. We are also grateful to S.V. Tsaun for his technical support; to Yu.V. Gribov, V. S. Mukhovatov, and A. R. Polevoi for their continuous interest in this work, for providing us with information, and for their valuable advice; and to V.D. Shafranov for his useful recommendations concerning the presentation of the results obtained.

REFERENCES

1. *ITER Physics Basis*, Nucl. Fusion **39**, 2137 (1999).
2. J. D. Galambos, L. J. Perkins, S. W. Haney, and J. Mandrekas, Nucl. Fusion **35**, 551 (1995).
3. Y. Shimomura, Y. Murakami, A. R. Polevoi, *et al.*, Plasma Phys. Controlled Fusion **43**, A385 (2001).
4. A. M. Garofalo, E. J. Strait, J. M. Bialek, *et al.*, Nucl. Fusion **40**, 1491 (2000).
5. T. C. Luce, M. R. Wade, P. A. Politzer, *et al.*, Nucl. Fusion **41**, 1585 (2001).
6. E. D. Fredrickson, J. Bialek, A. M. Garofalo, *et al.*, Plasma Phys. Controlled Fusion **43**, 313 (2001).
7. A. M. Garofalo, M. S. Chu, E. D. Fredrickson, *et al.*, Nucl. Fusion **41**, 1171 (2001).

8. M. Okabayashi, J. Bialek, M. S. Chance, *et al.*, Phys. Plasmas **8**, 2071 (2001).
9. L. C. Johnson, M. Okabayashi, A. M. Garofalo, *et al.*, in *Proceedings of the 28th EPS Conference on Controlled Fusion and Plasma Physics, Funchal, 2001*; ECA **25A**, 1361 (2001); http://www.cfn.ist.utl.pt/EPS2001/fin/pdf/P4.008.pdf.
10. M. Okabayashi, J. Bialek, M. S. Chance, *et al.*, Plasma Phys. Controlled Fusion **44**, B339 (2002).
11. A. D. Turnbull, D. P. Brennan, M. S. Chu, *et al.*, Nucl. Fusion **42**, 917 (2002).
12. E. J. Strait, J. Bialek, N. Bogatu, *et al.*, in *Proceedings of the 19th IAEA Fusion Energy Conference, Lyon, 2002*, Paper IAEA-CN-94/EX/S2-1.
13. M. Shimada, V. Mukhovatov, G. Federici, *et al.*, Nucl. Fusion **44**, 350 (2004).
14. A. R. Polevoi, S. Yu. Medvedev, V. D. Pustovitov, *et al.*, in *Proceedings of the 19th IAEA Fusion Energy Conference, Lyon, 2002*, Paper IAEA-CN-94/CT/P-08.
15. Y. Gribov and V. D. Pustovitov, in *Proceedings of the 19th IAEA Fusion Energy Conference, Lyon, 2002*, Paper IAEA-CN-94/CT/P-12.
16. *Technical Project of the T-15M Device* (Efremov Inst. of Electrophysical Apparatus, St. Petersburg, 2002).
17. S. Yu. Medvedev and V. D. Pustovitov, Fiz. Plazmy **29**, 1088 (2003) [Plasma Phys. Rep. **29**, 1009 (2003)].
18. L. Degtyarev, A. Martynov, S. Medvedev, *et al.*, Comput. Phys. Commun. **103**, 10 (1997).
19. A. B. Mikhailovskii and B. N. Kuvshinov, Fiz. Plazmy **21**, 835 (1995) [Plasma Phys. Rep. **21**, 789 (1995)].
20. C. Beidler, G. Grieger, F. Herrnegger, *et al.*, Fusion Technol. **17**, 148 (1990).
21. G. Grieger, W. Lotz, P. Merkel, *et al.*, Phys. Fluids B **4**, 2081 (1992).
22. Y. Q. Liu and A. Bondeson, Phys. Rev. Lett. **84**, 907 (2000).
23. G. S. Lee, D. P. Ivanov, H. L. Yang, *et al.*, J. Plasma Fusion Res. **5**, 261 (2002).
24. Y. Q. Liu, A. Bondeson, C. M. Fransson, *et al.*, Phys. Plasmas **7**, 3681 (2000).
25. A. Bondeson, Yueqiang Liu, C. M. Fransson, *et al.*, Nucl. Fusion **41**, 455 (2001).
26. A. Bondeson, Y. Q. Liu, D. Gregoratto, *et al.*, Nucl. Fusion **42**, 768 (2002).
27. A. Bondeson, Y. Q. Liu, D. Gregoratto, *et al.*, Phys. Plasmas **9**, 2044 (2002).
28. M. S. Chance, M. S. Chu, M. Okabayashi, and A. D. Turnbull, Nucl. Fusion **42**, 295 (2002).
29. V. D. Pustovitov, Rep. No. NIFS-723 (Nat. Inst. Fusion Sci., Toki, 2002).
30. V. D. Pustovitov, Plasma Phys. Controlled Fusion **44**, 295 (2002).
31. V. D. Pustovitov, J. Plasma Fusion Res. **5**, 278 (2002).
32. E. N. Bondarchuk, Yu. N. Dnestrovskij, V. M. Leonov, *et al.*, Plasma Devices Op. **11**, 219 (2003).
33. V. D. Pustovitov, Fiz. Plazmy **27**, 209 (2001) [Plasma Phys. Rep. **27**, 195 (2001)].
34. R. Fitzpatrick and E. P. Yu, Phys. Plasmas **5**, 2340 (1998).
35. C. Cates, M. Shilov, M. E. Mauel, *et al.*, Phys. Plasmas **7**, 3133 (2000).
36. R. Fitzpatrick, Phys. Plasmas **8**, 871 (2001).
37. J. Bialek, A. H. Boozer, M. E. Mauel, and G. A. Navratil, Phys. Plasmas **8**, 2170 (2001).
38. Hogun Jhang, S. H. Ku, and Jin-Yong Kim, Phys. Plasmas **8**, 3107 (2001).
39. S. Ishida, K. Abe, A. Ando, *et al.*, in *Proceedings of the 19th IAEA Fusion Energy Conference, Lyon, 2002*, Paper IAEA-CN-94/FT/2-5.
40. A. M. Garofalo, R. J. La Haye, and J. T. Scoville, Nucl. Fusion **42**, 1335 (2002).
41. V. D. Pustovitov, Pis'ma Zh. Éksp. Teor. Fiz. **78**, 727 (2003) [JETP Lett. **78**, 281 (2003)].
42. A. P. Popryadukhin, Preprint No. 038-88 (Moscow Engineering Physics Inst., Moscow, 1988).
43. A. H. Boozer, Phys. Plasmas **5**, 3350 (1998).

Translated by V.D. Pustovitov

Plasma Physics Reports, Vol. 30, No. 11, 2004, pp. 907–917. Translated from Fizika Plazmy, Vol. 30, No. 11, 2004, pp. 976–987.

TOKAMAKS

Model Magnetic Field Configurations with Islands

A. N. Chudnovskiy

Nuclear Fusion Institute, Russian Research Centre Kurchatov Institute, pl. Kurchatova 1, Moscow, 123182 Russia

Received January 14, 2004

Abstract—Helical perturbations of the tokamak magnetic field can give rise to magnetic islands in the vicinity of the rational magnetic surfaces at which the pitch of the magnetic field lines coincides with that of the perturbation. The widely known relationship between the magnetic island width and the perturbation amplitude is valid under the assumptions that the island width is small in comparison to the radius of the rational surface and that the perturbation amplitude is constant in the radial direction. The latter assumption indicates that the island width is small in comparison to the radial size of the region where the perturbation current is localized. The calculations carried out for four model magnetic field configurations show that the geometry of the magnetic islands depends on the extent to which the perturbation current is localize and that the width of the magnetic islands is smaller than that calculated from the familiar relationship. The larger the perturbation amplitude, the greater this difference: it may be as large as 25% for the strong perturbations arising during disruptions. The calculations are based on the solution of the geometric problem of constructing the lines of the magnetic field determined by the given distributions of the initial current and perturbation current; the equilibrium equation is not considered. The question of the direction of the perturbation current within the island relative to the direction of the initial unperturbed current is discussed. The perturbation current flowing in an island is directed opposite to the initial current with a radially decreasing density; for this reason, such an island can naturally be called a "negative" island. Together with the formation of negative islands, the formation of "positive" ones is also considered. The latter are shown to form under the following conditions: the perturbation current density should be higher than the density of the current that produces the unperturbed field and the perturbation current itself should be localized in a sufficiently narrow radial layer. The positive islands are smaller in size than negative ones. © *2004 MAIK "Nauka/Interperiodica".*

1. INTRODUCTION

The onset of tearing instability [1] is accompanied by the formation of magnetic islands about the rational magnetic surfaces at which the pitch of the magnetic field lines coincides with that of the perturbation. The formation of magnetic islands inside the plasma column indicates the enhancement of radial transport in their vicinity [2]. The width of the magnetic island is traditionally estimated from the following well-known relationship [3–7]:

$$W = 4r\sqrt{\left|\frac{B_{r1}}{B_\theta}/m\frac{rq'}{q}\right|_{r_s}}. \qquad (1)$$

Here, B_{r1} is the amplitude of the perturbed radial field, B_θ is the initial unperturbed poloidal field of the toroidal current, $q = \dfrac{rB_T}{RB_\theta}$ is the safety factor, B_T is the toroidal magnetic field, r_s is the radius of the rational magnetic surface at which $q = \dfrac{m}{n}$, and m and n are the poloidal and toroidal mode numbers of the perturbation. Relationship (1), which contains the local values of the parameters at the rational magnetic surfaces, is valid for magnetic islands whose width is quite small in comparison to the radius of the rational surface, $W < r_s$, and under the assumption that the perturbation amplitude is constant in the radial direction, $\tilde{B}_r(r) \cong \tilde{B}_r(r_s)$ [8, 9]. The approximate character of relationship (1) is emphasized, e.g., in the book by Bateman [10] by using the approximate equality sign in it. The assumption $\tilde{B}_r(r) \cong \tilde{B}_r(r_s)$ implies that the width of the islands is small in comparison to the radial size of the region where the perturbation current is localized. In order to estimate how the extent to which the perturbation current is localized affects the geometry of the magnetic islands, the magnetic field lines were analyzed for four model magnetic field configurations. The magnetic configuration was specified by the initial current and perturbation current; the equilibrium equation was not considered. Analytic solutions to the equations for the magnetic field lines were obtained. These expressions determine, in particular, the magnetic island width. One such magnetic field configuration was used by Rutherford [11] to study the nonlinear growth of a tearing mode in plane geometry. The use of plane geometry simplifies the analysis and provides an adequate approximation for sufficiently narrow islands ($W < r_s$) in cylindrical geometry. Rutherford [11] derived a relationship between the magnetic island width and the amplitude of the perturbed magnetic field and showed the way in which this relationship can be generalized to

1063-780X/04/3011-0907$26.00 © 2004 MAIK "Nauka/Interperiodica"

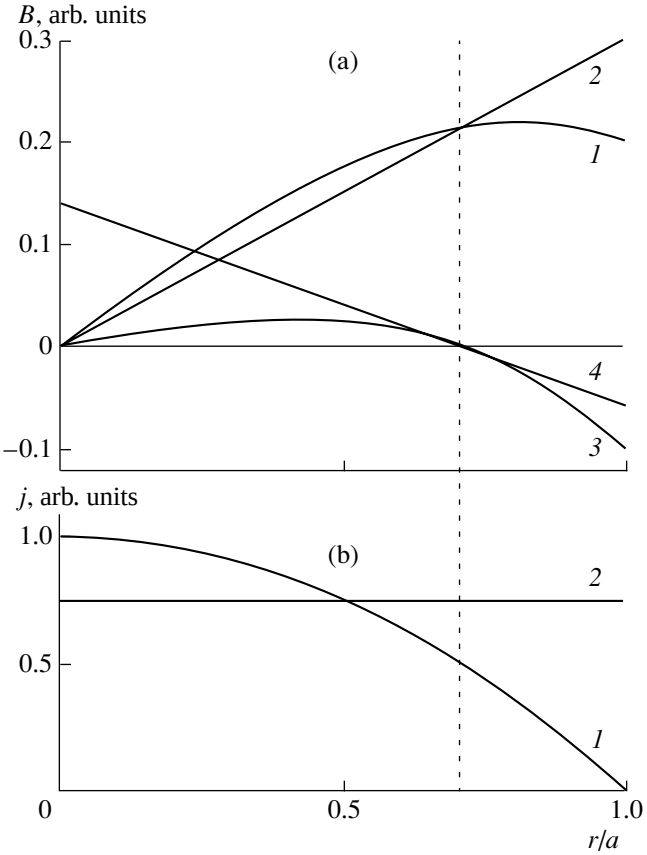

Fig. 1. Schematic representation of Kadomtsev's auxiliary field: (a) radial profiles of (*1*) the field B_θ of the toroidal current j_0, (*2*) the field of the uniform current j_u, (*3*) Kadomtsev's auxiliary field B_θ^*, and (*4*) the linear approximation to Kadomtsev's field; (b) radial profiles of (*1*) the toroidal current density j_0 and (*2*) the uniform current density j_u. The vertical dashed line shows the position of the rational surface of radius r_s.

the case of cylindrical geometry and which leads to relationship (1).

Besides studying the dependence of the magnetic island width on the perturbed magnetic field, we will also discuss the question about the relative directions of the perturbation current within the island and the current producing the initial field. It is well known (see, e.g., [12]) that, when the plasma current density is radially decreasing, the perturbation current flowing in the island is negative, so that such an island can naturally be called a negative island. In recent years, the question of the formation of not only negative but also positive magnetic islands has been discussed [12]. In the present study, the widths of both negative and positive islands are calculated. The conditions for the onset of positive islands are shown to be close to that determined in [12].

The paper is organized as follows. Section 2 contains a detailed analysis of the structure of magnetic islands in plane geometry in the magnetic field configuration considered in [11]. For this field configuration, the solution to the equation for the magnetic field lines can be represented in the form of an explicit dependence of the radial coordinate of the field line on its poloidal coordinate; this substantially simplifies the analysis of the structure of magnetic islands. In [11], the perturbation field was specified to be independent of the radial coordinate; this corresponds to a magnetic island whose width is much smaller than the size of the region where the perturbation current is localized. Section 3 is devoted to studying the opposite situation, in which the magnetic island width is much larger than the size of the localization region of the perturbation current. This situation, which is also treated in plane geometry, corresponds to the limiting case of a surface perturbation current. The magnetic islands produced by a perturbation current that is localized in a finite-width layer are described in plane geometry in Section 4. The magnetic islands produced by a surface perturbation current are considered in cylindrical geometry in Section 5. Finally, Section 6 summarizes the main results of this study.

2. MAGNETIC ISLAND IN PLANE GEOMETRY. THE MODEL OF A WIDE DISTRIBUTION OF THE PERTURBATION CURRENT

Before considering magnetic islands in plane geometry, we discuss a correspondence between the parameters of the magnetic field models in plane and in cylindrical geometry. In cylindrical geometry, it is convenient to study the magnetic islands in a cross section that is orthogonal to the magnetic field line on the rational magnetic surface of radius r_s. However, instead of describing the magnetic islands in such a cross section, Kadomtsev [13] proposed using an auxiliary magnetic field B_θ^*. The field B_θ^* is defined as the difference between the initial field, which is produced by the current of density $j_0(r)$, and a field that increases linearly in the radial direction in such a way that the auxiliary field vanishes at the rational surface r_s (Fig. 1a):

$$B_\theta^* = B_\theta - B_\theta(r_s)\frac{r}{r_s}.$$

This linearly increasing field can be created by a uniform current whose density j_u is equal to the mean density of the initial current $j_0(r)$ inside the rational surface (Fig. 1b). In a typical case of a radially decreasing initial current density, the density of the resulting current in the vicinity of the rational surface r_s is negative. The auxiliary field in a narrow layer around the rational surface is usually described by the linear approximation to Kadomtsev's field,

$$B_\theta^* \approx -B_\theta(r_s)\frac{q'(r_s)}{q(r_s)}(r-r_s) = \mu_0 j_0^*(r-r_s), \qquad (2)$$

where $j_0^* = j_0(r_s) - j_u$. It should be stressed that Kadomtsev's field changes sign at $r = r_s$.

In plane geometry, the problem is treated in a rectangular coordinate system in which $x = r - r_s$ is the radial coordinate and $y = \theta r_s$ is related to the poloidal angle. The initial unperturbed magnetic field, which changes sign at $x = 0$, is created by a uniform current flowing in a layer that is infinite in the y direction but finite in the x direction and is symmetric about the $x = 0$ plane. The initial field is related to the density j_0 of this current by the relationship

$$B_y = B'_y x = \mu_0 j_0 x. \quad (3)$$

The perturbation current density is taken to be $\tilde{j} = j_1 \cos m\theta$. This corresponds to the magnetic field perturbation $B_x = B_{x1} \sin m\theta$ (with $B_{x1} = -\frac{\mu_0 j_1}{k}$ and $k = m/r_s$), which is constant in the direction of the radial coordinate x (the case that is usually considered in the literature; see, e.g., [8, 9]). The amplitude j_1 is assumed to be positive. This model of a "wide" distribution of the perturbation current density describes magnetic islands whose radial width is substantially smaller than the size of the region where the current is localized. A similar magnetic field configuration was considered by Rutherford [11] in analyzing the nonlinear growth of a tearing mode. The solution to the equation for the magnetic field lines, $\frac{dx}{B_{x1} \sin m\theta} = \frac{r_s d\theta}{B'_y x}$, has the form

$$\cos m\theta = C \pm 2\frac{x^2}{h^2}, \quad (4)$$

where

$$h = 2r_s \sqrt{\left|\frac{B_{x1}}{m r_s B'_y}\right|}, \quad (5)$$

and the sign is chosen in accordance with the sign of B'_y.

We first consider the case in which $B'_y < 0$ and the initial current j_0 is directed opposite to the z axis. This direction of the current j_0 agrees with that of the resulting current j_0^*, which produces Kadomtsev's auxiliary field in the case of a radially decreasing current density. In this case, the explicit expression for the radial coordinate x of the magnetic field line has the form $x = \pm h \sqrt{\frac{C - \cos m\theta}{2}}$. The constant of integration $C = 1$ determines the separatrix $x = \pm h \left|\sin \frac{m\theta}{2}\right|$, which separates the closed magnetic field lines from the lines extending from $-\infty$ to $+\infty$ along the coordinate $y = r_s\theta$ and that do not cross the x axis. The centers of the closed magnetic field lines are at the so-called o-points of the magnetic islands with the coordinates $x = 0$ and $m\theta = (2l + 1)\pi$. The separatrix is self-intersecting at the so-called x-points with the coordinates $x = 0$ and $m\theta = 2l\pi$. In this case, the negative and the positive phases of the perturbation current correspond to the o- and x-points of the island, respectively. Hence, the direction of the perturbation current at the o-point of the island coincides with the direction of the current j_0, which produces the field B_y, or, in other words, the island forms around the perturbation current flowing in the direction of the current j_0. Note that the o- and x-points constitute a family of singular points of the equation for the magnetic field lines: at these points, both field components vanish. The parameter h, which characterizes the perturbation amplitude, is equal to the half-width of the magnetic island. Figure 2 shows the pattern of the magnetic field lines that form an $m = 2$ island and correspond to solution (4) with $B'_y < 0$ and $h = r_s$. The characteristic parameter h of the perturbation is chosen to be sufficiently large in order to illustrate how the field line patterns differ from one another in different model magnetic field configurations (see Figs. 2, 3, 7).

For $B'_y > 0$, when the current j_0 flows along the z axis, the explicit expression for x takes the form $x = \pm h \sqrt{\frac{-C + \cos m\theta}{2}}$. The constant $C = -1$ determines the separatrix $x = \pm h \left|\cos \frac{m\theta}{2}\right|$. In this case, the pattern of the magnetic islands is shifted by $\Delta m\theta = \pi$ with respect to that shown in Fig. 2. The closed magnetic field lines are centered at the points with the coordinates $x = 0$ and $m\theta = 2l\pi$, and the separatrix is self-intersecting at the points with the coordinates $x = 0$ and $m\theta = (2l + 1)\pi$. Accordingly, the positive and the negative phases of the perturbation current correspond to the o- and x-points of the island, respectively. Therefore, when the current j_0 is directed along the z axis, the islands also form around the perturbation current flowing in the direction of the current j_0.

Hence, regardless of the relative magnitudes and relative directions of the initial current j_0 (which produces the field B_y) and the perturbation current j_1, the island in the plane model configuration in question always forms only around the perturbation current whose direction coincides with that of the current j_0. In this model, the closed magnetic field lines cannot form around the perturbation current j_1 flowing in the direction opposite to that of the current j_0.

Note that, in a typical case in which the current density j_0 is radially decreasing (see below), the island in cylindrical geometry forms around the perturbation current j_1 whose direction coincides with that of the current j_0^* (which produces Kadomtsev's field) but is opposite to that of the current j_0. By virtue of the fact that the perturbation current flowing through the

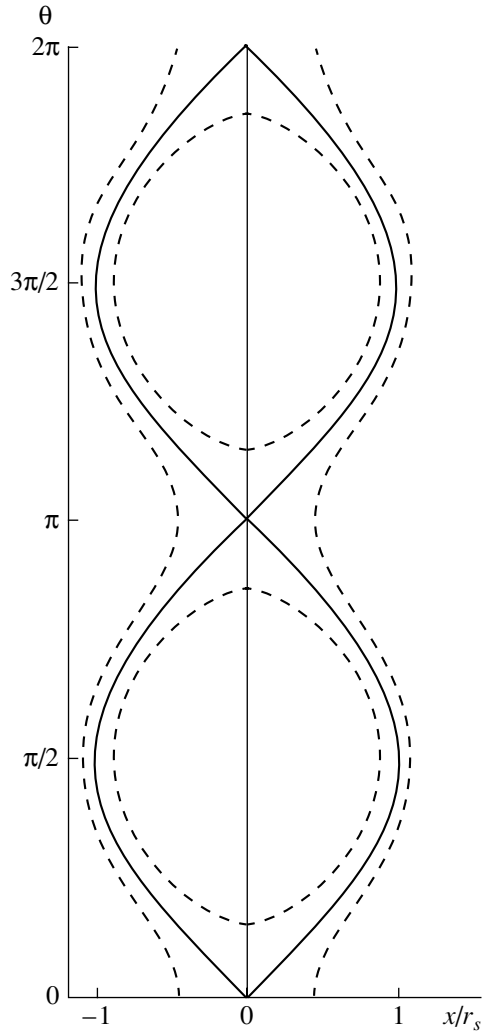

Fig. 2. Pattern of the magnetic field lines of an $m = 2$ magnetic island in plane geometry for a perturbation with the amplitude $h = r_s$ and for a wide distribution of the perturbation current density. The solid curve is the separatrix.

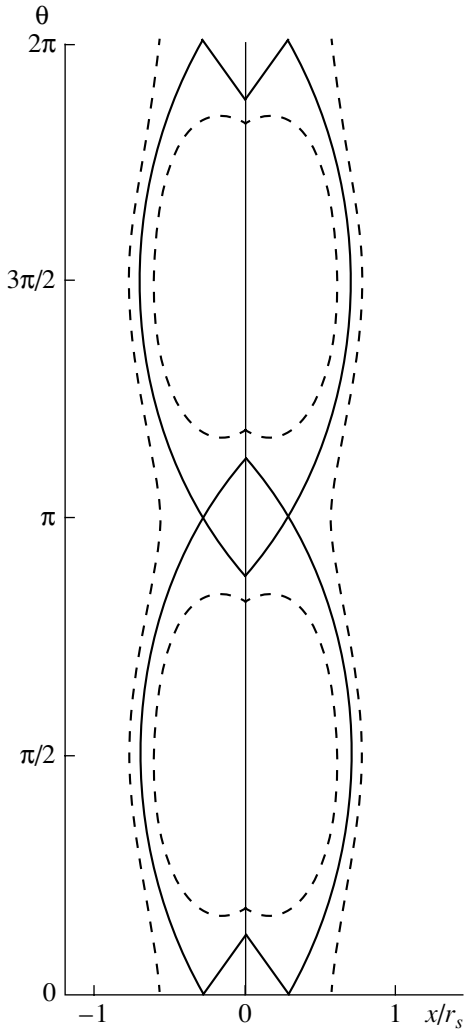

Fig. 3. Pattern of the magnetic field lines of an $m = 2$ magnetic island in plane geometry for a perturbation with the amplitude $h = r_s$ and for a surface perturbation current. The solid curve is the separatrix.

o-point of the island is negative, such an island is usually called a negative island.

The total width of a magnetic island is expressed as $W = 4r_s\sqrt{\left|\frac{B_{x1}}{mr_sB_y'}\right|}$. According to [11], this expression can be generalized to cylindrical geometry by the replacement $B_y' \longrightarrow r\frac{d}{dr}\left(\frac{B_\theta}{r}\right)$ and $B_{x1} \longrightarrow B_{r1}$. This somewhat implicit procedure leads to relationship (1) for the width of the magnetic island. It is this relationship that is widely used [3–7] to estimate the island width from a given perturbation and a given initial magnetic field configuration. Relationship (1) is derived under the assumption that the perturbation current is distributed over the entire space; this corresponds to a magnetic island whose width is much smaller than the radial size of the region where the perturbation current flows. We now turn to a discussion of the opposite case, in which the radial size of the localization region of the perturbation current is much smaller than the island width—the case of a surface perturbation current.

3. MAGNETIC ISLAND IN PLANE GEOMETRY. THE MODEL OF A SURFACE PERTURBATION CURRENT

As in the previous section, the initial magnetic field is specified by expression (3). Let us consider the case in which the magnetic perturbation is created by a surface current that is directed along the *z* axis and is dis-

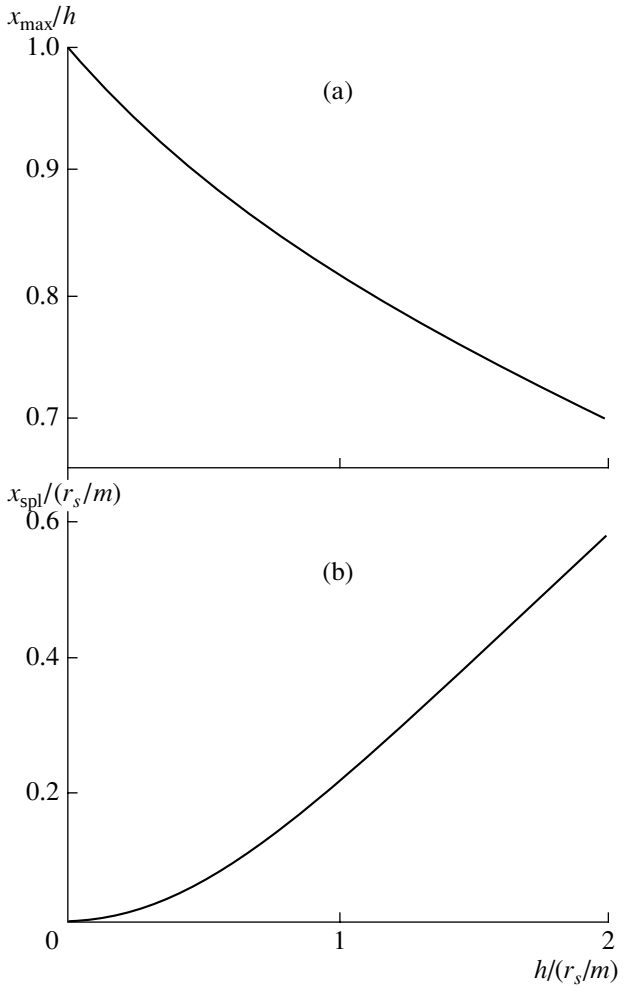

Fig. 4. Relative half-width of (a) a large and (b) a small magnetic island vs. perturbation amplitude in plane geometry.

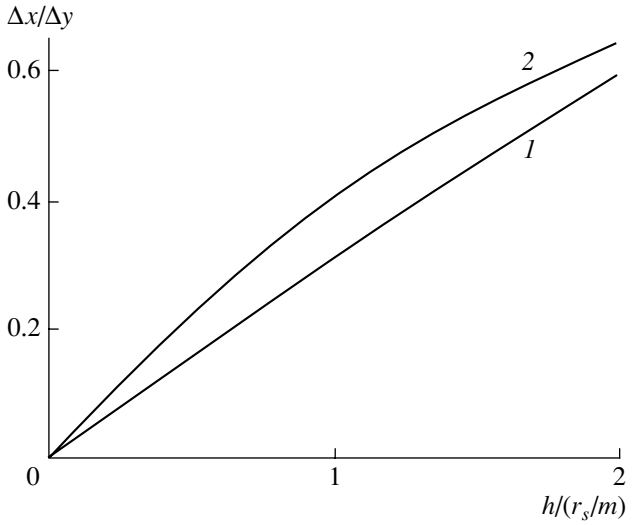

Fig. 5. Elongation of (*1*) a large and (*2*) a small magnetic island vs. perturbation amplitude.

tributed in the $x = 0$ plane as $\tilde{\iota} = \iota_1 \cos m\theta$. The components of the magnetic field perturbation have the form

$$\tilde{B}_x = B_{x1} \exp(-k|x|) \sin m\theta,$$

$$\tilde{B}_y = -\mathrm{sgn}(x) B_{y1} \exp(-k|x|) \cos m\theta,$$

where $k = m/r_s$ and $B_{x1} = B_{y1} = -\dfrac{\mu_0 \iota_1}{2}$.

In contrast to the magnetic field of a current distributed over the entire space, the magnetic field produced by a surface current has a nonzero component $\tilde{B}_y$. In this case, the singular points of the equation for the magnetic field lines (the points where both of the components $\tilde{B}_x$ and $B_y + \tilde{B}_y$ of the total magnetic field vanish) lie not at the $x = 0$ axis but at a certain distance from it. The distance x_{spl} from the singular points to the $x = 0$ axis is determined by the relationship

$$\frac{x_{spl}}{r_s} \exp\left(m \frac{x_{spl}}{r_s}\right) = \frac{m}{4}\left(\frac{h}{r_s}\right)^2, \qquad (6)$$

where the parameter h is given by formula (5). The fact that the singular points do not lie at the $x = 0$ axis leads to a field line pattern differing from that considered above.

The solution to the equation for the magnetic field lines

$$\frac{dx}{\tilde{B}_x} = \frac{r_s d\theta}{B'_y x + \tilde{B}_y} \qquad (7)$$

has the form

$$\cos m\theta = \left(C \pm 2\frac{x^2}{h^2}\right) \exp(k|x|), \qquad (8)$$

where, as in solution (4), the sign is also chosen in accordance with the sign of B'_y. Again, the perturbation is characterized by the parameter h; however, this parameter is not now the half-width of the magnetic island. In contrast to solution (4), solution (8) contains the factor $\exp(k|x|)$, which substantially changes the behavior of the field lines. The pattern of the magnetic field lines for the $m = 2$ perturbation corresponding to solution (8) with $B'_y < 0$ and $h = r_s$ is shown in Fig. 3.

Let us recall that, in the case of a wide distribution of the perturbation current density, the islands form around the perturbation current only when its direction coincides with that of the initial current j_0. In the case of a surface perturbation current, additional islands form around the previous positions of the x-points ($x = 0, m\theta = 2l\pi$), where the perturbation current flows in the direction opposite to the initial current j_0. In this case, the x-point splits into two points ($x = \pm x_{spl}$, $m\theta = 2l\pi$), where x_{spl} is determined by relationship (6). In the vicinity of the o-points ($x = 0$, $m\theta = (2l + 1)\pi$), the per-

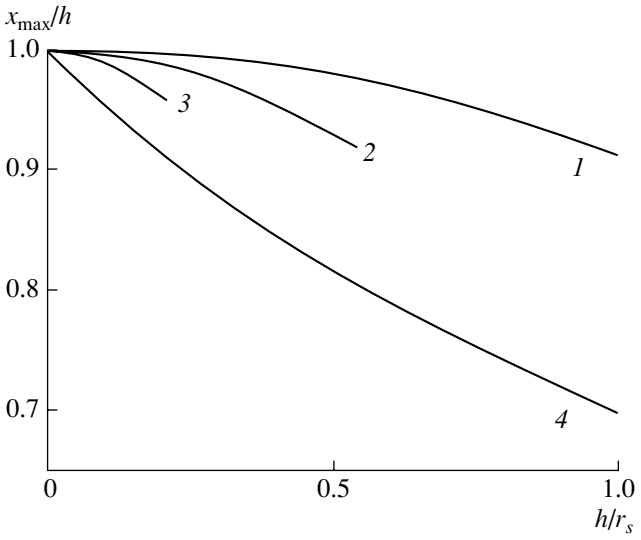

Fig. 6. Relative half-width of an $m = 2$ magnetic island vs. perturbation amplitude for $d = (1)\ r_s$, $(2)\ 0.5r_s$, and $(3)\ 0.2r_s$. Curve *4* refers to the case of a surface perturbation current.

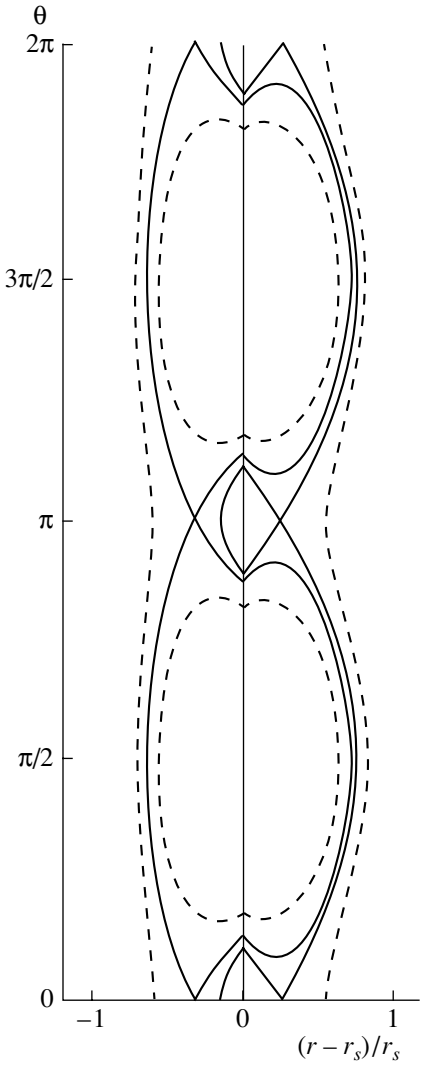

Fig. 7. Pattern of the magnetic field lines of an $m = 2$ magnetic island in cylindrical geometry for a perturbation with the amplitude $h = r_s$ and for a surface perturbation current. The solid curves are the separatrices.

turbation current $\tilde{\iota} = \iota_1 \cos m\theta$ is negative; i.e., it flows in the direction of the initial current. In the case of the reversal initial current, the field line pattern is phase shifted in such a way that the direction of the perturbation current at the *o*-points, as before, coincides with the direction of the initial current. Hence, the model of a surface perturbation current implies that, regardless of the relative directions of the initial current j_0 (which produces the field B_y) and the perturbation current $\tilde{\iota}$, a large island forms around the perturbation current whose direction coincides with that of the current j_0, while a small island forms around the perturbation current flowing in the opposite direction. The magnetic field line that passes through the two split points is the separatrix (Fig. 3). From Fig. 3, we can see that the maximum distance x_{max} between the separatrix and the $x = 0$ axis is less than $h = r_s$. It is the distance x_{max} that is the half-width of the large magnetic island, and it is the distance x_{spl} that is the half-width of the small island.

Figure 4 shows how the half-width x_{max} of a large magnetic island and the half-width x_{spl} of a small island depend on the characteristic parameter h of the perturbation. The parameter h and the half-width x_{spl} of a small island are normalized to the characteristic period r_s/m of the perturbation in order for the curves in Fig. 4 to be universal for perturbation modes with arbitrary poloidal numbers m. The half-width of a large magnetic island is normalized to the characteristic parameter of the perturbation, h, which is equal to the island half-width (5) in the case of a wide distribution of the perturbation current density. Hence, Fig. 4a shows the amount by which the half-width of a magnetic island in the model of a surface perturbation current differs from that in the model of a wide distribution of the perturbation current density. This difference increases approximately linearly with the perturbation amplitude. For weak perturbations such that $h \ll r_s$, and $x_{spl} \ll r_s$, the half-width x_{spl} of a small magnetic island is quadratic in h,

$$\frac{x_{spl}}{r_s} = \frac{m}{4}\left(\frac{h}{r_s}\right)^2, \qquad (9)$$

while the half-width x_{max} under the same conditions increases linearly with the perturbation amplitude, $x_{max} \approx h$. For weak perturbations, we have $x_{spl} \ll x_{max}$. For any finite value of the characteristic parameter h of the perturbation, the half-width x_{spl} is less than the half-width x_{max}. As h increases without bound (e.g., due to

an increase in B_y'), the half-width x_{spl} approaches the half-width x_{max} from below.

In Section 5, in discussing the magnetic islands in cylindrical geometry, it will be explained why, for a radially decreasing current density, the large island is called negative and the small island is called positive. As was pointed out in [12], the elongation of the positive islands is greater than that of the negative islands, which should lead to an asymmetry in the distribution of the magnetic field perturbation $\tilde{B}_\theta$ outside the plasma column. The dependence of the elongation of the magnetic islands on the perturbation amplitude is shown in Fig. 5, in which the elongation is defined as the ratio of the width of the magnetic island ($2x_{max}$ or $2x_{spl}$) to its length Δy along the $x = 0$ line. It can be seen that, in accordance with [12], the elongation of a positive (small) island is in fact greater than that of a negative (large) island. Nevertheless, when there is only one perturbation mode with the poloidal number m, the greater elongation of the positive island does not lead to any asymmetry of the distribution of $\tilde{B}_\theta$ outside the plasma column.

In this section and in Section 2, we have considered two limiting cases of the distribution of the perturbation current density: infinitely wide and infinitely narrow distributions. In the next section, we will analyze the case of a perturbation current density distributed over a layer of finite radial width.

4. MAGNETIC ISLAND IN PLANE GEOMETRY. THE MODEL OF A PERTURBATION CURRENT DISTRIBUTED OVER A FINITE-WIDTH LAYER

As in the previous two cases, the initial magnetic field is given by expression (3). We consider the case in which the perturbation is driven by a current that flows along the z axis and whose density is distributed according to the law $\tilde{j} = j_1 \cos m\theta$ over the layer $-d < x < d$. The distribution of the field components within the layer has the form

$$\tilde{B}_x = \frac{\mu_0 j_1}{k}(\exp(-kd)\cosh kx - 1)\sin m\theta,$$

$$\tilde{B}_y = \frac{\mu_0 j_1}{k}\exp(-kd)\sinh kx \cos m\theta,$$

where, as before, $k = m/r_s$. As in the case of a surface perturbation current, the magnetic field components outside the layer decrease exponentially,

$$\tilde{B}_x = B_{xd}\exp(-k|x|)\sin m\theta,$$

$$\tilde{B}_y = -\mathrm{sgn}(x)B_{xd}\exp(-k|x|)\cos m\theta,$$

where $B_{xd} = -\frac{\mu_0 j_1}{k}\sinh k\,d$.

The condition for the formation of magnetic islands around the perturbation current flowing in the direction opposite to that of the initial current j_0 is that both of the components of the total magnetic field should vanish at the points lying off the $x = 0$ axis. This condition is satisfied if the perturbation field $\tilde{B}_y$ exceed in absolute value the initial field. The maximum value of $|\tilde{B}_y|$ is reached at the boundary of the current layer. Consequently, the condition for the formation of such magnetic islands has the form $|\tilde{B}_y(x = d, m\theta = 2l\pi)| > |B_y(d)|$ or

$$j_1 > |j_0|\frac{kd\exp kd}{\sinh kd}. \tag{10}$$

Since $\frac{kd\exp kd}{\sinh kd} \geq 1$, the inequality $j_1 > j_0$ must at least be satisfied. If we introduce the characteristic parameter of the perturbation,

$$h = 2r_s\sqrt{\left|\frac{B_{x1}}{mr_s B_y'}\right|}, \tag{11}$$

where $B_{x1} \equiv \tilde{B}_x(x = 0, m\theta = 2l\pi) = -\frac{\mu_0 j_1}{k}(1 - \exp(-kd))$, then condition (10) for the perturbation current magnitude can be rewritten as the following restriction on the radial size d of the region where the perturbation current is localized:

$$\begin{aligned}\frac{d}{r_s} &< \frac{m}{4}\left(\frac{h}{r_s}\right)^2 \quad \text{for} \quad d \ll r_s,\\ \frac{d}{r_s} &< \frac{m}{8}\left(\frac{h}{r_s}\right)^2 \quad \text{for} \quad d \gg r_s.\end{aligned} \tag{12}$$

Hence, at a fixed perturbation amplitude h, a necessary condition for the formation of magnetic islands around the perturbation current directed opposite to the initial current j_0 is that the perturbation current should be localized in a sufficiently narrow layer. Condition (12) implies, in particular, that the half-width of the current layer should be less than the half-width x_{spl} (9) of a small magnetic island in the case of a surface perturbation current.

Let us consider the structure of the magnetic field lines in the case where the magnetic field perturbation is no stronger than the initial field and an island is localized inside the current layer. The solution to field line equation (7) within the layer has the form

$$\cos m\theta = \left(C \pm 2\frac{x^2}{h^2}\right)\frac{\exp kd - 1}{\exp kd - \cosh kx}, \tag{13}$$

where the parameter h is given by relationship (11) and the sign is chosen in accordance with the sign of B_y'. The structure of solution (13) is well known: the right-hand side of an expression like (4) is multiplied, as in

solution (8), by a function that increases with distance from the $x = 0$ axis. Because of the presence of such a factor in solution (13), the width of a magnetic island differs from the value of the parameter h calculated for a wide current layer. Figure 6 shows that this difference increases with perturbation amplitude more gradually than it does for a surface perturbation current. Recall that, in Fig. 4, the parameter h is normalized to r_s/m. In the case at hand, however, this normalization does not ensure that the corresponding dependences are universal for perturbation modes with different poloidal numbers m because the model now contains a new scale length—the half-width d of the current layer. This is why Fig. 6 illustrates the calculated results only for the $m = 2$ mode and why the parameter h was normalized to r_s. The calculations for current layers with the half-widths $d = 0.2r_s$ and $d = 0.5r_s$ were restricted to such h values for which the island lay entirely within the current layer; i.e., the half-width $x_{\max}$ was less than the corresponding d value. It can be seen from Fig. 6 that the difference between the half-width of the $m = 2$ magnetic island and the h value calculated using formula (11) does not exceed 10%.

5. MAGNETIC ISLAND IN CYLINDRICAL GEOMETRY

In analyzing the magnetic islands in cylindrical geometry, it is convenient to use Kadomtsev's auxiliary field (2) as an unperturbed magnetic field. Let us consider the case in which the perturbation is produced by a surface current that flows along the z axis and is distributed over a rational surface with the radius $r = r_s$ as $\tilde{\iota} = \iota_1 \cos m\theta$, where the amplitude ι_1 is assumed to be positive. The components of the perturbing field are given by the expressions

$$\tilde{B}_r = B_{r1}\left(\frac{r}{r_s}\right)^{m-1}\sin m\theta \text{ and } \tilde{B}_\theta = B_{\theta 1}\left(\frac{r}{r_s}\right)^{m-1}\cos m\theta,$$

$$\text{for} \quad 0 < r < r_s,$$

$$\tilde{B}_r = B_{r1}\left(\frac{r}{r_s}\right)^{-m-1}\sin m\theta,\ \tilde{B}_\theta = B_{\theta 1}\left(\frac{r}{r_s}\right)^{-m-1}\cos m\theta,$$

$$\text{for} \quad r > r_s, \quad \text{where} \quad B_{\theta 1} = B_{r1} = -\frac{\mu_0 \iota_1}{2}.$$

The solution to the equation for the magnetic field lines, $\frac{dr}{\tilde{B}_r} = \frac{rd\theta}{-B_\theta(r_s)\frac{q'(r_s)}{q(r_s)}(r - r_s) + \tilde{B}_\theta}$, has the form

$$\cos m\theta = \left(C \pm 2\frac{x^2}{h^2}\right)(1 + x/r_s)^{-m} \quad \text{for} \quad 0 < r < r_s, \quad (14)$$

$$\cos m\theta = \left(C \pm 2\frac{x^2}{h^2}\right)(1 + x/r_s)^{m} \quad \text{for} \quad r > r_s, \quad (15)$$

where $x = r - r_s$, $h = 2r\sqrt{\left|\frac{B_{r1}}{B_\theta}/m\frac{rq'}{q}\right|_{r_s}}$; and the sign is chosen in accordance with the sign of the current $j_0^* = -\frac{B_\theta(r_s)}{\mu_0}\frac{q'(r_s)}{q(r_s)}$, which generates Kadomtsev's field.

Solutions (14) and (15) are close in structure to solution (8), which was obtained for a surface perturbation current in plane geometry. In cylindrical geometry, however, the field is not symmetric with respect to the rational surface; as a result, the field line pattern changes qualitatively (Fig. 7). The magnetic field lines that originate on both sides of the rational surface from the two split points do not coincide at this surface. Accordingly, there are two separatrices that bound a layer of magnetic field lines that do not belong to any of the islands but, instead, make excursions from the inner region of the rational surface to its outer region and vice versa.

When the current density j_0^* is negative (Fig. 7), a large island forms around the o-point with the coordinates $x = 0$ and $m\theta = (2l + 1)\pi$, at which the perturbation current density $\tilde{\iota} = \iota_1 \cos m\pi$ is also negative. For a positive current density j_0^*, the field line pattern is shifted in such a way that the perturbation current density $\tilde{\iota} = \iota_1 \cos m\pi$ at the o-point of the large island is positive. Consequently, a large magnetic island forms around the perturbation current flowing in the same direction as the current j_0^*, which generates Kadomtsev's field. The current j_0^* is directed opposite to the initial current j_0 if the density of the latter is radially decreasing. In this case, a large island forms around the perturbation current flowing in the direction opposite to that of the initial current. In other words, the perturbation current that flows within the large island is negative. The perturbation current that flows within the small island is positive. Hence, in accordance with the relative directions of the perturbation current $\tilde{\iota}$ and the initial current j_0, the large islands can be called negative and the small islands can be called positive [12]. Outside the rational surface, the poloidal component of the perturbation field is in phase with the perturbation current. Consequently, the experimentally determined position of a minimum in the perturbation $\tilde{B}_\theta$ corresponds to the position of the o-point of the large island. The current j_0^* has the same direction as the initial current j_0 if the density of the latter is increasing radially. In this case, the perturbation current flowing through the o-point of the large island is positive and the poloidal position of

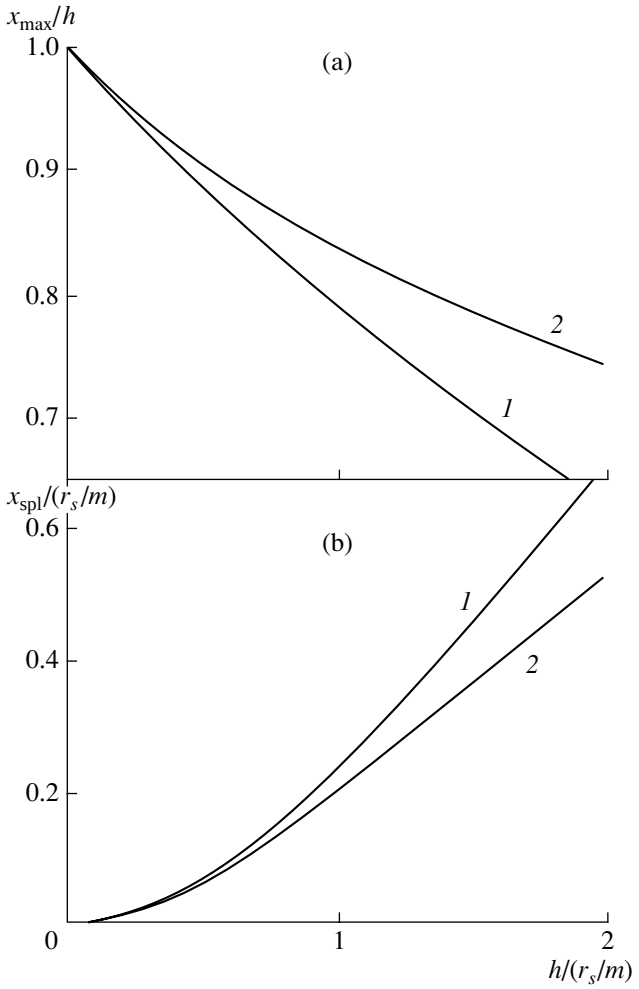

Fig. 8. Dependences of (a) the maximum relative distances x_{max}^{in} and x_{max}^{out} of the separatrices from the rational surface and (b) the distances x_{spl}^{in} and x_{spl}^{out} of the split points from the rational surface on the amplitude of an $m = 2$ perturbation in cylindrical geometry. Curves *1* and *2* refer to the inner and outer regions of the rational surface, respectively.

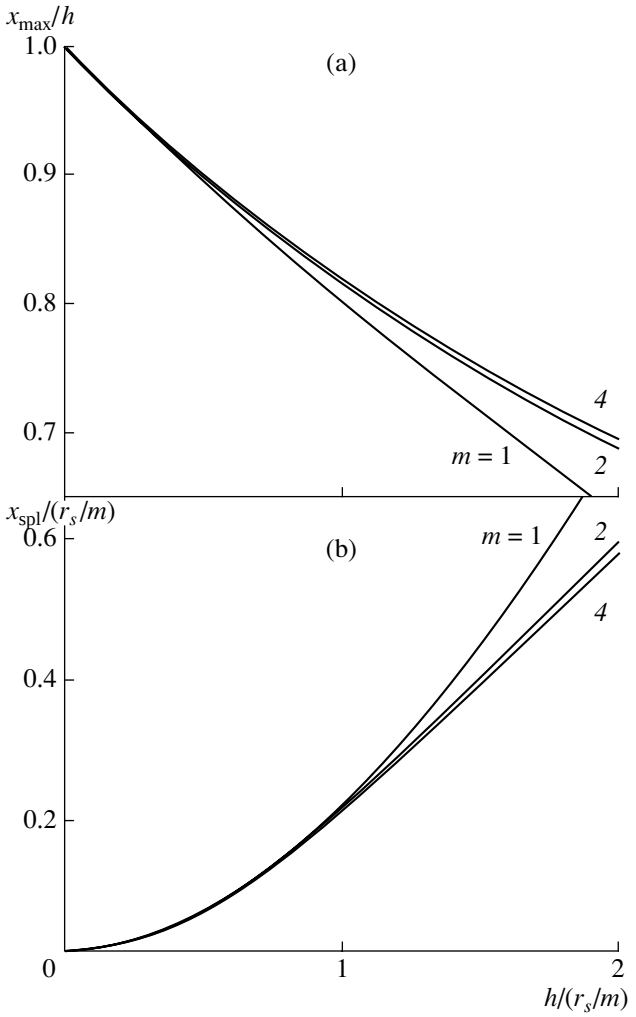

Fig. 9. Dependence of the relative half-width of (a) a large and (b) a small magnetic island on the perturbation amplitude in cylindrical geometry. The curves referring to different perturbation modes are denoted by the corresponding poloidal mode numbers.

the *o*-point corresponds to the position of a maximum in the perturbation $\tilde{B}_\theta$.

Since the field in cylindrical geometry does not possess symmetry about the rational surface, the distance from the rational surface to the split point x_{spl}^{in} lying in the inner region of this surface turns out to be larger than the distance to the split point x_{spl}^{out} lying in the outer region. For definiteness, let the separatrix that passes through the inner split point x_{spl}^{in} be called the inner separatrix, and let the separatrix that passes through the outer split point x_{spl}^{out} be called the outer separatrix. Note that the maximum distance x_{max}^{in} between the inner separatrix and the rational surface is smaller than the maximum distance x_{max}^{out} between the outer separatrix and this surface. Figure 8 shows how the parameters x_{spl}^{in}, x_{spl}^{out}, x_{max}^{in}, and x_{max}^{out} depend on the amplitude of the $m = 2$ perturbation mode. In order to estimate the half-widths of large and small islands, we introduce the mean parameters $x_{max} = (x_{max}^{in} + x_{max}^{out})/2$ and $x_{spl} = (x_{spl}^{in} + x_{spl}^{out})/2$. The dependence of the parameters x_{max} and x_{spl} on the perturbation amplitude is shown in Fig. 9 for the modes with $m = 1$, 2, and 4. The curves in this figure are seen to differ only slightly from one another. It is also seen that, as functions of the perturbation amplitude, the parameters x_{max} and x_{spl} in cylindrical geometry differ insignificantly from those in plane geometry (Fig. 4).

The parameters of the magnetic islands in plane geometry remain formally valid for perturbations with arbitrarily large amplitudes. For sufficiently strong perturbations, the magnetic islands in cylindrical geometry are radically different in structure from those in plane geometry. The reason for this is that, in cylindrical geometry, the space inside the rational surface where the islands can develop is limited. Thus, for the $m = 1$ perturbation mode, the formula for the position of the split point in the inner region of the surface, $\frac{x_{\text{spl}}^{m=1}}{r_s} = -\frac{1}{4}\frac{h^2}{r_s^2}$, fails to hold for $h \geq 2r_s$. The restrictions imposed on the possible values of h by the deviation of the linear approximation from Kadomtsev's auxiliary field (Fig. 1) are even more stringent.

Formulas (14) and (15) imply that, for weak perturbations such that $h \ll r_s$, the width of a magnetic island is equal to $W \approx 2h = 4r\sqrt{\left|\frac{B_{r1}}{B_\theta}/m\frac{rq'}{q}\right|_{r_s}}$, which agrees with relationship (1). In order to clarify the possible effect of the nonuniformity of the distribution of the perturbation current density on the width of the magnetic islands, we estimate the typical h values from experimental data. According to direct measurements of the perturbation field and initial field in a plasma column [14], the ratio $\left.\frac{B_{r1}}{B_\theta}\right|_{r_s}$ is about 1% for quasi-steady perturbations and about 6% for perturbations arising during disruption. In most experiments, the value of the ratio $\tilde{B}_\theta/B_\theta$ is measured near the tokamak chamber wall. For quasi-steady perturbations, the ratio $\tilde{B}_\theta/B_\theta$ is about 1% [3, 5]. The perturbations $\tilde{B}_\theta$ that occur during disruption are the strongest: their relative amplitudes are about 10% [15–18] and, in some cases, may be even as large as 20% [19]. These values can be used to estimate the ratio $\left.\frac{B_{r1}}{B_\theta}\right|_{r_s}$. The amount by which the perturbation field $\tilde{B}$ increases from the wall toward the rational surface is greater than that for the current field B_θ. For quasi-steady perturbations, the rational surface lies deeper inside the plasma than for perturbations arising during disruption; consequently, the ratio $\tilde{B}_r/B_\theta$ for quasi-steady perturbations should be expected to increase by a greater amount. The value of the characteristic parameter rq'/q is about 0.5–1.5. For quasi-steady perturbations, the quantity $\left.\frac{B_{r1}}{B_\theta}/m\frac{rq'}{q}\right|_{r_s}$ can be estimated at 0.02 and, for perturbations arising during disruption, it can be estimated at 0.15. Accordingly, the ratio h/r_s is estimated to be 0.3 and 0.8, respectively. The numerical results presented in Fig. 8 show that the width of an $m = 2$ magnetic island can differ from that calculated from relationship (1) by more than 10% for quasi-steady perturbations and by about 25% for perturbations arising during disruption. In this case, the width of a small island for quasi-steady perturbations and for perturbations arising during disruption is equal to about 1/5 and 1/3 of the width of a large island, respectively.

6. CONCLUSIONS

In this paper, the structure of the magnetic field lines of magnetic islands has been analyzed for four model configurations of the magnetic field by using analytic expressions for the solutions to the equations for the lines of the magnetic field produced by the initial current and the perturbation current. The simplest and most illustrative results have been obtained for a familiar plane model configuration [11] of a magnetic field in the case of a perturbation current with a wide radial density distribution. Such a distribution ensures that the perturbation field is constant in the radial direction across the magnetic islands; this is a necessary condition for the validity of relationship (1) between the width of the island and the amplitude of the magnetic field perturbation [8, 9]. In the case of a wide distribution of the perturbation current density, the islands can form around the perturbation current only when it flows in the direction of the current that produces the initial magnetic field. These are the so-called negative magnetic islands. In the region of the perturbation current flowing in the opposite direction, there are the x-points of the magnetic islands. An analysis of an infinitely narrow distribution of the perturbation current density in plane geometry (the model of a surface perturbation current) allowed us to clarify the effect of the nonuniformity of the distribution of the perturbation current density on the structure of the magnetic field lines of a magnetic island. In the case of a surface perturbation current, positive islands can also form around the perturbation current flowing in the direction opposite to that of the current producing the initial magnetic field. An analysis of a perturbation current whose density is distributed over a finite-width layer made it possible to estimate the conditions for the formation of positive magnetic islands. The geometric parameters of the islands have been considered in cylindrical geometry for the case of a surface perturbation current and have been found to be close to those of the islands in the model of a surface perturbation current in plane geometry.

An analysis of the structure of magnetic islands in the case of a nonuniform radial distribution of the perturbation current density has shown that the relationship between the width of the magnetic islands and the amplitude of the magnetic field perturbation differs from the well-known relationship (1). For a perturbation current whose density is distributed over a finite-

width layer (as well as in the limiting case of a surface perturbation current), the magnetic island width turns out to be smaller than that calculated from relationship (1). The larger the perturbation amplitude, the greater this difference: it does not exceed 10% for quasi-steady perturbations and it may amount to 25% for the strong perturbations arising during disruptions. In order for the positive magnetic islands to form, the perturbation current density should be greater than the initial current density and the perturbation current should be localized in a sufficiently narrow layer. The positive islands are smaller in size than the negative islands. For quasi-steady perturbations, the width of a positive island can amount to about one-fifth of the width of a negative island. For the strong perturbations arising during disruption, the width of a positive island can be as large as one-third of the width of a negative island. Under conditions corresponding to the formation of positive magnetic islands in cylindrical geometry, two separatrices appear that bound a layer of the magnetic field lines that do not belong to any of the islands but, instead, make excursions from the inner region of the rational surface to its outer region and vice versa.

ACKNOWLEDGMENTS

I am grateful to N.V. Ivanov, A.M. Kakurin, and V.D. Pustovitov for fruitful discussions. This work was supported in part by the Nuclear Science and Technology Department of the RF Ministry of Atomic Energy.

REFERENCES

1. H. P. Furth, J. Killen, and M. N. Rosenbluth, Phys. Fluids **6**, 459 (1963).
2. B. B. Kadomtsev and O. P. Pogutse, in *Reviews of Plasma Physics*, Ed. by M. A. Leontovich (Atomizdat, Moscow, 1967; Consultants Bureau, New York, 1970), Vol. 5.
3. B. Carreras, B. V. Waddell, and H. R. Hicks, Nucl. Fusion **19**, 1423 (1979).
4. K. Toi, K. Sakurai, S. Tanahashi, and S. Yasue, Nucl. Fusion **22**, 465 (1982).
5. M. F. Turner and J. A. Wesson, Nucl. Fusion **22**, 1069 (1982).
6. F. Alladio, E. Barbato, G. Bardotti, *et al.*, in *Proceedings of the 11th EPS Conference on Controlled Fusion and Plasma Physics, Aachen, 1983*; ECA **7D** (I), 27 (1983).
7. A. A. Bagdasarov, N. L. Vasin, V. V. Volkov, *et al.*, Fiz. Plazmy **14**, 1284 (1988) [Sov. J. Plasma Phys. **14**, 750 (1988)].
8. A. B. Mikhailovskii, Contrib. Plasma Phys. **43**, 125 (2003).
9. C. C. Hegna, Phys. Plasmas **5**, 1767 (1998).
10. G. Bateman, *MHD Instability* (MIT Press, Cambridge, 1979; Énergoizdat, Moscow, 1982).
11. P. H. Rutherford, Phys. Fluids **16**, 1903 (1973).
12. S. V. Mirnov, Fiz. Plazmy **24**, 875 (1998) [Plasma Phys. Rep. **24**, 813 (1998)].
13. B. B. Kadomtsev, Fiz. Plazmy **1**, 710 (1975) [Sov. J. Plasma Phys. **1**, 389 (1975)].
14. D. C. Robinson and K. McGuire, Nucl. Fusion **19**, 115 (1979).
15. S. V. Mirnov and I. B. Semenov, in *Proceedings of the 6th IAEA Conference on Plasma Physics and Controlled Fusion, Berchtesgaden, 1976*; Nucl. Fusion Suppl. **1**, 291 (1977).
16. V. V. Volkov, N. V. Ivanov, A. M. Kakurin, *et al.*, Fiz. Plazmy **16**, 295 (1990) [Sov. J. Plasma Phys. **16**, 813 (1990)].
17. P. Savrukhin, D. J. Campbell, M. De Benedetti, *et al.*, Rep. No. JET-R(95)06 (JET Joint Undertaking, Abingdon, 1995).
18. J. A. Wesson, R. D. Gill, M. Hugon, *et al.*, Nucl. Fusion **29**, 641 (1989).
19. V. S. Vlasenkov, V. M. Leonov, V. G. Merezhkin, and V. S. Mukhovatov, in *Proceedings of the 5th IAEA Conference on Plasma Physics and Controlled Fusion, Tokyo, 1974* (IAEA, Vienna, 1975), Vol. 1, p. 33.

Translated by G.V. Shepekina

Plasma Physics Reports, Vol. 30, No. 11, 2004, pp. 918–936. Translated from Fizika Plazmy, Vol. 30, No. 11, 2004, pp. 988–1007.

DUSTY PLASMA

Formation of Vortex Dust Structures in Inhomogeneous Gas-Discharge Plasmas

O. S. Vaulina*, A. A. Samarian, O. F. Petrov*, B. James**, and F. Melandso*****

** Institute for High Energy Densities, Associated Institute for High Temperatures, Russian Academy of Sciences, Izhorskaya ul. 13/19, Moscow, 125412 Russia*

*** School of Physics, University of Sydney, NSW 2006, Sydney, Australia*

**** University of Tromsoe, N-9037, Tromsoe, Norway*

Received August 5, 2003; in final form, January 9, 2004

Abstract—A generalized analytical model of instabilities in a dusty plasma with a nonzero grain charge gradient in a field of nonelectrostatic forces is considered. A review is given of different experimental observations of the dust self-oscillations that occur in the plasmas of an rf capacitive discharge and a dc glow discharge and whose appearance can be explained in terms of the proposed model. It is shown that the change in the grain charge gives rise to dynamic dust structures in laboratory gas-discharge plasmas. Attention is focused on the analysis of the onset of vortex motion of the dust grains. *© 2004 MAIK "Nauka/Interperiodica".*

1. INTRODUCTION

In the physics of dusty plasmas, there is now increased interest in problems associated with the onset and development of various instabilities. Papers devoted to analyzing the conditions for the self-excitation of dust oscillations in plasma are constantly appearing [1–19]. Some of them are aimed at experimental observation of the vortex dust motion in different plasmas, such as the plasma of a dc gas discharge [5, 12, 14], the plasma of an rf capacitive discharge [1, 8], and nuclear excited plasmas [6]. It is worth mentioning here the first attempt to crystallize a dust system under microgravity conditions (onboard the *Mir* space station) [7] and recent experiments [13] that were carried out onboard the *Alpha* international space station and in which the formation of dust vortices in an rf discharge chamber was observed.

Dynamic dust structures (such as waves or vortices) are stable distributions of the densities of moving dust grains whose directed velocity is nonzero, in contrast to liquid- and solidlike quasi-steady structures, in which the mean directed velocity of thermal motion is zero.

In a viscous medium (e.g., a weakly ionized laboratory plasma), dynamic dust structures can arise only in the presence of potential sources that compensate for energy dissipation. Since the dust is observed to execute vortex motion in different plasmas, it is natural to suppose that this motion is driven by electric forces. One possible mechanism for converting the potential energy of an external electrostatic field into the energy of dust motion is associated with spatial or temporal variations in the grain charge eZ_d [4, 9, 15–20]. The grain charge gradient in dusty plasma, $\boldsymbol{\beta} = \nabla Z_d$, is governed by the nonuniform conditions under which dust grains become charged (namely, by the gradients of the temperatures and densities of the components of the surrounding plasma, the spatial variations in the illumination of the surfaces of the emitting grains, variations in the grain surface temperature, etc.). The nonequilibrium nature of such dust systems may stem from the collective effects associated with the stochastic spatial variations δZ_d in the grain charges. These variations, in turn, give rise to fluctuations in the intergrain interaction forces $\propto Z_d \delta Z_d / l_d^2$ that are exerted on an individual grain by the remaining grains in the dust cloud (here, l_d is the mean distance between the grains) [4, 9, 19, 20]. Although these fluctuations can lead to anomalous dust heating (i.e., can set the grains into a stochastic motion whose kinetic energy is far higher than the temperature of the surrounding gas), they alone cannot explain the excitation of regular motions of the dust grains and the formation of dynamic dust structures; therefore, additional sources compensating for energy dissipation need to be invoked.

In a system with a nonzero grain charge gradient $\boldsymbol{\beta}$, regular dust self-oscillations can be induced in the presence of nonelectrostatic forces $\mathbf{F}_{\text{non}}$ (such as the gravity force, the thermophoretic force, and the ion drag force) that act on the dust grains in plasma [12, 15–19]. The role of the nonelectrostatic forces in exciting oscillations in a system of likely charged grains is governed by their ability to confine a dust cloud within the region of an uncompensated electric field $\mathbf{E} = \mathbf{F}_{\text{non}}/(eZ_p)$. When the curl of the forces acting in the system is nonzero ($\boldsymbol{\beta} \times \mathbf{E} \neq 0$, this electric field can perform positive work $A \propto (F_{\text{non}}/(eZ_d))^2$, which compensates for the dissipative energy losses of a particle moving along a closed path. Under the condition $(eZ_d/l_d)^2 \ll F_{\text{non}}$, this mechanism for the excitation of dust oscillations is more effi-

1063-780X/04/3011-0918$26.00 © 2004 MAIK "Nauka/Interperiodica"

cient than the effects associated with collective dust fluctuations.

To conclude the introduction, let us note that the rotation of dust with a nonzero grain charge gradient along the axis of a cylindrical system in the field of the radial ion drag force was first revealed in numerical experiments conducted by Zhakhovskiĭ *et al.* [10]. At that time, however, an analytic model capable of predicting the conditions for the onset of such a rotation, as well as its direction and angular velocity, was lacking. A theory for the excitation of vortices in an inhomogeneous dusty plasma was proposed by Boushoule *et al.* [15], who considered for the first time the self-consistent problem of the development of convective (dispersive) instability in the field of the ion drag force with allowance for the distributions of the dust and plasma densities and determined the threshold for the onset of this instability with allowance for dissipation by neutral particles. The effect of the ion drag force on the formation of vortex dust motion under the conditions of experiments carried out onboard the *Alpha* international space station was also mentioned by Fortov *et al.* [13], who analyzed the dynamics of dust rotation using a model that was constructed to describe the dynamics of an absolute (dissipative) instability in a dust system with a nonzero grain charge gradient in the gravity field [11]. The mechanism for the onset of various dust oscillations in inhomogeneous plasmas of a dc glow discharge and an rf discharge under the Earth's gravity conditions was investigated qualitatively in [1, 12, 14]. In the present paper, an analytic model is described that generalizes the analysis of instabilities in a dusty plasma with a nonzero grain charge gradient to arbitrary nonelectrostatic forces. Attention is focused on analyzing of the dissipative instability, which drives a large-scale rotation of the dust and leads to the formation of dust vortices regardless of the magnitude of the frictional forces present in the system (in contrast to the dispersive instability, which is critical to the dissipation of the energy of dust grains by neutrals [11, 15]). A review is given of different experimental observations of the dust self-oscillations that occur in the plasmas of an rf capacitive discharge and a dc glow discharge and whose appearance can be explained in terms of the proposed model.

2. THEORY

2.1. Conditions for the Formation of Dust Self-Oscillations in an Inhomogeneous Plasma

Existing mathematical models for investigating the conditions for the onset of self-oscillations in nonlinear nonequilibrium systems are based on solving differential wave equations. These models are capable of describing two main types of instability: (i) the *dissipative* instability in systems with energy dissipation and (ii) the *dispersive* instability in systems in which dissipation is weak or absent [21]. Note that, in the literature, these instabilities are sometimes called absolute and convective, respectively [22]. We are using the terms *dissipative* and *dispersive* because they better reflect the physical picture of the development of these instabilities. This classification of instabilities is based on the following analysis: Let us consider the response of a stable system G to a small perturbation ϕ in the form of a harmonic wave with wave vector $\mathbf{k}$, frequency ω, and amplitude b,

$$\phi = b\exp(ikx - i\omega t), \quad (1)$$

where x is the spatial coordinate and t is the time. In this case, the differential wave equations can be written in operator form as $\hat{G}(ik; -i\omega)b$, and the dispersion relation $L(\omega, k) \equiv \det\hat{G} = 0$ shows whether or not the model under consideration contain terms describing dissipation. For a system with dissipation, the function $L(\omega, k)$ and the roots of the equation $L(\omega, k) = 0$ are complex, $\omega = \omega_R + i\omega_I$. In case (i), i.e., for $\omega_I > 0$, the solution increases in time and thus is unstable. In case (ii), the function $L(\omega, k)$ is real and the roots of the equation $L(\omega, k) = 0$ can appear in a conjugate pair, $\omega = \omega_R \pm i\omega_I$. Consequently, the solution increases exponentially for any $\omega_I \neq 0$. Note that, in many physical problems concerning simulations of hydrodynamic systems, introduction of even a low viscosity can substantially distort the dispersive solutions in case (ii) and, moreover, can make them impossible [21, 23].

Let us analyze the stability of a discrete system of N_d charged grains in a two-dimensional cylindrical electrostatic trap, assuming that the spatial variation of the grain charge is given by the expression $Z(r, y) = Z_d + \Delta Z(r, y)$, where $Z_d = Z(0, 0)$ and $r = (x^2 + z^2)^{1/2}$ is the radial coordinate of the grain. We write the equation of motion for each grain with allowance for such factors as the external electric field $\mathbf{E}_{\text{ext}}(r, y) = \mathbf{i}E^y_{\text{ext}} + \mathbf{j}E^r_{\text{ext}}$ (where $\mathbf{i}$ and $\mathbf{j}$ are unit vectors in the $\mathbf{y}$ and $\mathbf{r}$ directions, respectively); the force of the pair interactions between the grains, $eZ(r, y)\mathbf{E}_{\text{int}}(r, y)$; the frictional force; the random force in Brownian motion F_{br} that is induced by collisions of the molecules of the surrounding gas with the grains; and the net nonelectrostatic force $\mathbf{F}_{\text{non}} = F^y_{\text{non}}\mathbf{i} + F^r_{\text{non}}\mathbf{j}$, which acts on the grains in a dust cloud in the plasma:

$$m_d\frac{d^2\mathbf{l}_k}{dt^2} = -m_d\nu_{fr}\frac{d\mathbf{l}_k}{dt} + eZ(\mathbf{l}_k)\mathbf{E}_\Sigma + \mathbf{F}_{\text{non}} + \mathbf{F}_{\text{br}}. \quad (2)$$

Here, $\mathbf{l}_k(r, y) = \mathbf{i}y + \mathbf{j}r$, $\mathbf{E}_\Sigma = \mathbf{E}_{\text{int}} + \mathbf{E}_{\text{ext}} \equiv E^y_\Sigma\mathbf{i} + E^r_\Sigma\mathbf{j}$ is the net electric field, $\mathbf{E}_{\text{int}} = \sum_m \frac{\partial\varphi}{\partial l}\Big|_{l = |\mathbf{l}_k - \mathbf{l}_m|}\frac{\mathbf{l}_k - \mathbf{l}_m}{|\mathbf{l}_k - \mathbf{l}_m|} \equiv E^y_{\text{int}}(r, y)\mathbf{i} + E^r_{\text{int}}(r, y)\mathbf{j}$, $\varphi = \frac{eZ(r, y)}{l}\exp\left(-\frac{l}{\lambda}\right)$ is the screened Coulomb potential, and l is the intergrain dis-

tance. In a system in which the curl of the forces acting on the dust grains is nonzero, the electric field can perform positive work that compensates for dissipative energy losses of a grain moving along a closed path. This indicates that infinitely small perturbations excited in the system by thermal or other fluctuations can grow. The system described by Eqs. (2) is nonconservative because, on the one hand, the energy in it is dissipated by friction and, on the other, the energy can be pumped into it due to the combined action of the electric field force and a nonelectrostatic force $\mathbf{F}_{\text{non}}$ (e.g., the thermophoretic force, the gravity force, the ion drag force, or a superposition of these forces). We recall that the modeling of the grain dynamics by means of Eqs. (2) is correct only when the dust motion does not perturb the external electric field $\mathbf{E}_{\text{ext}}$ induced by the distributions of the electron and ion densities (n_e and n_i) in the surrounding plasma. The condition for the perturbations of the surrounding plasma to be weak is satisfied for dust clusters in which the number of dust grains at the cluster boundary is comparable to the total number of grains in the cloud. For extended dust systems, this condition can be represented as $Z_d n_d \ll n_e$. In such a situation, the analysis of the instability conditions for a system described by Eqs. (2) remains qualitatively the same if we assume that, by the time of the onset of instability, a small displacement of an individual grain in an initially stable dust cloud has a correspondingly slight effect on the electron and ion density distributions in the plasma.

We analyze linearized equations of motion (2) under the assumption that the random force in Brownian motion F_{br} and the collective effects associated with the spatial fluctuations of the grain charges in a dust cloud play only a minor role at the time when the instability occurs. We consider a grain with a charge Z_0 that is in a stable position at a point (r_0, y_0) and determine how it responds to certain displacements ($\delta r \equiv r$, $\delta y \equiv y$) from this equilibrium position:

$$d^2r/dt^2 = -\nu_{\text{fr}} dr/dt + a_{11} r + a_{12} y, \tag{3a}$$

$$d^2y/dt^2 = -\nu_{\text{fr}} dy/dt + a_{22} y + a_{21} r, \tag{3b}$$

where $a_{11} = (e^2 Z_0^2 \partial E_\Sigma^r/\partial r - e\beta_r F_{\text{non}}^r + eZ_0 \partial F_{\text{non}}^r/\partial r)/(eZ_0 m_d)$, $a_{12} = (e^2 Z_0^2 \gamma_0 - e\beta_y F_{\text{non}}^r + eZ_0 \partial F_{\text{non}}^r/\partial y)/(eZ_0 m_d)$, $a_{22} = (e^2 Z_0^2 \partial E_\Sigma^y/\partial y - e\beta_y F_{\text{non}}^y + eZ_0 \partial F_{\text{non}}^y/\partial y)/(eZ_0 m_d)$, $a_{21} = (e^2 Z_0^2 \gamma_0 - e\beta_r F_{\text{non}}^y + eZ_0 \partial F_{\text{non}}^y/\partial r)/(eZ_0 m_d)$, $F_{\text{non}}^r \equiv F_{\text{non}}^r(r_0, y_0)$, $F_{\text{non}}^y \equiv F_{\text{non}}^y(r_0, y_0)$, $\beta_r = \partial Z(r, y)/\partial r$, $\beta_y = \partial Z(r, y)/\partial y$.

The first derivatives in Eqs. (3a) and (3b) are taken at the point (r_0, y_0). The parameter γ_0 determines the response of the system to longitudinal perturbations and, by virtue of the potential nature of the electric field, $\nabla \times \mathbf{E}(r, y) = 0$, satisfies the relationship $\gamma_0 = \left.\frac{\partial E_\Sigma^y}{\partial r}\right|_{r_0, y_0} \equiv \left.\frac{\partial E_\Sigma^r}{\partial y}\right|_{r_0, y_0}$ not only for immobile charged grains but also for $Z(r, y) \longrightarrow$ const. Note again that, in the absence of nonelectrostatic forces ($\mathbf{F}_{\text{non}} = 0$), the system is stable ($a_{21} = a_{12}$) and thus cannot perform any positive work, provided that the collective effects associated with the spatial fluctuations of the grain charge in the dust cloud, which lead to random variations in the net electric field of the grains, are ignored.

Linearized Eqs. (3a) and (3b) do not contain spatial derivatives and can be used to examine the conditions for the onset of the instability [21]. An analysis of the response of the system to a small perturbation $\varphi = b\exp(-i\omega t)$ in the **r** or **y** direction yields the dispersion relations $L(\omega) \equiv \det \hat{G} = 0$, which determine the range of existence of nontrivial unstable solutions for a system $\hat{G}(-i\omega; \mu)b$ described by Eqs. (3a) and (3b):

$$\omega^4 + (a_{11} + a_{22} - \nu_{\text{fr}}^2)\omega^2 + (a_{11}a_{22} - a_{12}a_{21}) + i\nu_{\text{fr}}\omega(2\omega^2 + a_{11} + a_{22}) = 0. \tag{4}$$

An analysis of Eq. (4) shows that, when the displacements of the grains are functionally independent of one another ($y \neq f(r)$, $a_{12}a_{21} = 0$), the system under investigation is stable, provided that a_{22} and a_{11} are real and negative. For $\nu_{\text{fr}} \neq 0$, the solution to Eqs. (3a) and (3b) also is stable; i.e., it implies that any small perturbation is asymptotically damped ($\omega_1 < 0$) under the conditions

$$a_{11}a_{22} - a_{12}a_{21} \geq 0, \tag{5a}$$

$$\nu_{\text{fr}}^2 \geq |a_{11} + a_{22}|/2. \tag{5b}$$

The equality sign in condition (5a) determines the neutral dispersion curve of dissipative instability ($\omega_R = 0$, $\omega_I = 0$), the condition for the onset of this instability being

$$a_{11}a_{22} - a_{12}a_{21} < 0. \tag{6}$$

The characteristic difference between dispersive instability in case (ii) and dissipative bifurcation in case (i) is that the former is especially sensitive to the value of the friction coefficient ν_{fr}. The motion can be dispersive ($\omega_R \neq 0$, $\omega_I = 0$) near a certain resonant frequency given by the relationship $\omega_c^2 = |a_{11} + a_{22}|/2$, when friction in the system is balanced by the incoming potential energy. With allowance for the appearance of complex self-conjugate roots ($\omega = \omega_R \pm i\omega_I$), the necessary condition for the existence of growing oscillating solutions has the form

$$\omega_c^2 \leq \left|4a_{12}a_{21} + (a_{11} - a_{22})^2\right|/(4\nu_{\text{fr}}^2). \tag{7}$$

The motion that is established as a result of the development of an instability of this type in the case of strong dispersion consists of harmonic oscillations at a frequency close to the bifurcation point of the system, ω_c [21]. Generally, oscillations at a certain frequency ω_c will grow when the damping does not destroy the structure of the dispersive solution ($\nu_{fr} \ll \omega_c$), i.e., when it is sufficiently weak and does not lead to a substantial shift of the neutral dispersion curve, at which $\omega_I = 0$. The neutral curve, given by the equality sign in condition (7), determines a singular solution to Eqs. (3a) and (3b).

From the physical point of view, small perturbations in the system will grow in the two cases considered above, namely, (i) when the perturbations are not subject to any restoring force (see condition (6)) and (ii) when the frequency of the perturbations is close to a certain resonant frequency that is characteristic of the system and at which the oscillations are not suppressed by the frictional forces (see condition (7)). If we draw an analogy with the familiar equations for the amplitudes of the perturbations, then, in case (i), we will arrive at a diffusion-like equation, and, in case (ii), we will see that the motion of a particle is described by an equation of the second order in time and that the instability arising in the system is of a dispersive nature.

In order to represent conditions (6) and (7) in a form convenient for analyzing the results of numerical and laboratory experiments, we assume that $\mathbf{F}_{non}(r, y) = \text{const}$ and $a|\Delta Z(r, y)| \ll |Z_0| \approx |Z_d|$. Taking into account the values of the parameters a_{ij} in the problem given by Eqs. (3a) and (3b), we obtain the following condition for the onset of dissipative instability:

$$\begin{aligned} &\omega_{cc}^4 - (eZ_d\gamma_0/m_d)^2 < \Psi \\ &\equiv -\gamma_0 e^2 Z_d(\beta_y F_{non}^r + \beta_r F_{non}^y)/m_d \\ &+ (\beta_y\beta_r F_{non}^r F_{non}^y)/(Z_d m_d)^2, \end{aligned} \tag{8}$$

where we have introduced the notation

$$\omega_{cc}^4 \approx \frac{e^2 Z_d^2}{m_d^2}\left(\frac{\partial E_\Sigma^r}{\partial r}\frac{\partial E_\Sigma^y}{\partial y}\right)\Bigg|_{r_0, y_0}.$$

Since $\omega_{cc}^4 > (eZ_d\gamma_0/m_d)^2$, the left-hand side of condition (8) is positive and the system is stable for $\beta_y \equiv \beta_r = 0$. Thus, the condition for the onset of dissipative instability does not involve the friction coefficient ν_{fr} and is determined by the parameters that govern the electric fields in the system: the grain charge Z_d, its gradients β_y and β_r, the dust density n_d, and the density of the surrounding plasma. Since, in this case, the second time derivative can be ignored, and since the curl $\mathbf{\Omega} = \nabla \times \mathbf{V}$ of the grain velocity $\mathbf{V}$ is nonzero, condition (8) describes the onset of vortex motion along a certain closed curve. For monotonic spatial distributions of the electric field and grain charge, $\mathbf{E}(r, y)$ and $Z(r, y)$, the direction of this rotational motion in a plane parallel to the force $\mathbf{F}_{non}$ is determined by the sign of Ω:

$$\Omega = (\beta_r F_{non}^y - \beta_y F_{non}^r)/(m_d Z_d \nu_{fr}), \tag{9}$$

The necessary condition for the development of a dispersive instability in case (ii) ($\mathbf{F}_{non} = \text{const}$, $|\Delta Z(\rho, y)| \ll |Z_0| \approx |Z_d|$) and, accordingly, for the growth of the oscillating solutions has the form

$$\nu_{fr}^2 < \omega_c^2 < |\Psi|/\nu_{fr}^2, \tag{10}$$

where

$$\omega_c^2 \approx \left|\frac{e^2 Z_d^2}{2m_d}\left(\frac{\partial E_\Sigma^r}{\partial r} + \frac{\partial E_\Sigma^y}{\partial y}\right)\right|_{r_0, y_0}\Bigg|.$$

Condition (10) determines the region where regular dust oscillations can be excited provided that the grains in the dust cloud execute synchronized motion [23].

Simpler relationships for the analysis of the conditions under which the instabilities in question occur can be derived under the assumptions that the nonelectrostatic force $\mathbf{F}_{non}$ acts in the chosen direction (the r or y direction) and that the dust cloud is extended and isotropic ($\omega_c \cong \omega_{cc}$). Under these assumptions, the condition for the onset of dissipative instability has the form

$$\omega_c^4 < |\gamma\Omega\nu_{fr}|, \tag{11}$$

where $\gamma = eZ_d\gamma_0/m_d$ and the condition for the onset of dispersive instability can be written as

$$\nu_{fr}^2 < \omega_c^2 < |\gamma\Omega/\nu_{fr}|. \tag{12}$$

For an extended cloud of the dust grains interacting via the Coulomb potential, the parameters γ and ω_c^2 are proportional to $\propto e^2 Z_d^2 n_d/m_d$. Under conditions (11) and (12), the modulus sign indicates that, in any case, there is an unstable position for each of the dust grains. For example, let us consider a dust cloud in the field of a constant force such as the gravity force $F_{non}^y \equiv -m_d g$ ($F_{non}^r \equiv 0$). In this case, for $\beta_r > 0$, the grains that are subject to the instabilities in question are in the lower region of the cloud (i.e., the region that is below the plane passing through the cloud center and in which $\gamma < 0$), and, for $\beta_r < 0$, the instabilities occur in the upper region of the cloud (where $\gamma > 0$). Moreover, in the field of the force $\mathbf{F}_{non}$ such that $F_{non}^r \equiv 0$ and $F_{non}^y \equiv \text{const}$, the grains that are in the region where their charges are minimal will move in the direction of this force and the grains that are in the region where their charges are maximal will move in the opposite direction.

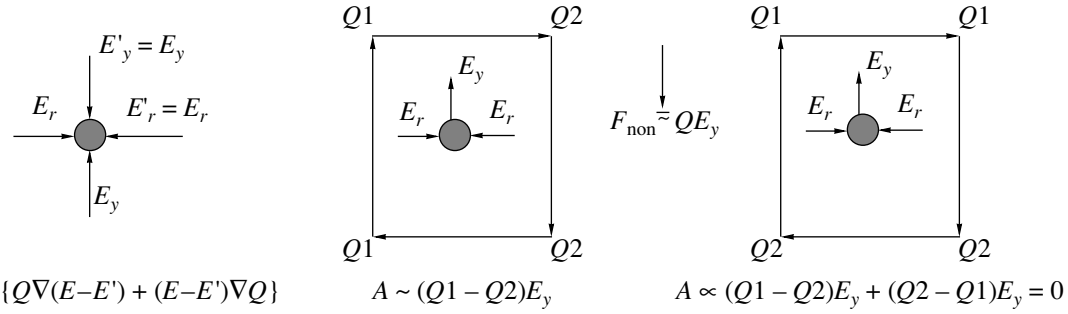

Fig. 1. Illustration of the motion of a grain with a variable charge Q in the field of a nonelectrostatic force $\mathbf{F}_{\text{non}}$.

A physical picture of how the nonelectrostatic force and the direction of the grain charge gradient influence the development of the above instabilities is illustrated in Fig. 1. We can readily see that, if a grain is in a stable state in the field of a potential electric force ($Q\mathbf{E} = Q\mathbf{E}'$, where $Q = eZ_d$), then the curl of the force experienced by it when it is displaced from its equilibrium position equals zero, regardless of whether the grain charge varies in space, $\boldsymbol{\beta} \sim \nabla Q = e\nabla Z_d$, or not. If the stable position of the grain is governed by the balance between the electric and nonelectrostatic forces ($F_{\text{non}} = QE_y$), then the field E_y can perform work on the grain displaced from its equilibrium position ($A \neq 0$) only when the grain charge gradient is nonzero and is orthogonal to the force $\mathbf{F}_{\text{non}}$. Moreover, this work is positive and can compensate for dissipative energy losses only when the grain moves along the direction of the force $\mathbf{F}_{\text{non}}$ in the region where its charge is minimum and along the opposite direction in the region where its charge is maximum (see Fig. 1).

Hence, the above two types of instabilities can occur only when the grain charge gradient is nonzero and is orthogonal to the nonelectrostatic force, in which case the conditions for the onset and development of dissipative instability are independent of frictional forces (i.e., they do not contain the friction coefficient ν_{fr}). Taking into account the tendency of the system to evolve through a preferential instability mode whose dispersion curve is close to the neutral dispersion curve [21–23], the frequency ω_Ω of the large-scale rotation established under condition (11) for the development of dissipative instability can be estimated by setting $\omega_c^4 \approx |\gamma\Omega\nu_{\text{fr}}|$. Assuming that $\omega_\Omega \propto \omega_c^2/\nu_{\text{fr}}$ (see above), we can estimate the angular velocity of the circular ($\omega_\Omega \approx |\Omega|/2$) motion by $\gamma \propto \omega_c^2 \propto e^2 Z_d^2 n_d/m_d$. We thus see that the frequency of this rotational motion depends on the frictional force, in contrast to the frequency of the regular oscillations that can be excited under condition (12) for the development of dispersive instability. Because of the dust inertia, these regular oscillations are excited at a frequency of about the resonant frequency ω_c of the system and their dispersion curve is close the neutral curve, the critical value of the friction coefficient, $\nu_c = \nu_{\text{fr}}$, for the formation of the dispersive motions being determined by condition (12). The nascent harmonic oscillation whose dispersion curve is close to the neutral curve can be described by the equations $dy/dt = -\omega_1 r$ and $dr/dt = \omega_2 y$ ($\omega_c^2 = \omega_1\omega_2$) and, instead of condition (12), the criterion for the onset of instability can be represented in the form [11, 23]

$$\nu_{\text{fr}} < \omega_c < |\Omega|/2. \tag{13}$$

To conclude this section, note that the above analysis yields an incomplete picture of the development of the instabilities in question, because it was performed with many simplifying assumptions and without allowance for the stochastic motion of the dust grains and the collective effects associated with the fluctuations in the intergrain interaction forces. It should also be noted that the model considered here provides merely a qualitative description of the conditions for the generation of the above two types of instabilities in an inhomogeneous plasma. A quantitative description of the thresholds for the onset of these instabilities (i.e., of conditions (11) and (12)) requires the data on the parameters of the plasma (the electric fields), the dust grains (the grain charge and the friction coefficients), and the nonelectrostatic forces acting in an actual physical system. The required information can be obtained in experiments (see Section 2.2 below) or by solving a self-consistent problem in a way similar to what Boushoule *et al.* [15] did when analyzing the conditions for the development of dispersive instability in the field of the ion drag force in the case of a dusty plasma in a low-pressure gas discharge. In order to quantitatively estimate the applicability of the model proposed here to actual laboratory experiments, in subsequent sections of this paper, we give an analysis of the possible grain charge gradients and possible nonelectrostatic forces acting on the grains under the conditions typical of gas discharge plasmas and present the results from numerical simulations of inhomogeneous dust systems involving numerous charged particles.

2.2. Grain Charge Gradients

Because of high electron mobility, nonemitting dust grains acquire a negative equilibrium charge $\langle Z_d \rangle$ consistent with the parameters of the surrounding plasma. Due to the temporal and spatial variations in plasma parameters, this charge can depend on time and also on the position of the grain. Spatial variations in the grain charge can be caused by the inhomogeneity of the background plasma surrounding the dust cloud, e.g., by the gradients of the electron and ion densities $n_{e,i}$ and electron and ion temperatures $T_{e,i}$. Such conditions are often encountered in the plasmas of inductive rf discharges and dc glow discharges [9–12, 24]. Thus, in the plasma of a discharge dominated by ambipolar diffusion, the grain charge gradient $\boldsymbol{\beta}$ can grow as large as $\beta \approx 0.3\langle Z_d \rangle$ cm^{-1} due merely to a small violation of the electroneutrality of the surrounding plasma, $|\delta n| = |n_i - n_e| \ll n_i \approx n_e$ [12].

When the directed velocities of the electrons and ions are ignored, the charging of a solitary nonemitting dust grain is described by the equation $\langle Z_d \rangle = -za_d T_e/e^2$, where $z \approx 2$–4 for most experiments with gas-discharge plasmas [20, 25]. Using this equation, we can obtain the amount $\Delta_T Z_d = (Z_d - \langle Z_d \rangle)$ by which the grain charge varies when the electron temperature over the plasma volume changes by an amount ΔT_e,

$$\Delta_T Z_d / \langle Z_d \rangle = \Delta T_e / T_e, \tag{14}$$

and, accordingly, can determine the grain charge gradient $\beta_y^T = \partial Z_d/\partial y$ in the direction in which the electron temperature is nonuniform (e.g., in the y direction),

$$\beta_y^T / \langle Z_d \rangle = (\partial T_e/\partial y) T_e^{-1}, \tag{15}$$

Using the formulas of the orbit motion limited (OML) approximation, we can estimate a slight change $\Delta_n Z_d$ in the equilibrium charge $\langle Z_d \rangle$ of a grain due to the violation of the electroneutrality of the surrounding plasma, $\delta n = n_i - n_e$ [12]:

$$\frac{\Delta_n Z_d}{\langle Z_d \rangle} \cong -\frac{\nabla \cdot \mathbf{E}}{4\pi e n_0 (1+z)}, \tag{16}$$

where $\mathbf{E}$ is the electric field strength and n_0 is the density of a neutral plasma ($n_e = n_i = n_0$). Obviously, the condition $\delta n \ll n_0$ automatically satisfies the requirement that the grain charge variation be small, $|\Delta_n Z_d| \ll \langle Z_d \rangle$. As a result, for Maxwellian velocity distributions of the ions and electrons, and for $|e\varphi/T_{e,i}| \ll 1$, we find that the change in the grain charge Z_d is proportional to the potential φ of the surrounding plasma. This approximation is sometimes used to estimate the spatial variation in the grain charge [9, 10].

An analogous estimate for the amount by which the grain charge changes over a plasma layer, $|\Delta_i Z_d| = |Z_d - \langle Z_d \rangle| \ll |\langle Z_d \rangle|$, can be obtained under the assumption $|e\varphi/T_e| \ll 1$ and under the condition that the directed velocity of the ions, u_i, is much higher than their thermal velocity v_{Ti}:

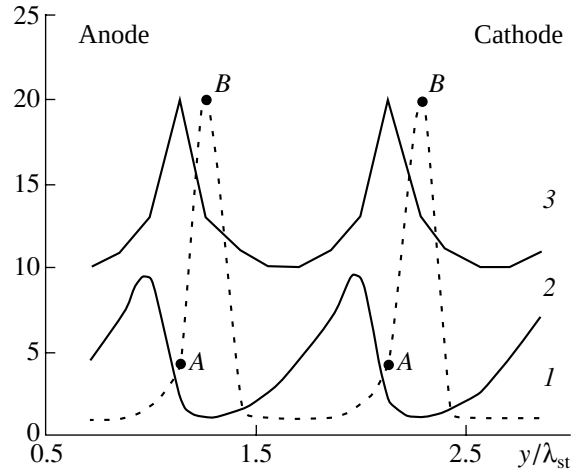

Fig. 2. Relative variations in (*1*) the field $E(y)/E^0$, (*2*) electron density n_e/n_e^0, and (*3*) electron temperature $10T_e/T_e^0$ along the discharge tube (in the y/λ_{st} direction) for a discharge in neon at PR = 2.7 cm torr and $\lambda_{st} \approx 7$ cm [23].

$$\frac{\Delta_i Z_d}{\langle Z_d \rangle} \cong -\frac{(2z\delta n/n_0 - e\varphi(z-s)/T_e)}{z(1+s+z)}, \tag{17}$$

where $\langle Z_d \rangle$ is the equilibrium grain charge in a plasma layer of density n ($\delta n \ll n$) and $s = m_i u_i^2/(2T_e)$. Relationship (17) can be used to estimate how much the grain charge changes near the upper boundary of the electrode sheath, i.e., in the region where levitating dust grains are usually observed. Taking into account the fact that the ions enter the sheath with the Bohm velocity $v_B = (T_e/m_i)^{1/2}$ and that $n = n_B \approx n_0/2.7$ (where n_0 is the unperturbed plasma density), we obtain $s = 0.5$. It should be noted that this approach is valid only for very low pressures such that the mean free path l_i of the ions with respect to their collisions with neutral gas particles is much greater than the electron Debye radius λ_{De}. For moderate pressures (0.05–1 torr), which are the working pressures in most experiments with dusty plasmas, we have $l_i \sim \lambda_{De}$. In this case, the ion velocity at the sheath boundary, $u_i(0)$, is lower than the Bohm velocity v_B by a factor of approximately$(\pi\lambda_{De}/2l_i)^{1/2}$ [26]. Note that relationship (17) was derived under the assumption that ionization processes in plasma can be ignored ($n_i u_i$ = const).

Let us estimate the grain charge gradient by analyzing, as an example, conditions typical of experiments with gas-discharge plasmas, such as the plasmas of a

stratified dc glow discharge and of the electrode sheath in an rf capacitive discharge [1, 5–8, 12–14].

2.2.1. DC glow discharge. Figure 2 shows representative profiles of the plasma parameters along the positive column of a stratified glow discharge in neon for PR = 2.7 cm torr and $\lambda_{st} \approx 7$ cm, where R is the radius of the gas discharge tube and λ_{st} is the wavelength of the striation [27, 29]. The variations in the parameters n_e, T_e, and $E(y)$ in Fig. 2 are qualitatively similar to those observed in numerous experiments with stratified discharges in noble gases [29]. Under laboratory conditions, negatively charged dust grains are usually observed to levitate in the region of the strong electric fields of the head of the stratum (see Fig. 2, zone [*A*, *B*]). Over this region, which is close to the narrow brightest region of the discharge, the degree to which the plasma deviates from quasineutrality is proportional to $\delta n(y)/n_0 \sim \lambda_{De}^2/(\Lambda^l L_{st})$, where n_0 is the plasma density in the positive column, $\lambda_{De} = (T_e/(4\pi e^2 n_0))^{1/2}$, Λ^l is the electron energy relaxation length (for neon, it is equal to Λ^l_{Ne} [cm] $\cong 10/P$ [torr]), and $L_{st} \sim 1$–3 cm is the length of the region where the electric field varies most abruptly [29]. Hence, within the region where the dust grains are suspended, the quantity $|\Delta_n Z_d/\langle Z_d\rangle| \ll 1$ is negligibly small in comparison to the quantity $|\Delta_T Z_d/\langle Z_d\rangle| = \Delta T_e(y)/T_e \sim 0.5$–1. Consequently, the variation in the grain charge along the tube axis (in the y direction) is determined by the electron temperature gradients and can be substantially reduced when the grains are displaced into the region of the strong electric field: $\beta_y/\langle Z_d\rangle = (\partial T_e/\partial y)\, T_e^{-1} \sim 0.5$–1 cm^{-1} (see Fig. 2). In the radial direction, the derivative $\partial T_e/\partial r$, in contrast, is close to zero; hence, the grain charge variation in this direction, $\Delta Z_d(r, y)/\langle Z_d\rangle$, is determined by the gradient $\delta n = n_i - n_e$.

For a discharge dominated by ambipolar diffusion ($R \gg \lambda_{De}$), the radial electric field can be represented as [29]

$$E(r) \approx -\frac{T_e}{en_e}\frac{\partial n_e}{\partial r} \approx \frac{T_e}{e\Lambda}, \qquad (18)$$

where Λ is the characteristic diffusion length, which is determined by the boundary conditions of the problem to within a numerical factor of about 2 [29] and, for a cylinder of radius R, is approximately equal to $\Lambda \sim R/2.4$. For distances $r > \lambda_{De}$ from the axis of a tube with the radius R = 3 cm and for the electron Debye radii in the range $\lambda_{De} < 1000$ μm (which is typical of glow discharges), we find from estimate (16) (with z = 2.5 for neon) that the ratio $|\Delta_n Z_d(r, y)/\langle Z_d\rangle| \approx 0.62\lambda_{De}^2/(Rr)$ is smaller than 0.03. This indicates that the condition for the grain charge variations to be small, $|\Delta_n Z_d(r, y)| \ll |\langle Z_d\rangle|$, which was used to derive estimate (16), is satisfied. For distances from the tube axis such that $r/\lambda_{De} \sim$ 1–10 and for $\Lambda \approx R/2.4$, the grain charge gradient $\beta_r = \partial Z_d/\partial r$ in the radial direction is estimated to be $\beta_r/\langle Z_d\rangle \cong 0.26\lambda_{De}^2/(r^2\Lambda) \sim 0.002$–$0.22$ cm^{-1}. Hence, the radial gradient β_r is positive (the grain charge increases toward the tube wall) and decreases with increasing radius r. It should be noted that a decrease in the radial gradient β_r with distance r from the tube axis agrees with the other known experimental approximations for the potential $\varphi(r) \sim r^b$ ($1 < b < 2$) of the radial electric field of a stratified glow discharge [9, 10].

2.2.2. RF capacitive discharge. In laboratory experiments on dusty plasmas in rf discharges, the dust grains are observed to be suspended near the upper boundary of the electrode sheath. In experiments with noble gases at pressures of P = 0.01–3 torr, the sheath thickness d_{max} varies from about 0.5 to 1.5 cm. An analytic theory developed for the electrode sheath of an rf discharge in the absence of ionization in the sheath was described in [26]. In this theory, it was assumed that there is a certain narrow region (presheath) of a weakly perturbed plasma ($\delta n/n_0 \ll 1$) between the sheath and an unperturbed electroneutral plasma ($\delta n = 0$). An analysis of the proposed set of equations [26] in the case of low pressures ($\lambda_{De} \ll l_i$) shows that, near the upper boundary of the electrode sheath, the profile of the averaged electric field $E(y)$ is almost linear,

$$E(y) = C_1 y. \qquad (19)$$

Solving the equations of the analytic theory [26] in the range of moderate pressures ($\lambda_{De} \sim l_i$) leads to a linear approximation for the gradient of the electric field $E(y)$:

$$E(y) = C_2 y^2 \qquad (20)$$

Let us estimate the grain charge gradients $dZ_d/dy \equiv d(\Delta_i Z_d)/dy$ that are associated with variations in the plasma parameters n_e, n_i, and u_i, i.e., in the conditions for the charging of grains with a radius of a_d = 1–2 μm and a density of ρ_d = 1.5–2 g cm^{-3}. To do this, we assume that the electric field E suspending the grains in the Earth's gravity field is about 1–4 V/cm, the plasma density at the sheath boundary is about $n_0 = 10^8$–10^9 cm^{-3}, the electron temperature is T_e = 2 eV, and the working gas is argon ($z \approx 3$–4 [20, 25]). In the field described by linear field profile (19) with C_1 = 12 V/cm^2, the grains will be suspended at heights of about $y = y_0 \approx 0.1$–0.33 cm above the upper boundary of the sheath, i.e., those at which the gravity force is balanced by the electric force, $m_d g + \langle Z_d\rangle eE(y_0) = 0$. According to relationship (17) and profile (19), which together represent a solution to the problem under study, the relative amount by which the grain charge gradient $\beta_y/\langle Z_d\rangle$ changes across this region is from $\beta_y/\langle Z_d\rangle = -0.1$ cm^{-1} to $\beta_y/\langle Z_d\rangle = -0.3$ cm^{-1}. Hence, in the model proposed here, the grain charge decreases

toward the electrode; moreover, the smaller the height above the electrode, the higher the rate of decrease in the grain charge. For nonlinear field profile (20), the situation remains qualitatively the same: in this case, the grain charge gradient in a dust suspended at heights of about $y_0 \approx 0.25$–0.5 cm above the upper boundary of the sheath ($C_2 = 12$ V/cm^3) changes by a relative amount of $\beta_y/\langle Z_d\rangle = -0.15$ cm^{-1} to -0.39 cm^{-1} with increasing height y_0.

Although the grain charge gradients are large, $|\beta_y/\langle Z_d\rangle| \sim 0.1$–$0.4$ cm^{-1}, the relative change in its value $\langle Z_d\rangle$ in all the cases under analysis did not exceed 7% ($|\Delta_i Z_d/\langle Z_d\rangle| < 0.07$), the degree to which the plasma ceases to be electrically neutral was $|\delta n/n_0| < 0.09$, and the potential was such that $|e\varphi/T_e| < 0.35$. These results provide a fairly good basis for linearizing the equations of the theory of an electrode sheath and the formulas of the OML model and, accordingly, for estimating the variations in the grain charge in the sheath from relationships (17), (19), and (20).

The results from measuring the variations in the relative potential $\varphi(r)/\varphi(0)$ of the radial electric field above the lower electrode (in the region where the dust grains are suspended) in the cylindrical chamber for initiating rf capacitive discharges [1] are illustrated in Fig. 3, which also shows the approximations of these changes by the functions

$$\varphi(r)/\varphi(0) = 1 - 0.6(r/R)^2 \quad \text{for} \quad r/R < 0.6, \qquad (21a)$$

$$\varphi(r)/\varphi(0) = 1 - (r/R)^4 \quad \text{for} \quad r/R > 0.6, \qquad (21b)$$

where $\varphi(0) = 50$ V and $R = 5.5$ cm. We can readily see that, at the chamber axis, $\nabla \cdot \mathbf{E} = \text{const}$ ($\delta n \approx 3 \times 10^6$ cm^{-3}); i.e., the plasma is inhomogeneous and $\beta_r = 0$. Near the electrode edges, the potential $\varphi(r)$ deviates substantially from being parabolic, which can give rise to radial gradients of the charge of the dust grains levitating in these edge regions. For $n_0 = 10^8$–10^9 cm^{-3} and $z \approx 2$–4, formula (16) gives the following estimate for the radial gradients: $\beta_r/\langle Z_d\rangle \cong -(0.02$–$0.5)$ cm^{-1}.

Hence, in gas discharges, the grain charge gradient $\boldsymbol{\beta}$ can amount to $|\boldsymbol{\beta}/\langle Z_d\rangle| \approx 0.1$–$0.5$ cm^{-1}. In this case, the grain charge can increase (in an rf discharge) or decrease (in a dc discharge) in the radial direction toward the wall of the discharge chamber. This result allows one to make predictions concerning the direction of rotation of the dust grains in the gravity field in these two types of discharges, provided that other nonelectrostatic forces are weaker than $m_d g$.

2.3. Nonelectrostatic Forces in a Gas-Discharge Plasma

The results of analytic investigations (see Section 2.1) show that regular self-oscillations of the dust grains can be generated when there is a nonzero grain charge gradient $\boldsymbol{\beta} = \nabla Z_d$ in the field of the nonelectrostatic forces

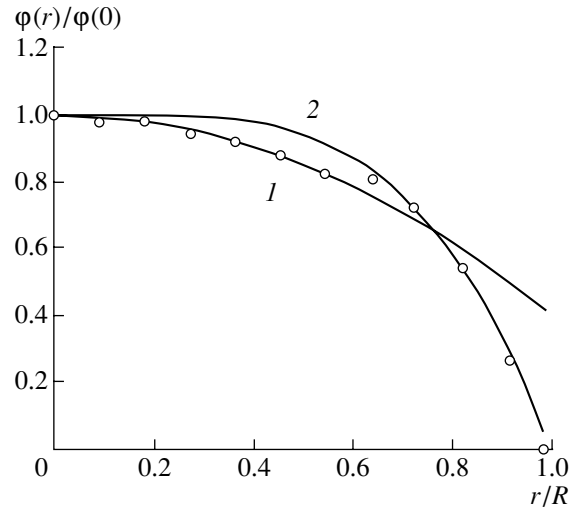

Fig. 3. Results from measurements of how the relative potential $\varphi(r)/\varphi(0)$ of the radial electric field varies from the center of an electrode of radius $R = 5.5$ cm [1] toward its edges and approximations of the measured results by formula (21a) (curve *1*) and formula (21b) (curve *2*).

$\mathbf{F}_{\text{non}}$ that are orthogonal to the gradient. In order to estimate how these forces affect the development of the dust oscillations, we compare the thermophoretic force F_{th} and ion drag force F_I that act on the grains in the plasmas of an rf discharge and a dc glow discharge, on the one hand, with the gravity force $m_d g$, on the other. This comparison is convenient for estimating the role of these forces in terrestrial experiments.

First, note that, for typical experimental parameters ($z \approx 3$, $T_e \approx 2$ eV, $a_d/l_d \sim 10^{-2}$, and $m_d > 5 \times 10^{-11}$ g, $(eZ_d/l_d)^2/m_d g \sim [(zT_e a_d/el_d]^2/(m_d g) \ll 1$), the *intergrain interaction force*, which is proportional to $\sim(eZ_d/l_d)^2$ and whose effect was ignored in analyzing the development of the instability of dust grains (see Section 2.1), is much weaker than the gravity force $m_d g$.

In order to analyze the *thermophoretic force*, which is driven by the gradient of the neutral gas temperature T_n, we use the relationship [30]

$$F_{\text{th}} = -\frac{16}{15}\sqrt{\frac{\pi m_n}{2T_n}}a_d^2\lambda_n|\nabla T_n|, \qquad (22)$$

where m_n is the mass of a gas atom or a gas molecule. In the hydrodynamic approximation, the thermal conductivity $\lambda_n = \lambda_{n_0}$ of the gas is independent of its pressure P. For noble gases such as neon and argon, we have $\lambda_{n_0} \approx 1.5$–$2 \times 10^3$ cm g/(K s^3) [29]. In this case, relationship (22) gives an upper estimate for the force F_{th}, provided that the radius a_d of the dust grains is less than or comparable to the mean free path l_n of the gas molecules [27]. Accordingly, for dust grains of density

$\rho_d \approx 3$ g/cm^3, we obtain $F_{th}/(m_d g) < 10^{-2}/(a_d\ [\mu m])$, where we took into account the fact that the gas temperature gradients in the above two types of discharges are such that $-|\nabla T_n| < 1$ K/cm [31, 34]. Consequently, for dust grains with radii greater than 1 μm, the thermophoretic force is negligibly weak in comparison to the gravity force. Nonetheless, the thermophoretic force F_{th} can play an important role in experiments with the plasmas of an inductive rf discharge and an anomalous dc glow discharge, in which the gas temperature gradients ∇T_n can be stronger, and also in experiments under microgravity conditions such that other nonelectrostatic forces (e.g., the ion drag force F_I) are insignificant in comparison to the thermophoretic force F_{th}.

We assume that the sought nonelectrostatic force $\mathbf{F}_{non}$ needed for the self-excitation of dust motions is driven by the directional motion of plasma ions with the velocity u_i relative to a dust grain, i.e., that the sought force is the *ion drag force* F_I [30]. It is of interest to examine two limiting cases: $u_i \ll v_{Ti}$ (where $v_{Ti} = \sqrt{T_i/m_i}$), which can occur in the electric field of the striations of a dc glow discharge, and $u_i \gg v_{Ti}$, which is possible in the electrode sheath of an rf capacitive discharge. The latter inequality permits us to use the cold ion model [30] to calculate the force acting on a dust grain:

$$F_I = \pi a_d^2 m_i n_i u_i^2 (\chi_1 + \chi_2),$$
$$\text{where} \quad \chi_1 = 1 + \frac{2Z_d e^2}{m_i u_i^2 a_d}, \quad \chi_2 = 2\left(\frac{Z_d e^2}{m_i u_i^2 a_d}\right)^2 \ln\Lambda, \tag{23}$$

$$\Lambda = \frac{\lambda_{De}^2 + b_0^2}{b_{coll}^2 + b_0^2}, \; b_0 = \frac{Z_d e^2}{m_i u_i^2}, \; b_{coll} = a_d\left(1 + \frac{2Z_d e^2}{m_i u_i^2}\right)^{1/2}, \text{ and}$$

λ_{De} is the electron Debye radius (recall that cold ions do not take part in the screening).

On the other hand, in a quasineutral plasma, the directed ion velocity can often be much lower than the ion thermal velocity, $u_i \ll v_{Ti}$. As was shown by Khrapak *et al.* [31], the momentum transfer in elastic scattering is the dominant transfer process; i.e., the ion drag force can be estimated by

$$F_I \approx \frac{2\sqrt{\pi}}{3} a_d^2 n_i m_i v_{Ti} (z\tau)^2 \Lambda_\kappa u. \tag{24}$$

Here, $\tau = T_e/T_i$; $\Lambda_\kappa \sim (4/z\tau)(\lambda_D/a)$ is a modified Coulomb logarithm; and the Debye radius is determined from the relationship $\lambda_D^{-2} = \lambda_{Di}^{-2} + \lambda_{De}^{-2}$, where λ_{Di} and λ_{De} are the ion and electron Debye radii, respectively.

Formulas (23) and (24) yield the following estimates for the ratio of the force F_I to the gravity force:

$$\frac{F_I}{m_d g} \approx \frac{8\sqrt{2\pi}}{3 v_{Ti}} e n_i \lambda_D \mu_i, \text{ for } u_i \ll v_{Ti}, \tag{25a}$$

$$\frac{F_I}{m_d g} \approx \frac{3}{a_d \rho_d g} z^2 T_e n_i \ln\left(\frac{\lambda_{De}/a_d}{(1+z)}\right), \text{ for } u_i \gg v_{Ti}. \tag{25b}$$

Here, for $u_i \ll v_{Ti}$, we set $u_i = \mu_i E$, where $E = m_d g/(e\langle Z_d\rangle)$. It should be noted that, for discharges in noble gases (such as neon and argon) at a pressure of $P \approx 1$ torr, these estimates are valid only for light grains having masses in the range $m_d < 10^{-10}$ g, because it is only in this case that the regular velocity u_i of the ions is lower than their thermal velocity v_{Ti}. In the second case, $u_i \gg v_{Ti}$, the regular ion velocity u_i was set to be equal to the Bohm velocity, $u_i \equiv v_B = (T_e/m_i)^{1/2}$.

Thus, for dust grains of density $\rho_d \approx 2.5$ g/cm^3 in a plasma with an ion density of $n_i \approx 10^9$ cm^{-3}, an electron temperature of $T_e \approx 2$ eV, and ion mobilities of $\mu_i \approx 1250$ cm^2/(s V) and 3200 cm^2/(s V), at $z = 3$ in a discharge in argon (or neon) at a pressure of $P \approx 1$ torr, we obtain the following estimates for the ratio of the ion drag force F_I to the gravity force $m_d g$: $F_I/(m_d g) \approx 0.1$–0.3 for $u_i \ll v_{Ti}$ and $F_I/(m_d g) \approx 0.35/a_d$ [μm] for $u_i \gg v_{Ti}$.

In concluding this section, we estimate the ion drag force F_I from relationship (24) for dust grains of radius $a_d \approx 2$ μm and for regular ion velocities $u_i \approx (0.12$–$0.25) v_{Ti}$, which correspond to directed ion motion in electric fields of strengths $E \sim 1$–2 V/cm. Such electric fields can be induced by the plasma polarization in discharges dominated by the ambipolar diffusion of plasma particles toward the wall of the working chamber. In this case, the ion drag force acting on grains with masses $m_d \approx 3 \times 10^{-11}$ g is $-F_I \approx (0.6$–$1.25) \times 10^8$ dyn, or $F_I \approx (0.2$–$0.4) m_d g$. Note that, for $|\nabla T_n| < 1$ K/cm, the thermophoretic force acting on such grains is weaker than the ion drag force by more than one order of magnitude.

Hence, under the conditions typical of terrestrial experiments, the most important force is the gravity force; next in importance is the ion drag force, $F_I/(m_d g) < 0.5$, and third in importance is the thermophoretic force, $F_{th}/(m_d g) < 0.1$. This is why the ion drag force may be important both in experiments under microgravity conditions and in terrestrial experiments. Since, under terrestrial experimental conditions, the ion drag force has a component in the direction of the gravity force, it may lead to a substantial shift of the neutral dispersion curves determined by conditions (11) and (12) toward higher values of the frequency ω_c and, thereby, to an increase in the frequency of the forming dust oscillations.

2.4. Kinetic Energy of the Dust Grains

One of the most important issues in investigating any kind of motion in nonconservative systems concerns the amount of energy transferred between the background plasma and the established oscillations. Since all stable motions of the charged dust grains in an electric device are finite, their kinetic energy K_x in some direction (e.g., the x direction) is determined by the amplitude of their motion, $A \sim (\langle x^2 \rangle)^{1/2}$ (where $\langle x^2 \rangle$ is the time-averaged displacement of the grain) and a certain characteristic frequency ω: $\langle K_x \rangle \approx m_d A^2 \omega^2/2$.

Generally, an increase in the potential energy (i.e., in the amplitude A and/or the frequency ω) of the dust system should be governed by dissipative processes. The amplitude A of the established oscillations cannot be estimated from a linear analysis because it applies only to the initial stages of the process, i.e., those during which the perturbations remain small: in the linear approximation, perturbations with frequencies $\omega_I > 0$ grow in amplitude without bound. The amplitude of the regular vortex oscillations that develop in case (i) can be estimated by taking into account the spatial scale on which the motion is established: $2l_d < A < L/2$, where $l_d = n_d^{-1/3}$ is the mean distance between the grains and L is the characteristic size of the dust cloud. In case (ii), as the oscillating motions of the individual grains in a dust cloud that is nearly crystalline in structure evolve to a steady state, the displacement of the grain from its equilibrium position should not exceed the radius of the Wigner–Seitz cell, $\sim A < l_d/2$.

During the development of instability, the dissipative effects influence the frequency ω of the nascent motions differently in different situations. After the development of dissipative bifurcation, the regular dust motion should obey the diffusion equation; consequently, the angular rotation velocity should be limited by the frictional forces in such a way that $\omega_\Omega^2 \equiv \Omega^2/4 \propto 1/\nu_{fr}^2$. In the case of dispersive instability, regular oscillations can be established only at a certain frequency, $\omega = \omega_c$, which is determined by the parameters of the system. As the frictional forces decrease further, an increase in the frequency ω is limited by progressive dissipative losses.

Let us estimate the kinetic energy $K_{(i)}$ that can be acquired by a dust grain along its path in the Earth's gravitational force field after the development of dissipative instability in a plasma in which the grain charge varies according to a linear law, $Z(r) \sim Z_0 + \beta_r r$. In this case, the squared frequency ω^2 can be set equal to $\omega_\Omega^2 \equiv \Omega^2/4 = (g\beta_r)^2/(2Z_0\nu_{fr})^2$ and the kinetic energy $K_{(i)}$ can be written as

$$K_{(i)} = m_d g^2 \chi^2/(8\nu_{fr}^2), \tag{26}$$

where the parameter $\chi = (A\beta_r/Z_0)$ determines the relative variations in the grain charge $Z(r)$ along the path of the grain. Let us find the values of the parameter χ for which the energy $K_{(i)}$ is higher than the thermal energy corresponding to the room temperature ($T_d \approx 0.027$ eV) and to dust grains with the radius $a_d = 5$ μm, the mass density of the grain material being $\rho_d = 2$ g/cm^3 ($m_d \cong 10^{-12}$ kg). We assume that the friction rate is equal to $\nu_{fr} = 20$ s^{-1}, which, in the free molecule approximation [27], corresponds approximately to the pressure $P = 0.5$ torr in a discharge in neon at room temperature. As a result, we find that, already at $\chi \cong 10^{-3}$, the kinetic energy $K_{(i)}$ exceeds T_d by almost one order of magnitude. For a higher buffer gas pressure ($P = 5$ torr) and a smaller grain radius ($a_d = 2$ μm), we have $K_{(i)}/T_d > 10$ at $\chi > 10^{-2}$. We thus see that even slight spatial variations in the parameter χ (i.e., in the grain charge) can result in efficient transfer of the potential energy from the background sources to the dust grains.

In the case of dispersive instability, the kinetic energy $K_{(ii)}$ of a dust grain can be estimated assuming that, when the variations in the grain charge are small, the frequency ω_c, which characterizes the motion of a grain in a preferred direction, is close to the characteristic frequency of vibrations of the particles in a crystal structure, e.g., in a body-centered cubic (bcc) lattice [32, 33]: $\omega_{bcc} \cong [2e^2 Z_0^2 n_d \exp(-\kappa)(1 + \kappa + \kappa^2/2)/(\pi m_d)]^{1/2}$, where $\kappa = l_d/\lambda$. In accordance with the conditions of experiments with gas-discharge plasmas, the grain charge Z_0 can be set equal to the equilibrium charge $\langle Z_d \rangle \approx 2 \times 10^3\, a_d$ [μm] T_e [eV] acquired by a dust grain as a result of charging by the fluxes of electrons and ions of the surrounding plasma. In this case, the kinetic energy $K_{(ii)}$ can be written in the form

$$K_{(ii)}\ [\text{eV}] \approx 5.76 \times 10^3 (a_d\ [\mu\text{m}]\ T_e\ [\text{eV}])^2 \psi^2 c_n/l_d\ [\mu\text{m}], \tag{27}$$

where $c_n = \exp(-\kappa)(1 + \kappa + \kappa^2/2)$ and $\psi = A/l_d < 0.5$ is a certain parameter determining the ratio of the amplitude A of the grain motion to the mean intergrain distance l_d. Taking into account the conditions for the observation of dust structures in laboratory gas-discharge plasmas, we set $\kappa \approx 1$–2, $l_d = 500$ μm, and $T_e = 1$ eV in order to determine the energy that can be acquired by a grain of radius $a_d = 5$ μm when the amplitude of its established motion corresponds to the value $\psi = 0.1$. According to formula (27), this energy considerably exceeds T_d and is as high as about $K_{(ii)} \approx 3$ eV. When dispersive instability develops without destroying the crystalline structure of the cloud, the kinetic energy of the grains is maximum at $\psi = 0.5$ and is equal to $K_{(ii)}^{lim} = c_n e^2 Z_0^2/(4l_d)$. For $\kappa \longrightarrow 0$, this gives $K_{(ii)}^{lim}/T_d = \Gamma/4$, where Γ is the coupling parameter.

Formulas (26) and (27) can overestimate the kinetic energy of the grains because of inaccuracies in determining the frequency ω of the established motion. The factors that can restrict the value of the frequency ω are associated with various collective effects that originate from the intergrain interaction forces and, phenomenologically, play the role of dissipative effects. It should be stressed that the processes by which the dust motion is established as a result of the development of the instabilities considered above are described by a particular solution to the set of nonlinear differential equations of our model. The spatial fluctuations of the charges of the neighboring grains can either change the frequency of the established oscillations of an individual grain, or they can set it into stochastic motion [4]. If the action of the nascent random forces F_{ran} does not correlate with the random force in Brownian motion F_{br}, then the kinetic temperature T_d of the system will increase and the increment in it will be determined by the formula $\Delta T_d \sim \langle F_{\text{ran}}^2 \rangle / [\nu_{\text{fr}}(\nu_{\text{fr}} + \eta)]$, where η is the characteristic frequency of the random forces F_{ran} [4, 20].

2.5. Numerical Simulations of a System with a Grain Charge Gradient

Three-dimensional problem (2) was solved by the molecular dynamics method. The external electric fields were assumed to be linear, $\mathbf{E}_{\text{ext}}(r, y) = \mathbf{i}(E_G + \alpha_y y) + \mathbf{j}\alpha_r r$, where E_G, α_y, and α_r are certain coordinate-independent parameters. The grain charge function was set to be $Z(r, y) = Z_0(1 + \beta_r^* r^2 + \beta_y^* y^2)$ or $Z(r, y) = Z_0(1 + \beta_r r + \beta_y y)$, where the coefficients β_r^*, β_y^*, β_r, and β_y were chosen so that the grain charge variations within the dust cloud were not greater than 30%. Unless otherwise indicated, the dust temperature T_d in all cases was assumed to be equal to the room temperature (~0.03 eV), the screening radius was $\lambda \cong 1000$ μm, and the radial gradient of the electric field was $\alpha_r \cong 3 N_d^{-1/3}$ V/cm^2 (where N_d is the number of grains in the system). The varied parameters were as follows: the friction rate ν_{fr}; the coefficients β_r^*, β_y^*, β_r, and β_y; the ratio of the electric field gradient α_y in the direction of the gravity force to the radial gradient α_r; and the ratio of the grain charge Z_0 to the grain mass m_d.

Under the conditions chosen, the system was found to relax to different dynamic equilibrium states, such as those with vortex, oscillating, or stochastic motions. In these states, the mean intergrain distance l_d, which was determined from the maximum in the correlation function, ranged from 300 to 2300 μm, depending on the values of the remaining parameters of the problem. The numerical results illustrated below were obtained for systems that consisted of 15 to 3000 dust grains and in which the grain charge and electric field varied monotonically. The constant nonelectrostatic force $\mathbf{F}_{\text{non}}$ was assumed to act along the system axis (the y axis); in most calculations, it was set equal to the gravity force $m_d g$. The values of the parameters of the relevant particular problems are given in the figure captions.

Under conditions close to condition (11), the system of dust grains was found to relax to an equilibrium state with *vortex motion.* The character of the established oscillations did not depend on the initial conditions and on some particular spatial ordering of the positions of the grains. In simulations with the linear charge function $Z(r, y)$, the character of the grain motion and its sensitivity to the viscosity of the buffer gas were found

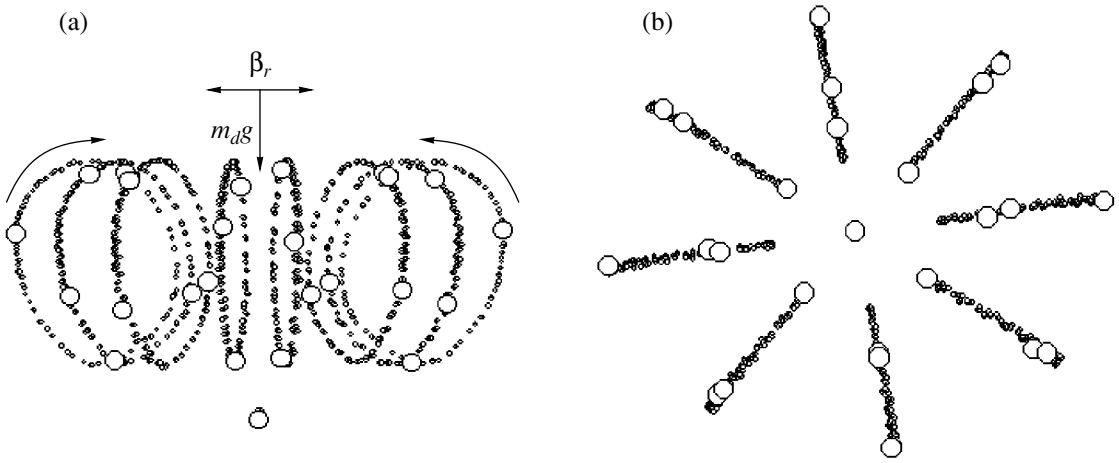

Fig. 4. Trajectory of a grain over the time $t = 100/\nu_{\text{fr}}$ in a system with the parameters $\nu_{\text{fr}} \cong 115$ s^{-1}, $\alpha_y/\alpha_r = 1$, $Z_0 = 8 \times 10^3$, $\beta_y^* = \beta_r^* \cong 5.5$ cm^{-2}, $N_d = 25$, $\langle K_x \rangle = \langle K_z \rangle \cong 0.85$ eV, and $\langle K_y \rangle \cong 2$ eV: (a) side view and (b) top view.

to be qualitatively the same as those computed with the quadratic charge function.

It was revealed that the system lost its stability as the asymmetry of the dust cloud decreased ($\alpha_y/\alpha_r \longrightarrow 1$) or the radial gradients (determined by the coefficients β_r^* and β_r) increased. The system also became unstable as the number of grains in small clusters increased (up to $N_d \approx 100$). For larger values of N_d, the dynamic parameters of the dust cloud remained essentially unchanged. The conditions for the excitation of oscillations were found to be independent of both the friction coefficient and the coefficients β_y^* and (β_y). The direction of rotation of the dust was determined by the value of β_r^* (β_r): for $\beta_r^* > 0$, the grains "sink downward" to the system axis, while in the opposite case, $\beta_r^* < 0$, they "rise upward." The quasi-harmonic synchronized motion of 25 grains is illustrated in Figs. 4a and 4b, which show how eight triples of grains move along eight closed trajectories and how one grain executes "high-frequency" oscillations at the center of the system.

The mean kinetic energy of the grains in their regular motion is $\langle K_x\rangle + \langle K_y\rangle + \langle K_z\rangle \equiv \langle K\rangle \propto 1/\nu_{fr}^2$. When the friction rate ν_{fr} falls below a certain threshold value, $\nu_{lim} \approx 0.1\omega_{bcc}$, the dust motion becomes stochastic and the grain velocity distribution becomes uniform in all directions ($\langle K_y\rangle \approx \langle K_x\rangle = \langle K_z\rangle$) and approaches a Maxwellian distribution with the temperature $T_d = 2\langle K\rangle/3 \propto 1/\nu_{fr}$. A further decrease in ν_{fr} (at $\omega_\Omega = |\Omega|/2 \longrightarrow \omega_{bcc}$) leads to the resonant growth of oscillations in the dust cloud. The time dependence of the amplitude of the oscillations of an individual grain in the y direction for different friction rates is presented in Fig. 5, and the dependence of the kinetic energy $\langle K\rangle$ of the dust system on the friction coefficient is given in Fig. 6. It should be noted that stochastization of the motion of the dust grains when the frictional forces are below the threshold can be attributed to their collective motion under spatially nonuniform conditions. This stochastization mechanism was described in detail in [4].

To conclude this section, we consider two numerical examples that illustrate the conditions for the observation of dust structures in terrestrial experiments with dc glow discharges [5] and in rf discharges in microgravity experiments [13]. In both cases, variations in the grain charge were described by the linear functions $Z(r, y) = Z_0(1 + \beta_r r + \beta_y y)$ and the gradients of the external electric fields $E(y)$ and $E(r)$ in the r and y directions were also assumed to be linear and were set equal to one another, $\alpha_y = \alpha_r$.

In the first case (i.e., in terrestrial experiments with glow discharges), the radius of the grains was chosen to be $a_d = 5$ μm, the mass density of the grain material was $\rho_d = 3.1$ g cm^{-3}, the friction coefficient was $\nu_{fr} \cong 11$ s^{-1} (for neon at the pressure $P = 0.25$ torr), the grain charge

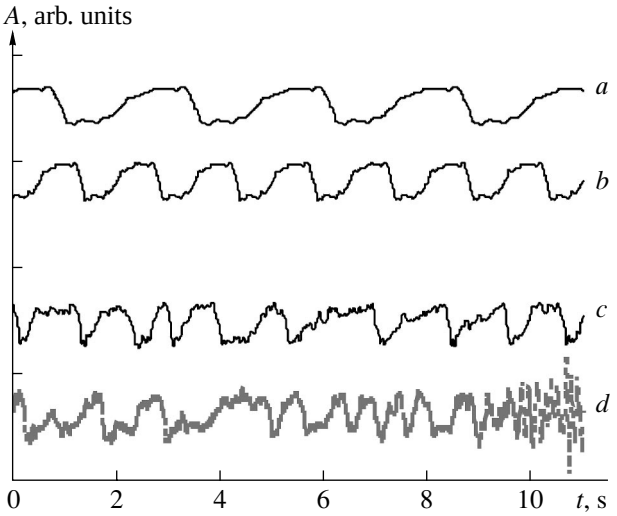

Fig. 5. Illustration of how the amplitude A of oscillations of an individual grain along the y axis depends on time t as the friction rate decreases: (*a*) $\nu_{fr} \cong 77$ s^{-1}, (*b*) $\nu_{fr}/2$, (*c*) $\nu_{fr}/6$, and (*d*) $\nu_{fr}/10$ for $t < 9$ s and $\nu_{fr}/20$ for $t > 9$ s.

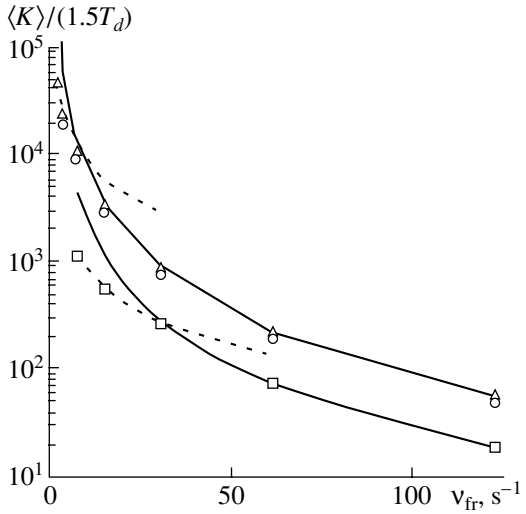

Fig. 6. Dependence of $\langle K\rangle/(1.5T_d)$ on ν_{fr} in a system with the parameters $\alpha_y/\alpha_r = 2$, $Z_0 = 4 \times 10^4$, $\beta_r^* \cong -12.5\, N_d^{-2/3}$ cm^{-2}, and $\beta_y^* = 0$ for different numbers of dust grains: $N_d = 15$ (squares), 60 (circles), and 500 (triangles). The solid curves show the approximation of the numerical data by $f_{an}(\nu_{fr}) \propto \nu_{fr}^{-2}$, and the dashed curves show the approximation by $f_{an}(\nu_{fr}) \propto \nu_{fr}^{-1}$.

was $Z_0 = 1.5 \times 10^4$, the grain charge gradients were $\beta_y \equiv \beta_r = 0.03$ cm^{-2}, and the screening radius was $\lambda = 580$ μm. The results from simulations of the motion of 3000 grains are displayed in Fig. 7. Under the condi-

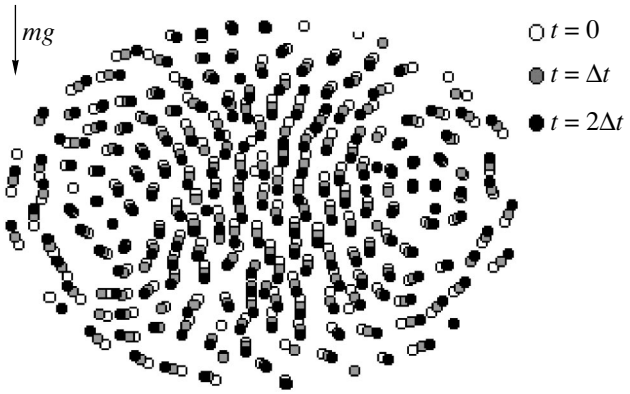

Fig. 7. Displacements of the dust grains at the end of the time interval $\Delta t = 1/\nu_{fr}$ in the cross section of a system with the parameters $\nu_{fr} \cong 11.25\ s^{-1}$, $\alpha_y/\alpha_r = 1$, $Z_0 = 1.5 \times 10^4$, $\beta_y = \beta_r \cong 0.03\ cm^{-2}$, $N_d = 3000$, $\langle K_x \rangle = \langle K_z \rangle \cong 2.1$ eV, and $\langle K_y \rangle \cong 6.5$ eV.

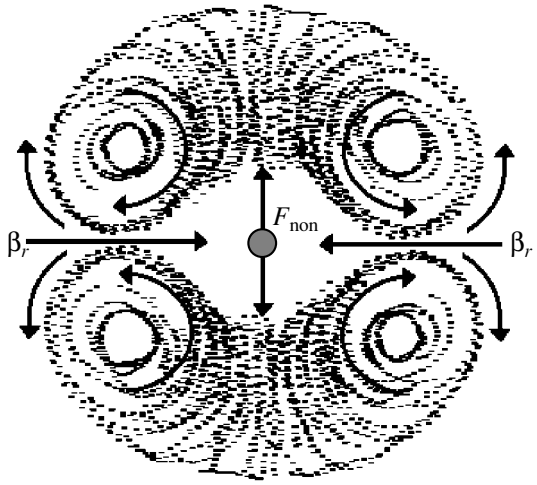

Fig. 8. Illustration of the results from numerical simulations of the rotation of dust grains and the formation of a void in the field of the mutually orthogonal nonelectrostatic force $\mathbf{F}_{non}$ and grain charge gradient β_r (in the cross section of a cylindrical system).

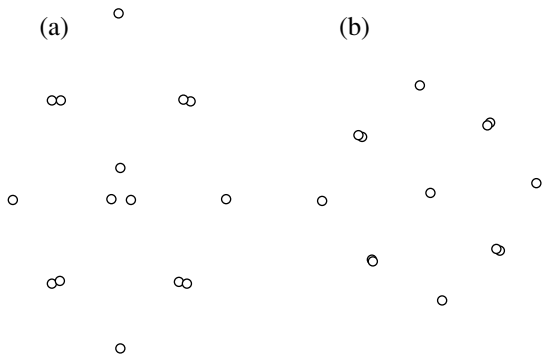

Fig. 9. Positions of the grains for $\nu_{fr} > \nu_c \cong 1\ s^{-1}$ in a system with the parameters $\alpha_y/\alpha_r = 0.4$, $Z_0 = 4 \times 10^4$, $\beta_r^* \cong -2\ cm^{-2}$, $\beta_y^* = 0$, and $N_d = 15$: (a) side view and (b) top view.

tions of dynamic equilibrium, the mean intergrain distance is about $l_d \sim 580$ μm ($\kappa \cong 1$) and the mean kinetic energy $\langle K \rangle$ of the rotating dust grains is two orders of magnitude higher than their thermal energy T_d corresponding to 300 K. In this case, the grain charge in the cloud varies by no more than 1% of its maximum value. The direction of dust rotation corresponds to that observed in the striations of a dc glow discharge [5, 12].

The results of numerically solving problem (2) for the conditions of experiments carried out with rf discharges onboard the *Alpha* international space station are illustrated in Fig. 8. The model experimental parameters were as follows: $N_d = 1000$, $\beta_r/(e\langle Z_d \rangle) = -0.3\ cm^{-1}$, $m_d \approx 3 \times 10^{-11}$ g, $\nu_{fr} = 200\ s^{-1}$, and $\langle Z_p \rangle = 6000 l_d \sim 220$ μm ($\kappa \cong 3$). The nonelectrostatic force, which was set equal to $F_{non} = 0.3 m_d g$ and was assumed to be directed outward from the axis of the cylindrical system, was found to lead to the formation of a void (i.e., a region free of dust grains) similar to those observed experimentally in [7, 13]. The magnitude of the force F_{non} was chosen to suit the estimates of the ion drag force in Section 2.3. The mean kinetic energy of the rotating grains was $\langle K \rangle \sim 0.2$ eV, which was close to the experimentally observed values [13]. The results of our simulations demonstrate that, in an inhomogeneous plasma, both a void and vortex motions can form simultaneously under the action of the ion drag force. It should be noted, however, that these simplified model simulations can neither describe the mechanism for void formation nor quantitatively analyze the picture of vortex motion. This can be done only by self-consistent computation of both the ion drag forces and the electric forces acting in the system of moving grains. Note that these forces can significantly perturb the density distributions in the surrounding plasma, provided that their charges and density are high (see Section 2.1). A detailed discussion of the mechanisms and conditions for the formation of voids and of their dynamics in a collisional and a collisionless plasma can be found in [34–39].

The *dispersive dust motion* can be described as follow. Let us analyze two different possible motions of the grains during the development of dispersive instability in a dust cloud in case (ii). This analysis may be useful for a qualitative explanation of some effects observed in experiments with dusty plasmas, namely, the onset of regular oscillations of individual grains and their anomalous heating. Recall that the self-consistent problem about the development of the convective (dispersive) instability in a plasma subsystem of numerous dust grains in the field of the ion drag force was considered in detail by Boushoule *et al.* [15]. The numerical results illustrated in the present paper were computed for dust systems consisting of a relatively small number of grains (from 15 to 60). Since dispersive bifurcation develops under condition (12) and cannot occur under condition (11), the requirement that there be a small number of dust grains is important in the sense that it readily satisfies condition (12) in situations that are

close to the development of dissipative instability but in which vortex motion is impossible. Since an increase in the grain charge gradient β_r can bring it within the scope of condition (11), we are left with a single control parameter—the friction coefficient ν_{fr}.

The development of the dispersive instability in the systems being modeled was found to lead to the formation of various types of regular oscillations and also to the onset of stochastic dust motion. The conditions for the development of the instability and the mean velocity of the chaotically moving grains depended on the friction coefficient ν_{fr}. When the coefficient ν_{fr} was decreased to a certain critical value $\nu_{fr} = \nu_c$, the systems lost their stability, in which case the grains oscillated at a frequency of $\omega \approx (0.5–1)\omega_{bcc}$.

Regular dust motions occurred at a fixed frequency $\omega = \omega_c$ and were observed only when the initial spatial positions of the grains were precisely symmetric. Figure 9 shows a steady-state cloud of 15 grains before the onset of the instability ($\nu_{fr} > \nu_c \cong 1\ s^{-1}$). The picture of the grain motion after the onset of dispersive instability is presented in Fig. 10.

The trajectories of the grains differ markedly from those in large-scale vortex motion. The frequency ω_c and the amplitude of the established oscillations are essentially independent of the friction rate ν_{fr} in the range of its values above a certain threshold ν_{lim}. A decrease in the friction rate ν_{fr} to ν_{lim} results in an appreciable phase mixing of the trajectories of individual grains. A further decrease in the friction rate ($\nu_{fr} < \nu_{lim}$) leads to a rapid heating of the dust, followed by the parametric growth of oscillations (in analogy to observations of vortex dust motions). The time dependence of the amplitude of the oscillations of an individual grain in the *y* direction is given in Fig. 11.

An asymmetry in the spatial positions of the grains was found to disrupt the synchronization of their motions; this, in turn, resulted in a stochastization of the grain velocities. For illustration, Fig. 12 depicts a steady-state cloud of 15 dust grains before the onset of dispersive instability ($\nu_{fr} > \nu_c \cong 4\ s^{-1}$, $\omega_{bcc} \approx 55\ s^{-1}$). The calculated grain trajectories after bifurcation ($\nu_{fr} < \nu_c$) for $\nu_{fr} \cong 1.5\ s^{-1}$ are shown in Fig. 13. The motion of the grains is irregular and their velocity distribution is isotropic and close to Maxwellian with a temperature of $T_d \approx 2\langle K\rangle/3$. The kinetic energy of the grains, $\langle K\rangle$, is not inversely proportional to ν_{fr} ($\langle K\rangle \sim 1/\nu_{fr}$). Thus, when the friction rate ν_{fr} was decreased from 4 to 2 s^{-1}, the kinetic energy $\langle K\rangle$ increased from about 2.5 T_d to 20 T_d. This dependence of $\langle K\rangle$ on ν_{fr}, on the one hand, can provide evidence that there are correlations between the nascent random forces and the Brownian motion of the grains and, on the other hand, can reflect a sequence of developing bifurcations that occur as the friction rate ν_{fr} decreases.

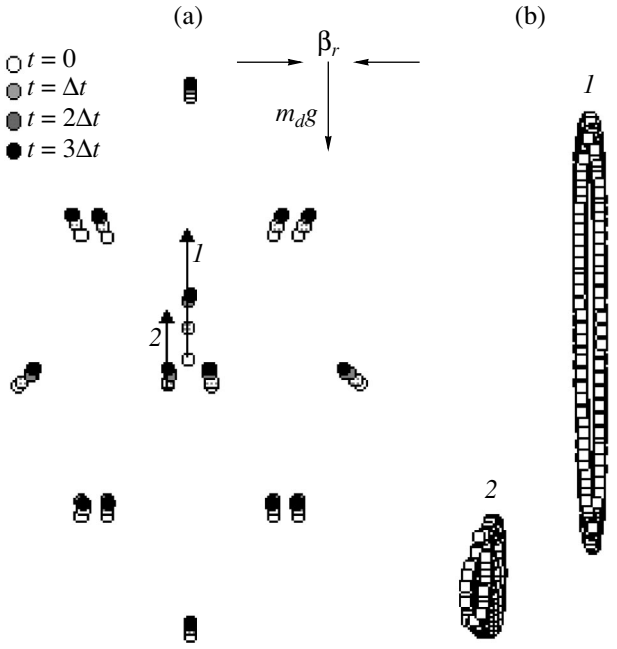

Fig. 10. (a) Displacements of dust grains at the end of the time interval $\Delta t \approx T_c/6$ (where T_c is the oscillation period) and (b) trajectories of two individual grains *1* and *2* in a system with the parameters $\alpha_y/\alpha_r = 0.4$, $Z_0 = 4 \times 10^4$, $\beta_r^* \cong -2\ cm^{-2}$, $\beta_y^* = 0$, $N_d = 15$, $\nu_{fr} \cong 0.96\ s^{-1}$. $\langle K_x\rangle = \langle K_z\rangle \cong 0.15$ eV, and $\langle K_y\rangle \cong 2.5$ eV.

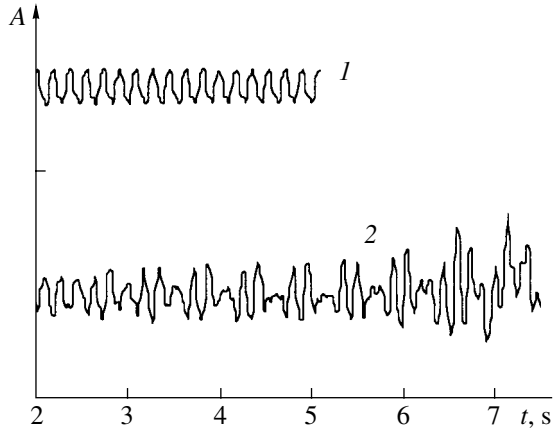

Fig. 11. Illustration of how the amplitude *A* of the oscillations (along the *y* axis) of an individual grain marked by *2* in Fig. 10 depends on the time *t* for (*1*) $0.38\ s^{-1} < \nu_{fr} < \nu_c$ and (*2*) $\nu_{fr} < 0.38\ s^{-1}$.

It should be noted that one of the most widely used models of the stochastic grain motion is based on the Lorentz set of equations, whose solutions are irregular functions of time over a wide range of parameters [21, 23].

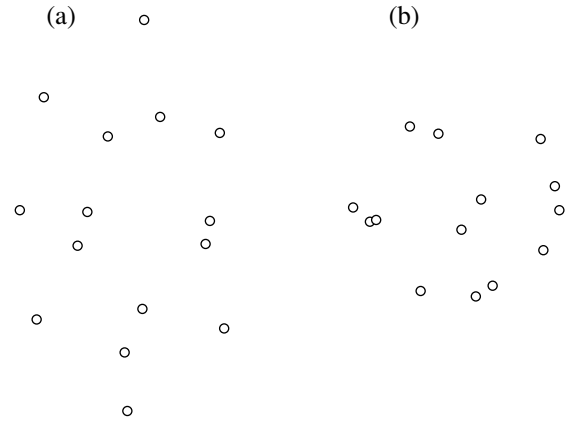

Fig. 12. Positions of the grains for $\nu_{fr} < \nu_c \cong 4\ s^{-1}$ in a system with the parameters $\alpha_y/\alpha_r = 0.41$, $Z_0 = 4 \times 10^4$, $\beta_r^* \cong -2\ cm^{-2}$, $\beta_y^* = 0$, and $N_d = 15$: (a) side view and (b) top view.

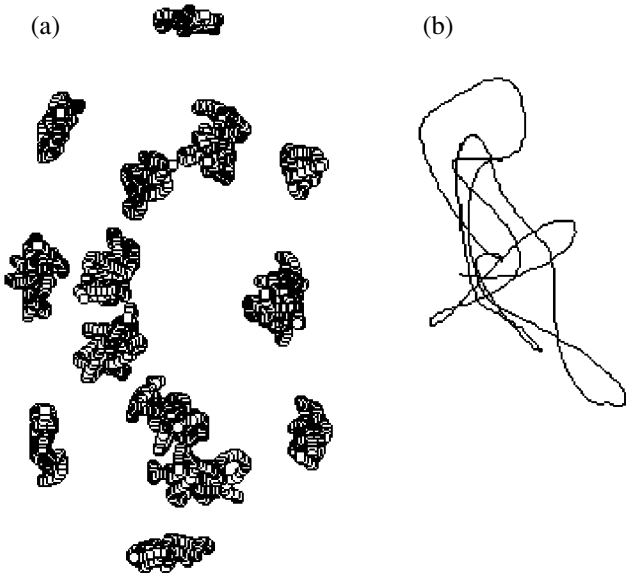

Fig. 13. (a) Illustration of the motion of dust grains over the time $t = 2/\nu_{fr}$ and (b) trajectory of an individual grain in a system with the parameters $\nu_{fr} \cong 1.5\ s^{-1}$, $\alpha_y/\alpha_r = 0.41$, $Z_0 = 4 \times 10^4$, $\beta_r^* \cong -2\ cm^{-2}$, $\beta_y^* = 0$, $N_d = 15$, and $\langle K_x \rangle = \langle K_y \rangle = \langle K_z \rangle \cong 0.5$ eV.

Even a slight variation in the parameters changes the solution to the Lorentz equations so substantially and, accordingly, disturbs the relevant physical system so strongly that the dust motion becomes chaotic. Such "few-mode" chaos is caused by a cascade of bifurcations, which lead to solutions in the form of complicated limiting cycles. In a computer analysis of the mean velocities of a system of dust grains, this effect manifests itself as an increase in the kinetic temperature of the grains. It is possibly this effect that was observed in experiments on the melting of dust crystals at a progressively decreasing gas pressure [41, 42]. To conclude this section, we emphasize that the above model of the behavior of dust systems allows one to successfully simulate both the anomalous heating effect and the formation of different types of dynamic structures.

3. EXPERIMENTAL OBSERVATIONS OF THE DUST SELF-OSCILLATIONS IN GAS-DISCHARGE PLASMAS

Theoretical analyses and numerical simulations show that, in order for regular dust self-oscillations to form in the field of the gravity force or some of the other nonelectrostatic forces $\mathbf{F}_{non}$ acting on the grains in the dust cloud, there should be a nonzero grain charge gradient $\boldsymbol{\beta} = \nabla Z_d$ orthogonal to these forces. Using the model proposed here, we now analyze the dynamics of the dust oscillations observed in the striations of a dc glow discharge and in the plasma of an rf capacitive discharge.

3.1. Dust Self-Oscillations in a Glow Discharge Plasma

A schematic of the experimental device for investigating the dynamics of the formation of dust self-oscillations in the striations of a glow discharge is shown in Fig. 14. The experiments were carried out with iron grains with a mean radius of $a_d \cong 3.5$ μm in argon at different discharge currents $I = 0.5$–15 mA and different pressures $P = 0.1$–1 torr. For these experimental conditions, the friction coefficient and equilibrium grain charge can be estimated by $\nu_{fr}\ [s^{-1}] \cong 30P$ [torr] and $\langle Z_d \rangle \approx 7 \times 10^3 T_e$ [eV], respectively.

The convection of dust grains is illustrated in Fig. 15, which shows the positions of the grains in the cloud and the trajectories of three moving grains (the exposure time being $t_{exp} \approx 4$ s) obtained by computer processing of video recordings. The direction of the dust rotation indicates that, in experiments, the grain charge increases toward the wall of the gas-discharge tube ($\beta_r > 0$), in agreement with the theoretical estimates made in Section 2.2. The radial gradient β_r can be estimated from the measured velocities $V \approx A\Omega/2$ of the grains and from the measured amplitude A of their rotation. In this way, we obtain $\beta_r/\langle Z_d \rangle = 2V\nu_{fr}/(Ag) \approx 0.012\ cm^{-1}$ (where $\nu_{fr} \cong 24\ s^{-1}$ for $P = 0.8$ torr).

Combined motion consisting of the rotation of the grains in the upper region of the cloud and their vertical oscillations in the base region of the dust structure is a phenomenon that is fairly typical of the striations of a glow discharge [5, 12]. In terms of the mechanism proposed here, it is easy to explain such combined motions by assuming that the grain charge varies differently in different regions of the gas discharge. Thus, the observed combined motion (Fig. 16) can be viewed as

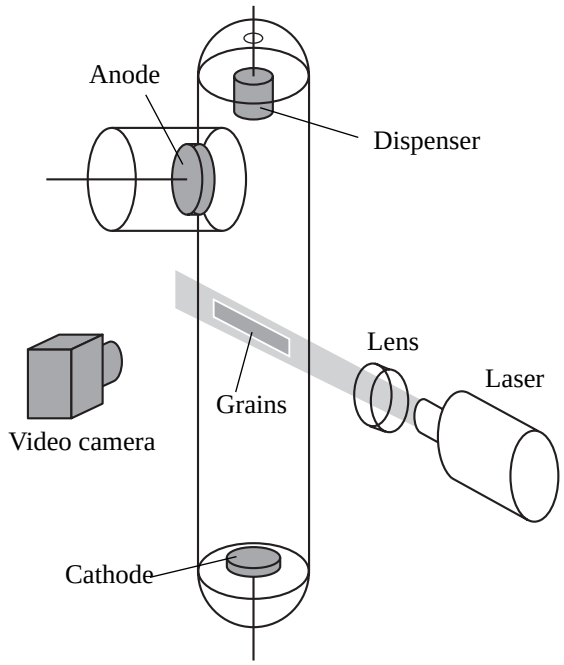

Fig. 14. Schematic of the device for experiments with dc discharges.

resulting from the simultaneous development of the two instabilities—dissipative and dispersive—in two different regions of the dust cloud.

Setting $2\pi e^2 Z_d \exp(-\kappa)/l_d^2 \approx E$, where $E \cong 2.4T_e/(eR)$, we can exclude the unknown $T_e (Z_d \propto T_e)$ from consideration and thereby estimate the screening parameter $\kappa = l_d/\lambda$ for different regions of the cloud. For the base region of the cloud ($\kappa \approx 0.8$, $l_d \approx 800$ μm), we have $\lambda \approx 1000$ μm. The observed oscillation frequency was $\omega \sim 30$–40 s^{-1}. As a result, we arrive at the following estimate for the grain charge gradient: $\beta_r/\langle Z_d \rangle \approx 2\nu_{fr}\omega/g \sim 0.27$–$0.37$ cm^{-1} ($^{-1}$ ($\nu_{fr} \cong 4.5$ s^{-1}, $P = 0.15$ torr). In the upper region of the cloud ($\kappa \approx 2$, $l_d \approx 450$ μm), the screening length λ is less than that in the base region and is equal to 225 μm. Note that these values of λ agree well those in the case where the electron density n_e increases toward the top of the cloud from 10^8 to 2×10^9 cm^{-3} at $T_e = 2$ eV (see Fig. 2) [24]. In this case, for different amplitudes of rotation of the grains, the measured ratio $V/A \approx 0.25$ s^{-1} yields $\beta_r/\langle Z_d \rangle \approx 2V\nu_{fr}/(Ag) \approx 0.002$ cm^{-1}. Hence, the ratio of β_r values for different regions of the dust cloud is not proportional to λ^2, as follows from the estimates made in Section 2.2. There are a number of reasons for this, one of which is the development of dissipative instability of the grains at the edge of the dust structure in its upper part, where the displacement parameter γ_0 is fairly large and satisfies condition (11). In contrast, as was shown above, the development of dispersive instability (in the lower part of the structure) is governed by the grains inside the dust cloud, where the gradient β_r is substantially larger. On the other hand, under the experimental conditions in question, the ion drag force can be strong enough to have a significant effect on the rotation frequency of the grains (see Section 2.3).

It should be noted that all of the types of dust self-oscillations considered above are also observed in the chambers for investigating inductive rf discharges with nonuniform parameters, as is the case with plasmas of stratified dc glow discharges.

3.2. Formation of the Dust Self-Oscillations in an RF Discharge Plasma

There are two main factors that hinder the development of the above instabilities of the dust in a plasma of an rf capacitive discharge: the first is associated with

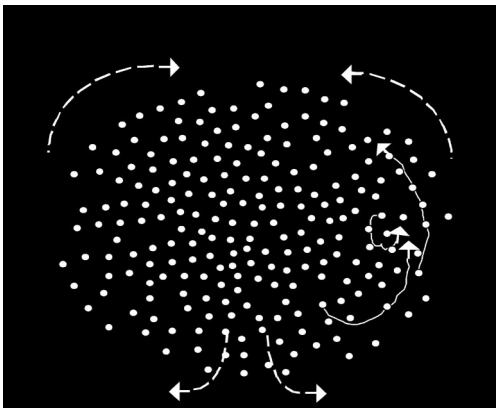

Fig. 15. Convection of dust grains in a striation of a glow discharge.

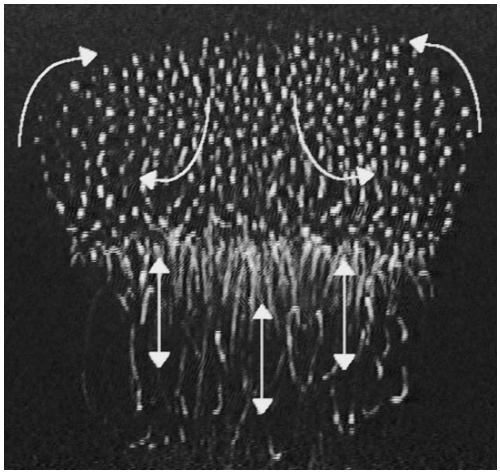

Fig. 16. Combined self-oscillations of dust grains in a striation of a glow discharge.

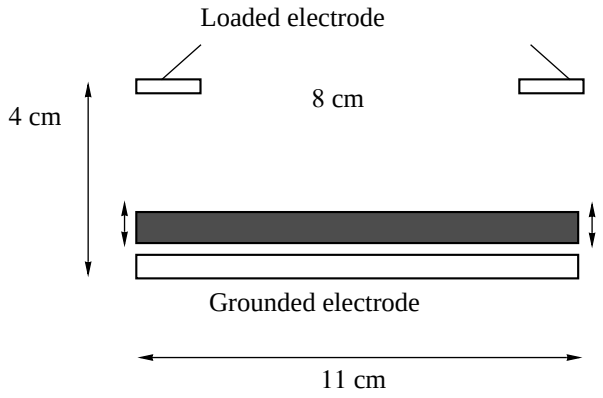

Fig. 17. Schematic of experiments for observing dust self-oscillations in an rf discharge.

Fig. 18. Video recording of the dust self-oscillations in an rf discharge.

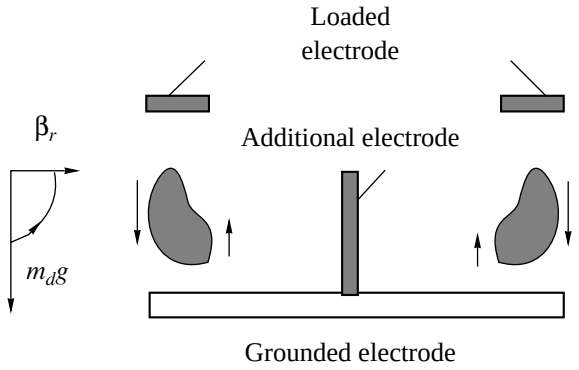

Fig. 19. Schematic of experiments aimed at forming dust clouds.

the plasma homogeneity, and the second, with the small number of dust layers (as is usually observed in such discharges) and, accordingly, with the small value of the displacement parameter γ_0 (see Section 2.1). The latter can explain why vortex dust motions are never observed under ordinary terrestrial experimental conditions. However, the formation of extended dust clouds under microgravity conditions [7, 13] or when the working chamber for experiments with rf discharges is equipped with additional electrodes [1, 8] can, under certain conditions, lead to the onset of dissipative instability, which, in turn, gives rise to the vortex dust motion. The development of dispersive instability in the electrode sheath of an rf capacitive discharge can be exemplified by the formation of regular vertical oscillations of the dust grains [42]. Other mechanisms that have been proposed to explain the onset of such oscillations do not provide reasonable quantitative estimates.

Here, we consider as an example several experiments in which the onset of regular dust motions can be attributed to the development of dissipative or dispersive instability in dust structures that form in a plasma of an rf capacitive discharge. A schematic of such an experiment is shown in Fig. 17. The experiments were carried out with melamine-formaldehyde grains with a radius of $a_d \cong 1.4$ μm, the mass density of the grain material being $\rho_d = 1.5$ g/cm^3, in argon at pressures of $P = 0.08$–0.2 torr. The working electrode was a 10-cm-diameter aluminum disk, and the grounded electrode was an 11.5-cm-diameter steel ring. The discharge power was about 65 W.

In these experiments, both stochastic and regular dust oscillations (see Fig. 18) were observed to occur in clouds composed of several layers of the dust grains. Such oscillations were generated near the radial cloud boundary, where the grain charge gradient β_r was the strongest. The increase in the grain charge gradient β_r away from the center of the device can be attributed to the behavior of the potential $\varphi(r)$ of the radial electric field near the edges of the working electrode. The measured shape of the profile $\varphi(r)$ is shown in Fig. 3. The grain charge decreases toward the electrode edges ($\beta_r < 0$), because the potential $\varphi(r)$ is not truly parabolic (see Section 2.2).

The presence of an additional electrode at the center of the working volume of an rf discharge can act to displace the dust grains toward the edges of the main electrodes. A simplified schematic of experiments on the formation of volume dust clouds by means of an additional electrode is shown in Fig. 19. A video recording of vortex dust oscillations formed under such conditions is shown in Fig. 20. The direction of the observed dust rotation corresponds to $\beta_r < 0$ (i.e., the dust rotates in a direction opposite to the rotation that is routinely observed in glow discharges). The measured dependence of the rotation frequency ω on the pressure P is displayed in Fig. 21. By assuming that $\omega \approx$

Fig. 20. Video recording of the vortex dust oscillations.

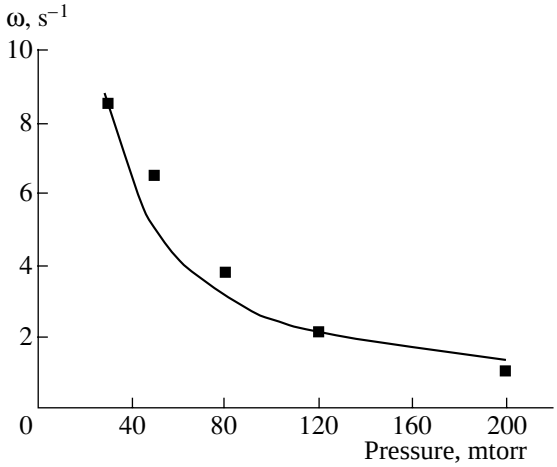

Fig. 21. Experimental dependence of the frequency ω on the pressure P (closed squares) and its approximation at $\beta_r/\langle Z_d\rangle \approx 0.1$ cm^{-1} (solid curve).

$|g\beta_r/(2\langle Z_d\rangle\nu_{fr})|$, where ν_{fr} [s^{-1}] $\cong 200P$ [torr], and by providing the best fit to the experimental data, we can estimate the grain charge gradient by $|\beta_r/\langle Z_d\rangle| \approx 0.1$ cm^{-1} (see Fig. 21).

4. CONCLUSIONS

We have considered two main types of instabilities in a dusty plasma with a nonzero grain charge gradient in the field of nonelectrostatic forces. We have proposed a model that describes the conditions for the onset of these instabilities and the dynamics of the formation of various self-oscillations associated with them. The results of our analytical study can readily be adapted to any nonconservative system that can be described by linearized equations similar in form to the equations considered above.

We have examined the effect of the density and velocity of the plasma ions and electrons on the charging of dust grains in gas discharges. We have derived simple relationships for estimating the grain charge gradients caused by variations in the conditions for grain charging.

We have presented the results from numerical investigations of the formation of dust self-oscillations in systems whose parameters are close to those in experiments with gas discharges. Numerical simulations show that the development of the instabilities in question can lead to the onset of various regular and stochastic oscillations in a dusty plasma. Moreover, it was found that these oscillations can be generated even by slight variations in the grain charge: thus, even a small grain charge gradient (about 1–2%) in the dust cloud can drive the grains into significant rotation. Nevertheless, it should again be emphasized that the qualitative picture of the vortex dust motion (namely, the spatial and velocity distributions of the grains) can only be obtained through self-consistent calculations of the forces that act in a system of moving grains and can seriously perturb the distributions of the particle densities in the surrounding plasma.

Based on the proposed model, we have analyzed the dynamics of the formation of dust vortices and various dust self-oscillations observed in experiments with gas-discharge plasmas. The experiments were carried out with dust grains of different sizes over a wide range of plasma parameters. It was shown that, under the Earth's gravity conditions, even a slight spatial variation in the grain charge can set the dust into vortex motion. In all the cases under analysis, the observed directions of dust rotation and the experimental estimates of the grain charge gradients were found to agree with theoretical predictions concerning the magnitude and direction of these gradients.

Hence, we have considered a possible mechanism for the onset and development of instabilities in a dusty plasma with a nonzero grain charge gradient and have constructed an analytic model capable of describing the formation and evolution of the instability-generated dust oscillations. An attractive feature of this mechanism is that it can provide insight into a wide scope of phenomena (such as anomalous dust heating and the onset of vortices and various regular motions of individual grains) observed in laboratory experiments with dusty plasmas. There may be some other factors responsible for the nonequilibrium nature of a dust system, e.g., fluctuations of the external electric fields or stochastic fluctuations in the grain charge. However, in terms of these factors alone, it is impossible to explain the onset of regular collective dust motions; hence, additional sources compensating for the energy scattering need to be invoked.

The question of the existence of a single mechanism and a single driving source for some of the regular and stochastic oscillations observed in laboratory experi-

ments with dusty plasmas remains open, although the results of theoretical studies are in good qualitative agreement with the experimental data on the dynamics of observed dust oscillations [12–14]. Whether there is a relation between the instability of the actual dust–plasma systems and the presence of a nonzero grain charge gradient can be established, first of all, in experiments aimed at demonstrating quantitative agreement among the magnitude of the grain charge gradient, the nonelectrostatic force, and the energy acquired by the dust grains as a result of the development of the instabilities considered above. Such experiments will not only show that the proposed mechanism is directly related to the observed dust self-oscillations, but will also make it possible to control the development of self-oscillations in a dusty plasma.

ACKNOWLEDGMENTS

This work was supported in part by the Russian Foundation for Basic Research (project no. 01-02-16658), INTAS (grant no. 01-0391), and the Australian Research Council. A.A. Samarian expresses his gratitude to the University of Sydney for the award of a research studentship.

REFERENCES

1. A. Samarian, O. Vaulina, W. Tsung, and B. James, Phys. Scr. **98**, 123 (2002).
2. A. V. Ivlev, D. Samsonov, J. Goree, *et al.*, Phys. Plasmas **6**, 741 (1999).
3. D. Winske and M. Rosenberg, IEEE Trans. Plasma Sci. **26**, 92 (1998).
4. O. S. Vaulina, A. A. Samarian, B. James, *et al.*, Zh. Éksp. Teor. Fiz. **123**, 1179 (2003) [JETP **96**, 1037 (2003)].
5. V. Molotkov, A. Nefedov, V. Torchinskiĭ, *et al.*, Zh. Éksp. Teor. Fiz. **116**, 902 (1999) [JETP **89**, 477 (1999)].
6. V. Fortov, A. Nefedov, V. Vladimirov, *et al.*, Phys. Lett. A **258**, 305 (1999).
7. G. Morfill, H. Thomas, U. Konopka, *et al.*, Phys. Rev. Lett. **83**, 1598 (1999).
8. D. A. Law, W. H. Steel, B. M. Annaratone, *et al.*, Phys. Rev. Lett. **80**, 4189 (1998).
9. V. V. Zhakhovskiĭ, V. I. Molotkov, A. P. Nefedov, *et al.*, Pis'ma Zh. Éksp. Teor. Fiz. **66**, 392 (1997) [JETP Lett. **66**, 419 (1997)].
10. V. V. Zhakhovskiĭ, V. I. Molotkov, A. P. Nefedov, *et al.*, in *Proceedings of the Conference on the Physics of Low-Temperature Plasma, Petrozavodsk, 1998*, p. 684.
11. O. S. Vaulina, A. P. Nefedov, O. F. Petrov, and V. E. Fortov, Zh. Éksp. Teor. Fiz. **118**, 1319 (2000) [JETP **91**, 1147 (2000)].
12. O. S. Vaulina, A. P. Nefedov, O. F. Petrov, *et al.*, Zh. Éksp. Teor. Fiz. **120**, 1369 (2001) [JETP **93**, 1184 (2001)].
13. V. E. Fortov, O. S. Vaulina, O. F. Petrov, *et al.*, Zh. Éksp. Teor. Fiz. **123**, 798 (2003) [JETP **96**, 704 (2003)].
14. A. K. Agarwal and G. Prasad, Phys. Lett. A **309**, 103 (2003).
15. A. Boushoule, G. Morfill, and V. Tsytovich, Comm. Modern Phys. C **1**, 131 (1999).
16. G. Morfill and V. Tsytovich, Fiz. Plazmy **26**, 727 (2000) [Plasma Phys. Rep. **26**, 682 (2000)].
17. V. N. Tsytovich, Fiz. Plazmy **26**, 712 (2000) [Plasma Phys. Rep. **26**, 668 (2000)].
18. V. Tsytovich and G. E. Morfill, Fiz. Plazmy **28**, 195 (2002) [Plasma Phys. Rep. **28**, 171 (2002)].
19. V. N. Tsytovich, G. E. Morfill, and H. Thomas, Fiz. Plazmy **28**, 675 (2002) [Plasma Phys. Rep. **28**, 623 (2002)].
20. O. S. Vaulina, S. A. Khrapak, O. F. Petrov, and A. P. Nefedov, Phys. Rev. E **60**, 5959 (1999).
21. R. K. Dodd, J. C. Eilbeck, J. Gibbon, and H. C. Morris, *Solitons and Nonlinear Wave Equations* (Mir, Moscow, 1988; Academic, New York, 1982).
22. E. M. Lifshitz and L. P. Pitaevskii, *Physical Kinetics* (Nauka, Moscow, 1979; Pergamon, Oxford, 1981).
23. T. Akhromeeva, S. Kurdyumov, and G. Malinetskiĭ, *Computers and Nonlinear Phenomena* (Nauka, Moscow, 1988).
24. Yu. V. Gerasimov, A. P. Nefedov, V. A. Sinel'shchikov, *et al.*, Pis'ma Zh. Tekh. Fiz. **24** (19), 62 (1998) [Tech. Phys. Lett. **24**, 774 (1998)].
25. J. Goree, Plasma Sources Sci. Technol. **3**, 400 (1994).
26. Yu. P. Raĭzer, M. N. Shneĭder, and N. A. Yatsenko, *High-Frequency Capacitive Discharge: Physics, Experimental Techniques, Applications* (Nauka, Moscow, 1995).
27. Yu. B. Golubovskiĭ and S. U. Nisimov, Zh. Tekh. Fiz. **65** (1), 46 (1995) [Tech. Phys. **40**, 24 (1995)].
28. Yu. B. Golubovskiĭ and S. U. Nisimov, Zh. Tekh. Fiz. **66** (7), 20 (1996) [Tech. Phys. **41**, 645 (1996)].
29. Yu. P. Raizer, *Gas Discharge Physics* (Nauka, Moscow, 1987; Springer-Verlag, Berlin, 1991).
30. T. Nitter, Plasma Sources Sci. Technol. **5**, 93 (1996).
31. S. A. Khrapak, A. V. Ivlev, G. Morfill, *et al.*, Phys. Rev. E **66**, 046 414 (2002).
32. O. S. Vaulina, S. V. Vladimirov, O. F. Petrov, and V. E. Fortov, Phys. Rev. Lett. **88**, 245 002 (2002).
33. O. S. Vaulina and S. V. Vladimirov, Phys. Plasmas **9**, 835 (2002).
34. V. Tsytovich, S. Vladimirov, G. Morfill, and J. Goree, Phys. Rev. E **63**, 056609 (2001).
35. J. Goree, G. Morfill, V. Tsytovich, and S. Vladimirov, Phys. Rev. E **59**, 7055 (1999).
36. V. Tsytovich, Phys. Scr. **T89**, 26 (2001).
37. V. Tsytovich, Comments Mod. Phys., Part C **1**, 1 (2000).
38. V. Tsytovich, G. Morfill, U. Konopka, and H. Thomas, New J. Phys. **5**, 1 (2003).
39. G. Morfill and V. Tsytovich, Phys. Plasmas **9**, 235 (2002).
40. A. Melzer, A. Homann, and A. Piel, Phys. Rev. E **53**, 2757 (1996).
41. G. E. Morfill, H. M. Thomas, U. Konopka, and M. Zuzic, Phys. Plasmas **6**, 1769 (1999).
42. A. Samarian, B. James, S. Vladimirov, and N. Cramer, Phys. Rev. E **64**, 025 402 (2001).

Translated by O.E. Khadin

Plasma Physics Reports, Vol. 30, No. 11, 2004, pp. 937–943. Translated from Fizika Plazmy, Vol. 30, No. 11, 2004, pp. 1008–1014.

PLASMA KINETICS

Ion Velocity Distribution in a Plasma with Low-Intensity Ion Acoustic Turbulence

I. V. Kuzora and S. A. Uryupin

Lebedev Physical Institute, Russian Academy of Sciences, Leninskiĭ pr. 53, Moscow, 119991 Russia

Received December 11, 2003

Abstract—The quasi-steady ion distribution in a plasma with a single ion species and with low-intensity ion acoustic turbulence is found. Conditions are determined under which the stimulated scattering of ion acoustic waves by ions leads to the formation of a superthermal ion distribution function that decreases with increasing velocity more gradually than does a Maxwellian distribution function. It is found that the plasma conductivity increases as a result of a decrease in the turbulence level due to an enhancement of the Cherenkov damping of ion acoustic waves by resonant ions, whose number increases because of the formation of a gradually decreasing distribution of superthermal ions. © *2004 MAIK "Nauka/Interperiodica".*

1. INTRODUCTION

The phenomenon of anomalous ion heating in high-current discharges was first discovered in the 1960s. During these years, it was also found that this phenomenon originates from the interaction of ions with ion acoustic turbulence (IAT), which arises in current-carrying plasmas because of the Cherenkov emission of ion acoustic waves by electrons [1, 2]. In the IAT theory, rapid heating of the so-called resonant ions (i.e., those whose velocities exceed the ion acoustic velocity v_s) is attributed to the quasilinear interaction of ion acoustic waves with the ions [3, 4], whereas the bulk thermal ions are heated due to the stimulated scattering of ion-acoustic waves by them [1]. However, although the cause of the efficient heating of thermal ions can be understood in terms of stimulated scattering, an analytic theory of turbulent ion heating has not yet been completely developed. Some progress in this direction has been achieved only for two limiting cases. First, turbulent ion heating was described for the case of a sufficiently dense plasma, when frequent ion–ion collisions force the distribution of ions with velocities below the ion acoustic velocity v_s to become nearly Maxwellian [5]. Second, an analytic description of turbulent ion heating was given for the limiting case in which ion–ion collisions can be ignored [6]. This description is, however, valid for the comparatively short time scales on which the formation of a gradually decreasing velocity distribution of the thermal ions with velocities $v < v_s$ can still be ignored (see [7, 8] for details).

In the present paper, a nonequilibrium ion distribution in a plasma with IAT is studied for another important limiting case. Specifically, we consider the conditions under which, on the one hand, the distribution of the bulk ions with velocities $v \ll v_s$ remains close to a Maxwellian distribution because of frequent ion–ion collisions, but, on the other hand, as the ion velocity increases from the ion thermal velocity to velocities lower than or on the order of the ion acoustic velocity, the ion distribution is formed under the influence of ion scattering by the low-frequency fields that are driven by the beating of ion acoustic waves involved in stimulated scattering. Under such conditions, the distribution function of superthermal ions decreases more gradually than does the Maxwellian distribution function and, at $v = v_s$, changes smoothly to the Maxwellian distribution function of the hot resonant ions. The quasi-steady ion distribution obtained is used to calculate the rate at which the ion acoustic waves are damped by resonant ions and thereby to determine the explicit dependence of the anomalous current density on the plasma parameters.

2. IAT SPECTRUM

We consider the interaction of ions with IAT under conditions such that the turbulence level is low and the distribution of thermal ions is mainly governed by ion–ion collisions. Under these conditions, the distribution function of the thermal ions is nearly Maxwellian and the number density of the ion acoustic waves, $N(\mathbf{k})$, is given by the expression (see, e.g., [5])

$$N(\mathbf{k}) = N(k)\Phi(\cos\theta_k). \tag{1}$$

Here, k is the wavenumber and θ_k is the angle between the wave vector $\mathbf{k}$ and the direction of the force driving the instability. In this case, the distribution of ion acoustic waves over the wavenumbers has the form

$$N(k) = \sqrt{2\pi^3} n_i m_i v_s \frac{\omega_{Li} r_{De}^2}{\omega_{Le} r_{Di}^2} k^{-4} (1 + k^2 r_{De}^2)^{-3/2} \times \left[\ln \frac{(1 + k^2 r_{De}^2)^{1/2}}{k r_{De}} - \frac{0.5}{1 + k^2 r_{De}^2} - \frac{0.25}{(1 + k^2 r_{De}^2)^2} \right]. \tag{2}$$

1063-780X/04/3011-0937$26.00 © 2004 MAIK "Nauka/Interperiodica"

Here, r_{De} is the electron Debye radius; ω_{Le} is the electron gyrofrequency; r_{Di}, ω_{Li}, and n_i, are the ion Debye radius, ion gyrofrequency, and ion density, respectively; m_i is the mass of an ion; and $v_s = r_{De}\omega_{Li}$. The angular distribution function of the ion acoustic waves, $\Phi(\cos\theta_k)$, is determined by the turbulent Knudsen number

$$K_N = \frac{6\pi|eE|r_{Di}^2}{m_e\omega_{Li}v_s r_{De}^2}, \quad (3)$$

where e and m_e are the charge and mass of an electron and E is the electric field strength in the plasma. In what follows, we will be interested in the limit of small Knudsen numbers,

$$K_N \ll (1+\delta)^2. \quad (4)$$

Here, the parameter δ, which characterizes the damping of ion acoustic waves by ions with velocities higher than v_s, is equal to

$$\delta = (2\pi)^{3/2}\left|\frac{e_i}{e}\right|\frac{m_e v_{Te}^3}{m_i n_i} f_0(v_s), \quad (5)$$

where v_{Te} is the electron thermal velocity, e_i is the charge of an ion, and $f_0(v) = \int d\Omega f(\mathbf{v})/4\pi$ is the isotropic part of the ion distribution function. Under inequality (4), the angular distribution of the number density of the ion acoustic waves has the form [5, 9]

$$\Phi(x) \cong \frac{4K_N}{3\pi(1+\delta)x}\frac{d}{dx}\frac{x^4}{(1+\varepsilon-x)^{1-\alpha_\varepsilon}}, \quad (6)$$

$$\alpha_\varepsilon \cong \frac{\ln 2}{\ln[3\pi(1+\delta)^2\ln 2/4K_N]} \ll 1, \quad (7)$$

$$\varepsilon \cong \frac{4K_N}{3\pi(1+\delta)^2\alpha_\varepsilon} \ll 1. \quad (8)$$

IAT spectrum (2) with angular distribution (6) is valid under the following two conditions. First, the thermal ions should obey a Maxwellian distribution. For this to be possible, it is necessary that the ion–ion collision frequency $\nu_{ii} = 4\pi\Lambda n_i e_i^4/m_i^{1/2}(\kappa T_i)^{3/2}$ (where T_i is the ion temperature, Λ is the Coulomb logarithm, and κ is Boltzmann's constant) exceed the reciprocal of the characteristic time between collisions of ions with the turbulent pulsations of the charge density,

$$\tau^{-1} = \left(\frac{1}{2v^2}\int_{-1}^{1} d\xi D_{vv}^{NL}(v,\xi)\right)\Bigg|_{v\approx v_{Ti}}. \quad (9)$$

Here, $\xi = \cos\theta_v = -(\mathbf{v}\cdot\mathbf{E})/vE$, $D_{vv}^{NL} = D_{\alpha\beta}^{NL}v_\alpha v_\beta/v^2$, $D_{\alpha\beta}^{NL}$ is the tensor describing the nonlinear diffusion due to the stimulated scattering of waves by ions [10],

$$D_{\alpha\beta}^{NL} = \frac{(2\pi)^3}{2m_i^2\omega_{Li}^4}\int d\mathbf{k}d\mathbf{k}'\omega\omega'^3 k_\alpha'' k_\beta'' N(\mathbf{k})N(\mathbf{k}') \times \delta(\omega'' - \mathbf{k}''\cdot\mathbf{v})|\Lambda(\mathbf{k},\mathbf{k}',\mathbf{v})|^2, \quad (10)$$

$(\omega, \mathbf{k})$ and $(\omega', \mathbf{k}')$ are the frequencies and wave vectors of the incident and scattered waves, respectively; $(\omega'', \mathbf{k}'') = (\omega - \omega', \mathbf{k} - \mathbf{k}')$ are the beat frequency and wave vector of the interacting waves; and the intensity $\Lambda(\mathbf{k}, \mathbf{k}', \mathbf{v})$ of the stimulated scattering is described by the approximate expression

$$\Lambda(\mathbf{k},\mathbf{k}',\mathbf{v}) \cong \frac{e_i^2}{(2\pi)^3 m_i\omega'}\frac{\mathbf{k}\cdot\mathbf{k}'}{kk'}\left(\left(\frac{\mathbf{k}}{\omega}+\frac{\mathbf{k}'}{\omega}\right)\cdot\mathbf{v}\right). \quad (11)$$

Hence, the first condition for the applicability of the IAT spectrum given by relationships (2) and (6) has the form

$$\nu_{ii}\tau \gg 1. \quad (12)$$

Second, if the ion distribution in the range of superthermal velocities is non-Maxwellian, then it is necessary to require that numerical differences between the integrals in the velocity moments determining the IAT spectrum and the same integrals corresponding to a Maxwellian ion distribution be small. The requirement of smallness of the differences between the velocity moments and their values corresponding to a Maxwellian ion distribution makes it possible to ignore the reverse effect of perturbations in the moments of the ion distribution on the IAT spectrum. Among the moments that determine the IAT spectrum, the second velocity moment is of the highest order and, consequently, is the slowest converging. Hence, we require that the root-mean-square velocity

$$\langle v^2\rangle = \frac{1}{3n_i}\int d\mathbf{v}\, v^2 f(\mathbf{v})$$

differ only slightly from $v_{Ti}^2 = \kappa T_i/m_i$, i.e., that the following inequality be satisfied:

$$\frac{\langle v^2\rangle - v_{Ti}^2}{v_{Ti}^2} \ll 1. \quad (13)$$

Inequalities (12) and (13) are sufficient conditions for the applicability of the analysis that follows.

3. KINETIC EQUATION FOR THE IONS

Theoretical investigation of the ion distribution is based on the time-independent kinetic equation for the ion distribution function $f(\mathbf{v})$,

$$\frac{e_i}{m_i}\mathbf{E}\cdot\frac{\partial f}{\partial\mathbf{v}} = St(f) + \frac{\partial}{\partial v_\alpha}[D_{\alpha\beta}^{QL}(\mathbf{v}) + D_{\alpha\beta}^{NL}(\mathbf{v})]\frac{\partial f}{\partial v_\beta}. \quad (14)$$

Equation (14) for the distribution function f takes into account the effects of (i) a constant electric field $\mathbf{E}$; (ii) ion–ion collisions, which are described by the Landau collision integral $\mathrm{St}(f)$; and (iii) quasilinear and nonlinear ion–wave interactions, which are described by the diffusion tensors $D^{QL}_{\alpha\beta}(\mathbf{v})$ and $D^{NL}_{\alpha\beta}(\mathbf{v})$, respectively. Since the distribution of thermal ions is assumed to be Maxwellian, we seek a solution to Eq. (14) in the velocity range $v > v_{Ti}$. In spherical coordinates, Eq. (14) has the form

$$\begin{aligned}
&\frac{\nu_{ii}v_{Ti}^3}{v^2}\frac{\partial}{\partial v}\left[\frac{v_{Ti}^2}{v}\frac{\partial f}{\partial v}+f\right]+\frac{\nu_{ii}v_{Ti}^3}{2v^3}\frac{\partial}{\partial\xi}(1-\xi^2)\frac{\partial f}{\partial\xi}\\
&+\frac{1}{v^2}\frac{\partial}{\partial v}\left[\nu^2 D_{vv}\frac{\partial f}{\partial v}+v\sqrt{1-\xi^2}D_{v\xi}\frac{\partial f}{\partial\xi}\right]\\
&+\frac{1}{v}\frac{\partial}{\partial\xi}\left[\sqrt{1-\xi^2}D_{v\xi}\frac{\partial f}{\partial v}+\frac{1-\xi^2}{v}D_{\xi\xi}\frac{\partial f}{\partial\xi}\right]\\
&-\frac{e_iE}{m_i}\left(\xi\frac{\partial f}{\partial v}+\frac{1-\xi^2}{v}\frac{\partial f}{\partial\xi}\right)=0,
\end{aligned}\tag{15}$$

where $D_{\alpha\beta}(\mathbf{v}) = D^{QL}_{\alpha\beta}(\mathbf{v}) + D^{NL}_{\alpha\beta}(\mathbf{v})$. Following [4], we describe the elements of the quasilinear diffusion tensor by the expression

$$\begin{aligned}
&\{D^{QL}_{vv}, D^{QL}_{v\xi}, D^{QL}_{\xi\xi}\}\\
&=\frac{\nu_E}{1+\delta}\frac{v_s^4}{vv_{Te}}\left\{\frac{v_s^2}{v^2}F_{vv}(v,\xi), \frac{v_s}{v}F_{v\xi}(v,\xi), F_{\xi\xi}(v,\xi)\right\}.
\end{aligned}\tag{16}$$

Here, $\nu_E = \sqrt{9\pi/8}\,|eE|/m_e v_s$, the parameter δ is given by expression (5),

$$\begin{aligned}
F_{\alpha\beta}(v,\xi)&\cong\frac{2(1+\delta)}{K_N}\int_0^\infty dx(1+x^2)^{-3}\\
&\times\left[\ln\frac{(1+x^2)^{1/2}}{x}-\frac{0.5}{1+x^2}-\frac{0.25}{(1+x^2)^2}\right]\\
&\times\int_0^1 dt\Phi(t)d_{\alpha\beta}\frac{\eta[(1-t^2)(1-\xi^2)-(v_s/v\sqrt{1+x^2}-t\xi)^2]}{[(1-t^2)(1-\xi^2)-(v_s/v\sqrt{1+x^2}-t\xi)^2]^{1/2}},
\end{aligned}\tag{17}$$

η is the Heaviside step function,

$$d_{vv} = (1+x^2)^{-1},$$

$$d_{v\xi} = -[t-\xi v_s/(v\sqrt{1+x^2})](1+x^2)^{-1/2}(1-\xi^2)^{-1/2},$$

$$d_{\xi\xi} = [t-\xi v_s/(v\sqrt{1+x^2})]^2(1-\xi^2)^{-1}.$$

For $v \geq v_s$, the quasilinear tensor given by expressions (16) and (17) determines the diffusion tensor in Eq. (15).

For $v < v_s$, all elements of quasilinear tensor (16) decrease rapidly with decreasing velocity; as a result, for $v \ll v_s$, we have $D^{QL}_{\alpha\beta} \propto (v/v_s)^{10}$. At the same time, for $v \ll v_s$, expressions (10) and (11) yield the following formula for the elements of the nonlinear diffusion tensor:

$$\begin{aligned}
&\{D^{NL}_{vv}, D^{NL}_{v\xi}, D^{NL}_{\xi\xi}\} = \frac{v^2}{8m_i^2n_i^2}\int\frac{d\mathbf{k}d\mathbf{k}'}{(2\pi)^5}N(\mathbf{k})N(\mathbf{k}')\\
&\times\delta(\omega''-\mathbf{k}''\cdot\mathbf{v})(\mathbf{n}_\mathbf{k}\cdot\mathbf{n}_{\mathbf{k}'})^2\omega\omega'\left(\frac{\mathbf{k}\cdot\mathbf{n}_\mathbf{v}}{\omega}+\frac{\mathbf{k}'\cdot\mathbf{n}_\mathbf{v}}{\omega'}\right)^2\\
&\times\left\{(\mathbf{k}''\cdot\mathbf{n}_\mathbf{v})^2, (\mathbf{k}''\cdot\mathbf{n}_\mathbf{v})\frac{(\mathbf{k}'', \mathbf{n}_\mathbf{E}-\xi\mathbf{n}_\mathbf{v})}{(1-\xi^2)^{1/2}}, \frac{(\mathbf{k}'', \mathbf{n}_\mathbf{E}-\xi\mathbf{n}_\mathbf{v})^2}{(1-\xi^2)}\right\},
\end{aligned}\tag{18}$$

where $\mathbf{n}_\mathbf{E}$, $\mathbf{n}_\mathbf{k}$, and $\mathbf{n}_\mathbf{v}$ are unit vectors in the directions of $e\mathbf{E}$, $\mathbf{k}$, and $\mathbf{v}$, respectively. All three of the tensor elements in (18) are on the order of v^2/τ, where the characteristic time τ is given by formula (9):

$$\begin{aligned}
\tau^{-1} &= \frac{1}{30m_i^2n_i^2}\int\frac{d\mathbf{k}d\mathbf{k}'}{(2\pi)^5}N(\mathbf{k})N(\mathbf{k}')\\
&\times\delta(\omega-\omega')[\mathbf{k}\cdot\mathbf{k}']^2(\mathbf{n}_\mathbf{k}\cdot\mathbf{n}_{\mathbf{k}'})^2.
\end{aligned}\tag{19}$$

Taking into account explicit expressions (2) and (6) for the IAT spectrum, we obtain from expression (19) the relationship

$$\tau^{-1} = \frac{K_N}{90\pi}\frac{r_{De}^4\omega_{Li}^3}{r_{Di}^4\omega_{Le}^2} = \frac{e_iEv_s}{15\kappa T_i}.\tag{20}$$

Equation (15) with explicit expressions (16) and (17) for the quasilinear diffusion tensor and explicit expression (18) for the nonlinear diffusion tensor serves as a basis for further analysis of the ion velocity distribution.

4. APPROXIMATE SOLUTION TO THE KINETIC EQUATION

We consider the isotropic part $f_0(v)$ of the ion distribution function. To do this, we represent $f(\mathbf{v})$ in the form

$$f(\mathbf{v}) = f_0(v) + f_a(v,\xi), \quad f_0(v) = \int_{-1}^1\frac{d\xi}{2}f(v,\xi).$$

We assume that the anisotropic part $f_a(v,\xi)$ is small in comparison to $f_0(v)$. Integrating Eq. (15) over the direc-

tions of the velocity vector, we arrive at the following equation for $f_0(v)$:

$$\frac{1}{v^2}\frac{\partial}{\partial v}v^2\left\{\nu_{ii}v_{Ti}^3\left(\frac{v_{Ti}^2}{v^3}\frac{df_0}{dv}+\frac{f_0}{v^2}\right)-\frac{e_iE}{4m_i}\int_{-1}^{1}d\xi(1-\xi^2)\frac{\partial f_a}{\partial\xi}\right.$$
$$\left.+\frac{1}{2}\int_{-1}^{1}d\xi\left[D_{vv}\frac{df_0}{dv}+\frac{\sqrt{1-\xi^2}}{v}D_{v\xi}\frac{\partial f_a}{\partial\xi}\right]\right\}=0. \quad (21)$$

The equation for the anisotropic part $f_a(v, \xi)$ of the ion distribution function is obtained by subtracting Eq. (21) from Eq. (15). Time-independent equation (21) is valid over the entire range of ion velocities except for those of runaway ions. Assuming that there is no source of ions with the velocity $v = 0$, we rewrite Eq. (21) as

$$\left[\frac{v_{Ti}^2}{v}+\frac{v^2}{2\nu_{ii}v_{Ti}^3}\int_{-1}^{1}d\xi D_{vv}\right]\frac{df_0}{dv}+f_0$$
$$=\frac{v^2}{2\nu_{ii}v_{Ti}^3}\int_{-1}^{1}d\xi\left[-\frac{\sqrt{1-\xi^2}}{v}D_{v\xi}+\frac{e_iE}{2m_i}(1-\xi^2)\right]\frac{\partial f_a}{\partial\xi}\Bigg\}. \quad (22)$$

Following [4], we first consider Eq. (22) in the velocity range $v \geq v_s$. In this case, the diffusion tensor is determined by the quasilinear contribution given by expressions (16) and (17). For velocities lying in this range, but only up to those of runaway ions, $v < v_R \approx (m_i/Zm_e)^{1/6}v_s$, the equation for the anisotropic part of the distribution function yields (see [4] for details)

$$\frac{\partial f_a}{\partial\xi}=-\frac{v}{\sqrt{1-\xi^2}}\frac{D_{v\xi}^{QL}}{D_{\xi\xi}^{QL}}\frac{df_0}{dv}.$$

We substitute this expression for $\partial f_a/\partial\xi$ into Eq. (22) and, on the right-hand side of this equation, ignore the electric field contribution, which is insignificant for $v_s \leq v < v_R$. As a result, we obtain the following equation for $f_0(v)$:

$$\frac{v_h^2}{v}\frac{df_0}{dv}+f_0=0, \quad (23)$$

where v_h is the effective thermal velocity, defined by the relationship

$$v_h^2=\frac{v^3}{2\nu_{ii}v_{Ti}^3}$$
$$\times\int_{-1}^{1}d\xi\left\{D_{vv}^{QL}(v\gg v_s,\xi)-\frac{[D_{v\xi}^{QL}(v\gg v_s,\xi)]^2}{D_{\xi\xi}^{QL}(v\gg v_s,\xi)}\right\}.$$

Using expressions (16), (17), and (20), we transform this relationship into

$$v_h^2=\frac{4.2}{(1+\delta)}\frac{v_{Te}}{v_{Ti}}(\nu_{ii}\tau)^{-1}v_s^2. \quad (24)$$

Note that the model used here to describe ions with velocities $v > v_s$ is valid only for $v_h^2 > v_s^2$ [4]. In this case, since ions with velocities $v_s \leq v < v_R$ interact with waves in a quasilinear fashion, the solution to Eq. (23) is close to a Maxwellian distribution function with the effective temperature higher than the electron temperature. Ions with such velocities are called hot resonant ions. Their distribution over velocities differs markedly from that of cold thermal ions, whose temperature is far lower. However, under the conditions considered below, the density of the resonant ions is so low that their contribution to the total ion density and total ion thermal energy is negligible.

We now examine Eq. (22) in the velocity range $v_{Ti} < v < v_s$, in which the diffusion tensor is determined by the nonlinear contribution given by expression (18). For simplicity, we restrict ourselves to conditions for which there is no need to consider the solution to the integrodifferential equation that describes $f_a(v, \xi)$ in this velocity range. In other words, we are interested in conditions under which the contribution of $f_a(v, \xi)$ to Eq. (22) can be ignored. Specifically, we are operating under the inequality

$$\nu_{ii}\tau\gg\frac{v_s^3}{v_{Ti}^3}. \quad (25)$$

Note that condition (12) holds automatically provided that condition (25) is satisfied. Under condition (25), we obtain from Eqs. (15) and (22) the following estimate for the anisotropic correction to the ion distribution function:

$$f_a\sim\left(\frac{e_iE}{m_i}+\frac{v}{\tau}\right)\nu_{ii}^{-1}\frac{v^3}{v_{Ti}^3}\frac{df_0}{dv}. \quad (26)$$

With allowance for relationship (20) between the field E and the time τ, estimate (26) becomes

$$f_a\sim\left(\frac{15v_{Ti}^2}{v_s}+v\right)(\nu_{ii}\tau)^{-1}\frac{v^3}{v_{Ti}^3}\frac{df_0}{dv}.$$

We thus arrive at the following estimate for the contribution of the anisotropic part of the ion distribution function to the right-hand side of Eq. (22):

$$\left(\frac{15v_{Ti}^2}{v_s}+v\right)^2(\nu_{ii}\tau)^{-2}\frac{v^5}{v_{Ti}^6}\frac{df_0}{dv}. \quad (27)$$

At the same time, the contributions to the left-hand side of Eq. (22) that do not contain f_a are on the order of

$$\left(\frac{v^4}{\nu_{ii}\tau v_{Ti}^3}+\frac{v_{Ti}^2}{v}\right)\frac{df_0}{dv},$$

which considerably exceeds contribution (27) over the entire velocity range $v_{Ti} < v < v_s$ provided that the following condition is satisfied:

$$\nu_{ii}\tau \gg \max\left[\frac{v_s^3}{v_{Ti}^3}, \left(15\frac{v_{Ti}}{v_s}\right)^4\right]. \quad (28)$$

Condition (28) includes condition (25) and the condition for the effect of the electric field to be weak. The latter condition is more difficult to satisfy for $v_s^2/v_{Ti}^2 < 22$. Hence, under condition (28), the anisotropic correction to Eq. (22) for the isotropic part of the ion distribution function in the velocity range $v_{Ti} < v < v_s$ can be ignored.

Note that, for velocities on the order of, but lower than, the ion acoustic velocity v_s, the nonlinear diffusion tensor does not reduce to v^2/τ because, for $v \sim v_s$, the expression for the intensity of stimulated scattering is more involved than expression (11). Since, for $v > v_s$, the elements of the nonlinear diffusion tensor decrease with decreasing velocity and since, for $v \ll v_s$, they all increase in proportion to v^2, the dependence $v \sim v_s$ should have a maximum at $D_{vv}^{NL}(v)$. Strictly speaking, the maximum value of the averaged (over the angles) diffusion coefficient at $v \approx v_s$ should be determined with allowance for the broadening of resonances corresponding to the Cherenkov interaction of ion acoustic waves with ions. Since we do not pretend here to develop such a detailed IAT theory, we will restrict ourselves to simple model representations. Namely, the correction that takes into account the non-quadratic dependence of the nonlinear diffusion tensor on velocity is described by the model expression

$$\frac{1}{2}\int_{-1}^{1} d\xi D_{vv}^{NL}(v,\xi) = \frac{v^2}{\tau}\left(1+\frac{av^b}{v_s^b}\right)^{-1}, \quad (29)$$

where a and b are numerical coefficients. Note that the results presented below remain essentially unchanged for b values lying in the range in which we are interested here, namely, for $2 \le b \le 5$. This is why, for definiteness, we will assume in our calculations that $b \approx 2$. This is not, however, the case for the coefficient a, which characterizes the value of the element D_{vv}^{NL} of the diffusion tensor at $v \approx v_s$. Below, we will show how changes in a affect the final theoretical results.

Relationships (23) and (29) put Eq. (22) in a comparatively simple form that makes it possible to determine $f_0(v)$ over the entire velocity range $v < v_R$:

$$\left[\frac{v_{Ti}^2}{v}+\frac{v^4}{(\nu_{ii}\tau)v_{Ti}^3}\left(1+\frac{av^b}{v_s^b}\right)^{-1}\eta(v_s-v) + \frac{v_h^2}{v}\eta(v-v_s)\right]\frac{df_0}{dv}+f_0 = 0. \quad (30)$$

This equation has the approximate solution

$$f_0(v) = \frac{n_i}{(2\pi)^{3/2}v_{Ti}^3}\exp\left\{-\int_0^v \frac{dv'v'}{v_{Ti}^2}\left[1+\frac{v'^5}{(\nu_{ii}\tau)v_{Ti}^5}\times\left(1+\frac{av'^b}{v_s^b}\right)^{-1}\eta(v_s-v')+\frac{v_h^2}{v_{Ti}^2}\eta(v'-v_s)\right]^{-1}\right\}, \quad v < v_R. \quad (31)$$

In deriving solution (31), we used the relationships $\int d\mathbf{v} f_0(\mathbf{v}) \approx n_i$ and $\langle v^2\rangle \approx v_{Ti}^2$, which follow from one of the basic assumptions of our model, namely, from inequality (13). In accordance with conditions (28), solution (31) in the range $v < v_{Ti}$ is nearly Maxwellian, which agrees with another basic assumption. However, under conditions (28), the distribution function $f_0(v)$ in the range $v > v_{Ti}$ differs from a Maxwellian function. In order to analyze this difference, it is necessary to determine the thermal velocity of the hot ions, $v_h = v_h(\delta)$, given by expression (24) and dependent on the parameter δ (5), which is uniquely related to the value of the function f_0 (31) at $v = v_s$.

5. EFFECT OF RESONANT IONS ON ANOMALOUS TRANSPORT

Using distribution function (31), we obtain the following expression for the parameter δ (5):

$$\delta = \delta_m \cdot \exp\left\{\frac{v_s^2}{2v_{Ti}^2}-\int_0^{v_s}\frac{dvv}{v_{Ti}^2}\times\left[1+\frac{v^5}{(\nu_{ii}\tau)v_{Ti}^5}\left(1+\frac{av^b}{v_s^b}\right)^{-1}\right]^{-1}\right\} > \delta_m, \quad (32)$$

where $\delta_m = Z\sqrt{m_i/m_e}(T_e/T_i)^{3/2}\exp(-ZT_e/2T_i)$ is the δ value corresponding to a Maxwellian distribution of ions with velocities $v < v_s$ and $Z = |e_i/e|$. Note that the value of δ is sensitive to the absolute value of the coefficient a. Let us consider how the parameter δ depends on $\nu_{ii}\tau$. To do this, we assume that $a \sim 1$, keeping in mind, however, that this assumption may lead to a quantitative error in determining δ. Figure 1 shows the dependence of the parameter δ (32) on $\nu_{ii}\tau$ in a singly

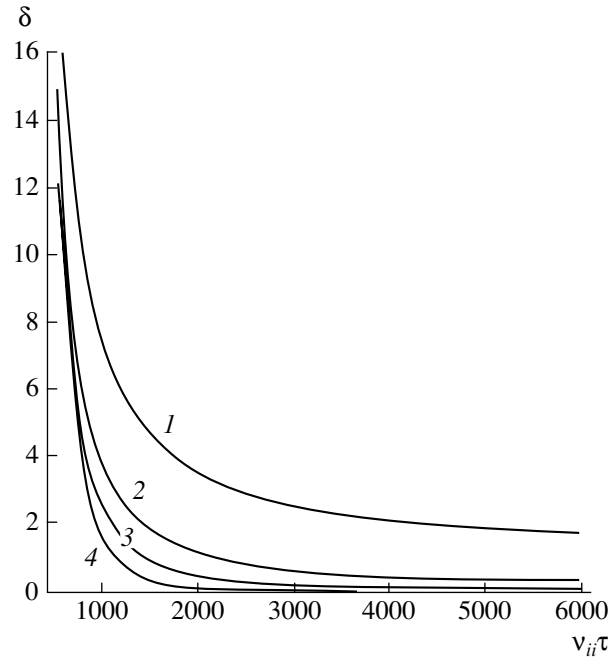

Fig. 1. Parameter δ (32), which characterizes the Cherenkov damping of ion acoustic waves by resonant ions, as a function of $\nu_{ii}\tau$ in a singly ionized argon plasma for v_s^2/v_{Ti}^2 = (*1*) 20, (*2*) 25, (*3*) 30, and (*4*) 50.

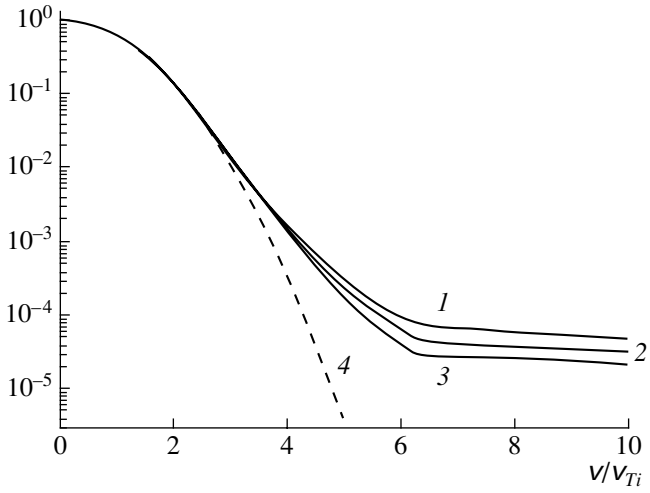

Fig. 2. Isotropic part of the ion distribution function, $(2\pi)^{3/2} v_{Ti}^3 n_i^{-1} f_0(v)$, vs. normalized velocity v/v_{Ti} in a singly ionized argon plasma with T_e/T_i = 40 for a = (*1*) 1, (*2*) 1.5, and (*3*) 2. Curve *4* corresponds to a Maxwellian distribution.

ionized argon plasma for $b = 2$, $a = 1$, and different values of the ratio $v_s^2/v_{Ti}^2 = T_e/T_i$: (*1*) 20, (*2*) 25, (*3*) 30, and (*4*) 50. The threshold for IAT corresponds to the value $\nu_{ii}\tau = 7.7 \times 10^3 \sqrt{T_e/T_i}$, which is beyond the range presented in Fig. 1. In the range of $\nu_{ii}\tau$ values given in Fig. 1, inequalities (4), (13), and (28), which are required to justify our approach, are also satisfied. For sufficiently large values of the parameter $\nu_{ii}\tau$, we have $\delta \approx \delta_m$, which corresponds to a Maxwellian distribution of ions with $v \le v_s$. It can be seen from Fig. 1 that, as the parameter $\nu_{ii}\tau$ decreases, the parameter δ increases; i.e., resonant ions enhance the damping of ion acoustic waves. This phenomenon, which has been known for a considerable time [4], can now be described in a self-consistent manner for the case in which the nonlinear interaction of superthermal ions with IAT is important. For small values of the turbulent Knudsen number, the plasma current density depends on the parameter δ as (see [5])

$$j = (2.1 + 0.9\delta) e n_e v_s.$$

We can see that, for $\delta \gg 2$, resonant ions have a decisive effect on the current density in a turbulent plasma, whereas, for $\delta \ll 2$, this effect can be ignored. It can be seen from Fig. 1 that, if the extent to which the plasma is nonisothermal is sufficiently high ($T_e/T_i > 25$), then the relationship $\delta \approx \delta_m \ll 2$ holds for large values of the parameter $\nu_{ii}\tau$, whereas, for smaller values of $\nu_{ii}\tau$, we have $\delta \gg 2$.

Finally, we analyze solution (31). Figure 2 shows how this solution, i.e., the isotropic part f_0 of the ion distribution function, depends on the normalized velocity v/v_{Ti} for a singly ionized argon plasma and for $v_s^2/v_{Ti}^2 = 40$, $\nu_{ii}\tau = 750$, and $b = 2$. Curves *1*, *2*, and *3* in this figure were calculated for α = 1, 1.5, and 2, respectively. For these curves, formula (32) gives $\delta \approx 5$, 3, and 2, respectively. In this case, expression (24) yields $v_h^2 \approx 2v_s^2$, $2.5v_s^2$, and $3v_s^2$; i.e., the temperature of hot resonant ions is higher than the electron temperature. Curve *4* in Fig. 2 corresponds to a Maxwellian distribution of the ions. A comparison of curves *1*, *2*, and *3*, on the one hand, with curve *4*, on the other, shows that, in the velocity range $v_{Ti} \ll v \le v_s$, distributions *1*, *2*, and *3* are very non-Maxwellian. Curves *1*, *2*, and *3* show that, at velocities of about $v/v_{Ti} \approx 6.3$ (which corresponds to the ion acoustic velocity), the behavior of the distribution function changes radically: in the range $v < v_s$, the distribution of the ions is governed by their nonlinear interaction with the waves, whereas, in the range $v > v_s$, the ion distribution is dominated by the quasilinear interaction. In turn, a comparison between curves *1*, *2*, and *3* shows that, when the parameter a (which is a free parameter in our theory) is varied from 1 to 2, the distribution function of the superthermal ions changes comparatively little. The amount by which the distribution function changes in the range $v \ge v_s$ as the coefficient a is varied is comparable to the above changes in the parameter δ.

Hence, we have derived a solution to the kinetic equation for the isotropic part of the ion distribution

function for a plasma with low-intensity IAT, such that condition (28) is satisfied. In this case, the effect of the IAT on the distribution of thermal ions can be ignored and it is possible to use the IAT spectrum calculated for a Maxwellian distribution of the bulk ions. We have obtained ion distribution (31) and have used it to describe the damping of ion acoustic waves by resonant ions with velocities higher than the ion acoustic velocity. In doing this, we have determined the parameter δ (32), which characterizes the effect of resonant ions on the IAT spectrum and on the current density in a turbulent plasma at small values of the turbulent Knudsen number. We have shown that the formation of a non-Maxwellian distribution of superthermal ions leads to an increase in the number of resonant ions; as a consequence, resonant ions enhance the damping of ion acoustic waves, the turbulence level reduces, and the plasma conductivity increases.

ACKNOWLEDGMENTS

We are grateful to V.P. Silin for encouraging this study and fruitful discussions of the results obtained. This work was supported in part by the Russian Foundation for Basic Research (project no. 02-02-16047) and the RF Program for State Support of Leading Scientific Schools (project no. NSh-1385.2003.2).

REFERENCES

1. E. K. Zavoĭskiĭ and L. I. Rudakov, At. Energ. **23**, 417 (1967).
2. E. D. Volkov, N. F. Perepelkin, V. A. Suprunenko, and E. A. Sukhomlin, *Collective Phenomena in Current-Carrying Plasma* (Naukova Dumka, Kiev, 1978), p. 86.
3. L. M. Kovrizhnykh, Zh. Éksp. Teor. Fiz. **52**, 1406 (1967) [Sov. Phys. JETP **25**, 934 (1967)].
4. V. P. Silin and S. A. Uryupin, Fiz. Plazmy **12**, 1042 (1986) [Sov. J. Plasma Phys. **12**, 596 (1986)].
5. V. Yu. Bychenkov, V. P. Silin, and S. A. Uryupin, Phys. Rep. **164**, 119 (1988).
6. V. Yu. Bychenkov, V. P. Silin, and S. A. Uryupin, Fiz. Plazmy **15**, 300 (1989) [Sov. J. Plasma Phys. **15**, 173 (1989)].
7. A. S. Kingsep, Zh. Éksp. Teor. Fiz. **62**, 2179 (1972) [Sov. Phys. JETP **35**, 1139 (1972)].
8. A. S. Kingsep and K. V. Chukbar, in *Proceedings of the All-Union Conference on the Interaction of Electromagnetic Waves with Plasma, Dushanbe, 1979*, p. 64.
9. V. P. Silin, Kratk. Soobshch. Fiz., No. 10, 55 (1987).
10. V. N. Tsytovich, *Theory of Turbulent Plasma* (Atomizdat, Moscow, 1971; Plenum Press, New York, 1974).

Translated by I.A. Kalabalyk

Plasma Physics Reports, Vol. 30, No. 11, 2004, pp. 944–952. Translated from Fizika Plazmy, Vol. 30, No. 11, 2004, pp. 1015–1024.

PLASMA DYNAMICS

Electric Explosion of Fine Tungsten Wires in Vacuum

A. G. Rousskikh, R. B. Baksht, A. Yu. Labetskiĭ, V. I. Oreshkin, A. V. Shishlov, and S. A. Chaĭkovskiĭ

Institute of High-Current Electronics, Siberian Division, Russian Academy of Sciences, Akademicheskiĭ pr. 4, Tomsk, 634055 Russia

Received September 24, 2003; in final form, December 8, 2003

Abstract—A study is made of the breakdown of a fine wire during its electric explosion in vacuum. The problem of how the wire diameter, the rate of energy deposition in the wire, and the insulation of the electrode surface near the electrode–wire contact influence the wire explosion and the accompanying breakdown is investigated experimentally. The wire explosion was performed at a positive polarity of the high-voltage electrode. A current density growth rate of 6×10^{11}–5×10^{16} A/(s cm^2) is achieved. It is shown that the breakdown along a wire is similar in many respects to the gas breakdown. The insulation of the wire surface makes it possible to avoid breakdown and to increase the deposited energy to values sufficient for the wire sublimation. © *2004 MAIK "Nauka/Interperiodica".*

1. INTRODUCTION

Although electric explosions of wires at both microsecond and nanosecond current-rise times have been studied in many papers, the processes accompanying the wire explosion still attract great interest. This interest is motivated by both the fundamental character of the processes occurring in wire explosions and their possible applications. Thus, metal (particularly tungsten) multiwire arrays are widely used to generate high-power soft X-ray (SXR) pulses [1–6]. To increase the efficiency of SXR generation in multiwire arrays, it is necessary to minimize the influence of the azimuthal inhomogeneity in the material distribution during the wire explosion and decrease the effect of a precursor on the implosion process.

One possible way of solving this problem is to ensure the rapid conversion of the wire material into a gaseous plasma. As was shown in [7], it is possible to substantially improve the uniformity of the expanding wire material and to increase the fraction of the wire material converted into a gaseous state by increasing the energy deposited in the wire. One of the factors inhibiting the increase in the deposited energy to values sufficient for the wire sublimation is an early breakdown of the interelectrode gap along the wire surface and the subsequent switching of the current from the wire to the conducting medium surrounding the wire. In [8], it was shown that the shunting breakdown is caused by the gas desorption from the wire surface. In this case, the breakdown of the interelectrode gap along the desorbed gas shunts the wire, thereby impeding the increase in the deposited energy to values sufficient for its complete evaporation.

Insulation of the wire surface with a thin varnish layer makes it possible to substantially increase the time interval before breakdown and, hence, to increase the deposited energy [7, 9]. As was pointed out in [10] and was also proved by our studies, the energy deposited before breakdown increases with increasing energy deposition rate. However, a complete understanding of these processes is still lacking. The energy deposited in the wire material can be limited by the specific properties of the gas breakdown and by the influence of other factors inhibiting or promoting breakdown of the gas desorbed from the wire surface.

The aim of this study is to investigate the mechanism for the development of the shunting breakdown along an exploding wire and to find ways of preventing this breakdown. We performed a number of experiments on the explosion of fine tungsten wires in vacuum. In these experiments, we studied how the wire diameter, the rate of energy deposition in the wire, and the insulation of the electrode surface near the electrode–wire contact influence the wire explosion and the accompanying breakdown. The assumption of the thermal expansion of the desorbed gas allowed us to represent the experimental data on the breakdown along a wire in different operating regimes as a dependence on the similarity parameters E_{br}/n and $n\tau_{br}$, i.e., in a form conventionally used in gas-discharge physics.

2. EXPERIMENT

2.1. Experimental Facility and Diagnostics

To study electric explosions of wires, a special LC generator was designed and created [11]. The design of the generator (see Fig. 1) allowed us to change the rate of energy deposition in the wire by varying the inductance and capacitance of the electric circuit and the charging voltage of the capacitor. In our experiments, the high-voltage electrode was charged positively relative to the return current posts; in this case, breakdown

1063-780X/04/3011-0944$26.00 © 2004 MAIK "Nauka/Interperiodica"

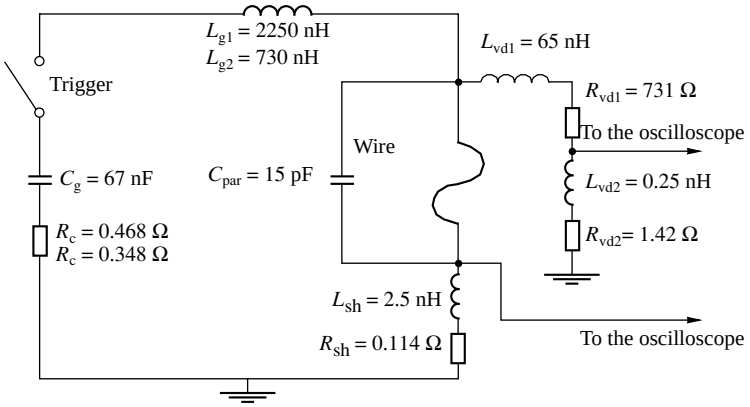

Fig. 1. Electric circuit of the LC generator.

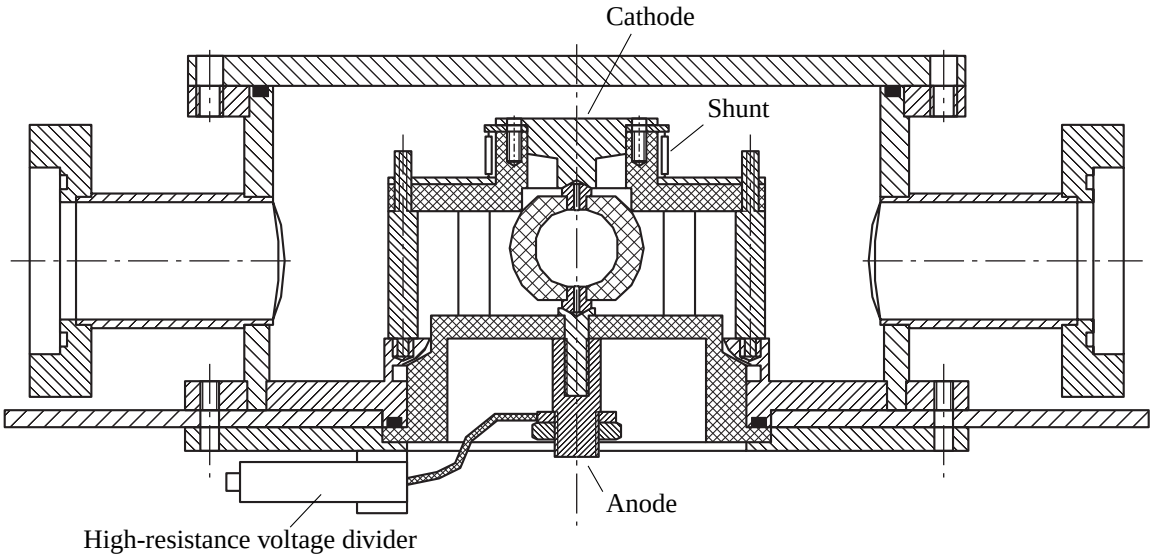

Fig. 2. Schematic of the vacuum chamber with the load unit.

along the wire occurred substantially later than in the case of a negatively charged high-voltage electrode [13]. This allowed us to substantially increase the energy deposited in the wire.

We performed experiments with 6.35- and 30.48-μm tungsten wires of length 20 ± 0.5 mm (six series of experiments for each diameter). The charging voltage U_0 of the capacitor was 10, 22, and 35 kV. The circuit inductance L_g was 730 and 2250 nH; in this case, the circuit resistance R_c (not including the resistance of the shunt and wire) was 0.234 and 0.354 Ω, respectively. The circuit capacitance C_g was 66.9 nF in all the experiments. As capacitive storages, we used commercial IKCh-50-0.035 capacitors. As a switch, we used a gas spark gap. Each series of the experiments consisted of ten shots.

The load unit was installed in the working chamber of the generator (Fig. 2). The working chamber had six diagnostic windows. As return current posts, we used six 1-cm-diameter rods equally spaced round a circle 10 cm in diameter. The return current posts were chosen such that the stray capacitance of the load unit was minimal. All the components of the chamber were made of nonmagnetic materials. In all the experiments, the vacuum chamber was pumped-out by an oil-free pump to a residual pressure of $(3–5) \times 10^{-5}$ torr.

In our experiments, we used the following electrical diagnostics: an active high-resistance divider, an inductive loop located on the side of the high-voltage electrode (anode), and a shunt located on the side of the ground electrode.

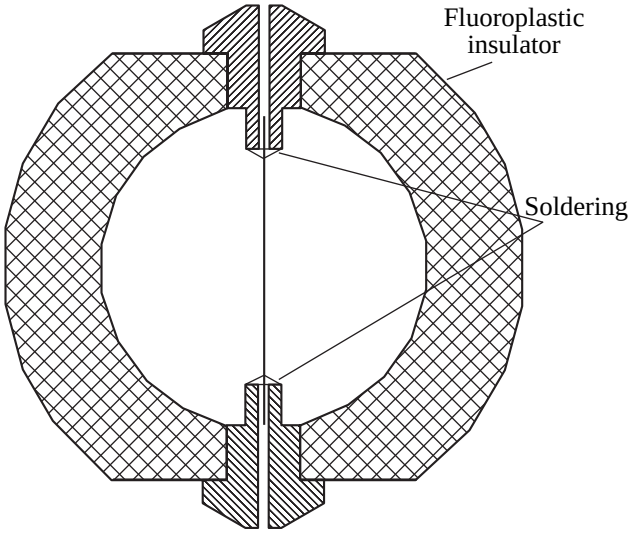

Fig. 3. Schematic of the wire holder.

The parameters of the active high-resistance divider were chosen such that, on the one hand, they ensured the required accuracy of the voltage measurements and, on the other, the effect of the divider on the operation of the main circuit of the generator was minimal. Nevertheless, as in almost any diagnostics, the divider could influence the processes occurring in the circuit. In subnanosecond wire explosions, we observed significant inductive jumps in the voltage and current. At the instants of these jumps, the power deposited in the wire could be close to the maximum power of the generator. As a result, due to the power loss in the active divider, the current and voltage in the main circuit decreased by 10–12% and the energy deposited in the wire decreased by 3–3.5%. This effect manifested itself only in the early stage of wire heating, when the power deposited in the wire was comparable to the generator power. In our calculations, knowledge of the circuit parameters allowed us to accurately take into account the influence of the active divider. Since the aim of our experiments was to study the parameters of the exploding wire for the known characteristics of the electric circuit, the influence of the divider on the parameters of the electric explosion was insignificant. In all the experiments, the maximum decrease in the current and voltage because of the finite resistance of the divider was no larger than 5%.

2.2. Preparation of the Wire

Test experiments on wire explosions showed that, when the contacts of the electrodes with a wire were not quite good, both the gap voltage and the resistance of the entire circuit could change abruptly at the beginning of the current pulse; such changes were practically impossible to take into account. Moreover, a plasma was produced at the site where the wire contacted the electrode; this could substantially influence the processes of wire heating and electric breakdown along the wire. To exclude the influence of contacts on the results of experiments, the wire was mounted in a special caprolan holder (Fig. 3) and the wire contacts with the electrodes were soldered. As a result, a reliable contact of the electrodes with the wire was ensured. After soldering, the holder was washed with water and ethanol.

2.3. Test Experiments on the Breakdown of a Gas-Filled Gap

To compare the parameters of breakdown along a wire to those of the breakdown of a gas-filled gap, we performed a series of test experiments. In these experiments, we studied the breakdown of a gap filled with hydrogen at different pressures. The holder with the wire (Fig. 3) was replaced with 3-cm-diameter plane electrodes, the interelectrode gap length being equal to 6 mm. When the generator (L = 730 nH) was switched on, a voltage pulse with a rise time of ≈10 ns was applied to the gap. We measured the time interval from the beginning of the voltage pulse to the instant of breakdown and the gap voltage at this instant for different gas pressures within the range from 3.6 to 736 torr. The measurements were performed in two regimes: with and without UV preionization. As a source of UV radiation, we used a spark discharge along a dielectric surface. The UV source was located in the middle of the gap at a distance of 5.5 cm from the symmetry axis of the system. The period of current oscillations in the circuit of the UV source was 6 μs. The time interval between the beginning of the preionization pulse and the instant at which the generator was switched on was 1.5 μs.

3. RESULTS AND DISCUSSION

3.1. Explosion of Wires in Vacuum

The main results of our experiments on the explosion of tungsten wires are presented in Figs. 4 and 5. Figure 4 shows the breakdown time τ_{br} (the time interval between the beginning of the current pulse and the instant of breakdown), the breakdown electric field E_{br} (the breakdown voltage divided by the wire length), and the energy W deposited in a wire as functions of the charging voltage U_0 and the circuit inductance L_g for a 6.35-μm wire. Figure 5 shows similar dependences for a 30.48-μm wire. In these figures, the symbols show the average values of the measured parameters (the averaging was performed over 10 shots) and the error bars show the maximum scatter in the measured parameters. The dotted lines show the energy range within which the wire was melted.

We calculated the energy deposited in a wire before the instant of breakdown τ_{br}. This instant was determined from the beginning of the sharp drop in the voltage and sharp rise in the current (Fig. 6). After the onset of the

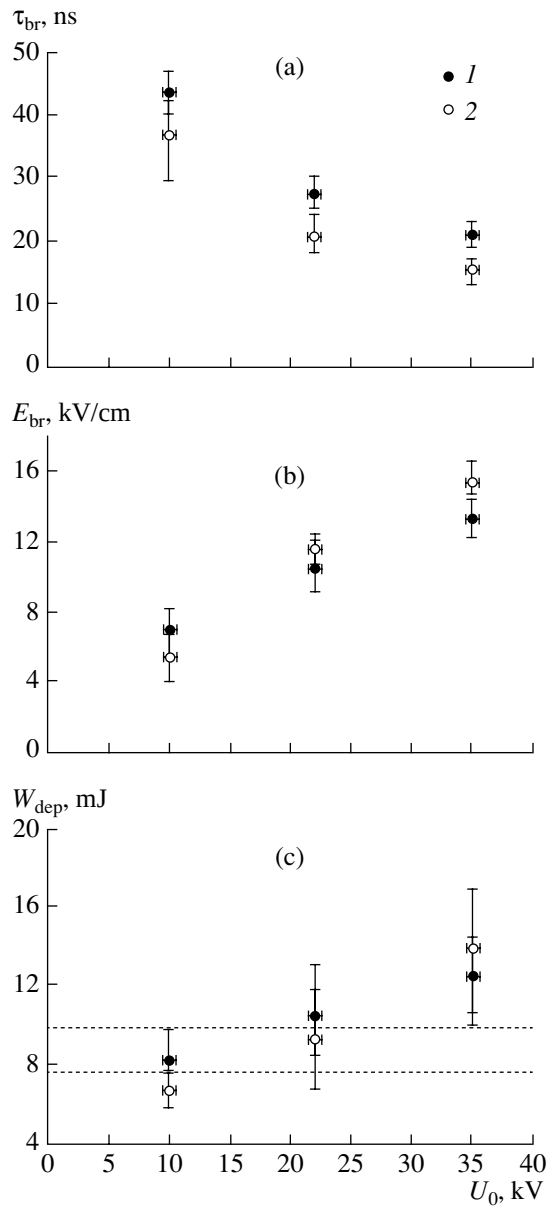

Fig. 4. Parameters of the electric explosion of a 6.35-μm tungsten wire with a length of 2 cm as functions of the capacitor charging voltage U_0 for L_g = (*1*) 2250 and (*2*) 730 nH: (a) the time interval τ_{br} from the beginning of the current pulse to the instant of breakdown, (b) the breakdown electric field E_{br}, and (c) the energy W_{dep} deposited in the wire by the instant of breakdown.

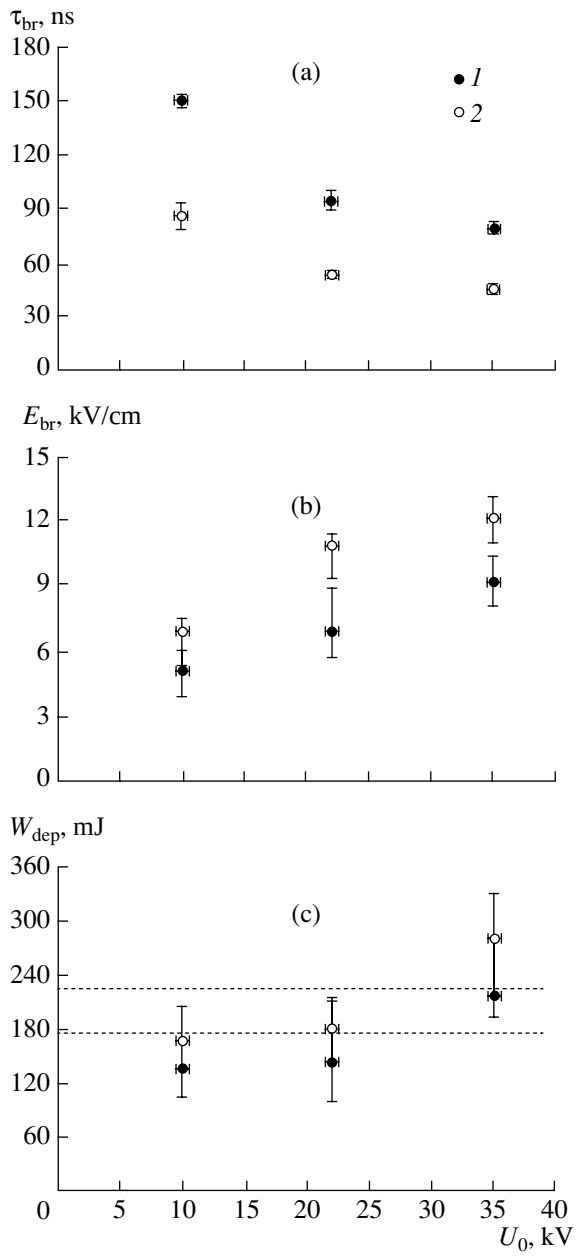

Fig. 5. Parameters of the electric explosion of a 30.48-μm tungsten wire with a length of 2 cm as functions of the capacitor charging voltage U_0 for L_g = (*1*) 2250 and (*2*) 730 nH: (a) the time interval τ_{br} from the beginning of the current pulse to the instant of breakdown, (b) the breakdown electric field E_{br}, and (c) the energy W_{dep} deposited in the wire by the instant of breakdown.

shunting breakdown, the generator energy was primarily deposited in the gas desorbed from the wire surface and practically no energy was deposited in the wire.

Figure 7 shows the energy W deposited in a wire and the breakdown electric field E_{br} as functions of the average input power P_{av} and the circuit inductance L_g for a 6.35-μm wire (plots (a), (b)) and 30.48-μm wire (plots (c), (d)). It can be seen that both the breakdown electric field and the energy deposited in the wire increase with increasing input power.

As the wire is heated by the current flowing through it, the adsorbed gas begins to be evolved from the wire surface. When the wire temperature reaches about 600°C, almost all the gas is desorbed from the wire sur-

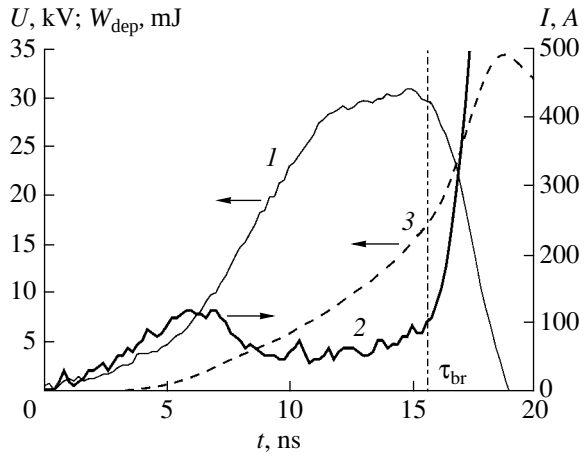

Fig. 6. Waveforms of (*1*) the voltage U across the anode–cathode gap, (*2*) the current I through the wire, and (*3*) the deposited energy W_{dep} calculated by these waveforms. The diameter of the tungsten wire is 6.35 μm, the wire length is 2 cm, the charging voltage is 35 kV, and the circuit inductance is 730 nH. The vertical dashed-and-dotted line shows the instant of breakdown τ_{br}.

face and a thin dense gas layer is produced around the wire. In [8], it was suggested that it is this desorbed gas that plays a key role in the breakdown along the wire.

In [14], it was shown that the surface density of hydrogen atoms adsorbed by a tungsten surface is on the order of 10^{15} cm^{-2}; moreover, there are also such elements as nitrogen, carbon, and oxygen on this surface. Since hydrogen is the lightest element, it is this gas that should determine the boundary of the gas layer. The number of hydrogen atoms adsorbed by the surface of a tungsten wire with a diameter d_w and length l_w is

$$N_0 \approx 10^{15}\pi d_w l_w. \quad (1)$$

As the wire is heated, the surrounded gas is also heated. The expansion velocity of the gas shell depends on the gas temperature. Taking into account that the gas density is fairly high and the distance from the wire surface is small, we will assume that the gas temperature

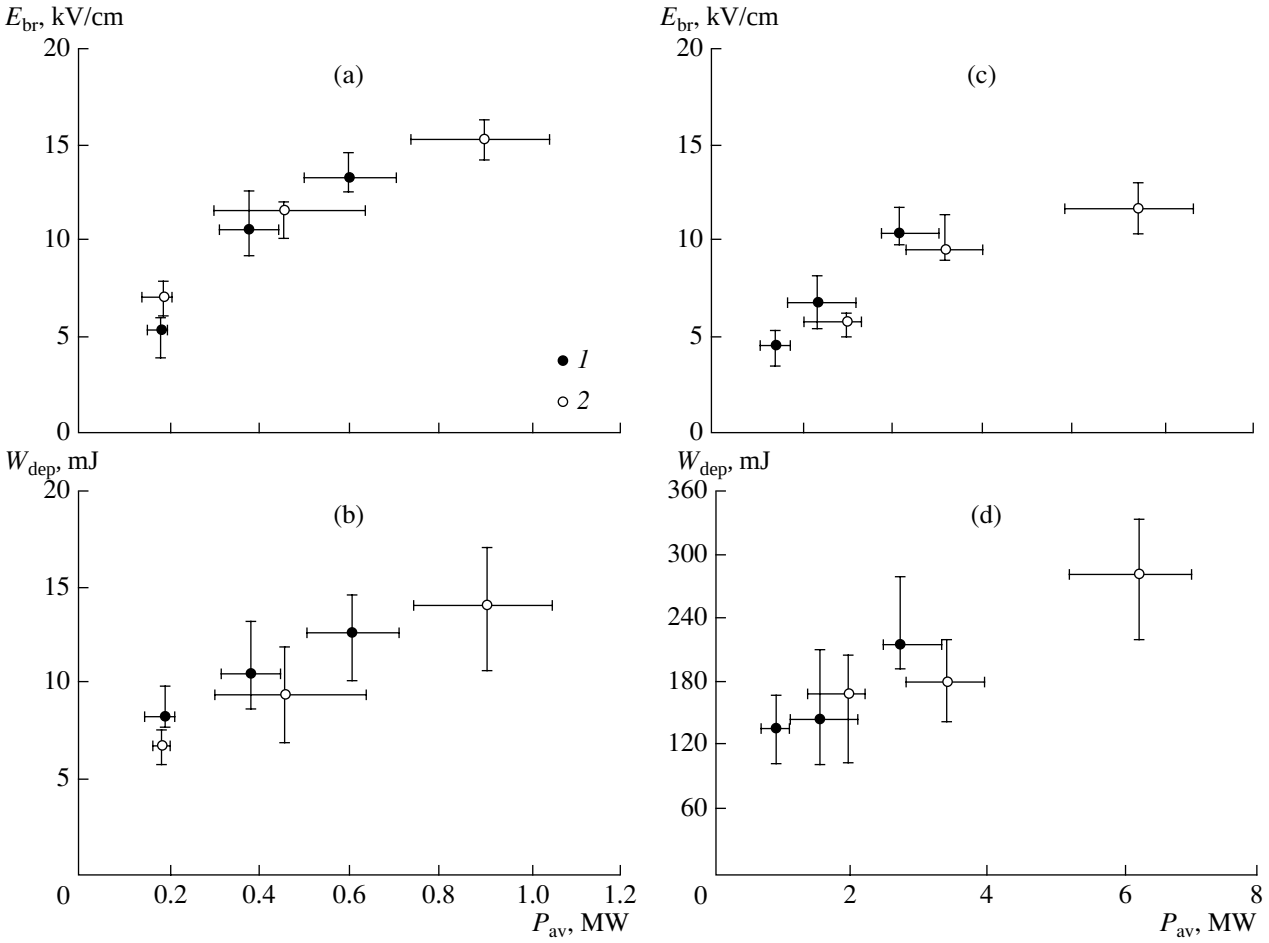

Fig. 7. Breakdown electric field E_{br} and the energy W_{dep} deposited in the wire as functions of the average input power P_{av} for L_g = (*1*) 2250 and (*2*) 730 nH and for wire diameters of (a, b) 6.35 and (c, d) 30.48 μm.

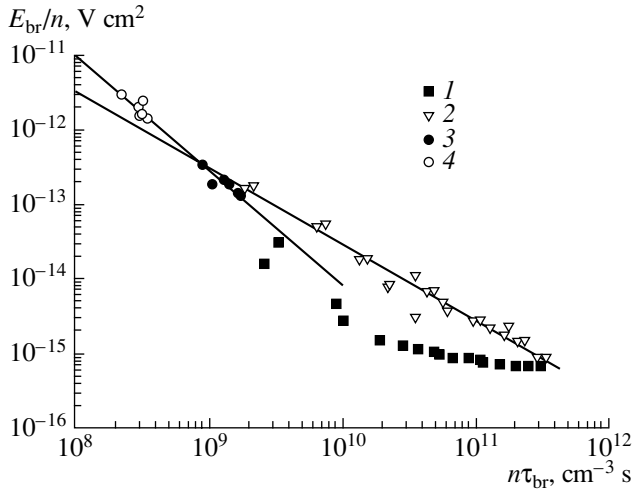

Fig. 8. Dependences of the parameter E_{br}/n on $n\tau_{br}$ observed in experiments on the breakdown of a gap filled with hydrogen (*1*) with and (*2*) without UV preionization and in experiments on the electric explosion of a (*3*) 6.35-μm and (*4*) 30.48-μm tungsten wire in vacuum. The solid lines show the power-law approximations of the data on the breakdown in hydrogen without UV preionization and on the electric explosion of a wire in vacuum.

$T(t)$ is equal to the wire temperature, which can be estimated from the energy deposited in the wire:

$$T(t) = [m_w C_W(T(t))]^{-1} \int I(t)U(t)dt, \quad (2)$$

where m_w is the wire mass and $C_W(T(t))$ is the tungsten heat capacity [15, 16]. Expression (2) is, in fact, an upper estimate of the gas temperature.

The average velocity of the thermal expansion of the atomic-hydrogen shell can be estimated as

$$v(t) \approx [kT(t)/m_{at}]^{1/2}, \quad (3)$$

where $k = 1.38 \times 10^{-23}$ J/K and m_{at} is the mass of a hydrogen atom.

By numerically integrating the expansion velocity of the gas shell from the beginning of the current pulse to the instant of breakdown, we find the radius of the gas shell R_{sh},

$$R_{sh} = 0.5d_w + \int v(t)dt. \quad (4)$$

The volume of the gas shell is

$$V(t) = \pi[R_{sh}^2(t) - r_w^2]l_w, \quad (5)$$

and the gas density $n(t)$ is

$$n(t) = N_0/V(t). \quad (6)$$

Using the measured values of the breakdown voltage U_{br} and the time interval between the time at which the generator is switched on and the instant of breakdown τ_{br}, we can plot the reduced electric field E_{br}/n as a function of the parameter $n\tau_{br}$. The resulting functional dependence of E_{br}/n on $n\tau_{br}$ will allow us to compare the parameters of breakdown along a wire in vacuum to those of gas breakdown.

3.2. Breakdown of a Gas-Filled Gap

We studied breakdown in hydrogen at different gas densities n by the method described in [17, 18]. Figure 8 shows the results of experiments on breakdown in hydrogen with and without UV preionization. As was expected, the curve $E_{br}/n = f(n\tau_{br})$ in the absence of UV preionization lies somewhat higher than that in the presence of preionization and is somewhat different in shape.

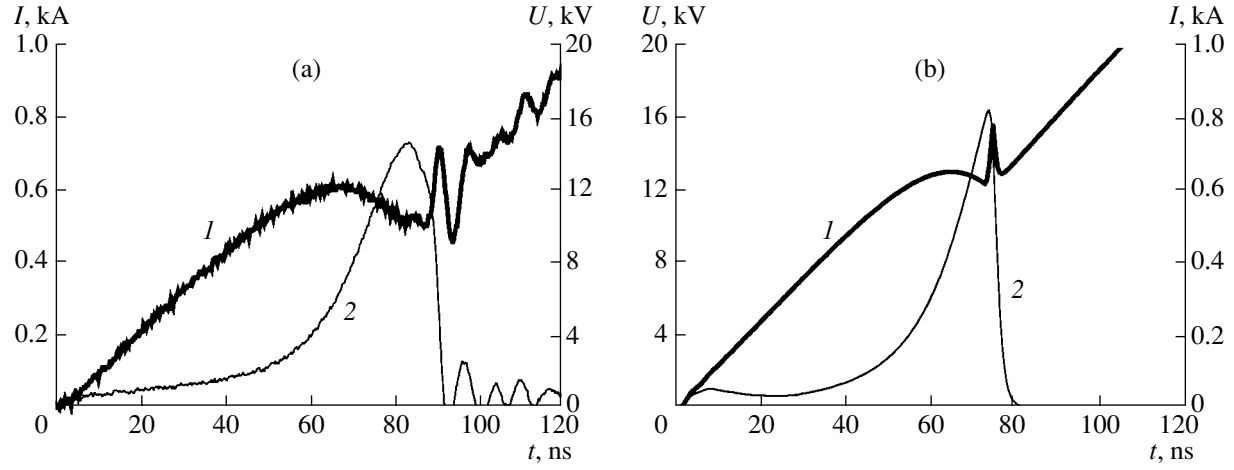

Fig. 9. (a) Measured and (b) calculated dependences of (*1*) the current I through the wire and (*2*) the voltage U across the anode–cathode gap during the explosion of a 30.48-μm tungsten wire. The wire length is 20 mm, the circuit inductance is 730 nH, the circuit capacitance is 66.9 nF, and the charging voltage is 10 kV.

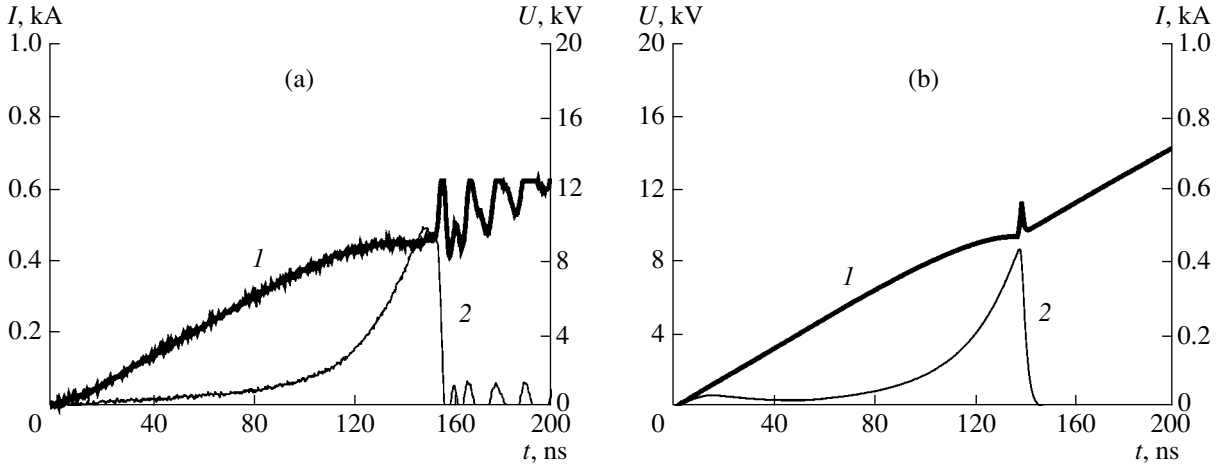

Fig. 10. (a) Measured and (b) calculated dependences of (*1*) the current *I* through the wire and (*2*) the voltage *U* across the anode–cathode gap during the explosion of a 30.48-μm tungsten wire. The wire length is 20 mm, the circuit inductance is 2251 nH, the circuit capacitance is 66.9 nF, and the charging voltage is 10 kV.

The closed and open circles in Fig. 8 show the data obtained during the explosion of tungsten wires in vacuum. The parameters E_{br} and τ_{br} were found experimentally and the density of the desorbed gas n was calculated by the method described in Section 3.1. The data presented in the figure refer to all of the twelve regimes of wire explosion under study: the upper group of symbols refers to 30.48-μm wires, and the lower group refers to 6.35-μm wires.

The above experimental dependences can be fitted by the function

$$E_{br}/n = \alpha(n\tau_{br})^{\beta}, \quad (7)$$

where E_{br} is in V/cm, n is in cm^{-3}, and τ_{br} is in seconds. For breakdown in hydrogen, the coefficients in formula (7) are $\alpha = 5.6 \times 10^{-4}$ and $\beta = -1.0274$. For breakdown along a wire, they are $\alpha = 28.13$ and $\beta = -1.5523$.

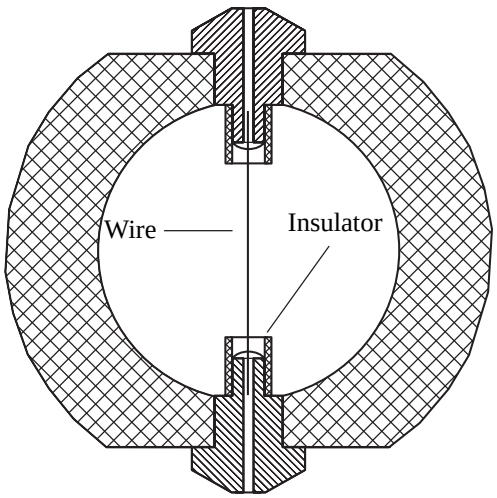

Fig. 11. Schematic of the wire holder with the insulation of electrodes.

A comparison of the curves shown in Fig. 8 shows that the parameters of breakdown along a wire are close to those of gas breakdown. The difference in the slopes of the curves is presumably related to the different initial conditions and to a rather simplified description of the processes of desorption, heating and gas breakdown.

It is likely that the instant of breakdown and, hence, the energy deposited in the wire is determined by the dynamics of the thermal expansion of the desorbed gas. This explains an increase in the deposited energy with increasing input power. The faster the wire is heated, the smaller the distance to which the desorbed gas has time to expand and the stronger the electric field required for the breakdown of this gas. As a result, the energy deposited in the wire increases.

The experimental data on the breakdown of fine tungsten wires (see Fig. 8) make it possible to determine the instant at which the energy deposited in the wire should be calculated when simulating an electric explosion of a wire in vacuum. If the simulation of electric explosion is performed with allowance for the thermal expansion of the desorbed gas, then the instant of breakdown is determined by expression (7).

To check the efficiency of the model, we performed magnetohydrodynamic (MHD) simulations of a wire explosion with allowance for the thermal expansion of the desorbed gas into a vacuum by the method described in Section 3.1. In simulations, we used the one-dimensional MHD code developed in [19]. In parallel with hydrodynamic equations, Maxwell's equations and heat conduction equations were solved. For tungsten, we used wide-range semiempirical equations of state [20], in which the effects of high-temperature

melting and evaporation of a wire material were taken into account.

In simulations of an electric explosion of a wire in vacuum, it was assumed that, when the voltage reached its breakdown value (this value is determined by formula (7)), a resistor with a resistance depending on time as

$$R = R_0 \exp\left(-\frac{(t-\tau_{br})}{\Delta\tau}\right) \quad (8)$$

was introduced in the circuit in parallel to the wire.

The parameters R_0 and $\Delta\tau$ were chosen such that, 5 ns after the introduction of the resistor, its resistance was 0.1 Ω.

In MHD simulations, the coefficients α and β in expression (7) were chosen such that the results of calculations agreed well with the above experimental data on electric explosions of wires in vacuum. The best agreement was achieved at $\alpha = 1.5 \times 10^{-3}$ and $\beta = -1.05$; these values are quite close to those for the analytic approximation of the breakdown curve in hydrogen (Fig. 8). The difference in the values of the coefficient α for these two cases shows that the breakdown voltage along a wire is higher than the breakdown voltage in pure hydrogen.

Figures 9 and 10 show the experimental and calculated curves for the explosion of tungsten wires in vacuum in two regimes with different times of energy deposition in the wire. It can be seen from these figures that the calculated curves are similar in shape to the experimental ones. In spite of a certain quantitative difference, this testifies that the method proposed is applicable for calculating the instant of breakdown and estimating the energy deposited in a wire during its electric explosion in vacuum.

3.3. Suppression of Breakdown during the Explosion of Wires in Vacuum

Taking into account that the parameters of breakdown along a wire are mainly determined by the parameters of the gas desorbed from the wire surface (rather than the parameters of the wire itself), we attempted to suppress this breakdown. For this purpose, the region of the electrode–wire contact was covered with an insulator; this made it possible to both eliminate the effect of the plasma arriving from the region of the wire–electrode contact and suppress electron emission from the cathode surface. The experiments were performed with different insulators. The insulator covered both the region of the wire–electrode contact and the electrode itself. The use of silicon hermetic adhesive as an insulator gave the best results. The results obtained are presented in Fig. 12, which shows the waveforms of the current and voltage for two regimes of the explosion of a fine tungsten wire: without and with insulating the electrode surface by hermetic adhesive. One can see that, with insulation, breakdown is absent; as a result, the duration of the high-voltage pulse applied to the wire and, hence, the energy deposited in the wire increase substantially. This makes it possible to increase the deposited energy to values sufficient for the wire sublimation.

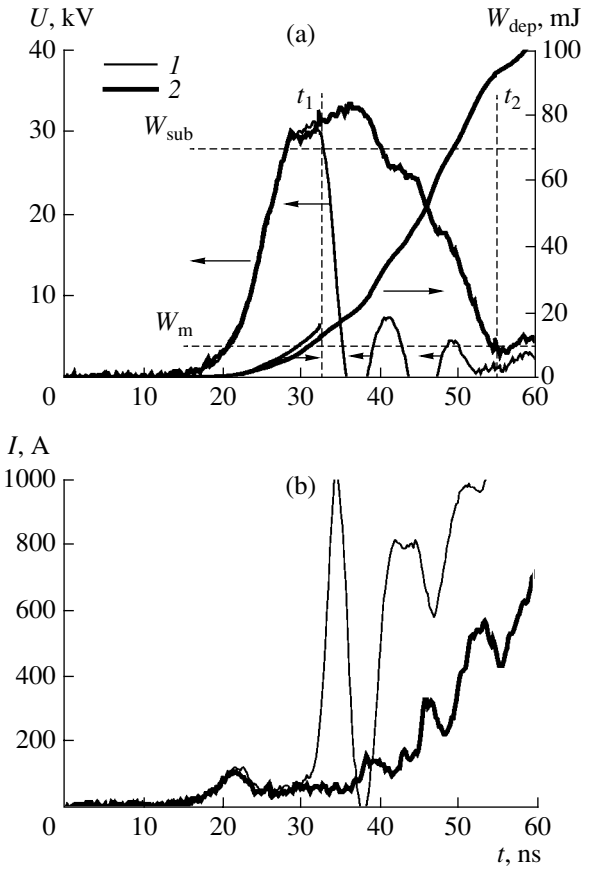

Fig. 12. Waveforms of (a) the voltage U across the anode–cathode gap and the energy W_{dep} deposited in a 6.35-μm tungsten wire and (b) the current I through the wire for (*1*) uninsulated and (*2*) insulated electrodes. The wire length is 2 cm, the charging voltage is 35 kV, and the circuit inductance is 730 nH. The dashed lines show the sublimation energy W_{sub}; the melting energy W_m; and the instants t_1 and t_2 till which the generator energy is deposited in the uninsulated and insulated wire, respectively.

4. CONCLUSIONS

In this paper, we have presented results from the studies of the electric explosion of a fine tungsten wire in vacuum and the shunting breakdown accompanying this explosion.

A comparison of the experimental results on the explosion of tungsten wires in vacuum with the results of test experiments on the breakdown of a gas-filled gap has shown that the breakdown along a wire is similar in many respects to the gas breakdown. A method has been proposed that takes into account the thermal expansion of the desorbed gas and makes it possible to

quite exactly determine the instant at which the shunting breakdown along a wire occurs.

The experimental results have shown that the insulation of both the electrodes and the wire surface near the electrodes makes it possible to avoid breakdown along the wire and to increase the deposited energy to values sufficient for the wire sublimation.

ACKNOWLEDGMENTS

We are grateful to Yu.D. Korolev, D.I. Proskurovskiĭ, and G.Yu. Yushkov for helpful discussions of the manuscript. This work was supported in part by the International Science and Technology Center, project no. 1826.

REFERENCES

1. R. B. Spielman, C. Deeney, G. A. Chandler, *et al.*, Phys. Plasmas **5**, 2105 (1998).
2. J. P. Apruzese, P. E. Pulsifer, J. Davis, *et al.*, Phys. Plasmas **5**, 4476 (1998).
3. C. Deeney, C. A. Coverdale, M. R. Douglas, *et al.*, Phys. Plasmas **6**, 2081 (1999).
4. I. H. Mitchell, J. M. Bayley, J. P. Chittenden, *et al.*, Rev. Sci. Instrum. **67**, 1533 (1996).
5. V. V. Alexandrov, I. N. Frolov, M. V. Fedulov, *et al.*, IEEE Trans. Plasma Sci. **30**, 559 (2002).
6. T. A. Shelkovenko, S. A. Pikuz, D. B. Sinars, *et al.*, Phys. Plasmas **9**, 2165 (2002).
7. D. B. Sinars, Min Hu, K. M. Chandler, *et al.*, Phys. Plasmas **8**, 216 (2001).
8. S. M. Karakhanov, Zh. Tekh. Fiz. **48**, 1474 (1978) [Sov. Phys. Tech. Phys. **23**, 832 (1978)].
9. D. B. Sinars, T. A. Shelkovenko, S. A. Pikuz, *et al.*, Phys. Plasmas **7**, 429 (2000).
10. V. S. Sedoi, G. A. Mesyats, V. I. Oreshkin, *et al.*, IEEE Trans. Plasma Sci. **27**, 845 (1999).
11. A. G. Rousskikh, R. B. Baksht, V. I. Oreshkin, and A. V. Shishlov, in *Proceedings of the 5th International Conference on Dense Z-Pinches, Albuquerque, 2002*; AIP Conf. Proc. **651**, 217 (2002).
12. S. M. Karakhanov and V. V. Polyudov, Zh. Tekh. Fiz. **41**, 1430 (1971) [Sov. Phys. Tech. Phys. **16**, 1125 (1972)].
13. S. V. Lebedev and A. I. Savvatimskiĭ, Usp. Fiz. Nauk **144**, 215 (1984) [Sov. Phys. Usp. **27**, 749 (1984)].
14. V. N. Ageev, N. I. Ionov, and Yu. K. Ustinov, Zh. Tekh. Fiz. **34**, 546 (1964) [Sov. Phys. Tech. Phys. **9**, 424 (1964)].
15. A. V. Arutyunov and L. P. Filipov, Teplofiz. Svoĭstva Veshch. Mater., No. 5 (1971).
16. S. V. Koval', N. I. Kuskova, and S. I. Tkachenko, Teplofiz. Vys. Temp. **35**, 876 (1997).
17. P. Felsenthal and J. M. Praud, Phys. Rev. A **139**, 1796 (1965).
18. Yu. D. Korolev and G. A. Mesyats, *The Physics of Pulsed Gas Breakdown* (Nauka, Moscow, 1991).
19. V. I. Oreshkin, V. S. Sedoĭ, and L. I. Chemezova, Prikl. Fiz., No. 3 (2001).
20. V. S. Vorob'ev, P. R. Levashov, I. V. Lomonosov, *et al.*, Preprint No. 1-448 (Associated Institute for High Temperatures, Russian Academy of Sciences, Moscow, 2000).

Translated by E.L. Satunina

Plasma Physics Reports, Vol. 30, No. 11, 2004, pp. 953–961. Translated from Fizika Plazmy, Vol. 30, No. 11, 2004, pp. 1025–1034.

LOW-TEMPERATURE PLASMA

Theoretical Investigation of the Bistability Effect in Non-Self-Sustained Discharges in Kr and Ar

N. A. Dyatko and A. P. Napartovich

Troitsk Institute for Innovation and Fusion Research, Troitsk, Moscow oblast, 142190 Russia

Received October 21, 2003; in final form, January 5, 2004

Abstract—The electron energy distribution function and the related plasma parameters in non-self-sustained discharges in Kr and Ar are studied theoretically. The investigations are carried out by numerically solving the corresponding Boltzmann equation for the electron energy distribution function with allowance for electron–electron collisions. The electron energy distribution and electron density are calculated self-consistently as functions of the intensity q of the source of secondary electrons and the magnitude of the reduced electric field E/N. The main goal of the investigations was to determine the conditions under which the plasma exhibits bistable parameters. Calculations show that, for discharges in Kr, there is a certain range of q and E/N values in which the Boltzmann equation has two different stable solutions. For an Ar plasma, such a bistability effect was not found: over the parameter range under consideration, the Boltzmann equation has a unique solution. Various plasma parameters (such as the effective electron temperature, electron drift velocity, and electron current density) are calculated for different discharge conditions, including those corresponding to the bistability effect.

1. INTRODUCTION

The possible effect of bistability of the parameters of a weakly ionized plasma was previously discussed in [1–10]. This phenomenon was predicted for plasmas of heavy noble gases in weak electric fields [1–5] and for afterglow plasmas in an $Ar : N_2$ gas mixture [6, 7] and in N_2 [8–10]. In addition, the bistability effect was investigated theoretically in [11] for positron swarms in a He plasma.

Gerasimov *et al.* [1] analyzed the bistability effect under the assumption that the electron energy distribution function (EEDF) is Maxwellian. They showed that, in a certain range of E/N values, the equation for the electron temperature has three steady solutions, two of which are stable. This result is attributed to the specific shape of the transport cross sections for electron scattering by the atoms of heavy noble gases. Ivanov and Prikhod'ko [2] studied the bistability of the EEDF by solving a simplified Boltzmann equation with allowance for electron–electron (e–e) collisions. In our recent paper [3], the bistability effect was investigated by numerically solving the Boltzmann equation with the use of modern data on transport cross sections for electron scattering by xenon and krypton atoms. It follows from [2, 3] that, in a certain range of parameters (namely, the reduced electric field E/N and the degree of ionization), the Boltzmann equation has two stable solutions. It should be noted that, in the calculations carried out in the cited papers, the electron density was treated as an independent parameter. Since the bistability effect persists at low values of the parameter E/N (for, e.g., a Xe plasma, it is as low as ~0.03 Td), the situation considered in [1–3] corresponds to the conditions of a decaying plasma.

In our earlier papers [4, 5], we investigated the possible existence of bistability effect in a Xe plasma under steady-state conditions. We considered the conditions corresponding to a non-self-sustained discharge (i.e., a discharge sustained by a beam of fast electrons) and numerically solved the relevant Boltzmann equation for the EEDF with allowance for e–e collisions. The EEDF and electron density were computed self-consistently as functions of the intensity of the source of secondary electrons and the magnitude of the reduced electric field. It was found that, in a certain range of the parameters q and E/N, the Boltzmann equation has two stable solutions. It should be stressed that the physical conditions considered in [4, 5] are radically different from those treated earlier in [1–3]: on the one hand, for a non-self-sustained electroionization discharge, the electron density is not an independent parameter and, on the other hand (and more importantly), the heating of the plasma electrons is governed not only by the electric field but also by the energy input from the fast electron beam.

Here, we investigate the possible existence of the bistability effect in Kr and Ar plasmas under steady-state conditions. All the simulations are carried out for a discharge sustained by a fast electron beam. In essence, the present work is a continuation of [4, 5].

2. MODEL CONDITIONS

We consider a homogeneous plasma created by a fast electron beam in the presence of an external elec-

1063-780X/04/3011-0953$26.00

tric field. All the simulations were carried out for a gas temperature of 300 K and at atmospheric pressure (760 torr). The reduced electric field was varied within the range E/N = 0–0.04 Td. For these values of the parameter E/N, the gas atoms are ionized exclusively by the beam electrons. The process of ionization of a gas by a steady-state fast electron beam (including cascade ionization processes) are characterized by the production rate of the secondary electrons. For a particular gas mixture, this rate can be estimated from a given density and energy of the beam electrons. It is the production rate of the secondary electrons that was considered as an independent variable parameter in our investigations.

The secondary electrons lose their energy in elastic and inelastic collisions and disappear when recombining with positive ions. A plasma with a steady ionization source relaxes to a steady state with a certain electron density and electron energy spectrum. If the intensity of the source of secondary electrons is not too high, then the mean energy of the plasma electrons is substantially lower than the ionization potential of the gas atoms. In this case, the plasma electrons can be characterized by the low-energy part of the EEDF in the range from zero energy to the ionization potential I. In what follows, the term EEDF will be used precisely for this part of the electron energy spectrum. In our investigations, we were interested exclusively in fairly low intensities of the source of secondary electrons (10^{13}–10^{17} cm^{-3} s^{-1}) and, accordingly, calculated only the low-energy part of the electron energy spectrum. We also assumed that the main plasma ions were molecular ions, the concentration of which was equal to the electron density.

3. BOLTZMANN EQUATION FOR THE EEDF IN A NON-SELF-SUSTAINED ELECTROIONIZATION DISCHARGE

Since we are considering fairly weak electric fields, we can assume that the electron velocity distribution in the plasma is nearly isotropic; this allows us to describe the distribution function in the so-called two-term approximation. Under the above conditions, the corresponding time-independent Boltzmann equation for the symmetric part of the electron distribution function can be written as

$$I_E(n_e f) + qS(u) + \mathrm{St}(n_e f) = 0. \quad (1)$$

Here, n_e is the electron density, u is the energy of an electron, $f(u)$ is the symmetric part of the distribution function, the term $I_E(n_e f)$ describes the heating of the plasma electrons by the electric field, the term $qS(u)$ accounts for a source that produces electrons with energies lying within the interval $0 \le u \le I$ and has the energy spectrum $S(u)$ and intensity q, and $\mathrm{St}(n_e f)$ is the collision integral. The function $f(u)$ is normalized according to the condition

$$\int_0^I \sqrt{u} f(u) du = 1,$$

the normalization condition for the energy spectrum of the source of secondary electrons being

$$\int_0^I S(u) du = 1.$$

The collision integral is represented as

$$\mathrm{St}(n_e f) = \mathrm{St}_{e-e}(n_e f) + \mathrm{St}_{el}(n_e f) + \mathrm{St}_{ex}(n_e f) + \mathrm{St}_{rec}(n_e f), \quad (2)$$

where the terms on the right-hand side describe e–e collisions, elastic electron scattering by atoms, electron impact excitation of the electronic levels of the atoms, and dissociative recombination of electrons with molecular ions, respectively. A detailed description of the terms $I_E(n_e f)$ and $\mathrm{St}(n_e f)$ can be found, e.g., in [12].

The equation for the electron density is obtained by integrating Eq. (1) over the energy:

$$q - n_e^2 \alpha_r = 0, \quad (3)$$

where α_r is the recombination rate constant.

4. CHOICE OF THE CROSS SECTIONS AND THE ENERGY SPECTRUM OF THE SOURCE OF SECONDARY ELECTRONS

The transport cross sections for electron scattering by Kr and Ar atoms are taken from the paper by Pack *et al.* [13]. The investigations carried out in [13] showed a remarkably good agreement between the calculated results and the experimental data on transport cross sections for electrons in Kr and Ar discharge plasmas over a wide range of E/N values. In particular, this concerns the range of weak electric fields, which is the subject of our analysis. The transport cross sections used in our simulations are presented in Fig. 1.

The cross sections for the electronic excitation of Kr atoms are taken from [14] and those for Ar atoms are taken from [15]. In the present work, we do not make a detailed analysis of the ion content of the plasma and, accordingly, describe the dissociative recombination of electrons with molecular ions of different species in terms of a single effective cross section whose energy dependence was chosen to have the form Au^{-1}. For such a shape of the cross section, the recombination rate constant depends on the electron temperature T_e as $\alpha_r \sim T_e^{-1/2}$, which agrees with both theoretical and experimental data [16]. For most of our calculations, the normalizing coefficient A was chosen to correspond to

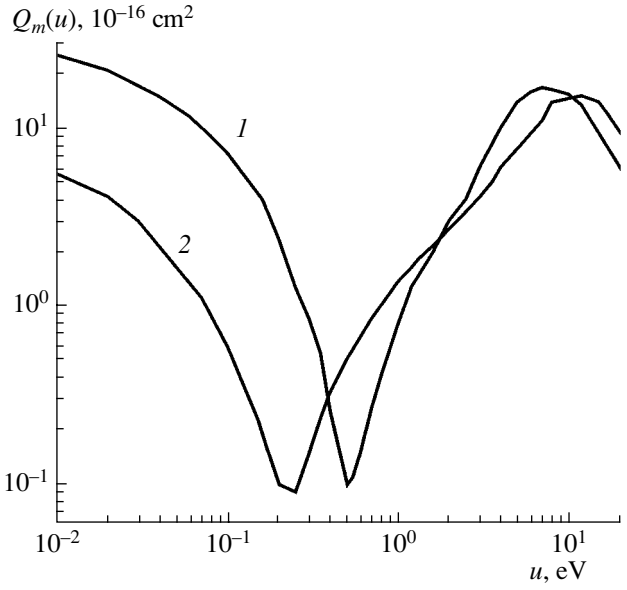

Fig. 1. Transport cross sections used in simulations of (*1*) a krypton and (*2*) an argon plasma.

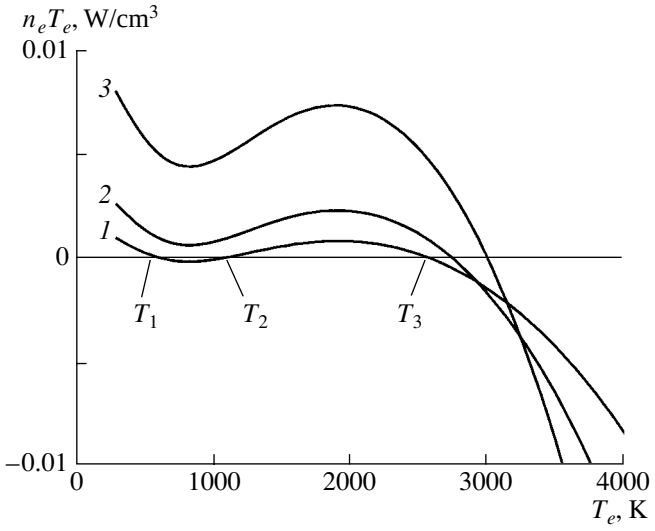

Fig. 2. Model of a Maxwellian EEDF: the function $\Phi(n_eT_e)$ was calculated for a krypton plasma at E/N = 0.01 Td and q = (*1*) 10^{15}, (*2*) 3×10^{15}, and (*3*) 10^{16} cm^{-3} s^{-1}.

$\alpha_r = 1.2 \times 10^{-6}$ cm^3 s^{-1} (for a krypton plasma) and $\alpha_r = 7 \times 10^{-7}$ cm^3 s^{-1} (for an argon plasma) at T_e = 300 K. These α_r values refer to the recombination of electrons with Kr_2^+ and Ar_2^+ ions, respectively [16]. In order to estimate how much the final results depend on the value of the effective cross section for dissociative recombination, we carried out additional test computations in which this cross section was increased by a factor of 1.6 for an argon plasma and 2 for a krypton plasma.

The energy spectrum of the source of secondary electrons with energies lying in the range $0 \le u \le I$ can be obtained by integrating the expression for the differential ionization cross section with a known high-energy ($u > I$) part of the electron energy spectrum that forms in a beam plasma (the degradation spectrum). It is in this way that the energy spectrum $S(u)$ was calculated in [17] for an argon plasma with the use of the degradation spectrum obtained in [18]. Following [17], the energy spectrum of the source of electrons $S(u)$ was chosen to be triangular in shape,

$$S(u) = \frac{2}{I_{\mathrm{Ar}}}\left(1 - \frac{u}{I_{\mathrm{Ar}}}\right), \qquad (4)$$

where I_{Ar} is the ionization potential of an Ar atom. Most of the calculations were carried out for the energy spectrum $S(u)$ given by expression (4) with I_{Ar} (or with I_{Kr} for a Kr plasma). In order to estimate how the shape of $S(u)$ affects the final results, we carried out additional test computations, in which the secondary electrons were assumed to be distributed uniformly over the energy range $0 \le u \le I$.

5. RESULTS AND DISCUSSIONS

5.1. Model Approach with the Use of a Maxwellian EEDF

In order to qualitatively explain how the bistability arises in a non-self-sustained discharge, let us consider a simplified model with a Maxwellian EEDF: $f(u) \sim \exp(u/T_e)$. In this case, the time-dependent equation for the electron temperature can be written in the form

$$\frac{d(n_eT_e)}{dt} = \Phi(n_eT_e, q, E/N) = H(n_eT_e, q, E/N) - L(n_eT_e, q, E/N), \qquad (5)$$

where the function H accounts for the heating of plasma electrons by the electric field and by the beam of fast electrons and the function L accounts for the electron energy loss in elastic and inelastic collisions. For given q and E/N values, the function $\Phi(T_e)$ can be calculated by multiplying Eq. (1) by u and by integrating the resulting equation over energy. Figure 2 shows the function $\Phi(T_e)$ calculated for a Kr plasma at E/N = 0.01 Td and at different intensities of the source of secondary electrons. It can be seen that the function $\Phi(T_e)$ is nonmonotonic. Moreover, for $q \le 10^{15}$ cm^{-3} s^{-1}, the function $\Phi(T_e)$ vanishes at three points, $T_1 < T_2 < T_3$. This indicates that Eq. (5) has three steady solutions, two of which, $T_e = T_1$ and $T_e = T_3$, are stable because, at these points, we have $\delta\Phi/\delta T_e < 0$. According to our simulations, the bistability effect can occur at arbitrarily low intensities of the source of secondary electrons, down to $q = 0$. Note that the limiting case $q = 0$ corresponds to the situation that was considered in [1].

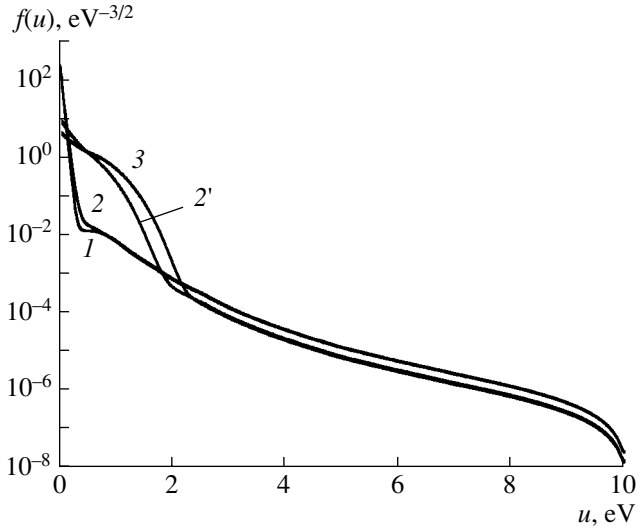

Fig. 3. EEDF in a non-self-sustained electroionization discharge in Kr for $q = 10^{15}$ cm^{-3} s^{-1} and E/N = (*1*) 0.005, (*2*, *2*') 0.012, and (*3*) 0.02 Td.

A detailed analysis of the terms $H(T_e)$ and $L(T_e)$ shows that the existence of two stable solutions in the range of low electron temperatures ($T_e = T_1$ and $T_e = T_2$) is attributed to a sharp decrease in the transport cross section $Q_m(u)$ in the energy range between 0 and 0.5 eV (see Fig. 1). The rate of loss of the electron energy in elastic collisions, L_m, is proportional to $Q_m(u)$, while the rate of heating of the electrons by the electric field, H_E, is inversely proportional to $Q_m(u)$. Simulations show that it is the relationship between $L_m(T_e)$ and $H_E(T_e)$ that gives rise to the bistability effect, which, moreover, can occur only when the energy input into a plasma with a low electron temperature T_e from the electric field is higher than or comparable to that from the fast electron beam. Since the energy input from the electric field is proportional to $\sim n_e \sim q^{1/2}$ and that from the fast electron beam is proportional to $\sim q$, the bistability effect persists only at relatively low q values and does not take place at higher intensities of the source of secondary electrons (Fig. 2; curves *2*, *3*).

Although the EEDF in an actual plasma is non-Maxwellian, the results obtained in this section indicate that, with allowance for e–e collisions, the Boltzmann equation can have two stable solutions because it is these collisions that cause the electron energy distribution to become Maxwellian. When e–e collisions are taken into account, Eq. (1) is nonlinear and, thus, can have two or more stable solutions.

5.2. Numerical Solution of the Boltzmann Equation

Boltzmann equation (1) was solved iteratively together with Eq. (3) for the electron density; in other words, the EEDF $f(u)$ and electron density n_e were calculated self-consistently. The initial approximation to $f(u)$ was chosen to be a Maxwellian EEDF with a given electron temperature T_{e0}. In the case of a unique solution, the iterative procedure converges to it for any reasonable T_{e0} value. In the case of two solutions (bistability), the iterative procedure converges to one of them for $T_{e0} > T_e^*$ and to the other for $T_{e0} < T_e^*$, where T_e^* is a certain boundary value of the electron temperature. The Boltzmann equation was solved on an energy interval from zero energy to the ionization potential. In some cases, however, the mean electron energy was very low, and, in order to achieve the reasonable accuracy of computations, it was necessary to divide the interval of integration into very many subintervals, which requires a large amount of computer time. This difficulty was overcome by using a nonuniform numerical grid on the energy axis, namely, a grid that becomes progressively finer toward zero energy.

5.2.1. Results for Kr. Figure 3 shows the EEDFs calculated for a Kr plasma at $q = 10^{15}$ cm^{-3} s^{-1} and at different E/N values. Calculations show that, for E/N = 0.005 and 0.02 Td, the Boltzmann equation has a unique solution (curves *1*, *3*). For E/N = 0.012 Td, there are two different stable solutions (curves *2*, *2*'). We also see that, in the range of low energies, the EEDF is close in shape to a Maxwellian function. In what follows, the EEDF will be characterized by the effective electron temperature $T_e = 2/3u_m$, where u_m is the mean electron energy.

Figure 4a shows the effective electron temperature calculated for different values of q and of E/N. Let us first consider the results obtained for $q = 10^{13}$ cm^{-3} s^{-1} (Fig. 4a, curve *1*). For $E/N < 0.01$ Td, the effective electron temperature T_e depends slightly on E/N and lies in the range 340–440 K. As E/N is increased from 0.01 to 0.014 Td, the effective electron temperature increases gradually to 900 K. As E/N is increased from 0.014 to 0.018 Td, the temperature T_e increases sharply from 900 to 3000 K. As E/N is further increased, the effective electron temperature again increases relatively gradually. In the range $10^{16} \geq q \geq 10^{14}$ cm^{-3} s^{-1} of intensities of the source of secondary electrons, the dependence $T_e(E/N)$ exhibits a different behavior (Fig. 4a; curves *2*, *3*, *4*). In this case, the Boltzmann equation has two stable solutions in a narrow range of E/N values. Thus, for $q = 10^{15}$ cm^{-3} s^{-1} (Fig. 4a, curve *3*), the bistability occurs for $0.011 \leq E/N \leq 0.0122$ Td; moreover, the calculated T_e values are very different: 550 and 2500 K, respectively. For $q > 10^{16}$ cm^{-3} s^{-1}, there is no bistability: the effective electron temperature is seen to increase monotonically with E/N (Fig. 4a, curve *5*). Note also that, for a krypton plasma, the bistability manifests itself at weaker electric fields ($E/N \sim 0.012$ Td) than it does for a xenon plasma ($E/N \sim 0.03$ Td) [4, 5].

Figures 4b–4d show the calculated electron drift velocity w, electron density, and electron current density. Like the effective electron temperature, these

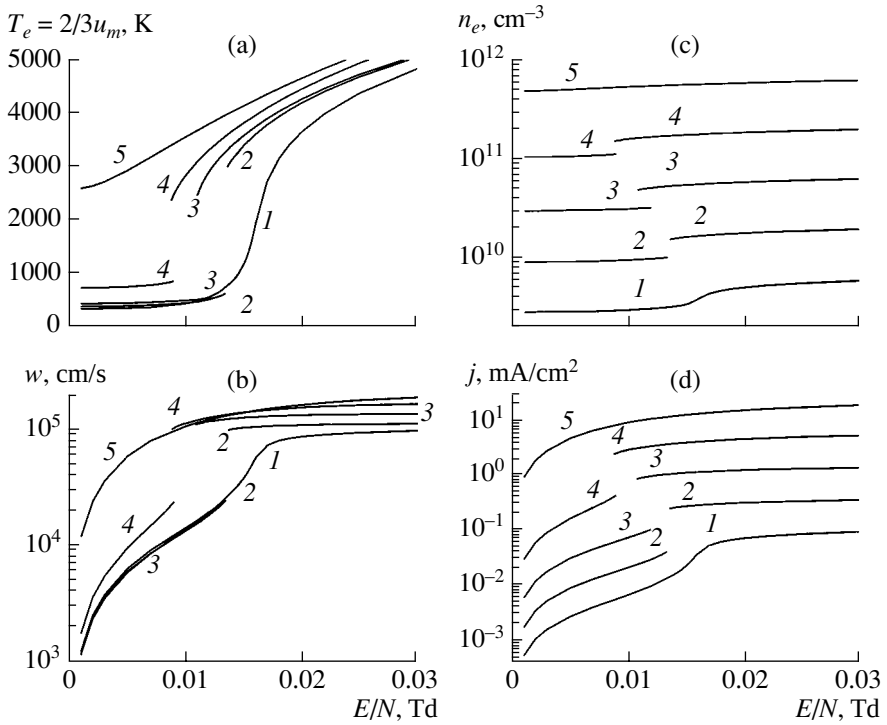

Fig. 4. Plasma parameters in a non-self-sustained electroionization discharge in Kr: (a) effective electron temperature, (b) electron drift velocity, (c) electron density, and (*4*) electron current density. The calculations were carried out for q = (*1*) 10^{13}, (*2*) 10^{14}, (*3*) 10^{15}, (*4*) 10^{16}, and (*5*) 10^{17} cm^{-3} s^{-1}.

parameters also change in a jumplike manner within the range of electric fields that correspond to bistability. Thus, for $q = 10^{15}$ cm^{-3} s^{-1}, the electron drift velocity increases by a factor of seven. In this case, however, the electron density changes by a substantially smaller amount (by a factor of only about 1.6); this is explained by the weak dependence of the density n_e of the electrons on their temperature, $n_e \sim \alpha_r^{-0.5} \sim T_e^{0.25}$. From the experimental viewpoint, the variation of the discharge current density is more interesting. Since $j \sim n_e w$, the current density changes by a factor of more than 10; such a large change is easy to measure experimentally.

It is also of interest to compare the energy input to the plasma from the electric field with that from the fast electron beam. Fig. 5 shows the ratio of these energy inputs calculated as a function of E/N and q for the conditions adopted here. From Fig. 5, we can see that, in the range of weak electric fields, the energy input from the fast electron beam dominates, whereas the range of energies above those at which the discharge current changes in a jumplike manner is dominated by the energy input from the electric field.

From the standpoint of possible future experiments, it is important to know how the bistability effect is sensitive to any impurities that may be present in krypton. One of the most probable impurities is nitrogen. This is why, in order to estimate the concentrations at which the bistability ceases to occur, we considered a Kr plasma with a nitrogen admixture. The effect of the admixture was taken into account by incorporating the processes of electron scattering by nitrogen molecules. The cross sections for these processes were taken from [6]. The calculations were carried out for $q = 10^{15}$ cm^{-3} s^{-1} and for different nitrogen concentrations. The calculated results are illustrated in Fig. 6. We can see that, for a krypton plasma with a nitrogen admixture, the upper portions of the plots of the effective electron temperature are lower than those in the absence of nitrogen, while the lower portions essentially coincide. As the nitrogen concentration is increased, the range where the bistability takes place becomes narrower and is displaced toward higher E/N values. At relative nitrogen concentrations higher than 0.3%, the effective electron temperature T_e does not exhibit any jumplike behavior. Such a level of impurities can easily be controlled in experiments.

We also point out a certain qualitative difference between the results obtained in this section and the results calculated for a Maxwellian EEDF. It was already mentioned above that, in the model of a Maxwellian EEDF, the bistability takes place in the range $0 \le q < q^*$. On the other hand, an analysis based on solving the Boltzmann equation shows that the bistability effect manifests itself in the range $0 < q_1 < q < q_2$; i.e., the bistability ceases to occur for $q < q_1$. This is presumably explained by the fact that, at low electron den-

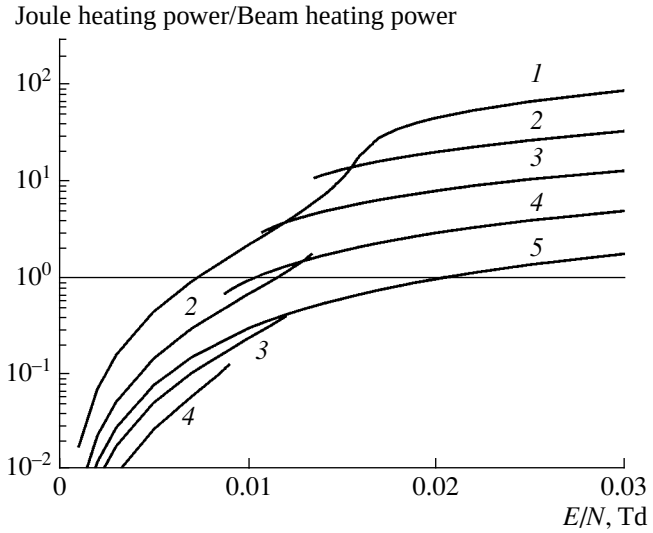

Fig. 5. Ratio of the Joule heating power to the power input from a fast electron beam in a non-self-sustained electroionization discharge in Kr for q = (*1*) 10^{13}, (*2*) 10^{14}, (*3*) 10^{15}, (*4*) 10^{16}, and (*5*) 10^{17} cm^{-3} s^{-1}.

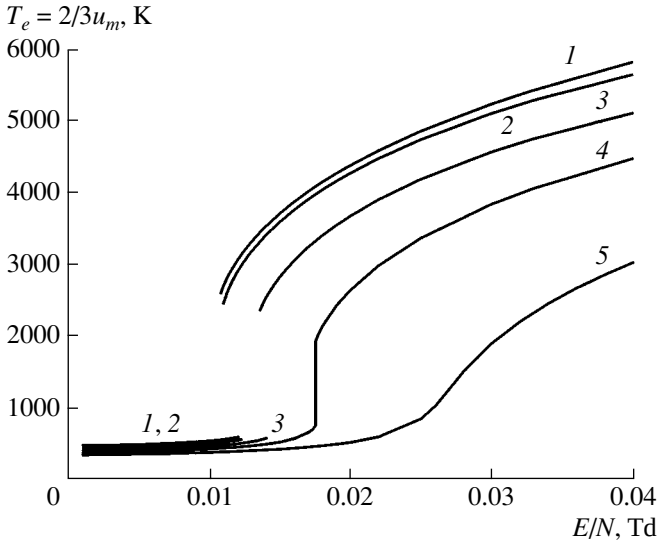

Fig. 6. Effective electron temperature in a non-self-sustained electroionization discharge in Kr : N_2 mixtures for $q = 10^{15}$ cm^{-3} s^{-1}: (*1*) pure Kr, (*2*) Kr + 0.01% N_2, (*3*) Kr + 0.1% N_2, (*4*) Kr + 0.3% N_2, and (*5*) Kr + 1% N_2.

sities, e–e collisions (i.e., those that are responsible for the onset of bistability) have an insignificant effect on the formation of the EEDF.

5.2.2. Results for Ar. The results calculated for Ar are demonstrated in Fig. 7. Figure 7a shows the effective electron temperature calculated for different values of q and E/N. We first consider the results obtained for $q = 10^{13}$ cm^{-3} s^{-1} (Fig. 7a, curve *1*). For $E/N < 0.001$ Td, the temperature T_e is almost independent of E/N and is approximately equal to 320 K. In the range of E/N values from 0.001 to 0.002 Td, the effective electron temperature increases gradually up to 500 K. For E/N values between 0.002 and 0.003 Td, the temperature T_e increases sharply from 500 to 1200 K. As E/N is further increased, the effective electron temperature again increases relatively gradually. It should be noted that the dependence $T_e(E/N)$ just described agrees qualitatively with the dependence $T_e(E/N)$ calculated for krypton at $q = 10^{13}$ cm^{-3} s^{-1} (Fig. 4a, curve *1*). The only difference is that the effective electron temperature T_e increases abruptly in the range of stronger electric fields. For higher values of the parameter q, the results obtained for argon differ qualitatively from those obtained for krypton: in an argon plasma, the effective electron temperature increases monotonically and continuously with the electric field. In other words, over the entire range of the q and E/N values under consideration, the Boltzmann equation has a unique solution.

It is evident that the above difference between the results obtained for Kr and for Ar is associated primarily with the difference between the corresponding transport cross sections. As may be seen from Fig. 1, these cross sections are very different. On the one hand, in the range of low energies, the cross section $Q_m(u, \mathrm{Ar})$ is much smaller than $Q_m(u, \mathrm{Kr})$. On the other hand, the energy at which the cross section $Q_m(u, \mathrm{Ar})$ has a minimum ($u \sim 0.25$ eV) is lower than that for $Q_m(u, \mathrm{Kr})$ ($u \sim 0.5$). In the analysis of the electron temperature in Kr in terms of a Maxwellian EEDF, it was noted that the bistability effect is attributed in part to the descending portion of the transport cross section. For Ar, this portion is less pronounced (the cross section is descending over a narrower energy range—from 0 to 0.25 eV) than that for Kr.

5.3. Further Comments

Recall that the energy spectrum of the source of electrons was chosen to be triangular in shape. In order to estimate how the shape of $S(u)$ affects the final results, we carried out additional test computations in which the energy spectrum of the source of secondary electrons was assumed to be uniform over the energy range $0 \le u \le I$. It was found that, even with such different shapes of the energy spectrum $S(u)$, the calculated values of the plasma parameters were nearly the same.

There is also a certain amount of uncertainty in the choice of the values of rate constants for recombination of electrons with molecular ions (the recombination cross sections). Let us recall that the rate constants used in simulations correspond to the processes of recombination of electrons with Ar_2^+ and Kr_2^+ ions. These processes have been studied fairly well. In a plasma, however, not only double ions but also triple Ar_3^+ and Kr_3^+ ions are produced. Unfortunately, the literature data on the rate constants for recombination of electrons with

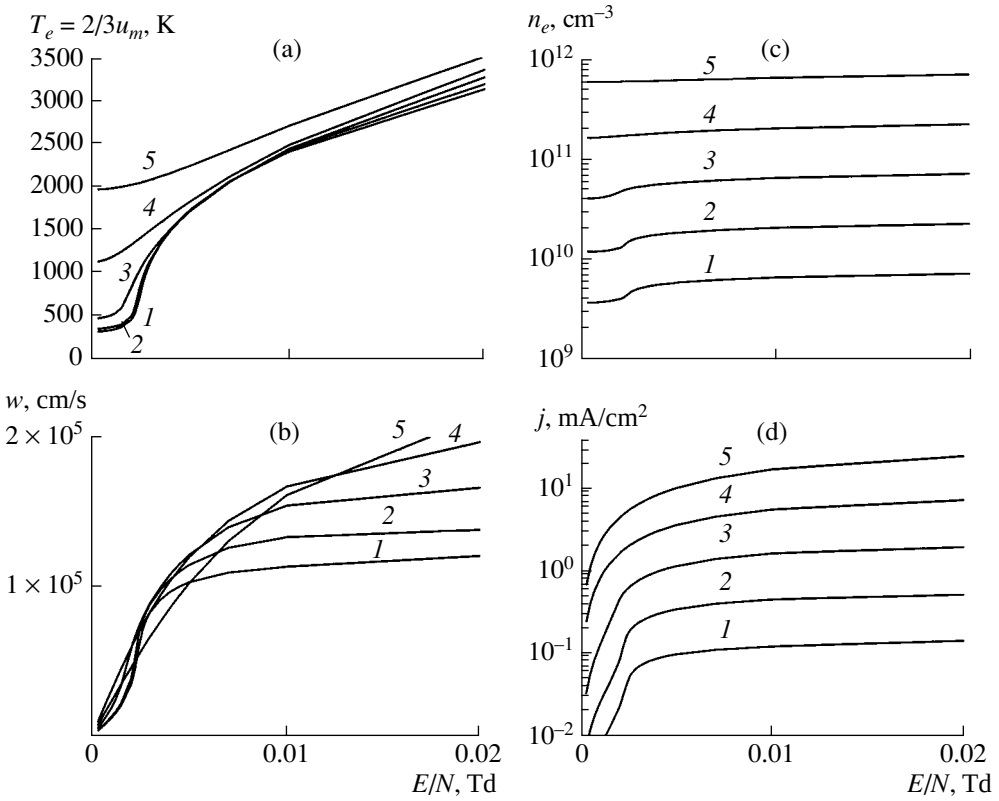

Fig. 7. Plasma parameters in a non-self-sustained electroionization discharge in Ar: (a) effective electron temperature, (b) electron drift velocity, (c) electron density, and (*4*) electron current density. The calculations were carried out for q = (*1*) 10^{13}, (*2*) 10^{14}, (*3*) 10^{15}, (*4*) 10^{16}, and (*5*) 10^{17} cm^{-3} s^{-1}.

triple ions are very poor. Thus, Elson and Rokni [19] obtained the following value (with an accuracy of 50%) of the rate constant for recombination of electrons with Ar_3^+ ions: $\alpha_3 = 1.6 \times 10^{-7} T_e^{-0.54}$ cm^3 s^{-1}, where T_e is the electron temperature in eV; i.e., the rate constant for recombination with Ar_3^+ ions exceeds the rate constant for recombination with Ar_2^+ ions, which was used in our calculations, by a factor of only 1.6. Simulations show that the increase in the recombination rate constant in an argon plasma by a factor of 1.6 leads merely to an insignificant quantitative change in the final results.

As for the recombination of electrons with Kr_3^+ ions, we note that Eckstrom *et al.* [20] modeled the ion–molecular kinetics of a krypton plasma by using the recombination rate constant $\alpha_3 = 4.9 \times 10^{-5} T_e^{-0.5}$ cm^3 s^{-1}, where the electron temperature T_e is in eV. This value is 250 times (!) greater than the rate constant for recombination of electrons with Kr_2^+ ions and would seem to be incorrect. We carried out test simulations in which the rate constant for electron recombination in a krypton plasma (the recombination cross section) was increased by a factor of 2 and obtained qualitatively the same results: as before, the bistability was found to persist, but over a somewhat narrower range of E/N values.

In our theoretical model, the processes involving excited M* atoms were ignored. The excited M* atoms affect the kinetics of the plasma electrons through the following processes:

(i) electron heating in superelastic collisions,

$$M^* + e \longrightarrow M + e; \quad (6)$$

(ii) electron production in chemoionization processes,

$$M^* + M^* \longrightarrow M + M^+ + e,$$
$$k(\mathrm{Ar}) = 1.2 \times 10^{-9} \text{ cm}^3 \text{ s}^{-1} \text{ [21]}, \quad (7)$$
$$k(\mathrm{Kr}) = 1.1 \times 10^{-9} \text{ cm}^3 \text{ s}^{-1} \text{ [21]};$$

(iii) electron-impact ionization of the excited atoms,

$$M^* + e \longrightarrow M^+ + e + e. \quad (8)$$

It is obvious that the role played by these processes in the formation of the EEDF depends on the concentration of M* atoms. The excited atoms are produced in the reactions of dissociative recombination of the plasma electrons with the M_2^+ ions,

$$M_2^+ + e \longrightarrow M^* + M$$

and in the excitation of atoms by the beam electrons. Consequently, under steady-state conditions, the total production rate of M* atoms is of the same order of magnitude as q. The excited atoms M* are quenched mainly in the processes

$$M^* + M + M \longrightarrow M_2^* + M,$$

$$k(\mathrm{Ar}) \approx 10^{-32}\ \mathrm{cm}^6\ \mathrm{s}^{-1}\ [22],$$

$$k(\mathrm{Kr}) \approx 3 \times 10^{-32}\ \mathrm{cm}^6\ \mathrm{s}^{-1}\ [22],$$

in particular, with allowance for the rapid radiative decay of dimers. Calculations show that, under the conditions in question, the steady-state concentration of the excited M* atoms is much lower than the electron density. For example, for Kr at $q = 10^{15}\ \mathrm{cm}^{-3}\ \mathrm{s}^{-1}$, the electron density is approximately equal to $(3–5) \times 10^{10}\ \mathrm{cm}^{-3}$, while the concentration of M* atoms is only about $10^8\ \mathrm{cm}^{-3}$. Simple estimates show that, for such concentrations of the excited atoms, processes (6)–(8) have essentially no impact on the formation of the EEDF. Nevertheless, we carried out additional test calculations in which we incorporated the above processes into the Boltzmann equation and regarded the concentration of M* atoms as an independent parameter. The results of these calculations support the conclusion drawn from simple estimates.

As was mentioned above, the rate of production of the secondary electrons in a gas is determined by the parameters of the fast electron beam. If these parameters are specified, then the rate q can be estimated, e.g., from the approximating formulas presented in [23]. Our estimates show that, in order to reach values of about $q = 10^{15}–10^{16}\ \mathrm{cm}^{-3}\ \mathrm{s}^{-1}$ in a krypton plasma under the conditions adopted here, the current density of the fast electron beam should be about $j_b \approx 0.4–4\ \mu\mathrm{A\ cm}^{-2}$. These estimates were made for an initial beam electron energy of 300 keV under the assumption that the electron gun was equipped with a 10-μm aluminum foil.

In our calculations and estimates, we fairly reliably determined the conditions under which the bistability can persist in krypton ($P = 760$ torr, $T = 300$ K, $j_b \approx 0.4–4\ \mu\mathrm{A\ cm}^{-2}$, $E/N \approx 0.012$ Td). We may expect that it is quite possible to achieve these conditions in experiments. One such experiment could be aimed at measuring the current–voltage characteristic $I(V)$. The voltage applied to the discharge gap should ensure the desired values of the reduced electric fields in the plasma, 0–0.4 Td. The bistability effect will manifest itself as a step in the dependence $I(V)$ at a certain voltage V. Another possible approach is to investigate the effects associated with transitions between two states of the system. Thus, if the discharge gap is subject to an alternating electric field with a certain amplitude and frequency, then the current will behave differently in response to an increase and a decrease in the applied voltage.

The range of E/N and q values at which a krypton plasma exhibits bistability was calculated for a given atomic number density N, which is determined by the pressure of the gas and its temperature. It can be shown that the results obtained are universal in terms of the two parameters, E/N and q/N^2. For a fixed energy of the beam electrons, the latter parameter can be rewritten as j_b/N. These parameters make it possible to calculate the E and q values at which the bistability effect takes place for given values of the gas pressure and gas temperature.

6. CONCLUSIONS

We have performed a theoretical study of the EEDF and the related parameters of the plasma of a non-self-sustained electroionization discharge in krypton and in argon. The investigations were carried out by numerically solving the Boltzmann equation for the EEDF with allowance for e–e collisions. The EEDF and electron density were calculated self-consistently for a given production rate of the secondary electrons and for a given electric field under the assumption that the density of the electrons is determined by their dissociative recombination with molecular ions. It was shown that, for a krypton plasma, the Boltzmann equation has two different stable solutions in a certain range of the parameters q and E/N. For an argon plasma, the Boltzmann equation has a unique solution over the entire parameter range under study. We also calculated the relevant plasma parameters—the effective electron temperature, electron drift velocity, and plasma current density. Our calculations showed that, in a plasma exhibiting the bistability effect, the difference between two possible values of the plasma current density is large enough to be easily measured in experiments. We have analyzed the sensitivity of the bistability effect to the presence of a nitrogen admixture in krypton and have shown that this effect ceases to occur only when the relative nitrogen concentration is fairly high (≥0.3%). We have also demonstrated that, under the conditions adopted, the excited atoms have essentially no impact on the formation of the EEDF. We have estimated the parameters of a fast electron beam that are required to create the conditions under which the bistability is predicted to occur in an atmospheric-pressure krypton plasma at a temperature of 300 K. According to our estimates, the current density of the fast electron beam should be about $j_b \sim 0.4–4\ \mu\mathrm{A\ cm}^{-2}$ for a beam energy of 300 keV and for a 10-μm aluminum foil in the electron gun.

ACKNOWLEDGMENTS

This work was supported in part by the Russian Foundation for Basic Research, project no. 00-02-17662.

REFERENCES

1. G. N. Gerasimov, M. N. Maleshin, and S. Ya. Petrov, Opt. Spektrosk. **59**, 930 (1985).
2. V. A. Ivanov and A. S. Prikhod'ko, Zh. Tekh. Fiz. **56**, 2010 (1986) [Sov. Phys. Tech. Phys. **31**, 1202 (1986)].
3. N. A. Dyatko and A. P. Napartovich, in *Proceedings of the 15th European Conference on the Atomic and Molecular Physics of Ionized Gases and the 5th International Conference on Reactive Plasmas, Grenoble, 2002*, Vol. 1, p. 215.
4. N. A. Dyatko and A. P. Napartovich, in *Proceedings of the International Conference on Physics of Low-Temperature Plasma, Kiev, 2003*, p. 4-1-9.
5. N. A. Dyatko and A. P. Napartovich, J. Phys. D **36**, 2096 (2003).
6. N. A. Dyatko, Yu. Z. Ionikh, N. B. Kolokolov, *et al.*, J. Phys. D **33**, 2010 (2000).
7. N. A. Dyatko, Yu. Z. Ionikh, N. B. Kolokolov, *et al.*, in *Proceedings of the 15th European Conference on the Atomic and Molecular Physics of Ionized Gases, Miskolc, 2000*; ECA **24F**, 154 (2000).
8. N. A. Dyatko and A. P. Napartovich, in *Proceedings of the 20th Summer School and International Symposium on the Physics of Ionized Gases, Belgrade, 2002*, p. 115.
9. N. A. Gorbunov, N. B. Kolokolov, and F. E. Latyshev, Fiz. Plazmy **27**, 1143 (2001) [Plasma Phys. Rep. **27**, 1079 (2001)].
10. N. A. Dyatko, I. V. Kochetov, and A. P. Napartovich, Fiz. Plazmy **28**, 1046 (2002) [Plasma Phys. Rep. **28**, 965 (2002)].
11. R. E. Robson, J. Chem. Phys. **85**, 4486 (1986).
12. N. A. Dyatko, I. V. Kochetov, and A. P. Napartovich, J. Phys. D **26**, 418 (1993).
13. J. L. Pack, R. E. Voshall, A. V. Phelps, and L. E. Kline, J. Appl. Phys. **71**, 5363 (1992).
14. V. G. Pevgov, Candidate's Dissertation in Mathematical Physics (Moscow Engineering Physics Institute, Moscow, 1977).
15. N. L. Aleksandrov and I. V. Kochetov, J. Phys. D **24**, 2164 (1991).
16. M. A. Biondi, in *Plinciples of Laser Plasmas*, Ed. by G. Bekefi (Wiley-Inerscience, New York, 1976; Énergoizdat, Moscow, 1982).
17. V. A. Adamovich, A. V. Dem'yanov, N. A. Dyatko, *et al.*, Zh. Tekh. Fiz. **57**, 937 (1987) [Sov. Phys. Tech. Phys. **32**, 568 (1987)].
18. J. Bretagne, G. Delouya, J. Godart, and V. Puech, J. Phys. D **14**, 1225 (1981).
19. E. Elson and M. Rokni, J. Phys. D **29**, 716 (1996).
20. D. J. Eckstrom, N. N. Nakano, T. Rothem, *et al.*, J. Appl. Phys. **64**, 1691 (1988).
21. *Handbook of Constants of Elementary Processes Involving Atoms, Ions, Electrons, and Photons*, Ed. by A. G. Zhiglinskiĭ (St. Petersburg State Univ., St. Petersburg, 1994).
22. C. Brow, in *Excimer Lasers*, Ed. by C. K. Rhodes (Springer-Verlag, New York, 1979; Mir, Moscow, 1981).
23. C. Cason, J. F. Perkins, and A. H. Werkheizer, in *Proceedings of the 15th AIAA Aerospace Sciences Meeting, Los Angeles, 1977*, Paper 77-65.

Translated by O.E. Khadin

Plasma Physics Reports, Vol. 30, No. 11, 2004, pp. 962–970. Translated from Fizika Plazmy, Vol. 30, No. 11, 2004, pp. 1035–1043.

LOW-TEMPERATURE PLASMA

Measurements of the Temperature of Subsonic CO_2 Induction Plasma Flows by Analyzing Their Emission Spectra

N. G. Bykova* and L. A. Kuznetsova**

**Institute for Problems of Mechanics, Russian Academy of Sciences, pr. Vernadskogo 101, Moscow, 117526 Russia*

***Moscow State University, Vorob'evy Gory, Moscow, 119899 Russia*

Received January 21, 2003; in final form, April 8, 2004

Abstract—Results are presented from measurements of the temperature characteristics of subsonic CO_2 plasma flows generated by a 100-kW induction plasmatron at the Institute for Problems of Mechanics, Russian Academy of Sciences. The atomic excitation temperature T_a and the population temperature T_e of the electronic states of C_2 molecules (both averaged over the jet diameter) were measured from the absolute intensities of the atomic spectral lines and the spectrum of C_2 molecules in different generation regimes at gas pressures of 25–140 hPa and anode supply powers of 29–72 kW. The longitudinal and radial profiles of the temperatures were determined for some of these regimes and compared to those obtained from numerical calculations of equilibrium induction plasma flows in the discharge channel. For some generation regimes, the dependences of the averaged (over the line of sight) rotational and vibrational temperatures (T_r and T_v) on the discharge parameters, as well as the radial profiles of these temperatures, were determined from the best fit of the measured and calculated spectra of C_2 molecules (Swan bands). The self-absorption of molecular emission was observed at sufficiently high temperatures and gas pressures, and its influence on the measured values of the molecular temperatures T_e, T_v, and T_r was examined. © *2004 MAIK "Nauka/Interperiodica".*

1. INTRODUCTION

Our investigations of CO_2 plasma flows were performed with the aim of determining the catalytic properties of heat-protection coatings and simulating the processes of heat transfer to the surfaces of space vehicles entering the Martian atmosphere [1, 2].

Inductive methods of plasma generation, which provide high temporal and spatial stability of the plasma over a wide range of gas pressures and deposited powers, conform well to the problem of developing high-accuracy diagnostics of the plasma jet parameters. An important factor here is also the spectral purity of the induction plasma.

This paper presents the results of a detailed study of the temperature characteristics of CO_2 plasma flows by analyzing their emission spectra.

2. EXPERIMENTAL SETUP

Figure 1 shows the layout of the experimental setup [1]. The optical system of the setup is arranged as follows: A 25-mm-diameter spherical mirror (*5*) with a focal length of f = 150 mm is placed at a distance of 850 mm from the axis of the discharge channel. The mirror produces a demagnified image of the plasma jet in the entrance plane of a 50-μm-diameter optical fiber (*6*) transmitting radiation to the entrance of an S1000 diffraction spectrograph equipped with a CCD consisting of 1024 elements and incorporated in a PC. The plasma emission spectra are recorded in two spectral ranges by using different color filters (*7*). The shape of the spectrograph instrument function is almost the same throughout the entire spectral range under study, and its full width at half-maximum is equal to 3 nm.

To determine the absolute values of the spectral line intensities, the optical system was calibrated by using a

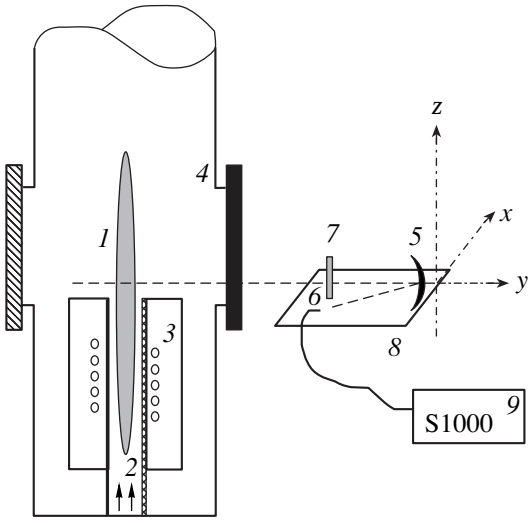

Fig. 1. Experimental arrangement of the VGU-4 plasmatron (f_{gen} = 1.76 MHz): (*1*) plasma jet, (*2*) quartz discharge tube (D_c = 80 mm), (*3*) five-turn copper inductor, (*4*) working chamber, (*5*) concave mirror, (*6*) fiber, (*7*) light filters, (*8*) mobile platform, and (*9*) S1000 spectrometer.

1063-780X/04/3011-0962$26.00 © 2004 MAIK "Nauka/Interperiodica"

tungsten lamp with the known emission characteristics in the brightness temperature range of 1000–2000°C at a wavelength of 659 nm. Data on the sensitivity of the optical system and the calculated accuracy of calibration were used in a program for processing the experimental results.

The radial temperature profiles were determined from a series of the emission spectra measured at different positions of the recording system across the jet. For this purpose, the spherical mirror, the holder of the light filters, and the entrance part of the fiber were mounted on a common mobile platform. The positions of the platform along the jet (along the z axis) and across it (along the x axis) were measured with an accuracy of 0.1 mm.

The radial profiles of the emission intensity were determined from the measured data by the Abel inversion procedure [3]. As was shown in [4], no additional weighting factors are required to apply this procedure to the results obtained with the help of the above optical system.

3. METHODS FOR TEMPERATURE MEASUREMENTS

To determine the temperature from the atomic line emission, we used the method of the absolute spectral line intensities. For an optically thin medium, assuming that the plasma is in a partial local thermodynamic equilibrium, the temperature of the zth plasma component is determined from the parameters of the plasma emission spectrum by the formula [5]

$$T_z = \frac{E_m}{k}\ln\left(\frac{h\nu_{mn}A_{mn}N_z(p,T_z)}{I_{mn}}\frac{g_{z(m)}}{g_z(T_z)}\right)^{-1},$$
$$g_z(T_z) = \sum_i g_{z(i)}\exp(-E_i/kT_z), \quad (1)$$

where I_{mn}, ν_{mn}, A_{mn} are the specific emission power, frequency, and probability of spontaneous emission via the m–n transition, respectively; E_m is the energy of the mth state (counted from the ground level); $g_{z(m)}$ is the statistical weigh of the level; $N(p, T_z)$ is the density of the particles of this species; and $g_z(T_z)$ is the statistical sum of the zth radiator.

To solve Eq. (1), the method of successive approximations with the convergence criterion $\delta T = 1$ K was used in the program for processing the experimental results.

The relative error in determining the temperature from Eq. (1) is

$$\frac{\delta T_z}{T_z} = \sqrt{\left(\frac{\delta A_{mn}}{A_{mn}}\right)^2 + \left(\frac{\delta I_{mn}}{I_{mn}}\right)^2}\frac{kT_z}{E_m}. \quad (2)$$

It can be seen from expression (2) that the stability of the Abel inversion against experimental errors depends on the factor kT_z/E_m, which increases linearly with temperature. We note that, for a low-temperature plasma, this factor is no larger than 0.1 because, for visible spectral lines, we have $k/E_m < 10^{-5}$ K^{-1}.

The values of the spectroscopic constants A_{mn} and the relative errors $\delta A_{mn}/A_{mn}$ for the spectral lines under study were taken from [6]. The values of A_{mn} for unresolved multiplets were calculated with allowance for the statistical weights and transition probabilities of all the components.

Taking into account experimental errors in determining $\delta I_{mn}/I_{mn}$, we find that $\delta T_z/T_z$ in the temperature range of 5000–1000 K is 3–6% for CI lines and 1.5–3% for OI lines.

The radial profiles of the emission intensity $F_{mn}(R)$ were determined from the measured radial (along the x axis) variations in the averaged (over the line of sight) emission intensity $I_{mn}(x)$ by using the Abel inversion procedure for an axisymmetric jet [3]:

$$F_{mn}(R) = -\frac{1}{\pi}\int_R^{R_\infty}\frac{\partial I_{mn}/\partial x}{\sqrt{x^2 - R^2}}dx. \quad (3)$$

Using the $F_{mn}(R)$ profile and Eq. (1), we calculated the $T_z(R)$ profile for the spectral line under study. When calculating $F_{mn}(R)$ by formula (3), the experimental data were approximated by a cubic spline; in this case, the resulting error for the central region of the jet was on the order of the error in determining the average temperature. The radial profiles $F_{mn}(R)$ were separately determined from $I_{mn}(x)$ for the regions $x > 0$ and $x < 0$. The point $x = 0$ was first assigned to the midpoint of the half-width of the $I_{mn}(x)$ profile; its position was then corrected step-by-step, presuming that $F_{mn}(R)$ was continuous at the center.

4. RESULTS OF TEMPERATURE MEASUREMENTS FROM ATOMIC LINES

Figure 2 presents an example of the spectrum of a CO_2 induction plasma with identified molecular bands and atomic lines. The temperature of the plasma atomic components was determined by applying the Abel inversion procedure to the OI 777-, 845-, and 927-nm spectral lines and the CI 833-, 910-, 940-, 962-, and 966-nm spectral lines. These lines are quite intense and are well separated from one another and from the molecular spectrum.

The measured dependences of the plasma atomic temperature (averaged over the line of sight) on the anode supply power N_{ap} and gas pressure p are shown in Fig. 3. It can be seen that the temperature values coincide (to within the measurement errors) for all of the lines of each atomic component and agree well for different components, except for the data on the CI 940-nm line, which gives an overestimated value of the

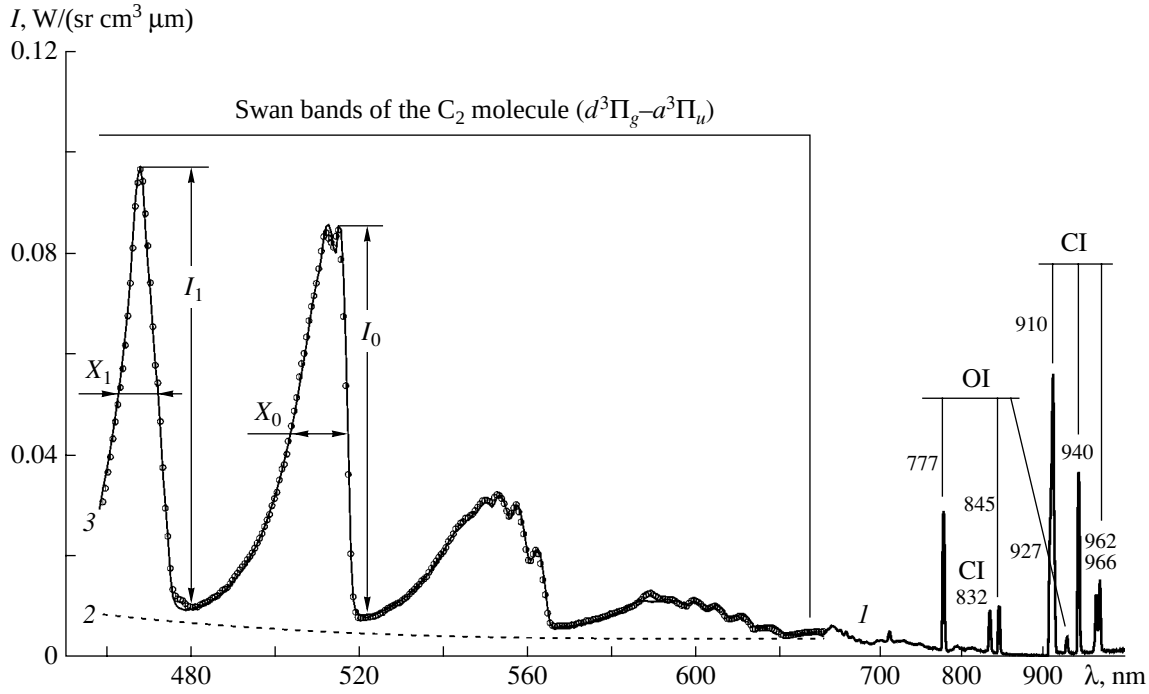

Fig. 2. Emission spectrum of CO_2 plasma at N_{ap} = 37 kW, p = 100 hPa, and G = 1.8 g/s: (*1*) the long-wavelength spectral region with the identified OI and CI lines used to determine the atomic temperature, (*2*) the background spectrum, and (*3*) the sum of the background spectrum and the calculated molecular spectrum for $T_r = T_V$ = 6250 K and T_e = 5950 K. The measures molecular spectrum is shown by the circles. The parameters of the molecular spectrum used to determine T_V and T_r are also indicated.

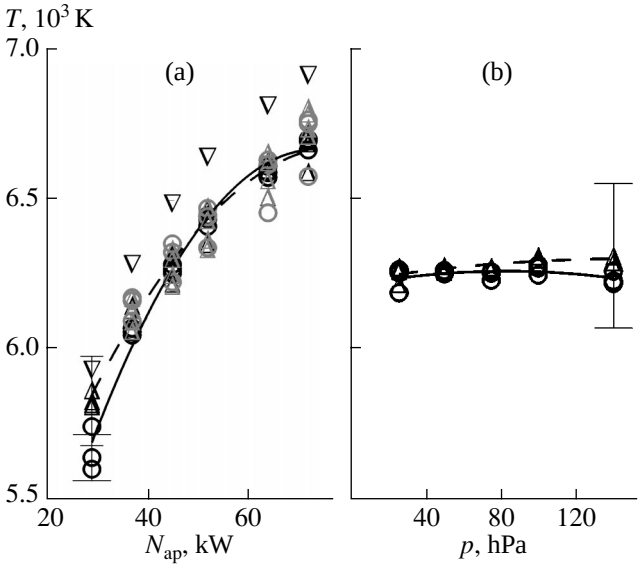

Fig. 3. Averaged (over the line of sight) atomic temperature of a CO_2 plasma near the end of the discharge channel as a function of (a) the anode supply power N_{ap} at p = 100 hPa (black symbols) and p = 25 hPa (gray symbols) and (b) the gas pressure at N_{ap} = 45 kW. The open circles correspond to OI lines, the open triangles corresponds to CI lines, and the inverted open triangles correspond to the CI 940-nm line. The gas flow rate is G = 1.8 g/s.

temperature. If the transition probability for this line, $(1.3 \pm 0.65) \times 10^7$ s^{-1} [6], is replaced with 2.0×10^7 s^{-1}, then the data obtained from all of the atomic lines agree well for all the generation regimes.

Figure 3 shows that the atomic temperature increases by nearly 1000 K when the anode supply power increases by a factor of 2.5. It can be seen that this temperature tends to saturate at high powers and depends only slightly on the pressure in the range 25–140 hPa.

The longitudinal and radial profiles of the atomic temperatures in the plasma jet are presented in Fig. 4. The atomic temperatures decrease almost linearly along the jet up to a distance of about the channel diameter D_c. The radial profiles of the atomic temperature obtained from the most intense OI 777-nm and CI 910-nm spectral lines were compared to the calculated temperature profiles for an equilibrium induction plasma flow for the two values of the power deposited in the plasma: N_{pl} = 19 and 23.5 kW (Fig. 4; curves *1*, *2*). The parameters of a CO_2 plasma flow in the discharge channel of the VGU-4 plasmatron were calculated based on the method described in [7], assuming that the plasma is in a local thermodynamic equilibrium. The results of these calculations are presented in [2]. In the major part of the plasma flow (R < 2.0 cm), the radial temperature profiles for carbon and oxygen

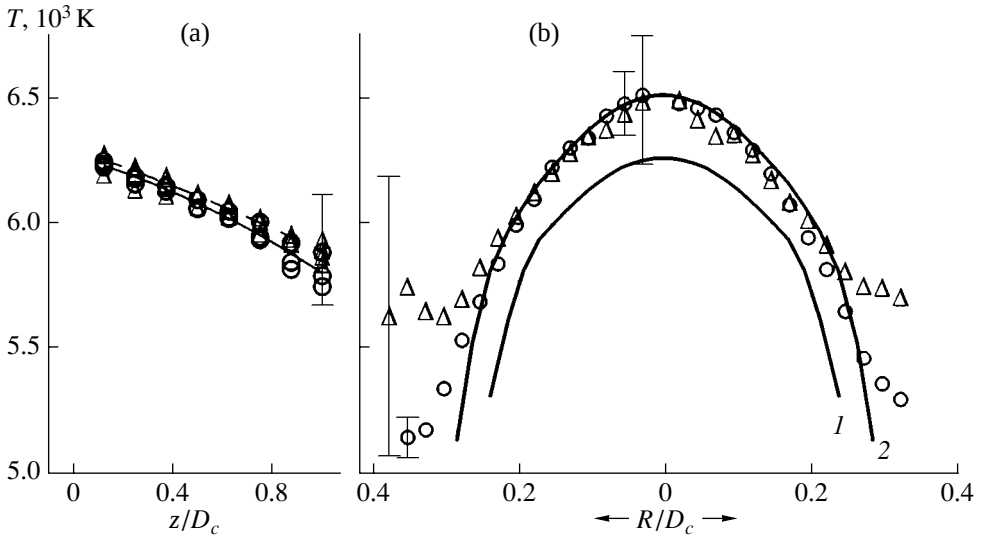

Fig. 4. (a) Averaged (over the line of sight) atomic temperature of a CO_2 plasma as a function of the distance from the end of the discharge channel (the circles correspond to OI lines, the triangles corresponds to CI lines, and the inverted triangles correspond to the CI 940-nm line) and (b) the radial profiles of the atomic temperature near the end of the discharge channel (the circles correspond to the OI 777-nm line, and the triangles correspond to the CI 910-nm line) for N_{ap} = 45 kW, p = 100 hPa, and G = 1.8 g/s. The solid lines show the calculated equilibrium temperature profiles for N_{pl} = (*1*) 19 and (*2*) 23.5 kW.

atoms agree with one another and with the calculated temperature profile for $N_{pl}/N_{ap} \sim 0.52$.

Thus, the data obtained show that, at gas pressures of 25–140 hPa and temperatures of 5800–6700 K, the atomic components in the central region of a subsonic CO_2 induction plasma flow are nearly in a local thermal and chemical equilibrium.

At the same time, a certain discrepancy between the temperatures of the atomic components was observed at $T_a \le 5800$ K (which corresponds to the minimal power required for stable generation: N_{ap} = 29 kW) and also at $z > D_c$. At the periphery of the jet ($R > 0.2D_c$), we always observed different temperatures of oxygen and carbon atoms ($\Delta T_a \sim 500$ K) and different deviations of these temperatures from their calculated equilibrium values.

5. METHOD FOR MEASURING THE TEMPERATURE CHARACTERISTICS FROM THE EMISSION SPECTRUM OF C_2 MOLECULES

In the emission spectrum of a CO_2 plasma (Fig. 2), we observed an intense emission of C_2 molecules in the wavelength range of 450–630 nm, including the sequences $\Delta v = v' - v'' = 1, 0, -1, -2$ of the Swan band system (the $d^3\Pi_g - a^3\Pi_u$ transition). Note that it is rather difficult to use these bands to determine the molecular temperatures. First, the rotational structures related to different vibrational transitions substantially overlap one another within each sequence. Second, the instrument function of the spectrograph is fairly wide (3 nm), the sequence width being 10–15 nm. Nevertheless, by comparing the observed and calculated spectra, we could determine the rotational and vibrational molecular temperatures with a reasonable accuracy.

The emission spectra of C_2 molecules were calculated by the scheme described in [8]. It was assumed that, for each of the three degrees of freedom (electronic, vibrational, and rotational), a Boltzmann distribution over energy holds, the corresponding temperatures being T_e, T_v, and T_r. The spectroscopic constants for the Swan system of the C_2 molecule were taken from [9]. The probabilities of the vibrational transitions were calculated by averaging the dipole-moment function of the electronic transition over the vibrational wave functions of the combining states (the RADEN code [10]). Vibrational transitions with quantum numbers in the range 0–15 were taken into account for the zeroth and first sequences, while those in the range 0–10 were taken into account for $\Delta_v = -1, -2$, and 2. The limiting energies for the rotational levels were taken from [11], and the probabilities of the rotational transitions were calculated using the code described in [12]. The final spectra were determined by convoluting the calculated molecular spectra with the instrument function of the spectrograph.

The values of T_v and T_r were determined by analyzing the following parameters of the spectrum (Fig. 2): the ratio $M = I_1/I_0$ of the maximum intensities of the first and zeroth sequences, the half-width X_0 of the zeroth sequence, and the half-width X_1 of the first sequence.

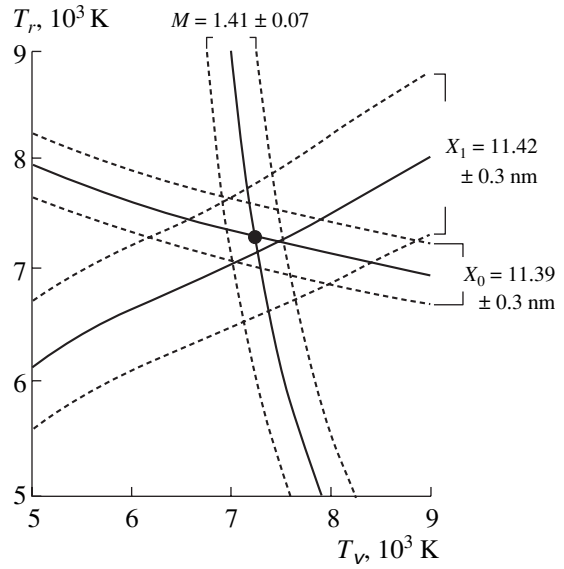

Fig. 5. Chart of the calculated dependences of the spectral parameters on T_v and T_r.

From a series of the calculated emission spectra for rotational and vibrational temperatures in the range 4000–1000 K, we determined the above parameters and spectral intensities at wavelengths of 481, 521, 567, and 620 nm as functions of T_v and T_r. These dependences were then approximated by polynomial distributions of the two variables with an accuracy of no worse than 0.5% and were used in the program for data processing. The dependences of the minimal intensities of the molecular spectrum on T_v and T_r were used to exclude the background component from the observed spectrum in order to determine the molecular spectrum itself.

Figure 5 illustrates the dependences of M, X_0, and X_1 on T_v and T_r for an operating regime with p = 25 hPa and N_{ap} = 64 kW (M = 1.41, X_0 = 14.39 nm, and X_1 = 11.42 nm) as an example. It can be seen that the value of M is primarily determined by the vibrational temperature, whereas the half-widths of the sequences depend largely on the rotational temperature. Taking into account the errors in measuring M, X_0, and X_1 (these are indicated by the dashed lines in the figure), the error in determining T_v can be estimated at ±300 K. The estimated error for T_r is ±400 K when the temperature is determined from X_0, and it is ±600 K when the temperature is determined from X_1. For the discharge parameters corresponding to Fig. 5, the intersection of the curves $M(T_v, T_r)$ and $X_0(T_v, T_r)$ gives T_v = 7200 ± 300 K and T_r = 7300 ± 400 K.

The population temperature T_e of the electronic molecular states was determined from the measured absolute value of the maximum intensity I_0 of the zeroth sequence by using the relationship

$$I^0 = I^0_{\text{calc}}(T_v, T_r)\frac{N_{C_2}(p, T_e)}{g(T_e, T_v, T_r)}\exp\left(-\frac{E_{\text{el}}}{kT_e}\right), \qquad (4)$$

where $I^0_{\text{calc}}(T_v, T_r)$ is the calculated intensity per molecule (including the statistical weight of the electronic state), $N_{C_2}(p, T_e)$ is the equilibrium density of C_2 molecules, and E_{el} is the energy of the upper electronic level. In solving Eq. (4) by the method of successive approximations, the function $g(T_e, T_v, T_r)$ was calculated by a separate subroutine using the procedure described in [11].

Calculations of the absolute intensity of the molecular spectrum as a function of T_e allow us to conclude that, in the temperature range of 5000–7000 K, the error in determining the averaged (over the line of sight) value of T_e is no larger than ±100 K.

The radial profiles of the molecular temperatures were determined by analyzing a series of spectra measured across the jet (along the x axis). The program input was a data array $I(\lambda, x)$ for wavelengths corresponding to each of the 284 detector elements covering the entire molecular spectrum and for up to 30 points along the x coordinate. The program for calculating the radial temperature profiles included the following procedures:

(i) For each λ value, the $I(\lambda, x)$ array was replaced with a continuous dependence $I^*(\lambda, x)$ obtained by smoothing with a cubic spline over seven neighboring points.

(ii) The Abel inversion was applied to $I^*(\lambda, x)$ to reconstruct the distribution $F^*(\lambda, R)$.

(iii) For a set of the R values, the background component was excluded step-by-step from the distribution $F^*(\lambda, R)$ in order to determine the molecular spectrum $F(\lambda, R)$, which was then used to determine the local molecular temperatures.

The calculations showed that, in our experiments, the error multiplication factor inherent in the Abel inversion was close to unity for $T_e(R)$, whereas for $T_v(R)$ and $T_r(R)$, it was 1.5 for the central region of the jet and increased to 3 at the jet periphery.

6. RESULTS OF MEASUREMENTS OF THE MOLECULAR TEMPERATURES

Figure 6 shows the measured molecular and atomic temperatures (averaged over the jet diameter) as functions of the anode supply power and the longitudinal profiles of these temperatures at a gas pressure of 25 hPa. As the generation power increases from 37 to 72 kW, the values of T_v and T_r are always higher than T_a by 500–600 K and slightly (within the measurement errors) differ from one another. We note that T_a and T_r

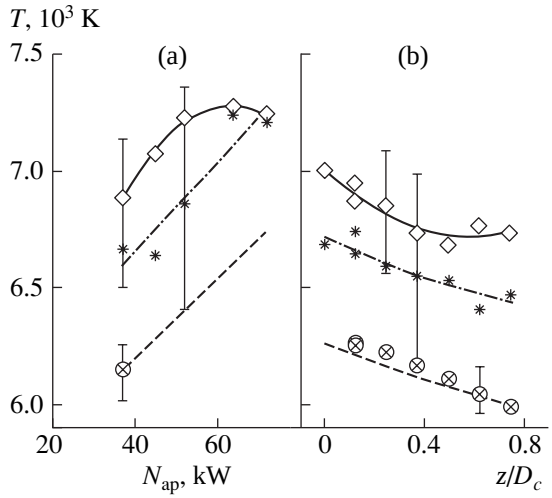

Fig. 6. (a) Molecular temperatures T_v (diamonds) T_r (asterisks), and T_e (crossed circles) near the end of the discharge channel as functions of the anode supply power at p = 25 hPa and G = 1.8 g/s and (b) the longitudinal profiles of the molecular temperatures at N_{ap} = 45 kW. The dashed line shows the same dependences for T_a.

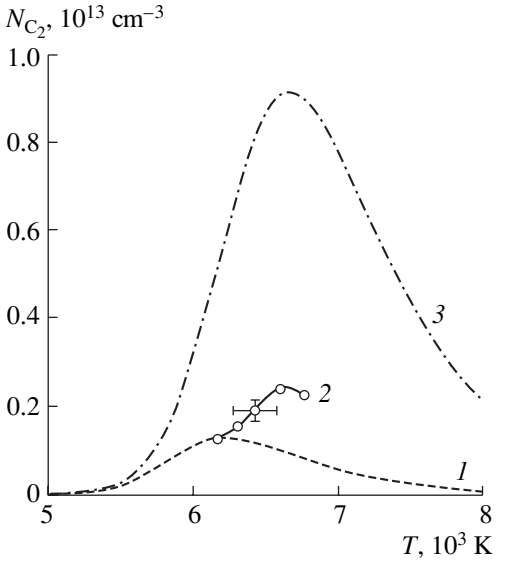

Fig. 7. (*1*) Equilibrium and (*2*) corrected densities of C_2 and CO_2 molecules for p = 25 hPa (the circles correspond to experimental data) and (*3*) the equilibrium density for p = 100 hPa as functions of the temperature T_e.

increase linearly with generation power, whereas T_v begins to decrease starting from $N_{ap} > 52$ kW. The value of the electronic molecular temperature at N_{ap} = 37 kW coincides with T_a.

It can be seen from the longitudinal profiles of the temperatures that, up to $z/D_c \sim 1$, all the temperatures decrease slightly with distance from the end of the discharge channel, the difference between the temperatures changes only slightly, and $T_e = T_a$.

As to the value of T_e at $N_{ap} > 37$ kW, it was impossible to find it from the calculated dependence $N_{C_2}(T_e)$. Indeed, the intensity of the molecular spectrum increases monotonically with increasing N_{ap} to 72 kW (T_a = 6750 K), whereas according to the calculated curve $N_{C_2}(T_e)$, which has a maximum at ~6250 K, the spectral intensity should decrease starting from $N_{ap} \sim$ 42 kW ($T_a \cong$ 6250 K). This discrepancy can be eliminated only by correcting the calculated dependence $N_{C_2}(T_e)$. Based on the fact that, in the region where $T_a \leq$ 6200 K, the atomic temperature almost coincides with the electronic molecular temperature (Fig. 6), we corrected the curve $N_{C_2}(T_e)$ by extending the equality $T_e = T_a$ to the region where $T_a > 6200$ K. The corresponding result is presented in Fig. 7 (curve *2*): the maximum density of C_2 molecules is twice as large as the calculated value and the maximum itself is shifted by 400 K toward the higher temperatures. When estimating the change in the density of C_2 molecules, it should be remembered that the maximum value of N_{C_2} is three to four orders of magnitude lover than the densities of OI, CI, and CO, which are the main components of a CO_2 plasma.

Let us now consider the results of measurements of the molecular temperatures at a gas pressure of 100 hPa (Fig. 8). We note that, in this case, the values of the plasma temperature measured from the atomic components fall into the increasing segment ($T_a \leq$ 6700 K) of the calculated dependence $N_{C_2}(T_e)$ (Fig. 7, curve *3*). This is why, for all of the generation regimes under study, the value of T_e can be determined from the equilibrium temperature dependence of the density of C_2 molecules.

Figure 8 demonstrates a substantially different behavior of the temperatures with increasing pressure: in contrast to T_a, which remains almost constant, and to T_e and T_r, which vary within their measurement errors, the vibrational temperature decreases monotonically by 1000 K (at p = 140 hPa, it becomes lower by 400 K than the other temperatures). The vibrational temperature T_v as a function of the generation power also exhibits specific behavior: in contrast to T_a, T_e, and T_r, which increase monotonically with increasing generation power, T_v increases only in the range 29–37 kW and then decreases well below the other temperatures. As the generation power increases, the difference between T_a and T_e increases monotonically because of the weaker effect of the generation power on the measured value of T_e. Specific features of the temperature T_v can also be observed in its longitudinal profile: in contrast to T_a, T_e, and T_r, which monotonically decrease with distance from the end of the discharge channel, T_v begins to decrease at $z/D_c \sim 0.5$. At shorter distances

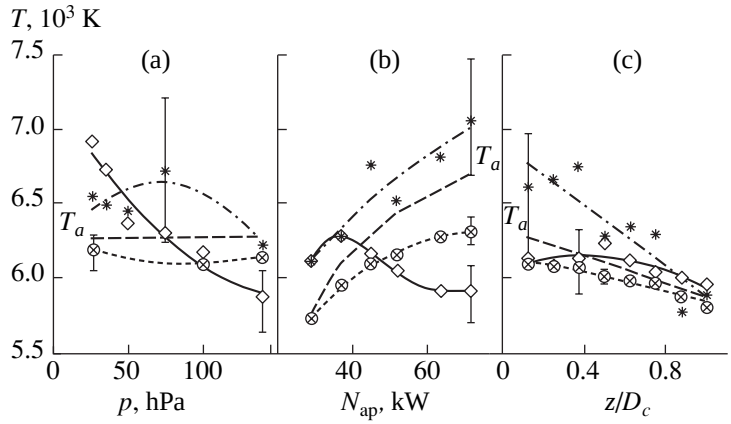

Fig. 8. Molecular temperatures T_v (diamonds), T_r (asterisks), and T_e (crossed circles) near the end of the discharge channel as functions of (a) the gas pressure at N_{ap} = 45 kW and (b) the anode supply power at p = 100 hPa and (c) the longitudinal profiles of the molecular temperatures at N_{ap} = 45 kW, p = 100 hPa, and G = 1.8 g/s.

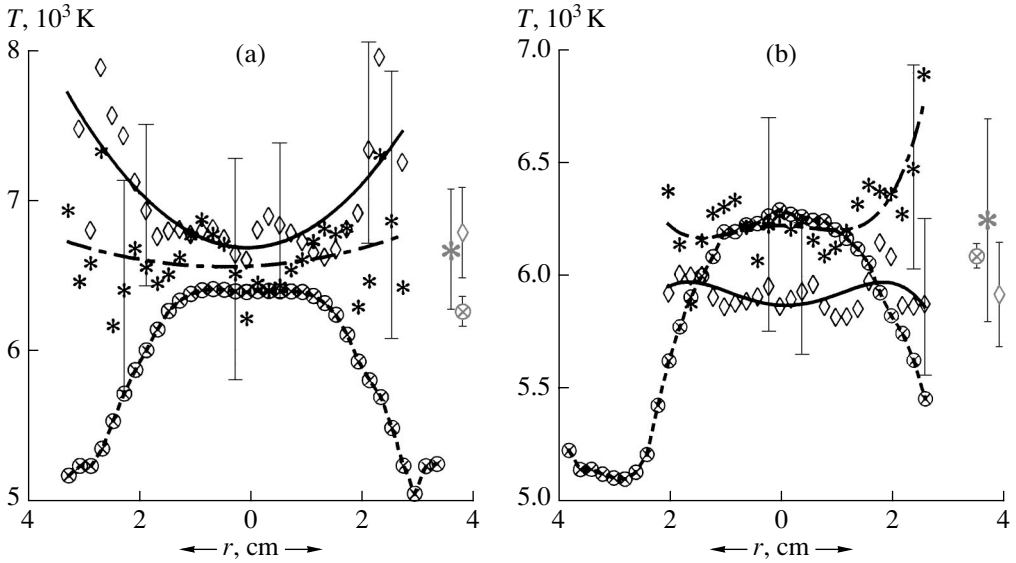

Fig. 9. Radial profiles of the molecular temperatures T_v (diamonds), T_r (asterisks), and T_e (crossed circles) near the end of the discharge channel at N_{ap} = 45 kW, p = (a) 25 and (b) 100 hPa, and G = 1.8 g/s. The gray symbols at the right sides of the panels show the molecular temperatures averaged over the jet diameter.

from the end of the discharge channel, the vibrational temperature varies only slightly. At $z/D_c \sim 1$, all of the temperatures relax to a common level, so the plasma in this region can be characterized by one temperature.

It follows from the experimental data that specific behavior of T_e and T_v correlates with an increase in the intensity of molecular emission. Therefore, the observed effects can be explained by an increase in the self-absorption of molecular emission (SME) with increasing molecular density and plasma temperature.

Figure 9 shows the calculated radial profiles of the molecular temperatures for N_{ap} = 45 kW and two values of the gas pressure.

In both cases, the molecular temperatures in the central region of the jet are close to their average values. All the temperature profiles are flat inside a radius of 15–20 mm. Beyond this radius, the vibrational and rotational temperatures (in contrast to the electronic molecular temperature) do not decrease and, at low pressures, even tend to increase. This easily reproducible effect allows us to conclude that the deviation of the plasma from an equilibrium state increases outside the jet core ($R/R_c \sim 3/8$), where the gradients of T_a and T_e are relatively large.

At a gas pressure of 100 hPa (Fig. 9b), T_v in the jet core is significantly lower than T_e. This means that, as the gas pressure increases, the SME more strongly

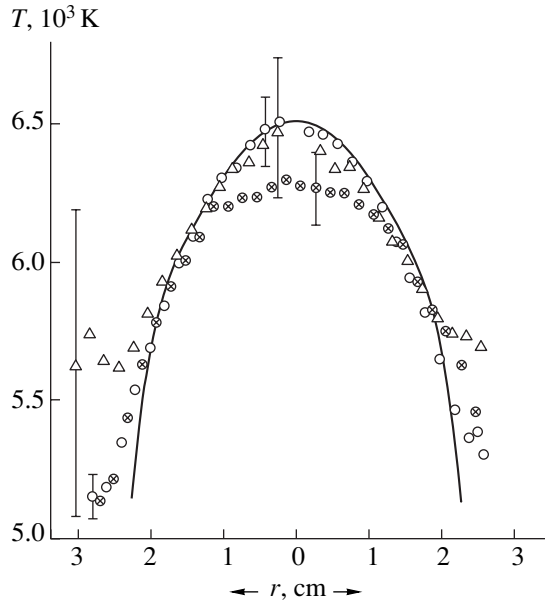

Fig. 10. Radial temperature profiles of atomic oxygen (the 777-nm line, circles) and atomic carbon (the 910-nm line, triangles) and the radial profile of the electronic temperature of C_2 molecules (crossed circles) in a CO_2 plasma near the end of the discharge channel for N_{ap} = 45 kW, p = 100 hPa, and G = 1.8 g/s. The solid line shows the calculated profile of the equilibrium temperature for N_{pl} = 23.5 kW.

influences the measured temperature, which, in this case, turns out to be lower than its true value.

In Fig. 10, the measured dependence $T_e(R)$ for a gas pressure of 100 hPa and N_{ap} = 45 kW is shown together with the profiles of the atomic temperatures and the calculated equilibrium temperature profiles for two values of N_{pl}. At N_{pl} = 23.5 kW, the atomic temperature profiles coincide with the calculated profile in the jet core and differ from the electron temperature profile, which cannot be brought into coincidence with the equilibrium profile at any value of N_{pl}. The reason is that the $T_e(R)$ profile contains a flat segment in the central region ($R <$ 10 mm), because the molecular emission from the jet core is absorbed at the jet periphery. Note that, in a CO_2 plasma, the SME only slightly affects the spatial distribution of the plasma temperature because of the lower (by a factor of 3–4) density of C_2 molecules in comparison to the main plasma components. In both the air and oxygen induction plasmas generated in the VGU-4 plasmatron, the self-absorption of emission from the main plasma components plays an important role and substantially influences the spatial distribution of the plasma temperature, resulting in flatter and more extended temperature profiles [4].

7. CONCLUSIONS

In this study, we have measured the averaged (over the jet diameter) temperatures of the atomic components and the averaged vibrational, rotational, and electron temperatures of C_2 molecules in subsonic CO_2 induction plasma flows generated in the VGU-4 plasmatron at gas pressures of 25–140 hPa and anode supply powers of 29–72 kW. For some regimes, the radial and longitudinal profiles of the atomic and molecular temperatures have been determined.

An analysis of the experimental data shows that, throughout the entire range of the gas pressures under study and at temperatures of 5800–6700 K, the local thermodynamic and chemical equilibrium takes place for the atomic components of the plasma in the central region of the jet ($R/D_c < 0.25$). This follows from the coincidence of the temperature values measured from all of the OI and CI atomic lines under study, especially in view of the substantially different behaviors of the calculated temperature dependences of the equilibrium densities of oxygen and carbon atoms in the given temperature range. This is also confirmed by the fact that the measured radial profiles of the atomic temperatures coincide with the calculated radial profiles of the equilibrium temperature. Since oxygen and carbon atoms, along with CO molecules, are most abundant in a low-temperature CO_2 plasma, it is the atomic temperature that characterizes the plasma temperature in our case.

By analyzing the spectra of C_2 molecules, it was found that the SME can influence the measured values of the molecular temperatures. At a gas pressure of 25 hPa and plasma temperatures of no more than 6700 K, the SME effect is of minor importance and the measured temperatures are the true values of the molecular temperatures. It follows from the measured radial profiles of the temperatures that, at T_a = 6300 K, the difference between the molecular temperatures is small in the central region of the jet. Consequently, the plasma in the jet core is nearly in a thermodynamic equilibrium. At the same time, the decrease in the atomic temperature and molecular electronic temperature toward the periphery of the plasma flow is accompanied by an increase in the difference between these temperatures, on one hand, and the vibrational and rotational temperatures, on the other. This indicates that the closer the jet periphery, the farther the plasma state from equilibrium.

One might expect that, at higher gas pressures, CO_2 plasma would remain in a thermodynamically equilibrium state. For p = 100 hPa, this is confirmed by the coincidence of the averaged temperatures for the generation regime with N_{ap} = 29 kW ($T_a \sim$ 5700 K), when the SME only slightly affects the measured molecular temperatures. For larger values of N_{ap}, this cannot be accurately verified because of the increased influence of the SME on the molecular temperature measurements.

ACKNOWLEDGMENTS

We are grateful to S.A. Vasilevskiĭ for providing us with the data from calculations of the radial tempera-

ture profiles and equilibrium densities of the CO_2 plasma. We also thank A.F. Kolesnikov for his continuing interest in this work and fruitful discussions. Invaluable help in conducting our experiments was rendered by I.S. Pershin. We are deeply sorrowed by the death of this remarkable man; he will always remain in our hearts. This work was supported in part by the International Science and Technology Center (project nos. 036 and 1549) and the Russian Foundation for Basic Research (project no. 02-01-00870).

REFERENCES

1. P. N. Baronets, N. G. Bykova, A. N. Gordeev, *et al.*, in *Proceedings of the 3rd European Symposium on Aerothermodynamics for Space Vehicles, Noordwijk, 1999*; ESA Bull. **SP-426**, 421 (1999).
2. A. F. Kolesnikov, I. S. Pershin, S. A. Vasil'evskii, and M. I. Yakushin, J. Spacecr. Rockets **37**, 573 (2000).
3. N. G. Preobrazhenskiĭ and V. V. Pikalov, *Unstable Problems of Plasma Diagnostics* (Nauka, Sib. Otd., Novosibirsk, 1982).
4. N. G. Bykova and L. A. Kuznetsova, Preprint No. 682 (Institute for Problems of Mechanics, Russian Academy of Sciences, Moscow, 2001).
5. *X-ray Diagnostics of Plasmas*, Ed. by W. Lochte-Holtgreven (American Elsevier, New York, 1968; Mir, Moscow, 1971).
6. *NIST Database for Atomic Spectroscopy* (National Institute of Standards and Technology, Gaithersburg, MD, 1995).
7. S. A. Vasil'evskiĭ and A. F. Kolesnikov, Mekh. Zhidk. Gaza, No. 5, 164 (2000).
8. L. A. Kuznetsova, N. E. Kuz'menko, Yu. Ya. Kuzyakov, and Yu. A. Plastinin, *Probabilities of Optical Transitions of Diatomic Molecules* (Nauka, Moscow, 1980).
9. C. V. V. Prasad and P. F. Bernath, Astrophys. J. **426**, 812 (1994).
10. L. A. Kuznetsova, E. A. Pozyuk, and A. V. Stolyarov, Zh. Fiz. Khim. **67**, 2271 (1993).
11. L. V. Gurvich, I. V. Veĭts, V. A. Medvedev, *et al.*, *Thermodynamic Properties of Substances* (Nauka, Moscow, 1978), Vol. 1.
12. E. E. Whiting, Rep. No. NASA TND-7268 (NASA, Moffett Field, CA, 1973).

Translated by N.F. Larionova

Plasma Physics Reports, Vol. 30, No. 11, 2004, pp. 971–982. Translated from Fizika Plazmy, Vol. 30, No. 11, 2004, pp. 1044–1056.

LOW-TEMPERATURE PLASMA

Spatiotemporal Evolution of the Current and the Integral and Spectral Emission Characteristics of a Negative Corona in Nitrogen during Its Transformation into a Spark

Yu. S. Akishev, G. I. Aponin, V. B. Karal'nik, A. E. Monich, and N. I. Trushkin

Troitsk Institute for Innovation and Fusion Research, Troitsk, Moscow oblast, 142190 Russia

Received November 18, 2003; in final form, February 25, 2004

Abstract—Results are presented from experimental studies of the conversion of a steady-state negative corona into a spark. It is found that a spark in a negative corona in nitrogen and air is formed in the absence of fast primary streamers. It is shown that, in atmospheric-pressure nitrogen, the conversion of a corona into a spark begins with the propagation of a plasma channel (secondary streamer) from the point electrode (cathode) to the plane electrode (anode). In contrast, the plasma channel in air originates near the plane electrode and then propagates towards the point electrode. The propagation velocity of the secondary streamer is very low, $V = 10^3$–10^4 cm/s. Two possible scenarios of the formation of the spark channel in a negative corona in nitrogen are described on the basis of the concept of a contracted volume glow discharge. Results are presented from time-resolved spectral measurements of plasma emission from different regions of the corona during its transformation into a spark. © *2004 MAIK "Nauka/Interperiodica".*

1. INTRODUCTION

By spark, we mean a bright flash arising in an interelectrode gap when it is bridged by a thin, highly conducting plasma filament (channel). The spark is accompanied by a loud click, whose intensity is determined by the spark current. In many gas-discharge devices, the spark (also called the gap breakdown) is generally an undesirable effect because it limits the operating parameter range and can even destroy a device.

The threshold voltage for the spark formation depend strongly on the composition, pressure, and temperature of the working gas, as well as on the geometry of the electrode system (the electrode configuration and interelectrode distance). When the discharge gap is asymmetric, the polarity of the electrode with a small radius of curvature is significant [1–4].

In view of the above, it should be noted that, in this study, we are dealing with spark formation in a point-to-plane gap no longer than a few centimeters (i.e., less than 10 cm). Interelectrode gaps of such lengths will henceforth be referred to as short. Gaps with lengths of a few tens of centimeters or more will be referred to as long. The point-to-plane electrode configuration is widely used in various applications, e.g., to ignite corona discharges in electric filters or in devices for surface treatment [5]. For this reason, studying the physics of corona breakdown in this electrode configuration is of practical importance.

In a short point-to-plane gap, the spark channel does not arise immediately after the voltage exceeding the threshold value is applied. The breakdown proceeds in several stages, each of which is characterized by its own spatial structure and specific mechanism for gas ionization in the current structure produced.

For an initially nonionized gap with a positive point electrode, the process of breakdown can be divided into three stages [2, 6]. In the first, whatever the gas species, so-called primary streamers begin to propagate toward the opposite electrode at high velocities (on the order of $V \cong 10^8$ cm/s). These primary streamers are the well-known conventional streamers, i.e., thin (with a thickness of about 100 μm) low-conductivity current filaments (see, e.g., [1, 2, 6]). Because of the low conductivity of primary streamers, the bridging of the gap by them does not lead to a sharp decrease in the interelectrode voltage.

The second stage is characterized by the propagation of a slower (with a velocity of $V \cong 10^6$ cm/s) secondary streamer from the point electrode. The secondary streamer arises near the point electrode due to the energy release from the primary streamers. It has a larger diameter and higher conductivity than the primary streamers [6]. In short gaps, no primary streamers are observed during the propagation of the secondary streamer.

In the final stage, which begins after the secondary streamer has bridged the interelectrode gap, the streamer is transformed into a bright spark channel. In this stage, the voltage across the gap sharply decreases (it is this decrease in the gap voltage that is usually called gap breakdown).

We note that, in long gaps with a positive point electrode, events similar to the above develop in space [7]. In this case, all three current structures are observed

1063-780X/04/3011-0971$26.00 © 2004 MAIK "Nauka/Interperiodica"

simultaneously in the gap: the primary streamers form a kind of sheaf emerging from the plasma channel (an analogue of the secondary streamer), which, at a certain distance, transforms into the so-called leader, whose parameters are close to the plasma parameters in the spark channel.

The process of breakdown in an initially nonionized gap with a negative point electrode is more complicated and less studied. According to the photograph in [3], the breakdown in such a gap develops as follows: As in the previous case, the process begins with the propagation of fast primary streamers from the point electrode toward the plane anode. Next, slower secondary streamers start from the point electrode and pass only a fraction of the gap length (about one-third). New secondary streamers then start from the plane electrode (from the points where the primary streamers have touched the anode) to meet the previous ones. The breakdown process is complete when the streamers propagating from the cathode and anode meet together, thus forming a spark channel.

Here, we will not concentrate on the variety of nonsteady spatial forms acquired by a discharge during breakdown (starting from applying the discharge voltage up to the spark formation). We only note the following general features of the sequence of the ionization mechanisms dominating in the current structures formed:

(i) Immediately after applying the voltage to a nonionized gap, the gas is not yet heated or excited. It is mainly ionized via direct electron impacts. Such a situation corresponds to the conditions in the head of the primary streamer.

(ii) As time elapses, the energy deposited in the gas increases, and a progressively higher number of the excited states of the initial gas particles, as well as newly born particles produced due to the dissociation of the initial gas molecules, become involved into the ionization process. Together with the gas heating, which decreases the density N of the neutral gas particles and thus increases the reduced electric field E/N, the gas excitation leads to an increase in the ionization rate at a given voltage. Such a nonequilibrium ionization occurs, first of all, near the point electrode, from which the primary streamers start, and near the current spots on the plane electrode.

(iii) Further gas excitation, which is accompanied by intense gas heating (up to $T > 1500$ K), brings the discharge plasma closer to an equilibrium state and increases the effect of thermal ionization in the current channel. Such a situation corresponds to the transformation of the secondary streamer into a spark channel.

In steady-state corona discharges, a spark arises in a random and an uncontrolled way as the threshold voltage is approached. This circumstance greatly impedes the study of the fast spark formation. In this case, it is expedient to carry out experiments in which a voltage pulse is applied to a gap where a corona discharge has already been ignited. The process of spark formation in a short gap against the background of a corona discharge is more complicated than the above scenarios because this process cannot be considered separately from the evolution of the corona as the gap voltage increases.

Although the process of spark formation in a corona discharge is a well-known phenomenon, it is still poorly studied. Here, one of the important features of the breakdown is that both the streamers and the spark are formed under the conditions such that the Meek–Raether criterion [3, 4] for streamer breakdown is not met.

Indeed, a corona discharge can be ignited at a significantly smaller coefficient K of electron multiplication in the gap,

$$K = \int_0^d \alpha(x)dx \cong \ln\frac{1}{\gamma} \cong 4\text{–}6, \qquad (1)$$

than that needed to form streamers according to the Meek–Raether criterion ($K \cong 18$–20). In expression (1), α is the Townsend ionization coefficient, which depends exponentially on the reduced electric field E/N, and γ is the total positive feedback coefficient for electron avalanches due to the surface electron emission caused by photons, ions, and metastable particles, as well as due to the volume photoionization.

When the only ionization mechanism within the generation zone of a corona is direct electron-impact ionization, the coefficient K is independent of the current; i.e., K cannot be increased from 4–6 to the required value of 18–20 only by increasing the current. Thus, for a spark to be generated by preionizing a point-to-plane gap with a corona discharge or by slowly increasing the voltage applied to the gap, there should be some other mechanisms for triggering the primary and secondary streamers. One of the aims of this study is to determine these mechanisms.

The development of a spark against the background of a corona discharge proceeds much more slowly than in a nonionized gap, all the other factors being the same. For example, it was shown in [8] that, when a spark arises in a short-gap positive corona in air or nitrogen, the propagation velocities of the primary and secondary streamers that started from the point electrode were a few tens of times lower than those in an nonionized gap at the same voltage. In contrast to the case of a nonionized gap, the secondary streamer in a positive corona arises with a great delay (a few hundreds of microseconds) after bridging the gap by primary streamers, rather than at (or before) the instant of bridging. Experiments also showed that the velocities of the primary and secondary streamers depend on the gas species. Thus, the streamer velocity is lower in nitrogen than in air; this was attributed in [8] to the fact that the corona operation voltage is lower in nitrogen than in air.

Another significant difference between the development of a spark against the background of a positive corona [8] and the breakdown of a nonionized gap [9–11] is related to the degree of streamer branching in air and nitrogen. In the case of breakdown against the background of a positive corona, the primary streamers in air are more branched than in nitrogen, whereas in the case of fast breakdown of an unionized gap [9–11], the situation is the opposite.

The spatiotemporal dynamics of the slow formation of a spark against the background of a negative corona (i.e., a corona in which the point electrode is at a negative potential) is still poorly studied. In this context, we can note papers [12, 13]. In [12], a photograph of a corona in air immediately before breakdown demonstrates the presence of a relatively short current channel near the plane anode (we consider this channel to be an analogue of the secondary streamer). In [13], the evolution of the radial distribution of the current in a negative corona in air during its transformation into a glow discharge and then into a spark was investigated. It was found that the spark was formed in the absence of primary streamers in the gap. However, no detailed studies of the evolution of the discharge structure during the transformation of a corona into a spark were performed in [12, 13].

This study is a continuation of [14], which was devoted to the phenomenology of a steady-state high-current negative corona in nitrogen. Here, we present the results from experimental studies of the evolution of the spatial structure and current of a corona during its transformation into a spark. The time evolution of the plasma emission spectrum from different regions of the discharge is also investigated. The results obtained provide new information about the physics of breakdown in a corona discharge and can be used to create new sources of nonequilibrium atmospheric-pressure plasma.

2. EXPERIMENTAL SETUP

As in our previous study [14], the experiments were performed with a cylindrical organic-glass discharge chamber with an inner diameter of 120 mm and a height of 150 mm. To perform optical measurements, four 50-mm-diameter optical windows were mounted on the side wall of the discharge chamber. In the point-to-plane electrode system, a 3-mm-diameter tungsten rod with a tip radius of $r_c = 0.1$ mm was used as a cathode. A 110-mm-diameter copper disc was used as a plane electrode (anode). The interelectrode distance was varied from 10 to 40 mm.

In our experiments, we used very high purity nitrogen (with a certified purity of 99.999%) and laboratory air. Before each experiment, the discharge cell was pumped out to a pressure of $P \cong 10^{-3}$ torr and then filled with nitrogen or air at a pressure slightly exceeding atmospheric pressure (usually, at P = 770 torr). To remove the products of plasmochemical reactions from the discharge zone and to maintain the certified purity of nitrogen, the experiments were carried out in a continuous gas-flow regime. The gas flow rate was low enough ($\leq 10^{-2}$ l/s) to exclude any gasdynamic effect on the discharge.

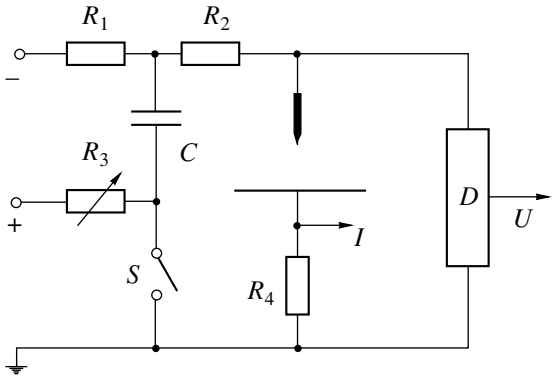

Fig. 1. Schematic of the experimental setup for studying the evolution of a negative corona after applying an overvoltage pulse: R_1 = 1–2 MΩ and R_2 = 78 kΩ are the ballast resistances, R_3 is the variable resistance for varying the rise time τ of the voltage pulse, R_4 is the current shunt, C is the capacitance of the circuit for voltage pulse formation, S is the switch of the circuit for voltage pulse formation, and D is the voltage divider.

A schematic of the experimental setup is shown in Fig. 1. A steady-state negative corona was powered from a stabilized ($\delta U/U \leq 10^{-6}$) high-voltage power supply. The voltage drop across the interelectrode gap was measured with an S-196 electrostatic voltmeter and a calibrated high-voltage divider. The average corona current was measured with a Ts4311 current meter. The ballast resistance R_1 in the external circuit was varied from 1 to 2 MΩ. The initial corona current was varied in the range $I_0 \approx 0.1$–2.5 mA.

A spark was initiated by applying an overvoltage pulse with an amplitude of 3–16.5 kV to a high-current steady-state corona [14]. The rise time of the overvoltage pulse was varied from 1 to 700 μs, and the duration of its plateau was a few milliseconds. The voltage pulse was applied to the discharge gap trough the resistance R_2 = 78 kΩ, passing by the high resistance R_1.

The waveforms of the discharge current and voltage were recorded with S8-17 and S1-104 oscilloscopes. An LV-03 electron-optical image tube was used to take images of the interelectrode gap in different stages of breakdown. The image tube operated either in a multiframe mode with a minimum exposure time of 50 ns for each frame or in a continuous scanning mode with a minimum time resolution of 1.5 ns. In parallel with recording electron-optical images, we performed time-resolved spectral measurements of the plasma emission from different regions of the high-current corona (the cathode and anode regions and the middle of the gap).

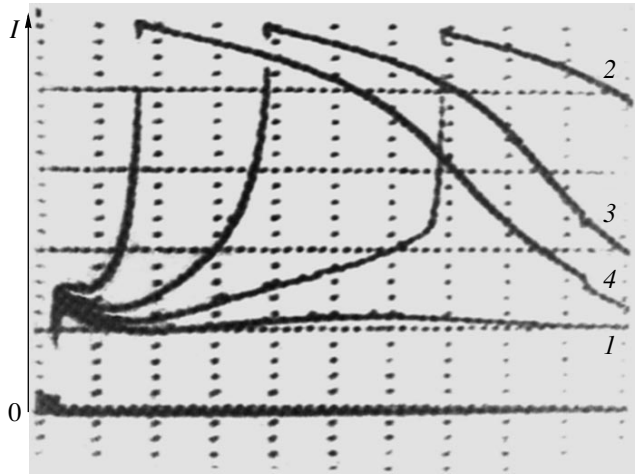

Fig. 2. Oscillograms of the corona current in the case of a stepwise increase in the voltage for $d = 40$ mm; $r_c = 0.1$ mm; $\Delta U = 15.5$ kV; and $I_0 = (1)$ 1, (2) 1.7, (3) 2, and (4) 2.3 mA. The time scale is 200 μs/division and the current scale is 10 mA/division.

In preliminary experiments, the most intense emission lines from the first positive (1^+), second positive (2^+), and first negative (1^-) nitrogen band systems were determined. These are the 585.4-nm, 580.4-nm, and 575.5-nm lines of the 1^+ system (the $v' = 10 \longrightarrow v = 6$, $11 \longrightarrow 7$, and $12 \longrightarrow 8$ transitions, respectively); the 405.94-nm, 375.54-nm, 371.05-nm, 389.46-nm, and 409.5-nm lines of the 2^+ system (the $0 \longrightarrow 3$, $1 \longrightarrow 3$, $2 \longrightarrow 4$, $3 \longrightarrow 6$, and $4 \longrightarrow 8$ transitions, respectively); and the 391.4-nm line of the 1^- system (the $0 \longrightarrow 0$ transition). Here, v' and v are the numbers of the vibrational levels of the upper and lower electronic states, respectively. The spectrum of the corona emission was measured with an MUM-2 monochromator with a 1200 groove/mm diffraction grating and an FEU-100 photomultiplier attached to the output of the monochromator. The spectral and time resolutions of these measurements were 0.8 nm and 1 μs, respectively.

3. EXPERIMENTAL RESULTS

We recall that the main object of our study is a high-current negative corona in nitrogen. The properties of this corona were described in detail in [14]. At a given duration and amplitude ΔU of the voltage pulse applied to a steady-state corona discharge, a spark can be initiated only at a certain value of the initial corona current I_0. Clearly, the higher ΔU, the lower the value of I_0 required for initiating a spark. The opposite is also true: the higher I_0 (i.e., the closer the corona to the threshold for spark ignition), the lower the required value of ΔU.

Table 1. Mean time τ_s of spark formation in a negative corona ($d = 40$ mm)

I_0, mA	1.5	2.0	2.5
ΔU, kV	τ_s, ms		
13.5	5	0.9	0.50
14.5	4	0.55	0.35
15.5	3	0.35	0.15

The above is illustrated in Fig. 2, which presents oscillograms demonstrating the response of a negative corona on the same overvoltage pulse with a 1-μs rise time for different initial corona currents. Note that these oscillograms were recorded using a scheme that cut off the current at a level of about 50 mA; therefore, the waveforms thus obtained do not correctly describe the time behavior of the trailing edge of the current pulse.

It can be seen that, after applying the voltage pulse, the current jump related to the spark formation is observed not for all the initial currents I_0. At low I_0 (in our case, at $I_0 = 1$ mA), the corona current first rapidly increases by 12–15 mA and then slowly (over a few milliseconds) decreases to its quasi-steady value determined by the sum of U_0 (the initial corona voltage) and ΔU. If U_0 and ΔU exceed certain critical values, this stage of a slow decrease in the current after its initial jump is replaced by a slow increase, which finishes with a sharp current jump.

In general, the increase in I_0 and ΔU leads to a decrease in the time interval τ_s between applying the overvoltage pulse and the spark discharge (see Table 1). Thus, at $I_0 = 1.5$ mA, $U_0 = 12.3$ kV, and $\Delta U = 14.5$ kV, this time is $\tau_s \approx 4$ ms, whereas for $I_0 = 2.5$ mA, $U_0 = 13$ kV, and $\Delta U = 15.5$ kV, it is $\tau_s \approx 150$ μs.

The evolution of the discharge current and voltage is shown in more detail in Fig. 3. The time evolution of the current and voltage over a rather long time interval after applying the overvoltage pulse is shown in Fig. 3a. The total voltage drop across the discharge does not exactly follow the applied voltage pulse because of the presence of the ballast resistance $R_2 = 78$ kΩ between the discharge and the pulse generator. Indeed, in the initial stage of the process, a strong overvoltage arises across the negative corona. Thus, Fig. 3a (which corresponds to $d = 40$ mm) shows that the voltage first rapidly increases from 13.5 to 26 kV and then slowly decreases in accordance with the current evolution. After the gap breakdown, the discharge voltage sharply drops to 4 kV and then slowly (over a time of a few milliseconds) returns to its initial value.

It can be seen from Fig. 3 that, after the initial jump caused by applying the overvoltage pulse, the discharge current varies slightly until the gap is bridged by the spark channel. At the instant of bridging, a short current spike with an amplitude of ~1 A is observed (the spike amplitude increases with increasing I_0 and ΔU). After this, the current sharply decreases (over a time less than 0.5 μs) to a value of 120–170 mA, which is determined

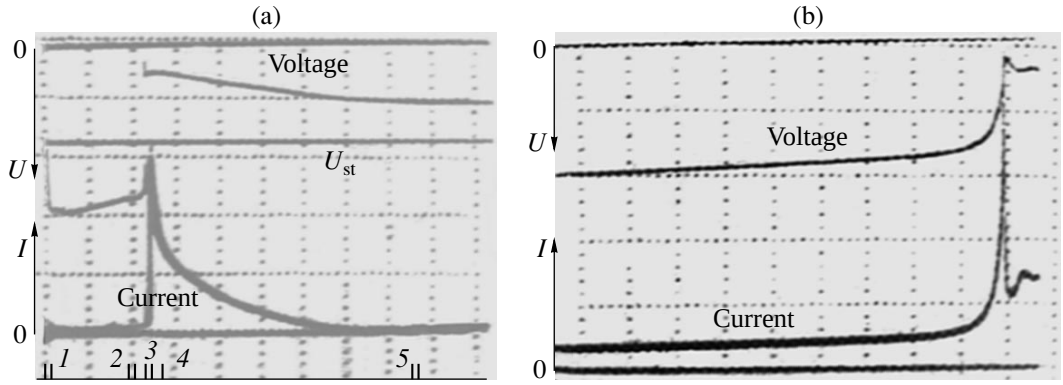

Fig. 3. Oscillograms of the current and voltage during the formation of a spark in a negative corona in nitrogen for P = 770 torr, d = 40 mm, r_c = 0.1 mm, I_0 = 2 mA, U_0 = 13.5 kV, and ΔU = 14.5 kV. The current scale is 100 mA/division, the voltage scale is 9.25 kV/division, and the time scale is (a) 0.5 ms/division and (b) 10 μs/division; U_{st} is the initial corona voltage. Marks *1–5* correspond to the discharge stages shown in the electron-optical photographs in Figs. 5–9.

by the external circuit. This current is approximately one order of magnitude higher than the corona current immediately after applying the overvoltage pulse; however, it is insufficient to maintain the high conductivity of the spark channel. As a result, the channel decays over about 2 ms; this is accompanied by a decrease in the discharge current and a slow increase in the discharge voltage.

Note that the spark current is approximately three orders of magnitude higher than the initial corona current. It is clear that such a high current cannot be continuously maintained by the external circuit: it can only be sustained over a short time by the charging of stray capacitances in the external circuit. This is why the spark duration is very short.

Let us now describe the visual picture of the transformation of a steady-state negative corona into a spark. First, for the sake of completeness, we describe the formation of a spark against the background of a point-to-plane negative corona in air. It turned out that, in contrast to the case where the voltage is applied to a nonionized gap (see Section 1), applying an overvoltage pulse with a large rise time to a negative corona in air does not lead to the formation of a sheaf of primary and secondary streamers propagating from the point cathode toward the plane anode (Fig. 4).

The increase in the voltage applied to a negative corona in air leads to an increase in the corona current and its transformation into a glow discharge [15]. This transformation is accompanied by the production of a plasma in the gap and the formation of an anode layer, which is unstable against contraction into current spots (see Fig. 4, which shows the oscillograms of the discharge current and voltage and a series of the discharge photographs, starting from the instant of the anode layer formation; note that, at earlier times, there was no glow in the interelectrode gap and at the anode). These spots provoke the formation of a plasma channel (an analogue of the secondary channel) near the anode (rather than near the point cathode), which then grows toward the cathode.

It may be said that, in this case, the formation of the spark channel does not proceed in accordance with the scenario described in Section 1 but is caused by the contraction of a glow discharge that is formed from a negative corona as the discharge current increases. An important point is that the discharge is contracted near the plane electrode, rather than near the point electrode. This kind of contraction is related to the onset of ionization instabilities and is typical of discharges in dense gases (see, e.g., [16–19]).

The above feature of the spark formation in a negative corona in air indicates that the generation of primary streamers in a short gap in the initial stage of breakdown is not a necessary condition for the development of the secondary streamers and spark. If there are some other physical factors enabling the formation of a plasma channel (an analogue of the secondary streamer) near one of the electrodes, then no primary streamers are needed. To illustrate, we note the well-known electric filter phenomenon referred to as a reverse corona [20]. In this case, the plasma channel (the secondary streamer) in a negative corona is induced by a current spot produced at the plane electrode due to the local breakdown of the highly resistive dust layer accumulated at the anode.

Let us now consider the visual picture of the spark development in a negative corona in nitrogen using electron-optical photographs in Figs. 5–8, which show the different phases of the spark formation. The time intervals corresponding to these phases are marked in Fig. 3a. Thus, the time evolution of the visual picture of discharge is related to the dynamics of the discharge current and voltage. Note that the photographs and oscillograms were taken under somewhat different discharge conditions; nevertheless, the waveforms of the

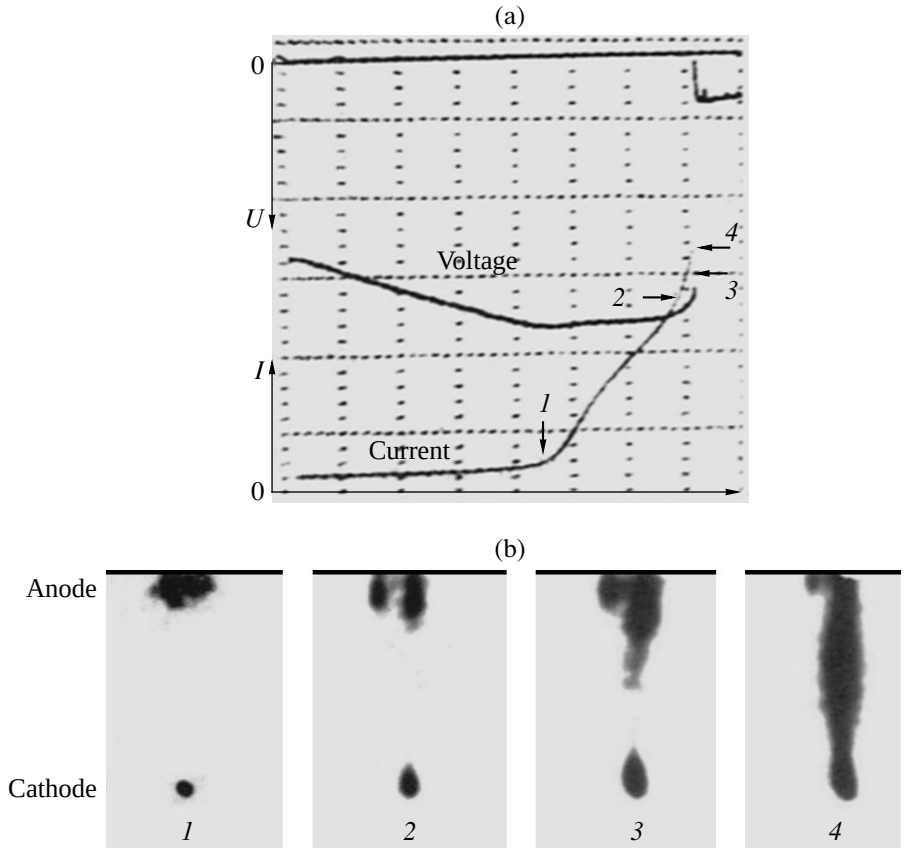

Fig. 4. (a) Oscillograms of the current and voltage and (b) the electron-optical photographs illustrating the formation of a spark in a negative corona in air for P = 300 torr, d = 10 mm, r_c = 0.1 mm, I_0 = 100 μA, U_0 = 4.9 kV, and ΔU = 5 kV. The current scale is 2 mA/division, the voltage scale is 1850 V/division, and the time scale is 100 μs/division. The exposure times in panel (a) are τ_{e1} = 5 μs, τ_{e2} = 2 μs, τ_{e3} = 1 μs, and τ_{e4} = 0.5 μs.

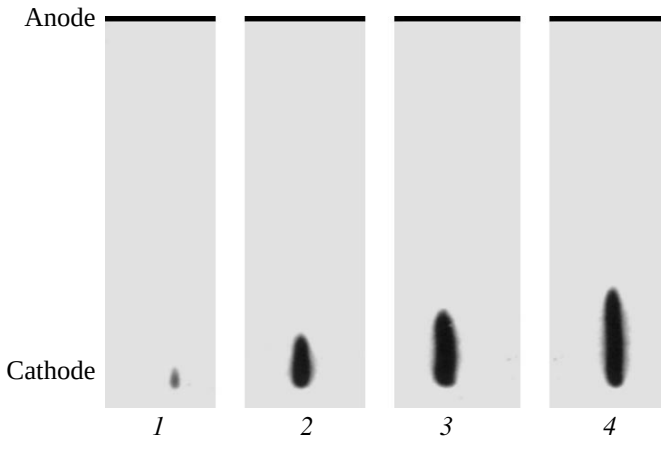

Fig. 5. Electron-optical photographs illustrating the formation of a spark in a negative corona in nitrogen for P = 770 torr, d = 40 mm, r_c = 0.1 mm, I_0 = 2.5 mA, U_0 = 14.3 kV, and ΔU = 15.5 kV. The exposure time is τ_e = 1 μs; the time intervals between the frames are t_{12} = 10 μs, t_{23} = 50 μs, and t_{34} = 10 μs. The photographs were taken between marks *1* in Fig. 3a.

discharge current and voltage in this cases are qualitatively similar. For this reason, the positions of the marks in Fig. 3a were chosen in accordance with the relative positions of the illustrated discharge phases in an actual current waveform.

In the case of a high-current corona in nitrogen, there is already a short (a few millimeters long) steady-state plasma channel near the point cathode. This channel is the source of a bright orange glow (see [14]) and can be regarded as an analogue of the secondary streamer. Indeed, after applying the overvoltage pulse to the gap, this streamer begins to extend toward the plane anode, as does the secondary streamer (see Figs. 5–8). In contrast to the case of a nonionized gap [3], no branching of the secondary streamer was observed in the corona. The propagation velocity of the secondary anode streamer in nitrogen is relatively low and varies in the range of $V_c = 10^3$–10^4 cm/s; i.e., it is two to three orders of magnitude lower than the velocity of the secondary streamer in an nonionized gap. Within this range, the propagation velocity of the secondary streamer increases with the initial corona current I_0 and the amplitude of the overvoltage pulse ΔU.

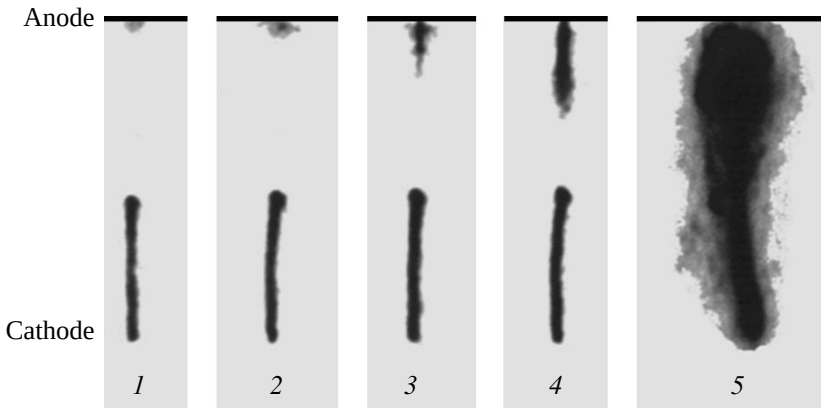

Fig. 6. Electron-optical photographs illustrating the formation of a spark in a negative corona in nitrogen for P = 770 torr, d = 40 mm, r_c = 0.1 mm, I_0 = 1.2 mA, U_0 = 13.3 kV, and ΔU = 14.5 kV. The exposure is τ_e = 1 μs for the first four frames and 0.5 μs for the last frame; the time intervals between the frames are t_{12} = 10 μs, t_{23} = 50 μs, and t_{34} = 10 μs. Photographs *1–4* were taken between marks *2* in Fig. 3a, and photograph *5* was taken at the instant indicated by mark *4* in Fig. 3a.

In the initial high-current corona, most of the gap is dark. There is emission only from the cathode region and the orange plasma channel adjacent to the point electrode. Such a situation is also retained after applying the overvoltage pulse until the plasma channel covers about 40% of the gap length. Then, a blue glow arises at the plane anode; i.e., there occurs an anode layer typical of a glow discharge.

The spatial structure of the anode glow depends on the length of the interelectrode gap d. At d = 40 mm, there is a continuous and diffuse anode glow with a characteristic diameter of about 7 mm (Figs. 6, 7). At d = 10 mm, the anode glow has the form of several (three to four) current spots (about 1 mm in diameter each) spaced a distance of about 1 mm from one another (Fig. 8). The characteristic current at which the anode layer is formed after applying the overvoltage pulse is I_{ap} = 10–15 mA at d = 40 mm, whereas in a steady-state corona, the anode layer arises at a much lower current of $I_{as} \cong 2.7$ mA. The critical currents I_{ap} and I_{as} are nearly proportional to d^2.

After the anode layer is formed, the spark develops much faster; however, it can develop in different ways, depending on I_0 and ΔU. Below, by low and high I_0 and ΔU values, we will mean those that are close to the minimum and maximum values of these parameters within the ranges I_0 = 0.9–2.5 mA and ΔU = 8.5–16.5 kV under study.

At low I_0 and ΔU, a new plasma channel (a secondary anode streamer) begins to propagate from the anode current spot toward the first (cathode) streamer (Fig. 6). The velocity of the plasma channel propagating from the plane anode is approximately ten times higher than that of the plasma channel propagating from the point electrode. When these two plasma channels (the cathode and anode secondary streamers) meet, the current sharply increases and the voltage across the gap

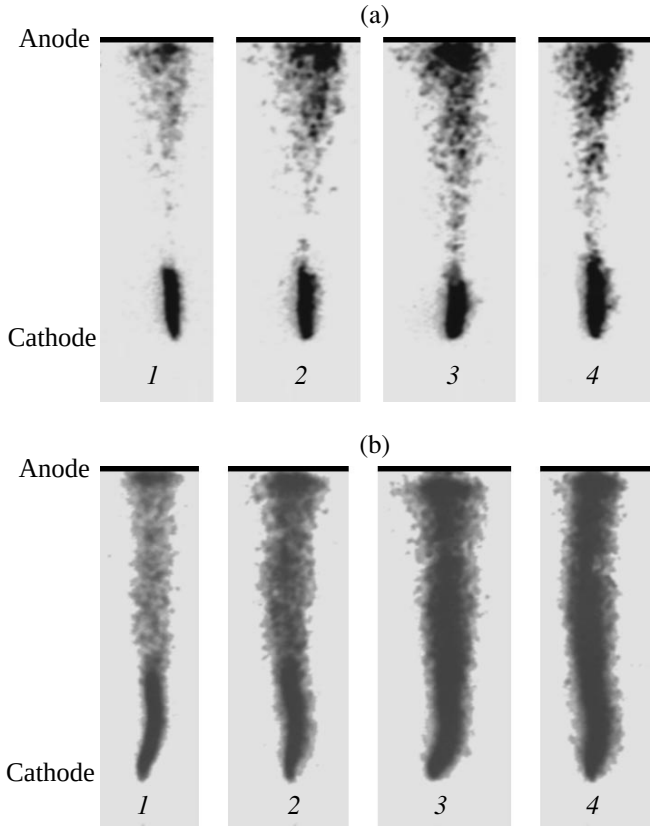

Fig. 7. Electron-optical photographs illustrating the formation of a spark in a negative corona in nitrogen at a high overvoltage for P = 770 torr, d = 40 mm, r_c = 0.3 mm, I_0 = 2.5 mA, U_0 = 24.5 kV, and ΔU = 15.5 kV. The exposure time is τ_e = 0.2 μs. The time intervals between the frames are t_{12} = 3 μs, t_{23} = 10 μs, and t_{34} = 3 μs, and the time interval between panels (a) and (b) is 20 μs. All the photographs were taken between marks *3* in Fig. 3a.

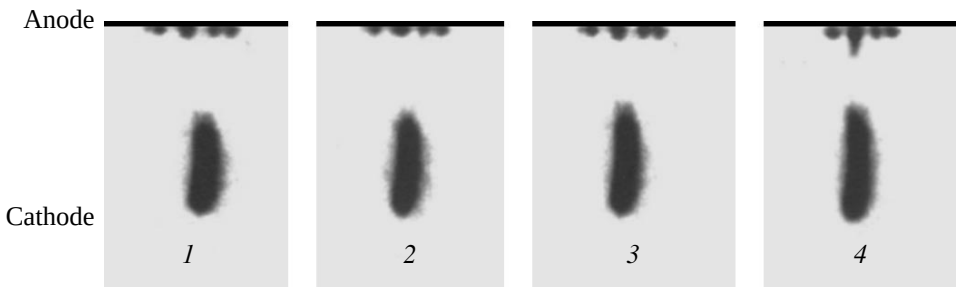

Fig. 8. Electron-optical photographs illustrating the formation of a spark in a short-gap negative corona in nitrogen for P = 770 torr, d = 10 mm, r_c = 0.1 mm, I_0 = 0.2 mA, U_0 = 2.5 kV, and ΔU = 9 kV. The exposure time is τ_e = 0.5 μs, and the time intervals between the frames are t_{12} = 3 μs, t_{23} = 10 μs, and t_{34} = 3 μs. All the photographs were taken between marks *3* in Fig. 3a.

decreases. Formally speaking, this scenario of the spark formation is similar to that described in [3] (see Section 1) for a nonionized gap filled with nitrogen. However, the mechanisms for the generation of the anode current spots that induce secondary streamers are very different. In [3], anode spots arose due to the bridging of a nonionized gap by primary streamers. In our case, there are no primary streamers and the anode spot arises due to the contraction of the anode layer of the glow discharge that precedes a spark.

At high I_0 and ΔU, the voltage drop between the anode and the head of the plasma channel propagating from the cathode (the secondary cathode streamer) is significantly higher than in the previous case. Due to the presence of the high electric field in this region, the glow intensity in the gap between the anode and the head of secondary cathode streamer sharply increases immediately after the anode layer is formed (Fig. 7). The glow is first shaped as a cone with the base resting on the anode layer and the vertex located at the cathode streamer head. The cone then begins to shrink in the radial direction (simultaneously along its length, but more rapidly near the anode) up to the transverse size of the secondary cathode streamer. As in the previous case, the bridging of the gap is accompanied by a sharp jump in the current and a decrease in the gap voltage.

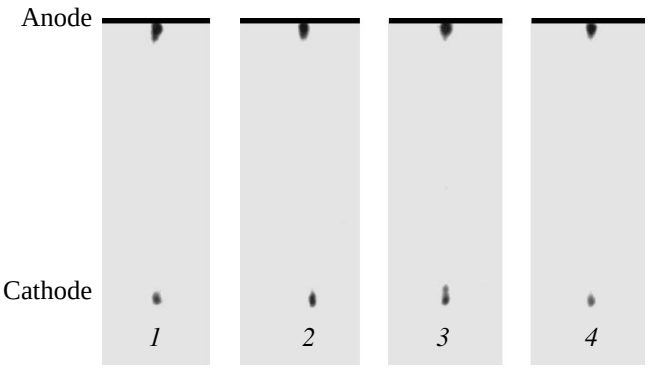

Fig. 9. Electron-optical photographs illustrating the decay of a spark in a negative corona in nitrogen for P = 770 torr, d = 40 mm, r_c = 0.1 mm, I_0 = 2.5 mA, U_0 = 14.3 kV, and ΔU = 15.5 kV. The exposure time is τ_e = 2 μs, and the time intervals between the frames are t_{12} = 10 μs, t_{23} = 50 μs, and t_{34} = 10 μs. All the photographs were taken between marks *5* in Fig. 3a.

The bridging of the gap by the plasma channel is also accompanied by an increase in the glow intensity. It was observed experimentally that the glow intensity from the spark channel reaches its maximum value with a some delay with respect to the maximum of the discharge current, which occurs at the instant of bridging. In the stage in which the current decreases, the glow intensity from the spark channel is still increasing and reaches its maximum value 50–100 μs after bridging the gap (Fig. 6, frame 5), when the current is about 100 mA. The glow intensity from a decaying spark then begins to decrease with different rates in different regions of the discharge. The glow intensity from the plasma channel decreases most rapidly (over about 1–2 ms). The glow from the anode spots lasts for ~4–5 ms (see Fig. 9). The glow from the cathode region near the point electrode lasts for approximately the same time.

Thus, we can note the following significant features of spark breakdown in a short gap against the background of a negative corona in nitrogen: First, the scenario of the spark channel formation in a corona corresponds to the development of the nonsimultaneous (along the gap length) discharge contraction induced by ionization instabilities. Second, the spark itself (i.e., a bright flash in the interelectrode gap) does not coincide with the instant at which the plasma channel bridges the gap (i.e., with the peak of the discharge current). Third, the consequences of spark breakdown (such as the glow from the anode spots, the glow of the plasma channel between the electrodes, and the increased glow from the cathode region) persist over quite a long time (a few milliseconds). Similar features are also characteristic of spark breakdown against the background of a negative corona in air (the only quantitative difference is in the propagation velocities of the secondary streamers and the spark decay times).

Let us now consider the time evolution of the emission spectrum from different regions of a corona dis-

charge during the formation of a spark. We note that, throughout the entire discharge gap, the time behaviors of the emission intensities of all the spectral lines were similar; the only quantitative difference was in the emission intensities.

Cathode region. Here, the line of the 1^- band system of molecular nitrogen was most intense; next in intensity were the lines of the 2^+ system and, then, the lines of the 1^+ system. Their intensities were approximately in the ratio of 1 : 0.5 : 0.05 (the line wavelengths were listed in Section 2). The emission intensities of all the lines in the cathode region strongly fluctuated with a characteristic frequency of several kilohertz; in our opinion, this was related to the unsteady behavior of the cathode layer because of its transformations into a prearc cathode spot [21] and back into the regime of a glow discharge.

After applying the overvoltage pulse, the emission intensity generally followed the time evolution of the discharge current; i.e., it increased over time (see Fig. 10). However, there was no jump in the emission intensity from the cathode region when the gap was bridged by the plasma channel. At the instant of the current jump, the emission intensity of the lines in question was often low (lower than before or after the jump).

After the current jump, the intensities of all the emission lines continued to increase over 100–300 μs and then slowly (over a few milliseconds) dropped to their initial values. The above fluctuations of the glow intensity in the cathode region were also observed in the stage in which the current decreased. It was also found that the higher I_0 and ΔU, the higher (on the average) the emission intensity of all the lines both before and after the current jump.

The middle of the gap. Under our experimental conditions, the maximum intensity of the emission line of the 1^- band system in the middle of the gap was approximately half as high as that in the cathode region. The intensity ratio between this line in the middle of the gap and the intensities of the lines from the 2^+ and 1^+ systems was approximately 1 : 0.6 : 0.2.

In the initial negative corona, there was no glow in the middle of the gap. It arises with a certain delay time τ_d after applying the overvoltage pulse. The delay time τ_d decreases with increasing I_0 and ΔU. Table 2 presents the τ_d values for a gap with d = 40 mm.

The glow in the middle of the gap arises and develops in different ways, depending on I_0 and ΔU. At low I_0 and ΔU, the glow arises here due to the arrival of the plasma channel slowly propagating from the cathode (the secondary cathode streamer). In this case, the glow intensity varies nonmonotonically over time and has two characteristic spikes (Fig. 11). The first spike is related to the arrival of the head of the secondary streamer: the glow intensity sharply increases and then slowly (over a time of approximately 0.5 ms, which is determined by the velocity of the streamer head propagating away from the observation zone) decays to a certain steady level determined by the emission from the homogeneous body of the streamer. This glow intensity is retained up to the current jump related to the bridging of the gap by the streamer. After the gap is bridged, the emission intensity from the observation zone again sharply increases over a characteristic time of about 100 μs. The intensity of the second spike is always higher than the intensity of the first spike, because it corresponds to the emission from the spark channel.

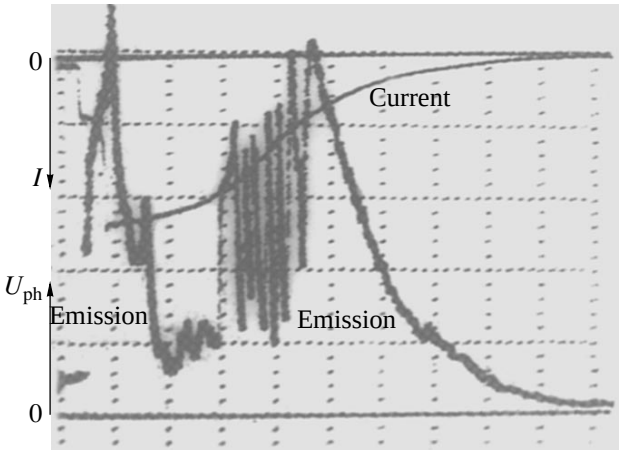

Fig. 10. Time evolution of the cathode glow (the signal U_{ph} of the 389.4-nm emission corresponding to the 3 ⟶ 6 transition of the 2^+ band system) in the course of spark formation for P = 770 torr, d = 40 mm, r_c = 0.1 mm, I_0 = 2.5 mA, U_0 = 14.3 kV, and ΔU = 15.5 kV. The current scale is 20 mA/division, the voltage scale is 50 mV/division, and the time scale is 0.5 ms/division.

As the streamer head propagates away from the observation zone, the emission intensity decreases; this indicates that the electric field in the head of the secondary streamer is significantly higher than in its homogeneous body. The length over which the homogeneous streamer body is established is much longer than the transverse size of the secondary streamer.

At high I_0 and ΔU, the spark develops much faster and the secondary cathode streamer does not reach the middle of the gap. In this case, the emission from the observation zone arises due to the formation of an uniformly and diffusely glowing channel between the head of the cathode streamer, which has not reached the mid-

Table 2. Mean delay time τ_d of the negative corona glow from the middle of the discharge gap

I_0, mA	1.5	2.0	2.5
ΔU, kV	τ_d, ms		
14.5	2	0.5	0.35
15.5	1	0.35	0.15

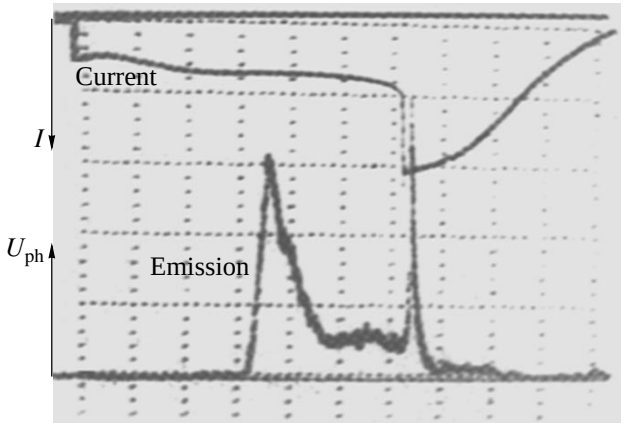

Fig. 11. Time evolution of the glow from the middle of the discharge gap (the signal U_{ph} of the 405.9-nm emission corresponding to the $0 \longrightarrow 3$ transition of the 2^+ band system) in the course of spark formation for $P = 770$ torr, $d = 40$ mm, $r_c = 0.1$ mm, $I_0 = 1.5$ mA, $U_0 = 12.3$ kV, and $\Delta U = 14.5$ kV. The current scale is 20 mA/division, the voltage scale is 20 mV/division, and the time scale is 0.5 ms/division.

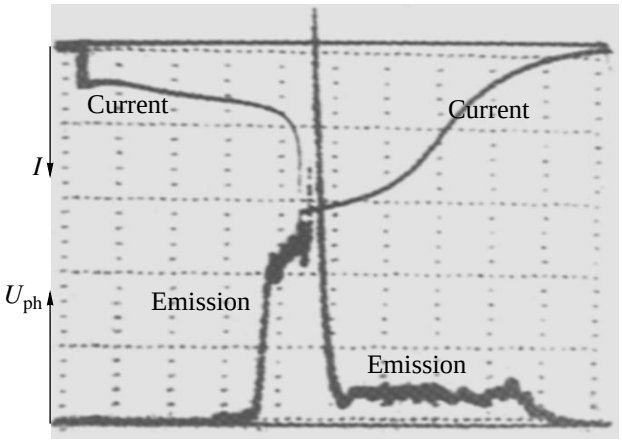

Fig. 12. Time evolution of the glow from the middle of the discharge gap (the signal U_{ph} of the 375.54-nm emission corresponding to the $1 \longrightarrow 3$ transition of the 2^+ band system) in the course of spark formation for $P = 770$ torr, $d = 40$ mm, $r_c = 0.1$ mm, $I_0 = 1.5$ mA, $U_0 = 12.3$ kV, and $\Delta U = 15.5$ kV. The current scale is 20 mA/division, the voltage scale is 20 mV/division, and the time scale is 0.5 ms/division.

dle of the gap, and the anode. The delay time τ_d of the glow is determined by the propagation time of the secondary streamer from the cathode over a distance of about 40% of the total gap length. Under these conditions, the emission intensity from the middle of the gap increases monotonically both before and after bridging the gap by the plasma channel (Fig. 12).

At high I_0 and ΔU, the maximum intensity of all the emission lines is also observed in the stage in which the current decreases. The characteristic time interval between the current jump and the maximum of the emission intensity from the middle of the gap is 50–100 μs. The average glow decay time in a decaying spark channel is 1–2 ms. This time decreases with increasing I_0 and ΔU (probably because of an increased production of nitrogen atoms, which quench the excited molecular states). It was also found that the emission intensity of the 1^- band system decreased 1.5 times faster than that of the 2^+ system, which, in turn, decreased faster than the intensity of the emission lines of the 1^+ system.

Anode region. The anode glow arises a certain time τ_a after applying the overvoltage pulse. This time decreases with increasing I_0 and ΔU and lies within the range of 0.1–1 ms. Table 3 presents the τ_a values for a 40-mm-long gap.

Table 3. Mean delay time τ_a of the anode glow

I_0, mA	1.5	2.0	2.5
ΔU, kV	τ_a, ms		
14.5	1	0.45	0.25
15.5	0.7	0.2	0.1

It can be seen that, for the same discharge parameters, we have $\tau_a < \tau_d$; i.e., the anode glow arises earlier than does the glow in the middle of the gap. The emission intensity of all the lines gradually increases until the gap is bridged by the plasma channel (Fig. 13). At the instant of bridging, a short spike in the emission intensities of all the lines is observed. For the lines of the 1^+ band system, the amplitude of this increase is much lower than for the other emission lines.

In the anode region, the emission at the $0 \longrightarrow 3$ transition of the 2^+ band system arises first. The emission at the other transitions of the 2^+ system ($1 \longrightarrow 3$, $2 \longrightarrow 4$, $3 \longrightarrow 6$, and $4 \longrightarrow 8$) occurs with a small time delay with respect to the emission at the $0 \longrightarrow 3$ transition. The emission from the 1^+ and 1^- systems arises after the emission from the 2^+ system; most often, it appears when the plasma channel bridges the gap.

For all of the lines, the intensity of the anode glow also continues to increase over approximately 100–200 μs after bridging the gap (the higher I_0 and ΔU, the shorter this time interval) in spite of the decrease in the current. After reaching its maximum value, the intensity of the anode glow slowly decreases over a time interval a few times longer than the characteristic decay time of the emission intensity from the middle of the gap. However, the ratio of the decay rates of the intensities of the different emission lines from the anode region is the same as that from the middle of the gap: the glow intensity of the 1^- system decreases one-and-a-half times faster than the glow intensity of the 2^+ system, whereas the longest (but the weakest) glow is observed in the emission lines of the 1^+ system.

4. DISCUSSION

The results obtained show clearly that the formation of a spark in a negative corona, in which the criterion of streamer breakdown is definitely not met, proceeds much more slowly than the breakdown of a nonionized gap. The scenarios of the spark formation in this cases are also very different. The presence of a corona provides conditions for the formation of a plasma channel (secondary streamer) in the gap due to the evolution of the corona structure with increasing current, rather than due to the generation of primary streamers. Thus, in nitrogen, the plasma channel at the point electrode exists already in the steady-state regime of a high-current (1–2 mA) corona. As the current increases after applying an overvoltage pulse, the corona transforms into a volume glow discharge in which a spark is formed as a result of discharge contraction due to the development of ionization instabilities both at the anode and in the gap.

Let us discuss in more detail the mechanism for the formation of a secondary streamer at the plane electrode (detailed experimental data on the transformation of a negative corona into a volume glow discharge, as well as on the origin and subsequent evolution of the anode layer, are presented in [13]). As was shown in [22], the transversely homogeneous anode layer of a volume glow discharge is characterized by a negative differential resistance; i.e., the current–voltage characteristic of the layer has a segment with a negative slope. For this reason, in the absence of stabilizing factors (e.g., turbulent diffusion caused by fast blowing of the working gas through the gap), this layer is unstable against the development of perturbations in the direction perpendicular to the current. As a result, the transversely homogeneous anode region shrinks into current spots (or a single current spot) with a high (up to 100 A/cm^2) "normal" current density [23], which increases quadratically with the gas pressure. In our opinion, it is the anode current spots that induce the formation of the plasma channel (secondary streamer) at the plane anode, because the increased energy release within and near the current spots provokes the onset of ionization instabilities and the subsequent increase in the conductivity in these regions.

An interesting effect that has not yet been noted in the literature is the time delay (approximately 100 μs) of the maximum intensity of the channel glow with respect to the instant at which the plasma channel (secondary streamer) bridges the gap. This effect is apparently related to gas heating, which leads to a decrease in the gas density inside the plasma channel and, as a result, to an increase in the reduced electric field E/N even at a constant voltage across the gap. Since the rate constants for the excitation of electronic states grow exponentially with E/N, the emission intensity from the plasma channel can increase even when the current flowing through the channel decreases, as was observed in our experiments.

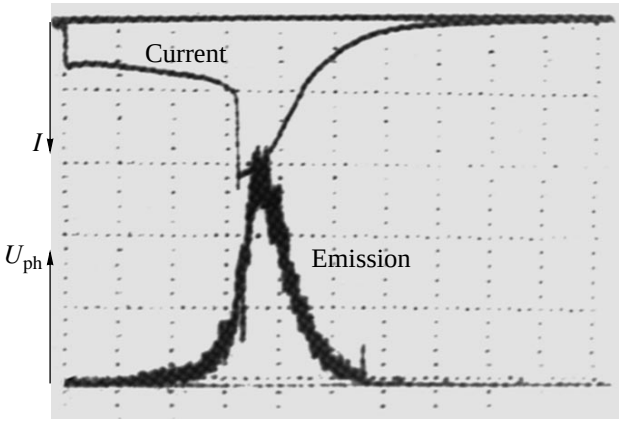

Fig. 13. Time evolution of the anode glow (the signal U_{ph} of the 405.9-nm emission corresponding to the 0 ⟶ 3 transition of the 2^+ band system) in the course of spark formation for P = 770 torr, d = 40 mm, r_c = 0.1 mm, I_0 = 1.5 mA, U_0 = 12.3 kV, and ΔU = 15.5 kV. The current scale is 20 mA/division, the voltage scale is 50 mV/division, and the time scale is 1 ms/division.

Intense gas heating in the spark channel is a well-known phenomenon. This heating also manifests itself in the sound effects (loud clicks) that accompany a spark discharge. Estimates show that, under our experimental conditions, the specific energy deposition in the plasma channel is rather high (about 4–6 kJ/l). However, calculations of the dynamics of the emission intensity by a self-consistent model that takes into account energy deposition in different degrees of freedom, the pushing of the gas out of the channel, and the effect of gas heating on the charge and chemical kinetics, as well as the kinetics of the excited states, is a rather complicated problem. Self-consistent simulations of the dynamics of high-current channels were performed in [24, 25], where the parameters of a long leader were calculated with allowance for its intense heating.

5. CONCLUSIONS

Our experiments performed in a point-to-plane discharge gap have shown that, in contrast to the case of a nonionized gap, a spark in a negative corona in air and nitrogen under conditions such that the criterion for streamer breakdown is not met is formed in the absence of fast primary streamers and, hence, the spark develops very slowly. In this case, the spark precursors (secondary streamers) arise either near the point electrode, from the plasma channel that exists in the initial corona discharge, or near the plane electrode, due to the contraction of the anode layer of the glow discharge into which the corona transforms as the current increases.

During the propagation of the plasma channel (the secondary streamer), the discharge current changes only slightly. The discharge current increases sharply

(nearly a hundredfold) when the streamer bridges the gap. The high current (about 1 A) at this instant is provided by a rapid (over a time less than 0.5 μs) charging of stray capacitances in the external circuit. Thereafter, the current decreases to a value of 120–170 mA, which is determined by the external circuit, and then slowly (over 1–2 ms) decreases to its initial value.

We note two important features of spark breakdown in a negative corona. First, the spark itself (i.e., a bright flash in the interelectrode gap) does not coincide in time with the peak of the discharge current, which occurs when the plasma channel bridges the gap. Second, the consequences of spark breakdown (such as intense optical emission from the anode spots, the plasma channel glow, and the enhanced cathode glow) persist over quite a long time (a few milliseconds) after bridging the gap.

ACKNOWLEDGMENTS

This study was supported in part by the Russian Foundation for Basic Research (project no. 02-02-16913) and the RF Program for State Support of Leading Scientific Schools (project no. NSh 794.2003.2).

REFERENCES

1. Yu. P. Raizer, *Gas Discharge Physics* (Nauka, Moscow, 1987; Springer-Verlag, Berlin, 1991).
2. L. B. Loeb, *Electrical Coronas: Their Basic Physical Mechanism* (University of California Press, Berkely, 1965).
3. *Electrical Breakdown in Gases*, Ed. by J. M. Meek and J. D. Craggs (Wiley, New York, 1978; Inostrannaya Literatura, Moscow, 1980).
4. H. Raether, *Electron Avalanches and Breakdown in Gases* (Butterworths, London, 1964; Mir, Moscow, 1968).
5. I. P. Vereshchagin, *Corona Discharges in Electron–Ion Technology* (Énergoatomizdat, Moscow, 1985).
6. E. Marode, F. Bastien, and M. Bakker, J. Appl. Phys. **50**, 140 (1979).
7. E. M. Bazelyan and I. M. Razhanskiĭ, *Spark Discharge in Air* (Nauka, Novosibirsk, 1988).
8. Yu. S. Akishev, V. A. Karal'nik, and N. I. Trushkin, in *Selected Research Papers on Spectroscopy of Nonequilibrium Plasma at Elevated Pressures*, Ed. by V. N. Ochkin (SPIE, Washington, 2002), p. 26.
9. W. J. Yi and P. F. Williams, J. Phys. D **35**, 205 (2002).
10. R. Ono and T. Oda, J. Phys. D **36**, 1952 (2003).
11. E. M. Veldhuizen and W. R. Rutgers, J. Phys. D **35**, 2169 (2002).
12. A. Goldman, M. Goldman, M. Rautureau, and C. Tchoubar, J. Phys. Paris **8**, 486 (1975).
13. Yu. S. Akishev, M. E. Grushin, V. B. Karal'nik, *et al.*, Fiz. Plazmy **29**, 198 (2003) [Plasma Phys. Rep. **29**, 176 (2003)].
14. Yu. S. Akishev, G. I. Aponin, V. B. Karal'nik, *et al.*, Fiz. Plazmy **30**, 835 (2004) [Plasma Phys. Rep. **30**, 779 (2004)].
15. Yu. S. Akishev, M. E. Grushin, I. V. Kochetov, *et al.*, Fiz. Plazmy **26**, 172 (2000) [Plasma Phys. Rep. **26**, 157 (2000)].
16. *Principles of Laser Plasma*, Ed. by G. Bekefi (Wiley, New York, 1976).
17. E. P. Velikhov, V. D. Pis'mennyĭ, and A. T. Rakhimov, Usp. Fiz. Nauk **122**, 419 (1977) [Sov. Phys. Usp. **20**, 586 (1977)].
18. E. P. Velikhov, V. S. Golubev, and S. V. Pashkin, Usp. Fiz. Nauk **137**, 117 (1982) [Sov. Phys. Usp. **25**, 340 (1982)].
19. Yu. I. Bychkov, Yu. D. Korolev, G. A. Mesyats, *et al.*, *Injection Gas Electronics* (Nauka, Novosibirsk, 1982).
20. S. Masuda, in *Proceedings of the 1st International Conference on Electrostatic Precipitation, Monterey, CA, 1981*, p. 340.
21. Yu. S. Akishev, A. P. Napartovich, V. V. Ponomarenko, and N. I. Trushkin, Zh. Tekh. Fiz. **55**, 655 (1985) [Sov. Phys. Tech. Phys. **30**, 388 (1985)].
22. A. M. Dykhne and A. P. Napartovich, Dokl. Akad. Nauk SSSR **247**, 837 (1979) [Sov. Phys. Dokl. **24**, 632 (1979)].
23. Yu. S. Akishev, A. P. Napartovich, P. I. Peretyat'ko, and N. I. Trushkin, Teplofiz. Vys. Temp. **18**, 873 (1980).
24. N. L. Aleksandrov, E. M. Bazelyan, I. V. Kochetov, and N. A. Dyatko, J. Phys. D **30**, 1616 (1997).
25. N. A. Popov, Fiz. Plazmy **29**, 754 (2003) [Plasma Phys. Rep. **29**, 695 (2003)].

Translated by N.N. Ustinovskiĭ